COMPUTATIONAL MODELING FOR ASSESSING CORONARY ARTERY PATHOPHYSIOLOGY

EDITED BY: Christos Bourantas, Rob Krams, Yoshinobu Onuma, Patrick W. Serruys, Peter Stone and Ryo Torii

PUBLISHED IN: Frontiers in Cardiovascular Medicine

frontiers Research Topics

ISSN 1664-8714
ISBN 978-2-83250-086-6
DOI 10.3389/978-2-83250-086-6

About Frontiers

Frontiers is more than just an open-access publisher of scholarly articles: it is a pioneering approach to the world of academia, radically improving the way scholarly research is managed. The grand vision of Frontiers is a world where all people have an equal opportunity to seek, share and generate knowledge. Frontiers provides immediate and permanent online open access to all its publications, but this alone is not enough to realize our grand goals.

Frontiers Journal Series

The Frontiers Journal Series is a multi-tier and interdisciplinary set of open-access, online journals, promising a paradigm shift from the current review, selection and dissemination processes in academic publishing. All Frontiers journals are driven by researchers for researchers; therefore, they constitute a service to the scholarly community. At the same time, the Frontiers Journal Series operates on a revolutionary invention, the tiered publishing system, initially addressing specific communities of scholars, and gradually climbing up to broader public understanding, thus serving the interests of the lay society, too.

Dedication to Quality

Each Frontiers article is a landmark of the highest quality, thanks to genuinely collaborative interactions between authors and review editors, who include some of the world's best academicians. Research must be certified by peers before entering a stream of knowledge that may eventually reach the public - and shape society; therefore, Frontiers only applies the most rigorous and unbiased reviews.
Frontiers revolutionizes research publishing by freely delivering the most outstanding research, evaluated with no bias from both the academic and social point of view. By applying the most advanced information technologies, Frontiers is catapulting scholarly publishing into a new generation.

What are Frontiers Research Topics?

Frontiers Research Topics are very popular trademarks of the Frontiers Journals Series: they are collections of at least ten articles, all centered on a particular subject. With their unique mix of varied contributions from Original Research to Review Articles, Frontiers Research Topics unify the most influential researchers, the latest key findings and historical advances in a hot research area! Find out more on how to host your own Frontiers Research Topic or contribute to one as an author by contacting the Frontiers Editorial Office: frontiersin.org/about/contact

COMPUTATIONAL MODELING FOR ASSESSING CORONARY ARTERY PATHOPHYSIOLOGY

Topic Editors:
Christos Bourantas, University College London, United Kingdom
Rob Krams, Queen Mary University of London, United Kingdom
Yoshinobu Onuma, National University of Ireland Galway, Ireland
Patrick W. Serruys, Imperial College London, United Kingdom
Peter Stone, Brigham and Women's Hospital, Harvard Medical School, United States
Ryo Torii, University College London, United Kingdom

Citation: Bourantas, C., Krams, R., Onuma, Y., Serruys, P. W., Stone, P., Torii, R., eds. (2022). Computational Modeling for Assessing Coronary Artery Pathophysiology. Lausanne: Frontiers Media SA. doi: 10.3389/978-2-83250-086-6

Table of Contents

frontiers | Frontiers in Cardiovascular Medicine

TYPE Editorial
PUBLISHED 17 January 2023
DOI 10.3389/fcvm.2023.1113835

OPEN ACCESS

EDITED BY
Salah D. Qanadli,
Université de Lausanne, Switzerland

REVIEWED BY
Umberto Morbiducci,
Polytechnic University of Turin, Italy
Stephanie Lehoux,
McGill University, Canada

*CORRESPONDENCE
Christos V. Bourantas
✉ cbourantas@gmail.com

SPECIALTY SECTION
This article was submitted to Cardiovascular Imaging, a section of the journal Frontiers in Cardiovascular Medicine

RECEIVED 01 December 2022
ACCEPTED 05 January 2023
PUBLISHED 17 January 2023

CITATION
Çap M, Torii R, Onuma Y, Krams R, Bennett MR, Stone PH, Serruys PW and Bourantas CV (2023) Editorial: Computational modeling for assessing coronary artery pathophysiology. *Front. Cardiovasc. Med.* 10:1113835. doi: 10.3389/fcvm.2023.1113835

Editorial: Computational modeling for assessing coronary artery pathophysiology

Murat Çap[1,2], Ryo Torii[3], Yoshinobu Onuma[4], Rob Krams[5], Martin R. Bennett[6], Peter H. Stone[7], Patrick W. Serruys[8] and Christos V. Bourantas[1,9]*

[1]Department of Cardiology, Barts Heart Centre, Barts Health NHS Trust, London, United Kingdom, [2]Department of Cardiology, University of Health Sciences Diyarbakir Gazi Yaşargil Education and Research Hospital, Diyarbakir, Turkey, [3]Department of Mechanical Engineering, University College London, London, United Kingdom, [4]Department of Cardiology, National University of Ireland Galway (NUIG), Galway, Ireland, [5]Department of Molecular Bioengineering Engineering and Material Sciences, Queen Mary University of London, London, United Kingdom, [6]Division of Cardiovascular Medicine, Addenbrooke's Hospital, University of Cambridge, Cambridge, United Kingdom, [7]Harvard Medical School, Brigham and Women's Hospital, Boston, MA, United States, [8]Faculty of Medicine, National Heart and Lung Institute, Imperial College London, London, United Kingdom, [9]Centre for Cardiovascular Medicine and Devices, William Harvey Research Institute, Queen Mary University of London, London, United Kingdom

KEYWORDS

coronary artery disease, computational fluid dynamics, intravascular imaging, endothelial shear stress, plaque structural stress

Editorial on the Research Topic
Computational modeling for assessing coronary artery pathophysiology

It has been more than 50 years since it has been shown that the local haemodynamic forces regulate atherosclerotic disease progression (1). *Ex vivo* and experimental studies have provided unique insights about their role on the formation of vulnerable plaques and their potential implications on plaque destabilization and rupture, while clinical studies have underscored their prognostic implications demonstrating that endothelial shear stress (ESS) and plaque structural stress (PSS) provide incremental information allowing more accurate prediction of cardiovascular events than standalone intracoronary imaging (2). Over the recent years an effort has been made to develop advanced methodologies for accurate vessel reconstruction and fast estimation of the ESS and PSS distribution at scale, and several experimental studies have been conducted to identify the mechanotransduction pathways that regulate plaque evolution. Moreover, computational modeling techniques have been introduced to assess lesion severity and vessel physiology from coronary imaging data and are expected to have broad applications in the management of patients with coronary artery disease. The special issue of Frontiers Cardiovascular Medicine on "*Computational Modeling for Assessing Coronary Artery Pathophysiology*" aimed to provide additional insights about the role of ESS and PSS on atherosclerotic evolution and the potential clinical value of computational modeling techniques. In total 11 articles were submitted, the findings of which are summarized below.

Siogkas et al. introduced a novel system to quantify fractional flow reserve (FFR) from angiographic data. The SmartFFR software relies on the use of a mathematical formula to derive the FFR from invasive coronary angiography (ICA) or computed tomography coronary angiography (CTCA). The system was validated against invasive FFR in 167 patients who underwent either CTCA and ICA or only ICA. A high correlation was noted between the estimations of SmartFFR and invasive FFR ($R_{CTCA} = 0.86$, $p < 0.001$, $R_{ICA} = 0.84$, $p < 0.001$). The smartFFR was able to accurately detect obstructive coronary artery disease with an overall accuracy of 89.1% (91.2% for ICA and 86.4% for CTCA) and required only 7 min to derive the FFR.

A similar solution was introduced by Li et al. that proposed a new method for computing FFR from ICA (AccuFFRangio). The vessel's 3D geometry was reconstructed from two ICA projections and the flow velocity was computed using TIMI frame count. The pressure drop across the lesion was computed using a formula that takes into account vessel geometry, flow rate, the viscous pressure drop, and the expansion pressure drop across the lesions. Validation of this system was performed against the estimations of the FFR in 300 patients with stable angina. The correlation between AccuFFRangio estimations and FFR was 0.83 ($p < 0.001$) while the accuracy of the system for detecting flow limiting lesions was 93.7%.

The potential applications of these systems were demonstrated in the study of Chen et al. that used computationally derived FFR—using the quantitative flow ratio (QFR) software—to assess the implications of the low-density lipoprotein cholesterol (LDL-C) levels on plaque evolution. The authors included 432 patients undergoing percutaneous coronary intervention (PCI) who had repeated ICA at 1 year follow-up. Patients with a strict LDL-C control had a lower area stenosis (36.57 ± 16.12 vs. 41.68 ± 17.39%, $p = 0.003$), a smaller change in QFR (Δ_{QFR}: 0.00 ± 0.07 vs. −0.02 ± 0.09, $p = 0.007$) and a lower incidence of flow limiting restenosis and major adverse cardiovascular and cerebrovascular events compared to patients with higher LDL-C at 1 year follow-up (2.1 vs. 8.4%, $p = 0.018$, 5.4 vs. 12.6%, $p = 0.021$, respectively).

Another application of the computational derived-FFR solutions was presented in a study of Yang et al. that included 72 patients (216 lesions) who had CCTA 1–24 months before suffering an acute coronary syndrome. Plaques characteristics in CTCA associated with increased vulnerability were used to classify lesion as high-risk or low-risk; the CTCA data were also used to measure the mean ESS, axial PSS, the pressure gradient, and the ΔFFR_{CT} across each lesion using the HeartFlow software (HeartFlow, Inc., Redwood City, California). All haemodynamic variables appeared independent predictors of plaques that caused events and provide incremental prognostic information to plaque morphology and FFR_{CT}. The predictive model including $FFR_{CT} \leq 0.80$, high-risk plaque morphology and ΔFFR_{CT} had a similar or superior discrimination ability to that including $FFR_{CT} \leq 0.80$, high-risk plaque phenotype, ESS, axial PSS, and the pressure gradient across each lesion. ESS, axial PSS, and the pressure gradient across lesions did not improve the performance of the model that included plaque phenotype, FFR_{CT} and ΔFFR_{CT} in predicting events.

The study of Dai et al. used the FlashAngio software (Rainmed Ltd., Suzhou, China) to extract the microcirculatory resistance (angio-IMR) from angiographic data and compared these estimations with the hyperemic microcirculatory resistance (HMR) computed as the ratio hyperaemic myocardial blood flow—derived from single photon emission tomography (SPECT)—and the distal coronary pressure during hyperemia derived from a flow wire. A moderate correlation ($r = 0.74$, $p < 0.001$) was found between these two indices; the accuracy of angio-IMR $\geq$ 25.1 to detect ischemia in patients with normal angiogram and ischemia on SPECT was 79.8. High angio-IMR was associated with an increased risk of cardiac death or readmission due to heart failure in patients who had PCI (hazard ratio: 11.15, 95% confidence interval: 1.76–70.42, $p = 0.010$). This analysis highlights the efficacy of angio-derived indices to measure microvascular dysfunction and their prognostic value.

Conversely, in the study of Wienemann et al. flow wire measurements were used to compare non-hyperaemic resting pressure ratios (NHPRs) indices, including the "resting full-cycle ratio" (RFR) with the FFR estimations in 712 lesions. A significant correlation was observed between RFR and FFR ($r = 0.766$, $p < 0.01$), while its diagnostic accuracy of RFR for detecting flow limiting stenosis was found to be 78%. All NHPRs had similar correlations with the FFR; as it has been reported in previous studies there was a ∼20% discordance between NHPRs indices and the FFR for the presence of flow limiting stenosis. This analysis provides additional insights about the performance of NHPRs and underscores their potential value in clinical practice.

Huang et al. examined for the first time the PSS distribution in intermediate lesions ($n = 50$) using optical coherence tomography (OCT) data. The authors found that diseased segments had higher PSS gradients, during the cardiac cycle than normal segments. In the studied lesions the PSS gradient was increased in the proximal shoulder and had its minimum value in the distal shoulder. In line with previous reports the authors reported a weak correlation between PSS gradient and plaque burden ($r = 0.37$, $p < 0.001$) or fibrous cap thickness ($r = -0.25$, $p = 0.004$). This analysis underscores the potential of OCT to measure the mechanical properties of the vessel wall and highlight the need for further validation of this concept using histology as reference standard.

In another study, Jin et al. compared the morphological and physiological characteristics of ruptured neoatherosclerotic plaques (PR-NA) and of plaques that ruptured in native vessels (PR-NV). PR-NV lesions had a larger minimum lumen area but similar length and area stenosis with the PR-NA group. The mean fibrous cap thickness and lipid index were smaller in the PR-NV group, but the incidence of calcific index and microchannels was higher compared to the PR-NA. Computational fluid dynamic analysis revealed higher ESS and lower PSS values in the PR-NA comparing the PR-NV. The authors argued that in PR-NA the high ESS is likely to affect the structural integrity of the fibrous cap leading to its instability and rupture by lower PSS compared to the native plaques.

The study of Thondapu et al. focused on the effect of blood behavior on the flow patterns and examined whether the common assumption of a Newtonian blood behavior gives similar results for the ESS distribution with a non-Newtonian model. Sixteen coronary arteries were reconstructed from OCT and angiographic data and pulsatile blood flow simulation was performed using a Newtonian and the Quemada non-Newtonian model. ESS values were higher in the non-Newtonian than the Newtonian model. Moreover, in contrast to the Newtonian model where blood viscosity had a fixed value in the non-Newtonian model there was significant temporal and spatial variation in the viscosity values. These findings underscore the limitations of a Newtonian blood behavior assumption in the assessment of the local haemodynamic milieu in the coronary arteries.

Dilba et al. focused on another arterial bed, the carotid arteries, and explored the implications of ESS and multidirectional ESS on the development of ulcers in these vessels detected by magnetic resonance imaging and CT at 2-year follow-up. The authors found that ulcers were seen more often in regions with high ESS and low relative residence time underscoring the potential importance of multidirectional shear indices in plaque destabilization.

Finally, Wu et al. provided a comprehensive review on the potential of coronary angiography in assessing the mechanical properties of the vessel wall. The presented the methodology that has been proposed to assess superficial wall strain from 4D-angiographic

images and the findings of *in silico* and *in vivo* validation studies that examined its efficacy in measuring vessel deformation. Moreover, the authors discussed the potential clinical implications of this methodology in detecting lesions that are prone to progress and cause events in native vessels, in predicting stent fracture following PCI, and in measuring the wall strain in bypass grafts that appears to affect their long-term patency. Future studies are expected to provide further insights about its value in clinical practice.

From the above it is apparent that there is a clear revolution in the field of computational modeling. Several methodologies have emerged over the recent years that appear capable to better predict cardiovascular risk and guide therapy. The advances in cardiac imaging, image processing, and computer sciences made feasible the real-time application of some of them enabling their use in clinical practice. Further research is needed to explore the full potential of the clinically applicable systems and simplify computationally expensive methods so as these to have future applications in the clinical practice and research.

Author contributions

MÇ and CB drafted the manuscript. RT, YO, RK, MB, PHS, PWS, and CB edited the manuscript. All authors have read and approved the submitted draft.

Funding

This work was funded by British Heart Foundation (BHF) grant (RG84554), the BHF Centre for Research Excellence, and the National Institute of Health Research Cambridge Biomedical Research Centre.

Conflict of interest

The authors declare that the research was conducted in the absence of any commercial or financial relationships that could be construed as a potential conflict of interest.

Publisher's note

References

1. Caro CG, Fitz-Gerald JM, Schroter RC. Arterial wall shear and distribution of early atheroma in man. *Nature.* (1969) 223:1159–60. doi: 10.1038/2231159a0

2. Thondapu V, Bourantas CV, Foin N, Jang IK, Serruys PW, Barlis P. Biomechanical stress in coronary atherosclerosis: emerging insights from computational modelling. *Eur Heart J.* (2017) 38:81–92. doi: 10.1093/eurheartj/ehv689

frontiers in Cardiovascular Medicine

REVIEW
published: 18 June 2021
doi: 10.3389/fcvm.2021.667310

Angiography-Based 4-Dimensional Superficial Wall Strain and Stress: A New Diagnostic Tool in the Catheterization Laboratory

Xinlei Wu[1,2,3†], Masafumi Ono[2,4†], Hideyuki Kawashima[2,4], Eric K.W. Poon[5], Ryo Torii[6], Atif Shahzad[3], Chao Gao[2,7], Rutao Wang[2,7], Peter Barlis[5,8], Clemens von Birgelen[9,10], Johan H.C. Reiber[11], Christos V. Bourantas[12,13], Shengxian Tu[14], William Wijns[2,3], Patrick W. Serruys[2,15] and Yoshinobu Onuma[2]*

[1] Institute of Cardiovascular Development and Translational Medicine, The Second Affiliated Hospital of Wenzhou Medical University, Wenzhou, China, [2] Department of Cardiology, National University of Ireland Galway (NUIG), Galway, Ireland, [3] Smart Sensors Lab, National University of Ireland Galway (NUIG), Galway, Ireland, [4] Department of Cardiology, Academic Medical Center, University of Amsterdam, Amsterdam, Netherlands, [5] Department of Medicine, Melbourne Medical School, St Vincent's Hospital, University of Melbourne, Melbourne, VIC, Australia, [6] Department of Mechanical Engineering, University College London, London, United Kingdom, [7] Department of Cardiology, Xijing Hospital, Xi'an, China, [8] Faculty of Medicine, Dentistry Health Sciences, Melbourne Medical School, University of Melbourne, Melbourne, VIC, Australia, [9] Thoraxcentrum Twente, Medisch Spectrum Twente, Enschede, Netherlands, [10] Department of Health Technology and Services Research, Technical Medical Centre, Faculty of Behavioural, Management, and Social Sciences, University of Twente, Enschede, Netherlands, [11] Department of Radiology, Leiden University Medical Center, Leiden, Netherlands, [12] Institute of Cardiovascular Science, University College London, London, United Kingdom, [13] Department of Cardiology, Barts Heart Centre, London, United Kingdom, [14] School of Biomedical Engineering, Biomedical Instrument Institute, Shanghai Jiao Tong University, Shanghai, China, [15] Imperial College London, National Heart and Lung Institute, London, United Kingdom

OPEN ACCESS

Edited by:
Antonios Karanasos, Hippokration General Hospital, Greece

Reviewed by:
Ankush Gupta, Military Hospital Jaipur, India
Philipp Stawowy, Deutsches Herzzentrum Berlin, Germany
Italo Porto, University of Genoa, Italy

***Correspondence:**
William Wijns
william.wyns@gmail.com

[†] These authors have contributed equally to this work

Specialty section:
This article was submitted to Cardiovascular Imaging, a section of the journal Frontiers in Cardiovascular Medicine

Received: *12 February 2021*
Accepted: *21 May 2021*
Published: *18 June 2021*

Citation:
Wu X, Ono M, Kawashima H, Poon EKW, Torii R, Shahzad A, Gao C, Wang R, Barlis P, von Birgelen C, Reiber JHC, Bourantas CV, Tu S, Wijns W, Serruys PW and Onuma Y (2021) Angiography-Based 4-Dimensional Superficial Wall Strain and Stress: A New Diagnostic Tool in the Catheterization Laboratory. Front. Cardiovasc. Med. 8:667310. doi: 10.3389/fcvm.2021.667310

A novel method for four-dimensional superficial wall strain and stress (4D-SWS) is derived from the arterial motion as pictured by invasive coronary angiography. Compared with the conventional finite element analysis of cardiovascular biomechanics using the estimated pulsatile pressure, the 4D-SWS approach can calculate the dynamic mechanical state of the superficial wall *in vivo*, which could be directly linked with plaque rupture or stent fracture. The validation of this approach using *in silico* models showed that the distribution and maximum values of superficial wall stress were similar to those calculated by conventional finite element analysis. The *in vivo* deformation was validated on 16 coronary arteries, from the comparison of centerlines predicted by the 4D-SWS approach against the actual centerlines reconstructed from angiograms at a randomly selected time-point, which demonstrated a good agreement of the centerline morphology between both approaches (scaling: 0.995 ± 0.018 and dissimilarity: 0.007 ± 0.014). The *in silico* vessel models with softer plaque and larger plaque burden presented more variation in mean lumen diameter and resulted in higher superficial wall stress. In more than half of the patients ($n = 16$), the maximum superficial wall stress was found at the proximal lesion shoulder. Additionally, in three patients who later suffered from acute coronary syndrome, the culprit plaque rupture sites co-localized with the site of highest superficial wall stress on their baseline angiography. These representative cases suggest that angiography-based superficial wall dynamics have the potential to identify coronary segments at

high-risk of plaque rupture and fracture sites of implanted stents. Ongoing studies are focusing on identifying weak spots in coronary bypass grafts, and on exploring the biomechanical mechanisms of coronary arterial remodeling and aneurysm formation. Future developments involve integration of fast computational techniques to allow online availability of superficial wall strain and stress in the catheterization laboratory.

Keywords: invasive coronary angiography, coronary artery dynamics, superficial wall strain, quantitative assessment method, computational coronary pathophysiology

INTRODUCTION

Coronary arteries are continuously subjected to biomechanical forces, including myocardial contraction and relaxation, intraluminal pulsatile blood pressure, flow drag forces, and constrained by surrounding tissues. These biomechanical forces generate dynamic strain and stress on the coronary arterial wall (**Figure 1A**). The dynamic wall stress induced by cyclic deformation, which is around $10^3 \sim 10^5$ times greater than fluid-induced endothelial shear stress (ESS) (2), can trigger the rupture of atherosclerotic fibrous cap and disruption of inflamed vulnerable plaque (3). With increased severity and extent of coronary artery disease, the vascular dynamic deformation performance could be deteriorated due to the loss of elasticity (4). Furthermore, the dynamic stress and deformation of atherosclerotic coronary arterial walls (**Figure 1B**) are particularly relevant to vascular remodeling acute clinical events, such as myocardial infarction or unstable angina (3), as well as the biomechanical compatibility of implanted stents and scaffolds (5).

The deformation of coronary arteries *in vivo* can be quantitatively measured by mechanical strain. The mechanical strain of arterial wall is defined as the stretching or compressing, and angular deformation relative to its predefined reference state. This wall strain caused by vessel deformation can be assessed from modern standard X-ray coronary angiography. Taking into account the maximum speed of 34.5–250.0 mm/s of the arterial motion in early systole (6, 7), coronary angiography with high frame rate (15–30 frames/s) and high spatial resolution (150–250 μm) can indeed capture the deformation of the vascular wall (8, 9). Only two angiographic image runs with different projections are needed to perform computation of four-dimensional superficial wall strain (4D-SWS) of coronary arteries (10, 11), since the dynamic deformation results from the various biomechanical forces, including cardiac contraction and blood pressure. The periodic variation in coronary arterial diameter ∼10–15% caused by pressure pulsation (12), which can be captured by angiography. Note that SWS is derived as a combination of radial diameter variation as well as deformation in the longitudinal and circumferential directions. Assuming specific material properties for the normal and stenotic arterial segments, dynamic superficial wall stress can be further calculated.

An attractive feature of this approach is an inverse computation method that the cyclic motion of coronary arteries *in vivo* is used to calculate the dynamic strain and stress of arterial walls for intraprocedural on-line computation and analysis. The arterial motion and deformation represent the resultant of various complex biomechanical and physiological alterations, including pulsatile blood pressure, vessel stretching, bending and twisting, and acting on both normal and diseased vessel segments, each with different wall composition and mechanical properties. Another promising feature of this approach is that it focuses on the biomechanical state of the superficial layer of vessel wall (i.e., the interface between lumen and subendothelial layer), which could be directly linked with plaque rupture or stent fracture.

To further understand the biomechanical triggering mechanisms of acute coronary events and eventually improve the prediction of future events, it may be of paramount importance to take SWS into account. Indeed, the angiography-based SWS reflects the dynamic deformation of coronary arteries during the cardiac cycle and "hot spots" may identify coronary segments at higher risk of plaque rupture or dissection. This review highlights the concept and validation of this new method and its potential value in identifying vulnerable coronary plaque and therefore at high risk of acute disruption or rapid disease progression.

CALCULATION MEHTODS OF ANGIOGRAPHY-BASED 4D CORONARY ARTERY DYNAMICS

The concept and application of this method are illustrated in **Figure 2**. Coronary angiograms with minimal vessel image overlap and foreshortening are selected (13). Several key time-points during the cardiac cycle are identified from the electrocardiogram or according to the different stages of vessel motion during heart contraction and relaxation (**Figure 2**) (14). The number of frames for cardiac cycle can be determined from one QRS wave to the next on the electrocardiogram, when available. Alternatively, the frame showing the initial clearance of contrast medium from the aorta by contrast-free blood during ventricular ejection identifies early systole. The combination of these signals is used to achieve time synchronization between frames from two single plane angiograms. The vessel geometries are reconstructed and then discretized into structured meshes

Abbreviations: ACS, acute coronary syndrome; BA, bifurcation angle; ESS, endothelial shear stress; FEA, finite element analysis; IVUS, intravascular ultrasound; LAD, left anterior descending; MACE, major adverse cardiovascular events; NIRS, near-infrared spectroscopy; OCT, optical coherence tomography; PCI, percutaneous coronary intervention; PSS, plaque structural stress; RCA, right coronary artery; SWS, superficial wall strain/stress; 4D, four-dimensional.

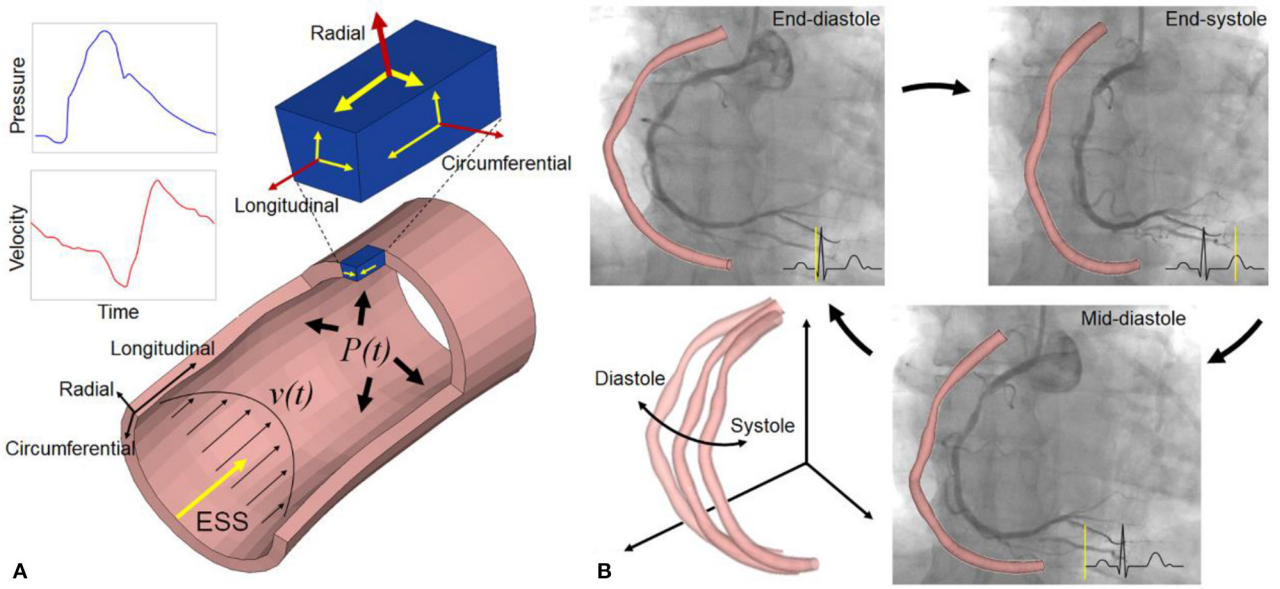

FIGURE 1 | Biomechanical forces and dynamic coronary arterial motion. **(A)** Time-varying blood flow induces endothelial shear stress (ESS) along the vessel lumen. Radial (normal) strain/stress caused by intraluminal blood pressure is perpendicular to the endoluminal wall (top surface of a small material volume, blue color), and two shear strain/stress couples also exist in circumferential and longitudinal directions on this surface. The volume has two other orthotropic surfaces with strain/stress (small arrows), such that a total of nine components are operative. Red and yellow arrows refer to normal and shear strain/stress, respectively. As an equivalent quantity without direction, von Mises stress and strain, calculated from the nine components, is used to describe the complex multi-dimensional mechanical state for easy understanding and application in clinical fields (1). **(B)** Coronary angiography and 3D geometries at three specific cardiac phases: end-diastole, end-systole, and mid-diastole. It shows the large cyclic motion and deformation of a right coronary artery in 3D space.

with identical node dimensions. The point-wise displacements of the deformed arterial wall are determined based on the principle of minimum potential energy. A global displacement function between two consecutive time instants will have its minimum value when all nodes between two consecutive configurations are matched to generate the one-to-one mapping relationship. Because at the stage of diastasis (i.e., mid-diastole) the ventricle is quiescent, the initial configuration for cyclic computation is selected at diastasis, when the kinetic and strain energy of the coronary arteries are at the lowest level throughout the cardiac cycle. Starting from diastasis, the displacements of the vessel wall at the next specific time-point are determined by the mapping relationship. Similarly, the displacements of the vessel wall at subsequent time-points are determined until the next diastasis. The superficial wall strain can be calculated by dividing the element length of structured mesh at the next time-point by that at the previous time-point. When the strain is determined for multiple time-points within cardiac cycle, the stress of arterial wall can be derived based on the assumption of material propeties. The artery was segmented into the normal and diseased parts based on local percent diameter stenosis and assumed to be nearly incompressible, homogenous, isotropic, and hyperelastic as described by Mooney-Rivlin strain energy density function: $W = C_1\left(\overline{I_1} - 3\right) + C_2\left(\overline{I_2} - 3\right)$. Here, C_1 and C_2 are empirically determined material constants. The corresponding material parameters of normal and diseased arterial segments were adapted from a previous study (15). $\overline{I_1}$ and $\overline{I_2}$ are the first and the second invariant of the unimodular component of left Cauchy-Green deformation tensor.

The clinical feasibility of this approach was first confirmed in a selected case with large coronary artery deformation and motion during cardiac cycle (**Figure 2**). The calculated motion of the left anterior descending (LAD) and the diagonal artery (**Supplementary Videos 1**, **2**) were consistent with the angiogram (**Supplementary Video 3**). The LAD moved longitudinally, while the tortuous diagonal artery exhibited remarkable curl motion (10). The time-averaged displacement of LAD (>4.00 mm) was larger than the motion of the diagonal artery (**Figure 3**). For both coronary arteries, the time-averaged maximum principal strain in the stenotic segment was 5.8%, which was significantly lower ($p < 0.001$) than in the normal segment (12.1%). Although, the locations of the peak wall stress changed with time during cardiac cycle, it was mainly concentrated at the proximal and distal shoulders of the stenotic segments or on the inner and outer walls in segments with large curvature (**Supplementary Videos 1**, **2**) (10). The time-averaged peak wall stress of the LAD was significantly higher than that of the diagonal artery (69.1 ± 11.4 kPa vs. 47.6 ± 8.5 kPa, $p < 0.001$).

IN SILICO AND *IN VIVO* VALIDATION STUDIES

The calculation of wall stress was first validated on *in silico* stenosis models ($n = 32$) (14). The idealized virtual stenosis

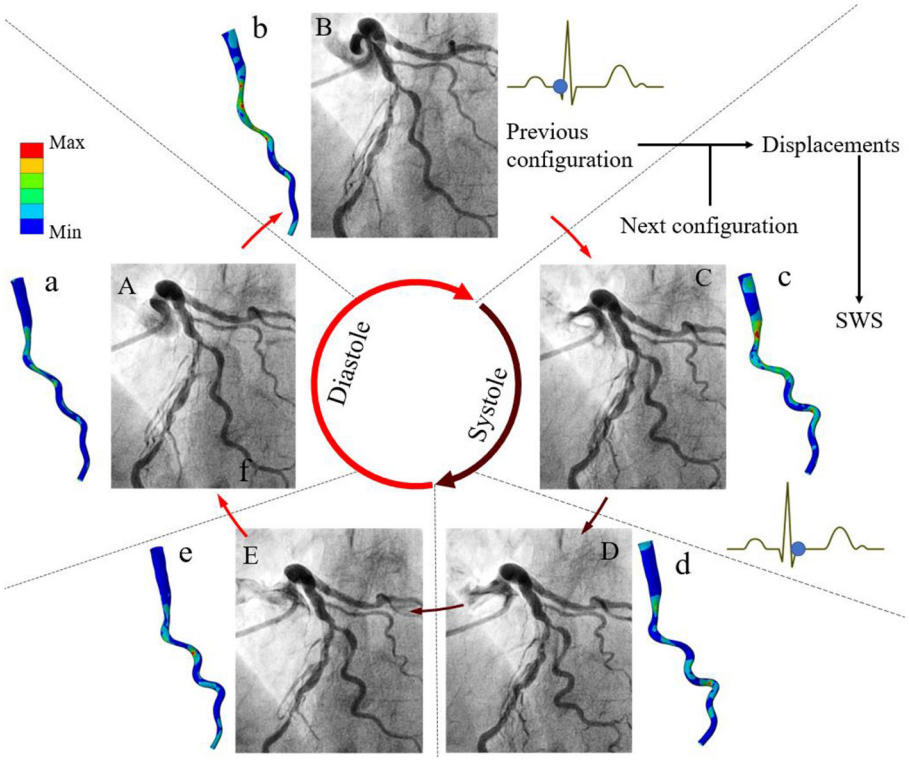

FIGURE 2 | Methods of angiography-based 4D coronary arterial wall dynamics assessment and calculation. Five frames corresponding to specific time-points during the cardiac cycle are identified from the electrocardiogram: **(A)** mid-diastole (diastasis), **(B)** end-diastole, **(C)** early-systole, **(D)** end-systole, and **(E)** early-diastole. Left coronary arteries present large deformations *in vivo*. The local displacements of the superficial wall are determined between these arterial geometries at two consecutive time instants. By using global point-wise displacement mapping relationship on the arteries at the current time-point, the wall strain is determined. Considering the material properties of normal and fibrous tissues, superficial wall stress is further calculated **(a–e)**. Modified from Wu et al. (10).

models were designed with lumen dimensions identical to human coronary arteries (normal lumen diameter of 3 mm). Vessels were 50 mm-long and showed a 10 mm-long concentric stenotic part with a 50% diameter stenosis in its mid-portion. To represent different scenarios of coronary arterial lesions, three different plaque components (i.e., calcified, fibrous, and lipid-rich) and three levels of plaque burden (i.e., 50.9, 62.6, and 69.1 percent volume) were constructed with three types of arterial remodeling (i.e., negative, none, and positive). Our 4D-SWS approach derived from vessel motion *in vivo* was compared with the results of conventional finite element analysis (FEA) with the mechanical force-based method, which generally uses forces as the known conditions to calculate deformation. The maximum wall stress of all types of plaques was not significantly different between both methods (41.6 ± 18.5 kPa vs. 38.9 ± 17.6 kPa, $p = 0.49$). Moreover, there is similar superficial wall stress distribution along the longitudinal superficial wall of all plaque types, including lipid-rich plaque models with three types of arterial remodeling calculated by both methods (**Figure 4**). The virtual stenotic models with lipid-rich plaques had numerically higher superficial wall stress than calcified and fibrous plaque models, and the superficial wall stress values increased with plaque burden. These results suggest that lipid-rich plaques with positive remodeling (i.e., an adaptive vessel enlargement in response to plaque accumulation) could lead to greater risk of plaque rupture. Indeed, the culprit plaque in patients with acute coronary syndromes (ACS) commonly shows lipid-rich content, high plaque burden, and positive remodeling (16–18).

For *in vivo* validation, our SWS computation procedures were performed on angiographic images from 16 patients with intermediate coronary stenoses included in the Functional Assessment by Various flOw Reconstructions (FAVOR) pilot study (19). Only lesions involving a single vessel segment without image overlap were included for analysis. Coronary segments were defined as normal or stenotic segments based on percent diameter stenosis >20%. The accuracy of superficial wall deformation was validated by comparing the similarity between the centerlines predicted by our 4D approach and the actual centerline that was reconstructed from angiograms at a randomly selected time instant. The morphology of centerline curve derived by these two methods was a good agreement assessed by the classical statistical shape method of Procrustes analysis (scaling: 0.995 ± 0.018 and dissimilarity: 0.007 ± 0.014) (20). This shows that continuous changes in vessel morphology

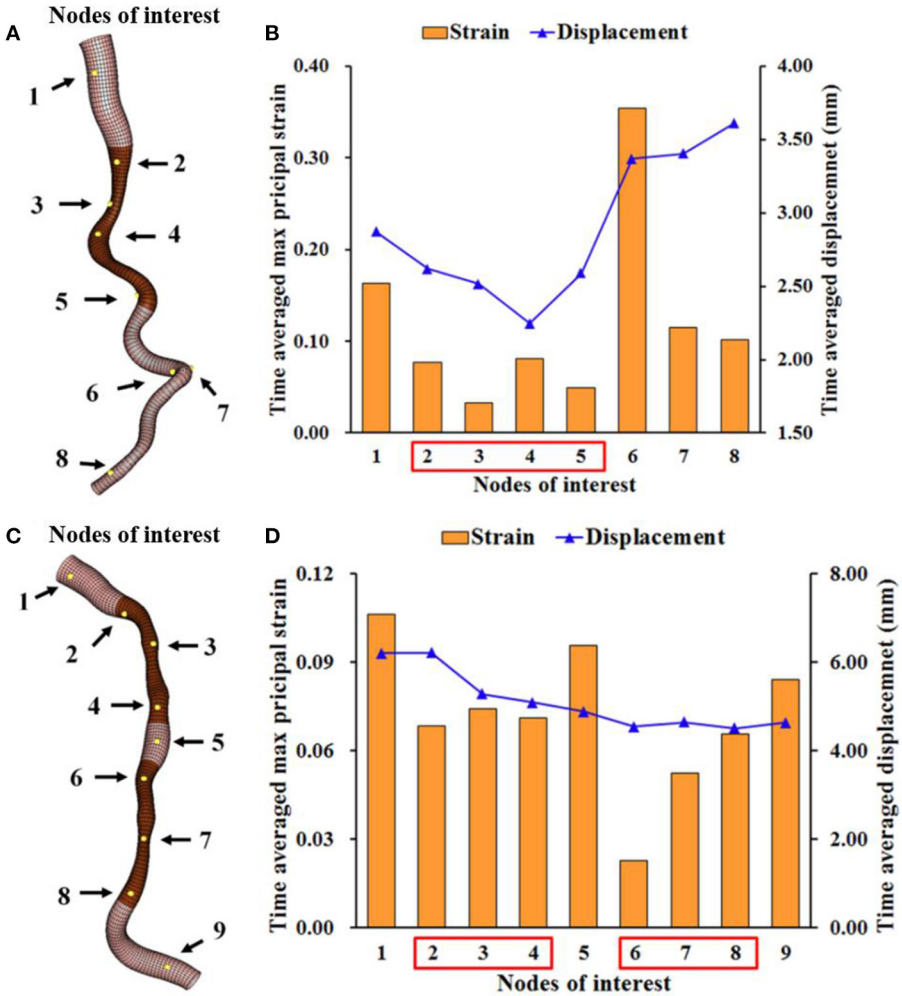

FIGURE 3 | Time-averaged maximum principal strain and displacement at several locations on the LAD and diagonal arteries. The time-averaged maximal principal strain and displacement at the numbered nodes of interest on the diagonal **(A,B)** and LAD **(C,D)** with stenostic segments (dark brown). These nodes at the stenotic segments have lower strain than those at the normal segments.

were adequately captured from the analysis of randomly selected cardiac frames ($p < 0.001$). Additionally, in the majority of patients (9 out of 16, 56%) the maximum wall stress was located in the proximal lesion shoulder, and less often in the mid-portion (25%, $n = 4$) or distal shoulder (19%, $n = 3$). This finding is consistent with a previous report showing that plaque rupture occurred most often at the proximal plaque shoulder (21).

ANGIOGRAPHY-BASED 4D CORONARY ARTERIAL WALL DYNAMICS: FUTURE DIRECTIONS AND LIMITATIONS

Table 1 summarizes the value and limitations of this method and its potential clinical usefulness, which is reviewed in greater detail in the following sections.

Localization of Coronary Plaque at Risk of Rupture and Prediction of Future Events in Patients With Mild or Non-obstructive Coronary Artery Disease (NOCA)

Histopathological post-mortem studies in victims of sudden coronary death demonstrated that acute thrombi are associated in 55–65% with the rupture of a thin fibrous cap atheroma (22). In patients undergoing primary PCI after STEMI, there is a significant residual risk of adverse events caused by non-target and non-flow limiting lesions (called NOCA) that do not need stenting at the time of the initial procedure (23). For example, the 2-year results of RESOLUTE All Comers trial demonstrated that approximately half of the patient-oriented composite endpoint (all-cause death, myocardial infarction, revascularization) might be attributed to the progression of lesions in the non-target vessels or in the target vessels outside of the culprit segments at index event (24). If these high-risk

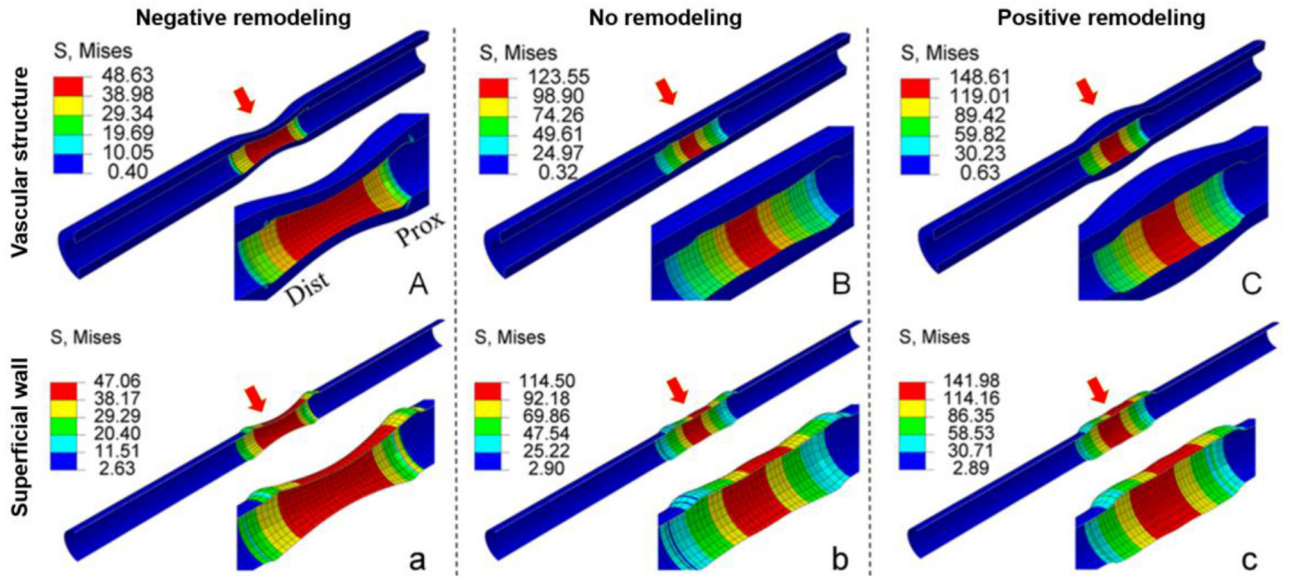

FIGURE 4 | Comparison of the stress distribution of lipid-rich plaque models calculated by the conventional structural mechanical force-based method and superficial wall displacement-based method. There is similar wall stress distribution along the longitudinal superficial wall of the lipid-rich plaque models calculated by the conventional structural mechanical force-based method **(A–C)** and by superficial wall displacement-based method **(a–c)**, regardless of the presence of arterial remodeling. Prox: Proximal; Dist: distal. Six red arrows show the lesion segments of two structural models with three types of arterial remodeling. Modified from Wu et al. (14).

TABLE 1 | Value and limitations of angiography-based 4D coronary artery dynamic method and clinical usefulness.

Value and limitations	
Value	1. Angiography-based solution and potential online availability in the catheterization laboratory.
	2. Realistic reflection of the cyclic motion of arterial wall *in vivo*.
	3. Assessment of the global and local features of the arterial wall with the amplitude and rate of changes in multiple parameters.
Limitations	1. Sensitive to the accuracy of lumen segmentation, especially at location of severe stenosis.
	2. Heart rate-dependent coronary motion.
	3. Further validation of clinical predictive potential needed.
Potential clinical applications	
	1. Assessment of the native vessel dynamics
	a. Identification of weak spots in a diseased vessel along the longitudinal direction.
	b. Differentiation of high-risk vessel segments in patients with non-obstructive coronary artery or multivessel disease.
	c. Biomechanical assessment of arterial remodeling, aneurysm formation, and lumen patency.
	2. Assessment of the implanted device dynamics
	a. Assessment of the fracture risk and fatigue life of coronary stents.
	b. Evaluation of the early discontinuity of bioresorbable scaffolds.
	c. Assessment of the effects of wall strain on the patency of (bioresorbable) bypass grafts

lesions were identifiable during the initial procedure, targeted pharmacological, or mechanical interventions could be applied to mitigate the risk of future ACS and to prevent recurrent heart attacks in these patients.

Although, several attempts have been made to establish the criteria that define such rupture-prone plaques using cardiac imaging, the absolute event rates predicted by intravascular imaging remain low under the current best of medical treatment (25, 26). In addition, systematic imaging of all three coronary arteries failed to be clinically cost-effective (27). Theoretically, plaque rupture represents the structural failure of its fibrous cap due to excessive mechanical stress or strain. Therefore, several studies of coronary image-based computational modeling attempted to improve the predictive accuracy by incorporation of mechanical indices (28–30). The threshold value of 300 kPa is commonly used as a high-stress value from the experimental fracture *in vitro* of human plaque caps (1). However, plaque rupture might be triggered at a lower level than this threshold, because coronary artery *in vivo* is a typical fatigue environment with high-cycle and low-level stress due to the repetitive cardiac

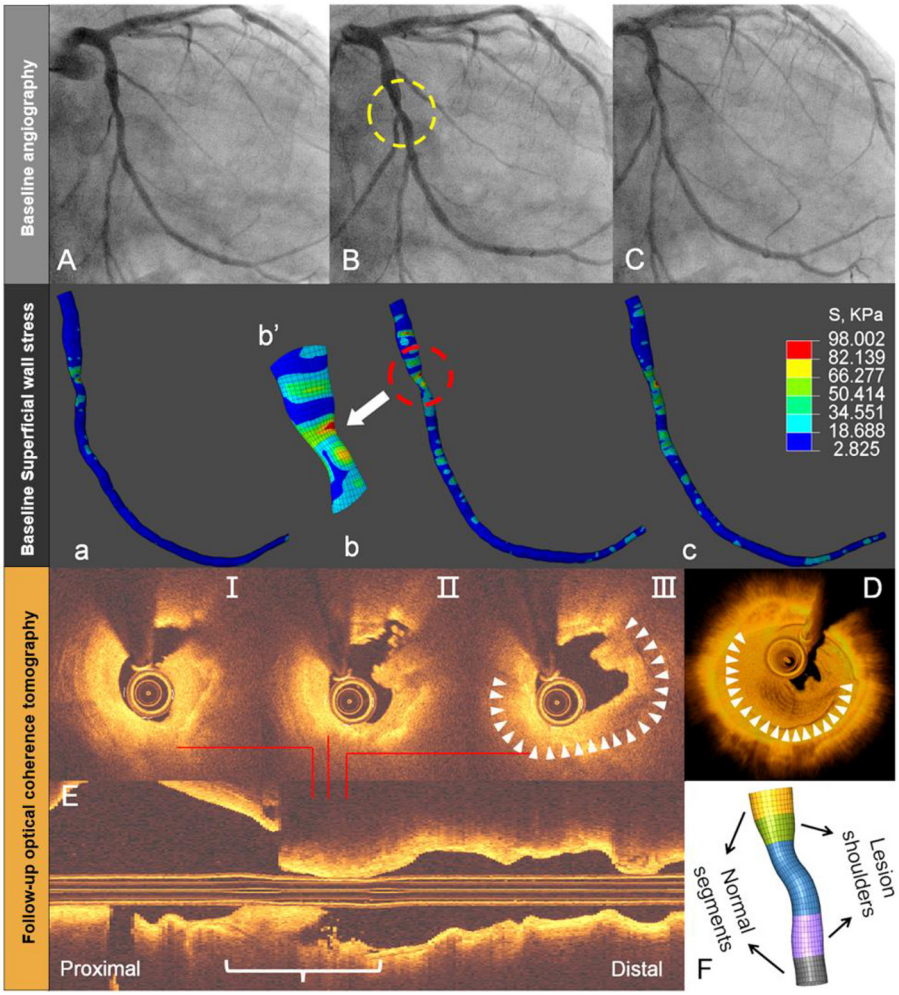

FIGURE 5 | Angiography-based superficial wall stress on diagnostic angiography and late plaque rupture. Baseline angiography shows (yellow circle) an intermediate mid-LCx lesion **(A–C)**. Superficial wall stress, calculated by the 4D approach at baseline angiography, reveals more local stress concentration in the stenotic segment (white arrow) or throat site **(a–c)**. This location corresponds with the site of lumen irregularity, thrombus, and plaque rupture during late acute coronary syndrome, as shown by OCT on selected cross-sections **(I-III)**, 3D rendering **(D)**, and longitudinal OCT **(E)**. The reconstructed throat segment and lesion shoulders are shown along with percent diameter stenosis **(F)**. Modified from Wu et al. (11).

contraction (31). Note that the stress and strain values of human coronary artery *in vivo* are significantly lower than those of *in vitro* failure. Under physiological conditions, the axial strain and stress of coronary arteries are up to 62% and 200 kPa (32). We recently reported two cases where the maximum superficial wall stress computed from a diagnostic angiogram using our method was co-localized with the sites of late plaque rupture, as confirmed by optical coherence tomography (OCT) during ACS several months later (**Figure 5**, case 2) (11).

Figure 6 shows another example to suggest the association between superficial wall stress and newly developed stenosis at follow-up. After physiological assessment during index PCI (**Figure 6A**, baseline angiography), RCA showed preserved iFR value and the stent implantation in the proximal and distal lesions was deferred. On day 785, the patient was admitted for recurrent unstable angina. Repeat angiography (**Figure 6B**) showed that RCA had only a TIMI grade 2 flow, which was predominantly caused by the progression of the distal lesion. The initial diagnostic coronary angiogram was analyzed by both superficial wall stress (**Figure 6C**) and ESS (**Figure 6D**) to investigate their impacts on possible plaque progression. In contrast to superficial wall stress calculated based on the deformation of coronary artery during cardiac cycle, ESS is the friction between intravascular blood flow and endothelial layer, and was analyzed by computational fluid dynamics. In **Figure 6C**, the high level of time-averaged superficial wall stress was found at the site of distal stenosis with rapid progression (**Figure 6B**, yellow arrow). **Figure 6D** shows that the high time-averaged ESS is located at the stenotic segments RCA (lesions left untreated), while the mid-segment exhibits a very low ESS (<1 Pa). The expanded view shows that ESS is correlated with lumen diameter

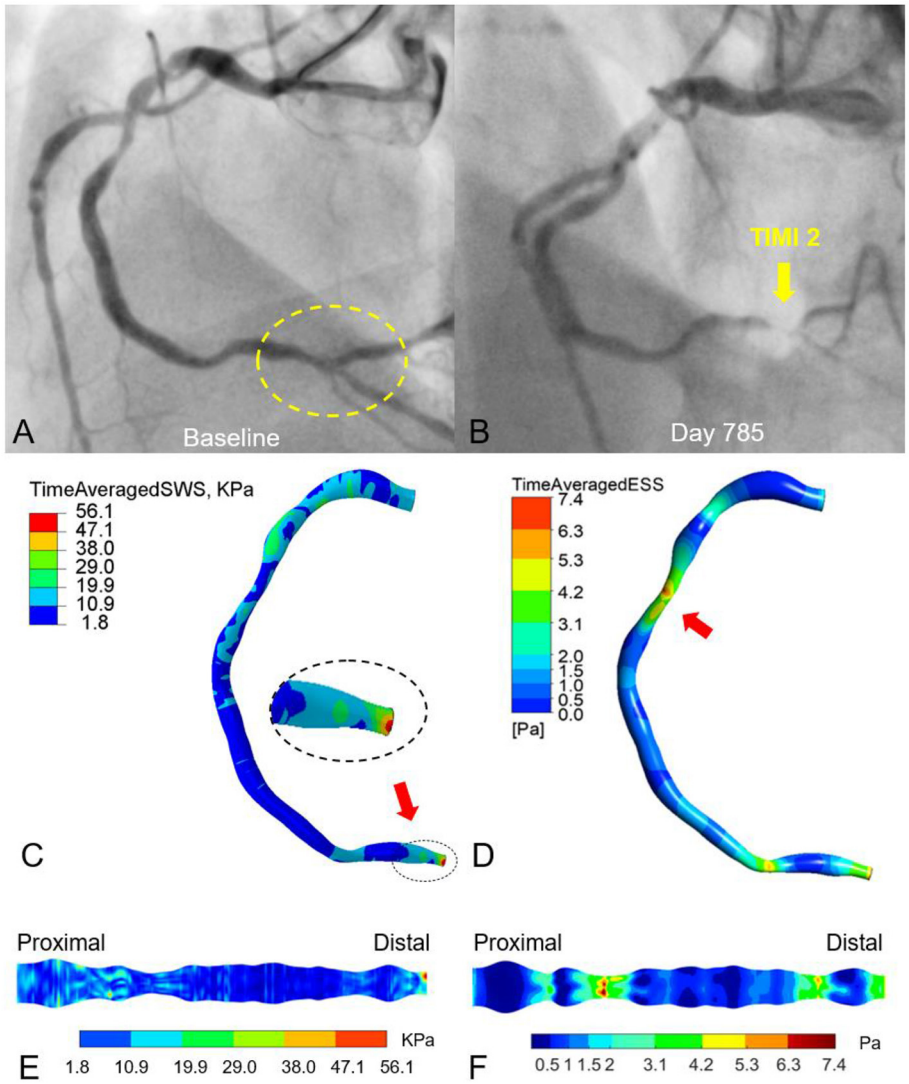

FIGURE 6 | Effects of vessel deformation-induced superficial wall stress and fluid-induced endothelial shear stress on plaque progression and clinical adverse events. The moderate lesions in proximal and distal RCA remained untreated according to physiological guidance with iFR **(A)**. On day 785, the patient was admitted to the hospital due to recurrent angina. Angiography demonstrated the progression of the distal RCA stenosis with impaired TIMI-2 coronary flow, suggesting plaque progression as well as potential atheroma rupture **(B)**. The time-averaged superficial wall stress was relatively high at the distal RCA with 56 kPa **(C)** and co-located with the site of late plaque rupture **(B)**. **(D)** Relatively high time-averaged endothelial shear stress (ESS) (6–7 Pa) was located at the stenotic segments of proximal and distal RCA (lesions left untreated), while the mid-segment exhibits a very low ESS (<1 Pa). **(E,F)** Expanded views of superficial wall stress and ESS distribution.

(**Figure 6F**). These observations illustrate the potential of angiography-based superficial wall stress for the identification of rupture-prone plaque. With further prospective validation, this technique can hopefully inform personalized patient care with optimized pharmacological therapy or local device-based plaque modification.

Assessment of the Mechanical Failure Risk of Coronary Stents

Histopathological studies have demonstrated that stent fracture is one of the potential causes of drug-eluting stent failure (33). Such mechanical failure, which typically occurs at kinking points in long or overlapping stents (34), is often the consequence of dynamic forces that result from the motion of coronary arteries. Once implanted, coronary stents will be exposed to cyclic deformation at least 86,400 times per day. Therefore, the indices of dynamic arterial morphology may be useful to estimate stent failure risk (35–37). For example, Girasis et al. (36, 37) analyzed the dynamic changes in 3D bifurcation angle (BA) of the left main coronary artery. After bifurcation stenting with a two-stent strategy, the proximal BA became larger and the distal BA narrower (36). A systolic-diastolic distal BA range $<10^{\circ}$ (i.e., a more rigid, "full metal jacket" bifurcation) had significantly

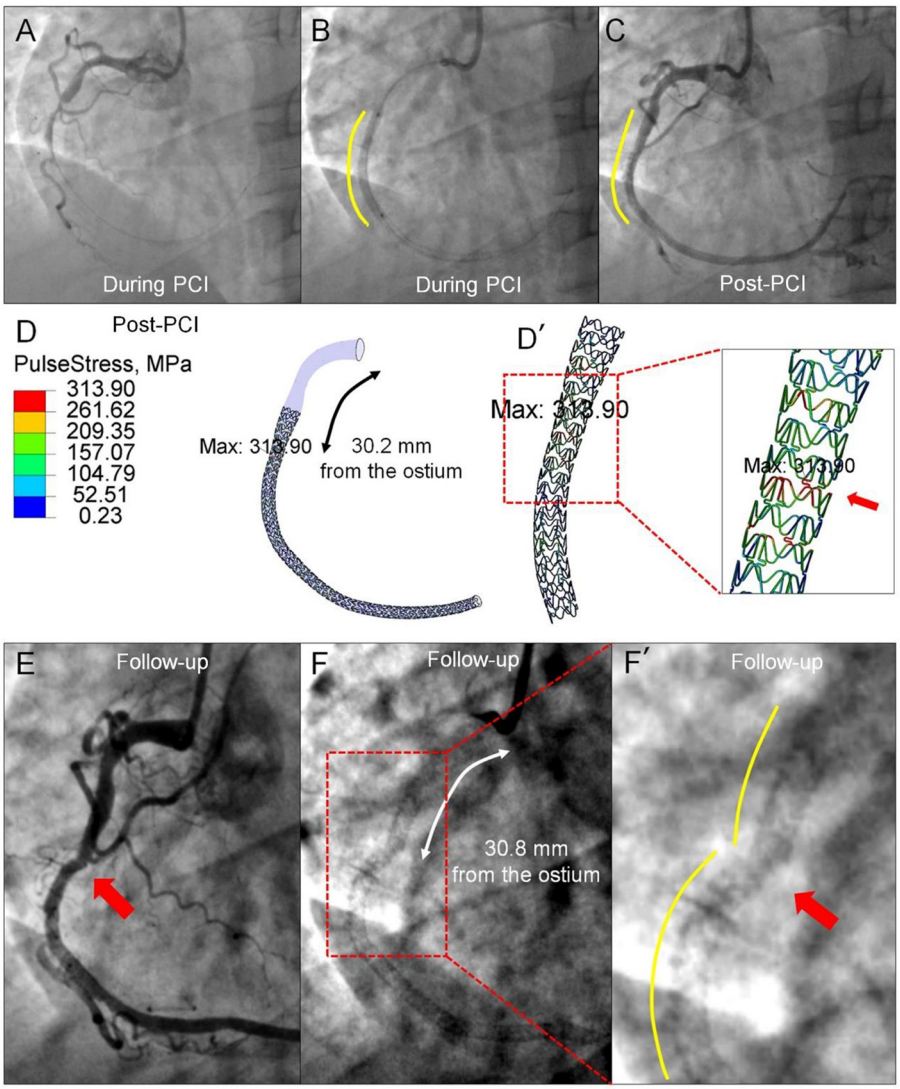

FIGURE 7 | Prediction of late stent fracture by the pulse stress on the implanted stent using angiography-based 4D coronary artery dynamic method. **(A)** Angiography prior to implantation shows a total occlusion of the mid-segment of the RCA and a smooth curve of the implanted stent. **(B)** Visible contours of the inflated balloon delineate the proximal and distal ends of the implanted stent (Xience V). **(C)** Straightening of the proximal segment occurs following stent implantation. **(D)** The highest pulse stress (313.90 MPa), derived from the difference between the stress state at end-systole and end-diastole, is found at the site of 30.2 mm from the ostium. [**(D')**, red arrow] The zoomed view shows the pulse stress distribution of the implanted stent. Angiograms 20 months later show stent fracture **(E)** located at 30.8 mm from the ostium, resulting in luminal irregularity **(F)**. The site of the highest pulse stress calculated by the angiography-based 4D dynamic method co-localizes with the stent fracture site [**(F')**, red arrow] documented 20 months later.

higher adverse event rates (50.8 vs. 22.7%, $p < 0.001$) and was associated with a higher 5-year adverse event rate (hazard ratio: 2.65, $p < 0.001$) (37).

Although, it is recognized that repetitive and fluctuating stress, induced by the dynamic deformation of coronary arteries, is an important mechanism of stent fracture, quantitative analysis on *in vivo* mechanical stress in association with a stent fracture using FEA is still limited (38). By using the angiography-based 4D dynamic method, it becomes relatively easy to calculate the dynamic stress on implanted stents *in vivo*. In **Figure 7**, the highest pulse stress on the stent, derived from the difference between the two stress states at end-systole and end-diastole, is localized 30.2 mm from the coronary ostium at the index procedure, at the exact location where stent fracture occurred 20 months later (30.8 mm from the ostium). This approach might be useful to estimate the stress distribution of devices and to predict the fracture risk when implanted in the specific coronary arteries with different deformation.

Relationship Between Dynamic Parameters, Vascular Remodeling, and Lumen Patency

Vascular remodeling can be considered as a dynamic functional and morphometric adaptive process of a vessel in response

TABLE 2 | Summary of cardiac imaging and computational modeling techniques.

Categories	Techniques	Theoretical strengths	Limitations	Application scenarios
Cardiac imaging	Angiography	• High spatial resolution (150∼250 μm) • High temporal resolution (33∼80 ms) • Dynamic blood flow • Dynamic motion and deformation of coronary tree	• Lacking 3D information	• Diagnosis of coronary artery anomalies and guide interventional therapy • 3D reconstruction of artery and centerline • 4D reconstruction of arterial dynamics
	IVUS	• High penetration depths for assessing plaque burden and detecting lumen size	• Low spatial resolution (axial: 100∼150 μm; lateral: 150∼300 μm) • Limited for assessing strut malapposition and detecting thrombus	• Measurement of lumen and vessel dimensions, lesion characterizations • Guide interventional therapy
	OCT	• High spatial resolution (axial: 10∼20 μm; lateral: 20∼90 μm) for accurately detecting lumen, thrombus, or stent-related morphologies	• Low tissue penetration depths (∼2 mm) • Limited for assessing plaque burden and detecting vessel size	• Measurement of lumen dimensions, lesion characterizations, evaluation of strut-level • Guide interventional therapy
	NIRS	• Quantitative assessment of lipid core burden index	• Limited for plaque structure and cap thickness	• Detection of lipid-rich plaque
Image reconstruction	ANGUS	• More accurate for 3D reconstruction model of vessels	• Need angiography and IVUS • 3D reconstruction only at end-diastole	• For endothelial shear stress analysis
Image-based computational modeling	ESS	• Assessing the hemodynamics of near-wall with a profound influence on vascular biology based on angiography or combined with intravascular images	• Static assessment at end-diastole	• Assessing plaque progression and thrombogenesis
	SWS	• Measuring the dynamics of the superficial wall base on angiography • Dynamic mechanical behavior of coronary arteries during a cardiac cycle	• Sensitive to arterial geometry • Heart rate-dependent coronary motion	• Assessment of the native vessel dynamics • Assessment of the implanted device dynamics (Detail see **Table 1**)
	PSS	• Assessing the stress state of the plaque structure based on IVUS	• Segmentation of detail plaque components • Require blood pressure and mechanical properties of plaque components	• Assessment of plaque rupture risk
	Elastography/ palpography	• Measuring plaque strain *in vivo* based on IVUS	• Sensitive to heart beating and the location of imaging sensor	• Detection of the vulnerable plaques with a high strain region at the surface in the close vicinity of low strain regions

ESS, endothelial shear stress; IVUS, intravascular ultrasound; NIRS, near-infrared spectroscopy; OCT, optical coherence tomography; PSS, plaque structural stress; SWS: superficial wall strain/stress.

to biomechanical stimuli that lead to changes in vascular structure and properties (39). A vessel composed of smooth muscle cells, elastin, and collagen fibers, each with different elastic performances, has to maintain its dynamic stability over a wide range of diameter variations under normal and abnormal biomechanical conditions. The chronic expansion and shrinkage of the vessel lumen are theoretically regulated by biomechanical stresses that result from the equilibrium relationship between transmural pressure P and circumferential stress σ_θ, which can be computed by the Laplace's law $\sigma_\theta = \mathrm{Pr}/t$, where, r is lumen radius and t is wall thickness. Generally, lumen narrowing appears when plaque burden exceeds about 40% of the vessel "normal" cross-sectional area, as defined by the external elastic membrane (40). Then, adaptive remodeling becomes exhausted, plausibly because the gradually increased circumferential stress counterbalances the transmural pressure, resulting in plaque encroachment on the lumen. In contrast, if transmural blood pressure dominates the process of vascular remodeling, vessels can undergo outward expansion and become even larger. In particular, vein grafts, transplanted from their native low-pressure environment, cannot bear the elevated circumferential stress caused by the pressure in the systemic arterial circulation (from ∼10 to ∼100 mmHg).

It has been suggested that cyclic motion of coronary bypass grafts plays an important role in lumen patency (41). The compliance mismatch at the anastomosis site between the distal end of the graft and the native artery could increase local wall strain and stress, leading to cumulative regional graft injury. A previous experimental study revealed that constraining graft wall motion by the use of an external casting stent may reduce the progression of graft disease (42), although, this kind of static casting might also impede flow through vasa vasorum and cause graft hypoxia. In the long-term, both mechanisms could result in post-necrotic neointimal overgrowth. Therefore, bioresorbable bypass grafts armored with nitinol rings in their wall could serve as a template to the restorative process of "Mother Nature." Currently, such innovative technology is being tested in an animal model and initial First-in-Human studies (NCT04545112) (43). The angiography-based examination of graft dynamics in this pre-clinical model, allows to detect weak spots or regions of high strain. These weak spots could be amended by local reinforcement of the graft wall, by changing the curvature of the graft, or by modifying the angulation of the anastomosis. Exploring the relationship between dynamic mechanical parameters and vascular remodeling and lumen patency may equally allow to quantify the process of vascular remodeling in native coronary arteries.

Many approaches have been evaluated for the prediction of events and the estimation of plaque propensity for rupture, thrombosis, or progression, including intracoronary imaging and image-based computational modeling. **Table 2** summarizes the strengths and limitations of relevant imaging modalities and imaging-based computational modeling techniques and application scenarios. From a biomechanical viewpoint, ESS (28), a friction stress caused by flowing blood acting on the wall, is calculated on a static model of coronary arteries at end-diastole from 3D reconstruction of angiography or in combination with intravascular images, such as ANGUS (44). The SWS approach instead focuses on the dynamic mechanical status of the superficial wall layer and is directly calculated from the deformation of arteries based on angiography during the entire cardiac cycle. Plaque structural stress (2, 30), which is calculated from plaque composition and architecture on intravascular cross-sectional images, estimates plaque stress status under the prevailing coronary arterial pressure. Previously reported techniques, such as elastography (45) and palpography (46), measure plaque strain *in vivo* based on the deformation of IVUS images under blood pressure. Since major adverse cardiovascular events (MACE) represents a combination of different clinical endpoints resulting from several different mechanisms, comparative evaluation of imaging-based computational modeling for MACE prediction requires further exploration. Further clinical validation of the angiography-based SWS is needed in order to demonstrate its incremental value for the prediction of future events, compared with other imaging modalities and conventional risk factors (e.g., age, gender, diabetes, etc.). Larger studies investigating the correlation between the distribution of SWS and clinical events are needed.

CONCLUSIONS

In silico and *in vivo* studies have revealed that angiography-based assessment of dynamic coronary artery deformation allows computation of superficial wall strain and stress, as reported by Wu et al. (10, 11, 14). Lipid-rich plaque models had numerically higher wall stress than calcified and fibrous plaques, and wall stress increased with plaque burden. In selected observations, high wall stress spots at baseline co-localize with the site of plaque rupture in patients with late clinical events. By the identification of weak spots over the full length of the diseased coronary artery tree, it may become possible to assess the fracture risk and fatigue life of implanted stents, and to explore biomechanical mechanism of arterial remodeling and lumen patency. Because this technique only requires angiographic data, essential steps (including high-precision and automatic lumen segmentation, vessel reconstruction, anatomical landmarks and cardiac frames detection) can be implemented in a seamlessly integrated workflow. As a result, the superficial wall strain and stress analysis can potentially become an available online tool in the catheterization laboratory in the future.

AUTHOR CONTRIBUTIONS

XW, WW, PS, and YO conceived the idea and wrote the first draft. All authors contributed substantially to the discussion of content and reviewed/edited the manuscript before submission.

FUNDING

This work is supported by the Natural Science Foundation of Zhejiang Province, China (LQ20H180004) and Science Foundation Ireland (15/RP/2765). XW, CG, RW, and WW are supported by SFI Grant 15/RP/2765. ST has a research Grant from National Natural Science Foundation of China (81871460). EP and PB are supported by Australia Research Council (LP150100233).

SUPPLEMENTARY MATERIAL

The Supplementary Material for this article can be found online at: https://www.frontiersin.org/articles/10.3389/fcvm.2021.667310/full#supplementary-material

Supplementary Video 1 | Superficial wall dynamics of the left anterior descending. The LAD moved longitudinally, and the peak superficial wall stress was mainly located at the proximal and distal shoulders of the stenotic segments during the cardiac cycle.

Supplementary Video 2 | Superficial wall dynamics of the diagonal artery. The tortuous diagonal artery exhibited remarkable curl motion, and the peak superficial wall stress was located at the proximal and distal shoulders of the stenotic segments or on the inner and outer walls in segments with large curvature during the cardiac cycle.

Supplementary Video 3 | Coronary angiogram of a selected case with large deformation and motion. The angiogram shows the LAD with diffuse lesion and the diagonal artery with narrowing at ostium.

REFERENCES

1. Holzapfel GA, Mulvihill JJ, Cunnane EM, Walsh MT. Computational approaches for analyzing the mechanics of atherosclerotic plaques: a review. *J Biomech.* (2014) 47:859–69. doi: 10.1016/j.jbiomech.2014.01.011
2. Brown AJ, Teng Z, Evans PC, Gillard JH, Samady H, Bennett MR. Role of biomechanical forces in the natural history of coronary atherosclerosis. *Nat Rev Cardiol.* (2016) 13:210–20. doi: 10.1038/nrcardio.2015.203
3. Arroyo LH, Lee RT. Mechanisms of plaque rupture: mechanical and biologic interactions. *Cardiovasc Res.* (1999) 41:369–75. doi: 10.1016/S0008-6363(98)00308-3
4. Sherratt MJ. Tissue elasticity and the ageing elastic fibre. *Age.* (2009) 31:305–25. doi: 10.1007/s11357-009-9103-6
5. Giri J, Saybolt MD. Coronary stent fracture: a new form of patient-prosthesis mismatch? *JACC: Cardiovasc Interv.* (2016) 9:1124–6. doi: 10.1016/j.jcin.2016.03.004
6. Shechter G, Resar JR, McVeigh ER. Displacement and velocity of the coronary arteries: cardiac and respiratory motion. *IEEE T Med Imaging.* (2006) 25:369–75. doi: 10.1109/TMI.2005.862752
7. Torii R, Keegan J, Wood NB, Dowsey AW, Hughes AD, Yang GZ, et al. MR image-based geometric and hemodynamic investigation of the right coronary artery with dynamic vessel motion. *Ann Biomed Eng.* (2010) 38:2606–20. doi: 10.1007/s10439-010-0008-4
8. Close RA, Abbey CK, Morioka CA, Whiting JS. Evaluation of layer decomposition for multiframe quantitative coronary angiography. *Med Phys.* (2002) 29:311–8. doi: 10.1118/1.1449494
9. Cimen S, Gooya A, Grass M, Frangi AF. Reconstruction of coronary arteries from X-ray angiography: a review. *Med Image Anal.* (2016) 32:46–68. doi: 10.1016/j.media.2016.02.007
10. Wu X, von Birgelen C, Wijns W, Tu S. Superficial wall stress assessed from 4-D analysis of coronary angiography *in vivo*. *Int J Cardiovasc Imaging.* (2017) 33:1–2. doi: 10.1007/s10554-017-1091-5
11. Wu X, von Birgelen C, Muramatsu T, Li Y, Holm NR, Reiber JH, et al. A novel four-dimensional angiographic approach to assess dynamic superficial wall stress of coronary arteries *in vivo*: initial experience in evaluating vessel sites with subsequent plaque rupture. *EuroIntervention.* (2017) 13:1099–103. doi: 10.4244/EIJ-D-16-01020
12. Muller O, Pyxaras SA, Trana C, Mangiacapra F, Barbato E, Wijns W, et al. Pressure-diameter relationship in human coronary arteries. *Circ Cardiovasc Interv.* (2012) 5:791–6. doi: 10.1161/CIRCINTERVENTIONS.112.972224
13. Tu S, Barbato E, Köszegi Z, Yang J, Sun Z, Holm NR, et al. Fractional flow reserve calculation from 3-dimensional quantitative coronary angiography and TIMI frame count. *JACC Cardiovasc Interv.* (2014) 7:768–77. doi: 10.1016/j.jcin.2014.03.004
14. Wu X, von Birgelen C, Li Z, Zhang S, Huang J, Liang F, et al. Assessment of superficial coronary vessel wall deformation and stress: validation of *in silico* models and human coronary arteries *in vivo*. *Int J Cardiovasc Imaging.* (2018) 34:1–13. doi: 10.1007/s10554-018-1311-7
15. Huang H, Virmani R, Younis H, Burke AP, Kamm RD, Lee RT. The impact of calcification on the biomechanical stability of atherosclerotic plaques. *Circulation.* (2001) 103:1051–6. doi: 10.1161/01.CIR.103.8.1051
16. Von Birgelen C, Klinkhart W, Mintz GS, Papatheodorou A, Herrmann J, Baumgart D, et al. Plaque distribution and vascular remodeling of ruptured and non-ruptured coronary plaques in the same vessel: an intravascular ultrasound study *in vivo*. *J Am Coll Cardiol.* (2001) 37:1864–70. doi: 10.1016/S0735-1097(01)01234-7
17. Stone GW, Maehara A, Lansky AJ, De Bruyne B, Cristea E, Mintz GS, et al. A prospective natural-history study of coronary atherosclerosis. *N Engl J Med.* (2011) 364:226–35. doi: 10.1056/NEJMoa1002358
18. Motoyama S, Ito H, Sarai M, Kondo T, Kawai H, Nagahara Y, et al. Plaque characterization by coronary computed tomography angiography and the likelihood of acute coronary events in mid-term follow-up. *J Am Coll Cardiol.* (2015) 66:337–46. doi: 10.1016/j.jacc.2015.05.069
19. Tu S, Westra J, Yang J, Von BC, Ferrara A, Pellicano M, et al. Diagnostic accuracy of fast computational approaches to derive fractional flow reserve from diagnostic coronary angiography: the international multicenter FAVOR pilot study. *JACC Cardiovasc Interv.* (2016) 9:2024–35. doi: 10.1016/j.jcin.2016.07.013
20. Gower JC. Generalized procrustes analysis. *Psychometrika.* (1975) 40:33–51. doi: 10.1007/BF02291478
21. Maehara A, Mintz GS, Bui AB, Walter OR, Castagna MT, Canos D, et al. Morphologic and angiographic features of coronary plaque rupture detected by intravascular ultrasound. *J Am Coll Cardiol.* (2002) 40:904–10. doi: 10.1016/S0735-1097(02)02047-8
22. Virmani R, Kolodgie FD, Burke AP, Farb A, Schwartz SM. Lessons from sudden coronary death - a comprehensive morphological classification scheme for atherosclerotic lesions. *Arterioscl Throm Vas.* (2000) 20:1262–75. doi: 10.1161/01.ATV.20.5.1262
23. Gershlick AH, Banning AS, Parker E, Wang D, Budgeon CA, Kelly DJ, et al. Long-term follow-up of complete versus lesion-only revascularization in STEMI and multivessel disease: the CvLPRIT Trial. *J Am Coll Cardiol.* (2019) 74:3083–94. doi: 10.1016/j.jacc.2019.10.033
24. Silber S, Windecker S, Vranckx P, Serruys PW, Investigators RAC. Unrestricted randomised use of two new generation drug-eluting coronary stents: 2-year patient-related versus stent-related outcomes from the RESOLUTE all comers trial. *Lancet.* (2011) 377:1241–7. doi: 10.1016/S0140-6736(11)60395-4
25. Nissen SE. Vulnerable plaque and einstein's definition of insanity. *J Am Coll Cardiol.* (2020) 75:1383–5. doi: 10.1016/j.jacc.2020.01.043
26. Waksman R, Di Mario C, Torguson R, Ali ZA, Singh V, Skinner WH, et al. Identification of patients and plaques vulnerable to future coronary events with near-infrared spectroscopy intravascular ultrasound imaging: a prospective, cohort study. *Lancet.* (2019) 394:1629–37. doi: 10.1016/S0140-6736(19)31794-5
27. Tomaniak M, Katagiri Y, Modolo R, Silva Rd, Khamis RY, Bourantas CV, et al. Vulnerable plaques and patients: state-of-the-art. *Eur Heart J.* (2020) 41:2997–3004. doi: 10.1093/eurheartj/ehaa227
28. Slager CJ, Wentzel JJ, Gijsen FJH, Thury A, van der Wal AC, Schaar JA, et al. The role of shear stress in the destabilization of vulnerable plaques and related therapeutic implications. *Nat Clin Pract Card.* (2005) 2:456–64. doi: 10.1038/ncpcardio0298
29. Stone PH, Saito S, Takahashi S, Makita Y, Nakamura S, Kawasaki T, et al. Prediction of progression of coronary artery disease and clinical outcomes using vascular profiling of endothelial shear stress and arterial plaque characteristics: the PREDICTION study. *Circulation.* (2012) 126:172–81. doi: 10.1161/CIRCULATIONAHA.112.096438
30. Costopoulos C, Maehara A, Huang Y, Brown AJ, Gillard JH, Teng Z, et al. Heterogeneity of plaque structural stress is increased in plaques leading to MACE: insights from the PROSPECT study. *JACC: Cardiovasc Imaging.* (2020) 13:1206–18. doi: 10.1016/j.jcmg.2019.05.024
31. Bank A, Versluis A, Dodge S, Douglas W. Atherosclerotic plaque rupture: a fatigue process? *Med Hypotheses.* (2000) 55:480–4. doi: 10.1054/mehy.2000.1096
32. Lawrence AR, Gooch KJ. Transmural pressure and axial loading interactively regulate arterial remodeling *ex vivo*. *Am J Physiol Heart Circ Physiol.* (2009) 297:H475–. doi: 10.1152/ajpheart.00972.2008
33. Nakazawa G, Finn AV, Vorpahl M, Ladich E, Kutys R, Balazs I, et al. Incidence and predictors of drug-eluting stent fracture in human coronary artery: a pathologic analysis. *J Am Coll Cardiol.* (2009) 54:1924–31. doi: 10.1016/j.jacc.2009.05.075
34. Kan J, Ge Z, Zhang JJ, Liu ZZ, Tian NL, Ye F, et al. Incidence and clinical outcomes of stent fractures on the basis of 6,555 patients and 16,482 drug-eluting stents from 4 centers. *JACC Cardiovasc Interv.* (2016) 9:1115–23. doi: 10.1016/j.jcin.2016.02.025
35. Zhang B, Tu S, Karanasos A, van Geuns RJ, de Jaegere P, Zijlstra F, et al. Association of stent-induced changes in coronary geometry with late stent failure: insights from three-dimensional quantitative coronary angiographic analysis. *Catheter Cardiovasc Interv.* (2018) 92:1040–8. doi: 10.1002/ccd.27520
36. Girasis C, Serruys PW, Onuma Y, Colombo A, Holmes DR, Feldman TE, et al. 3-Dimensional bifurcation angle analysis in patients with left main disease a substudy of the SYNTAX trial (SYNergy between percutaneous coronary intervention with TAXus and cardiac surgery). *JACC Cardiovasc Interv.* (2010) 3:41–8. doi: 10.1016/j.jcin.2009.10.019
37. Girasis C, Farooq V, Diletti R, Muramatsu T, Bourantas CV, Onuma Y, et al. Impact of 3-dimensional bifurcation angle on 5-year outcome of patients after percutaneous coronary intervention for left main coronary artery disease:

a substudy of the SYNTAX trial (Synergy between percutaneous coronary intervention with taxus and cardiac surgery). *JACC Cardiovasc Interv.* (2013) 6:1250–60. doi: 10.1016/j.jcin.2013.08.009
38. Everett KD, Conway C, Desany GJ, Baker BL, Choi G, Taylor CA, et al. Structural mechanics predictions relating to clinical coronary stent fracture in a 5 year period in FDA MAUDE database. *Ann Biomed Eng.* (2016) 44:391–403. doi: 10.1007/s10439-015-1476-3
39. Hayashi K, Naiki T. Adaptation and remodeling of vascular wall biomechanical response to hypertension. *J Mech Behav Biomed.* (2009) 2:3–19. doi: 10.1016/j.jmbbm.2008.05.002
40. Glagov S, Weisenberg E, Zarins CK, Stankunavicius R, Kolettis GJ. Compensatory enlargement of human atherosclerotic coronary arteries. *N Engl J Med.* (1987) 316:1371–5. doi: 10.1056/NEJM198705283162204
41. John LCH. Biomechanics of coronary artery and bypass graft disease: potential new approaches. *Ann Thorac Surg.* (2009) 87:331–8. doi: 10.1016/j.athoracsur.2008.07.023
42. Izzat MB, Mehta D, Bryan AJ, Reeves B, Newby AC, Angelini GD. Influence of external stent size on early medial and neointimal thickening in a pig model of saphenous vein bypass grafting. *Circulation.* (1996) 94:1741–5. doi: 10.1161/01.CIR.94.7.1741
43. Xeltis. *Xeltis Coronary Artery Bypass Graft (XABG) First in Human (FIH) (XABG-FIH)*. NLM identifier: NCT04545112. Available online at: https://www.clinicaltrials.gov/ct2/show/NCT04545112?term=NCT04545112&draw=2&rank=1 (accessed September 10, 2020).
44. Slager CJ, Wentzel JJ, Schuurbiers JCH, Oomen JAF, Kloet J, Krams R, et al. True 3-dimensional reconstruction of coronary arteries in patients by fusion of angiography and IVUS (ANGUS) and its quantitative validation. *Circulation.* (2000) 102:511–6. doi: 10.1161/01.CIR.102.5.511
45. de Korte CL, Carlier SG, Mastik F, Doyley M, van der Steen AF, Serruys PW, et al. Morphological and mechanical information of coronary arteries obtained with intravascular elastography: feasibility study *in vivo*. *Eur Heart J.* (2002) 23:405–13. doi: 10.1053/euhj.2001.2806
46. Schaar JA, van der Steen AFW, Mastik F, Baldewsing RA, Serruys PW. Intravascular palpography for vulnerable plaque assessment. *J Am Coll Cardiol.* (2006) 47:C86–91. doi: 10.1016/j.jacc.2006.01.035

Conflict of Interest: CB reports institutional research grants (Thoraxcentrum Twente) from Abbott Vascular, Biotronik, Boston Scientific, and Medtronic, outside the submitted work. ST reports institutional research grants from Pulse medical imaging technology, Shanghai, China. WW reports institutional research grant and honoraria from MicroPort.

The remaining authors declare that the research was conducted in the absence of any commercial or financial relationships that could be construed as a potential conflict of interest.

frontiers in Cardiovascular Medicine

ORIGINAL RESEARCH
published: 18 June 2021
doi: 10.3389/fcvm.2021.679599

Effect of Low-Density Lipoprotein Cholesterol Goal Achievement on Vascular Physiology Evaluated by Quantitative Flow Ratio in Patients Who Underwent Percutaneous Coronary Intervention

Long Chen[1,2,3†], *Qin Chen*[1,2,3†], *Jiaxin Zhong*[1,2,3†], *Zhen Ye*[1,2,3†], *Mingfang Ye*[1,2,3], *Yuanming Yan*[1,2,3], *Lianglong Chen*[1,2,3] *and Yukun Luo*[1,2,3*]

[1] Department of Cardiology, Fujian Medical University Union Hospital, Fuzhou, China, [2] Fujian Institute of Coronary Artery Disease, Fuzhou, China, [3] Fujian Heart Medical Center, Fuzhou, China

Purpose: The change in coronary physiology from lipid-lowering therapy (LLT) lacks an appropriate method of examination. Quantitative flow ratio (QFR) is a novel angiography-based approach allowing rapid assessment of coronary physiology. This study sought to determine the impact of low-density lipoprotein cholesterol (LDL-C) goal achievement on coronary physiology through QFR.

Methods: Cases involving percutaneous coronary intervention (PCI) and 1-year angiographic follow-up were screened and assessed by QFR analysis. Patients were divided into two groups according to the LDL-C level at the 1-year follow-up: (1) goal-achievement group (LDL-C < 1.8 mmol/L or reduction of $\geq 50\%$, $n = 146$, lesion $= 165$) and (2) non-achievement group ($n = 286$, lesion $= 331$). All QFR data and major adverse cardiovascular and cerebrovascular events (MACCEs) at 1 year were compared between groups.

Results: No differences between the groups in quantitative coronary angiography (QCA) data or QFR post-PCI were found. At the 1-year follow-up, lower percentage diameter stenosis (DS%) and percentage area stenosis (AS%) were recorded in the goal-achievement group (27.89 ± 10.16 vs. 30.93 ± 12.03, $p = 0.010$, 36.57 ± 16.12 vs. 41.68 ± 17.39, $p = 0.003$, respectively). Additionally, a better change in QFR was found in the goal-achievement group (0.003 ± 0.068 vs. -0.018 ± 0.086, $p = 0.007$), with a lower incidence of physiological restenosis and MACCEs (2.1 vs. 8.4%, $p = 0.018$, 5.4 vs. 12.6%, $p = 0.021$, respectively).

Conclusion: Evaluated by QFR, patients who achieved the LDL-C goal appear to have a better coronary physiological benefit. This group of patients also has a better clinical outcome.

Keywords: percutaneous coronary intervention, LDL—cholesterol, quantative flow ratio, cornoray physiology, physiological restenosis

OPEN ACCESS

Edited by:
Christos Bourantas, University College London, United Kingdom

Reviewed by:
Radu Tanacli, German Heart Center Berlin, Germany
Grigoris Karamasis, University General Hospital Attikon, Greece

***Correspondence:**
Yukun Luo
luoyukun@hotmail.com

†These authors have contributed equally to this work and share first authorship

Specialty section:
This article was submitted to Cardiovascular Imaging, a section of the journal Frontiers in Cardiovascular Medicine

Received: *12 March 2021*
Accepted: *20 May 2021*
Published: *18 June 2021*

Citation:
Chen L, Chen Q, Zhong J, Ye Z, Ye M, Yan Y, Chen L and Luo Y (2021) Effect of Low-Density Lipoprotein Cholesterol Goal Achievement on Vascular Physiology Evaluated by Quantitative Flow Ratio in Patients Who Underwent Percutaneous Coronary Intervention. Front. Cardiovasc. Med. 8:679599. doi: 10.3389/fcvm.2021.679599

INTRODUCTION

Although the prognosis of patients with coronary artery disease (CAD) has been much improved by percutaneous coronary intervention (PCI), patients who undergo this treatment still have an increased risk of recurrent cardiovascular events (1). Therefore, appropriate disease management is of increasing significance. As a crucial part of cardiac disease management, lipid modification is associated with reduced cardiovascular mortality. It is well-established that decreasing the low-density lipoprotein cholesterol (LDL-C) concentration in very high-risk patients is the primary target to reduce the risk of cardiovascular events (2, 3). Indeed, lipid-lowering therapy (LLT) has been the cornerstone of medical therapy for primary and secondary prevention of atherosclerotic cardiovascular disease (ASCVD) (4, 5).

The 2019 European Society of Cardiology (ESC)/European Atherosclerosis Society (EAS) guidelines for the management of dyslipidemia recommend an LDL-C reduction of ≥50% from baseline and an LDL-C goal of <1.4 mmol/L (<55 mg/dl) in very high cardiovascular disease risk patients [reduced from <1.8 mmol/L (70 g/dl) in the 2016 guidelines] (3, 6). Clinical benefits of LDL-C goal achievement have been demonstrated by numerous landmark studies (7, 8). In addition to lowering serum cholesterol levels, LLT induces plaque stabilization and improves endothelial function (9). As novel technologies [i.e., intravascular ultrasound (IVUS), optical coherence tomography (OCT), fractional flow reserve (FFR)] emerge, more precise methods to evaluate outcomes from LLT are gradually implemented. Emerging data obtained by novel imaging modalities suggest that LLT might have a greater impact on modulating lipid content vs. plaque volume, which makes multidisciplinary assessment of clinical outcome from LLT an important concern. The level of LDL-C and plaque volume can be obtained from laboratory tests, with information on plaque composition by IVUS or OCT. However, there is no appropriate method to assess the change in coronary physiology due to LLT.

In recent years, Hashikata et al. found a significant negative correlation between follow-up LDL-C levels and coronary physiology variation (FFR value) (10), which reflects the potential of physiologic assessment in tracing coronary physiology changes by treatment. Overall, the above worth is being further explored for use in coronary physiologic assessment in the LLT process. Although FFR can provide information on flow physiology, measurement of FFR is accompanied by certain problems, such as the requirement of introduction of an invasive pressure wire and increased patient discomfort, complication risk and costs associated with the catheterization procedure (11, 12). The quantitative flow ratio (QFR) is a promising angiography-based approach allowing fast computation of the FFR by 3D coronary artery reconstruction and fluid dynamics computation (11). The accuracy of QFR has been verified by previous studies (11–13); moreover, no requirement of pressure wires and a quicker procedural time make QFR a suitable choice for the evaluation of coronary physiology (12). Nevertheless, the impact of LDL-C goal achievement on vascular physiology evaluated by QFR remains unknown. This study aimed to investigate changes in coronary physiology in patients who achieve LDL-C goals at a 1-year follow-up through QFR analysis.

METHODS

Study Design

This study was approved by the Ethics Committee of Union Hospital, Fujian Medical University (No. 2020KY098). From June 2015 to December 2016, a total of 734 lesions in 606 patients who underwent PCI at Fujian Medical University Union Hospital were collected. QFR was assessed in all cases, and pre-PCI, post-PCI, and 1-year angiographic follow-up were collected as clinical characteristics. Post-PCI indicates the immediate time after successful PCI.

Patients diagnosed with stable angina, unstable angina, or postacute myocardial infarction (≥72 h) were eligible for enrollment when angiographic inclusion criteria were met. The indications for QFR computation were (1) diameter stenosis (DS) of at least one lesion between 50 and 90% (visual assessment) and (2) reference vessel diameter size ≥ 2.5 mm (visual assessment). Patients with any of the following clinical characteristics were excluded: (1) acute myocardial infarction (AMI) within 72 h; (2) lack of follow-up data; and (3) situations where QFR computation could not be performed, including only one lesion with DS < 50% or > 90% and thrombolysis in myocardial infarction (TIMI) grade < 3; reference vessel diameter size < 2 mm; lack of two optimal angiographic projections at least 25° apart; lesion involving myocardial bridge or bypass graft; severe overlap or tortuosity of target blood vessels; and poor angiographic image quality.

In light of our data acquired from June 2015 to December 2016, an LDL-C value of <1.8 mmol/L or an LDL-C reduction of ≥50% was chosen as an LDL-C goal based on 2016 ESC/EAS Guidelines for the Management of Dyslipidemias (6). All subjects were divided into two groups according to the LDL-C level at the time of 1-year follow-up: (1) goal-achievement group (patients achieved an LDL-C goal); (2) non-achievement group (patients failed to achieve an LDL-C goal).

QFR Computation and Quantitative Coronary Angiography Analysis

The QFR computation and QCA analysis were performed by two independent investigators blinded to the clinical data using the AngioPlus system (Pulse Medical Imaging Technology Shanghai, China) according to standard operating procedures. Based on automated contouring, a three-dimensional (3D) QCA model of the target vessel was reconstructed using two angiographic projections recorded at 15 frames/s and at least 25° apart. Proximal and distal reference points were applied to indicate the region of interest, and "flagging" was used to indicate lesion segments. After 3D QCA reconstruction, the vessel QFR was computed by contrast flow velocity models (11, 14). In addition, 3D reconstruction of the vessel provides QCA information of the target vessel comprising percentage diameter stenosis (DS%), percentage area stenosis (AS%), and late lumen loss (LLL). The delta QFR was chosen to present physiological changes, which

was defined as a difference in value between follow-up QFR and post-PCI QFR (delta QFR = follow-up QFR minus post-PCI QFR). LLL was defined as the difference in the minimal lumen diameter between post-PCI and follow-up.

PCI Procedure, Data Collection, and Follow-Up

PCI was performed according to the revascularization guidelines at that time. Nitrates had been given before each angiography. The type and expansion of the stent were determined by experienced cardiologists based on their own judgment. All patients received dual antiplatelet therapy for at least 12 months after PCI. A 1-year angiographic follow-up strategy was routinely recommended to all treated patients.

For all enrolled patients, relevant clinical data, laboratory results, and major adverse cardiovascular and cerebrovascular events (MACCEs) during hospitalization and at the 1-year follow-up were recorded. Serum biochemical levels, such as LDL-C, N-terminal pro brain natriuretic peptide (NT-proBNP), C-reactive protein (CRP), glucose, and creatinine were measured in the hospital clinical laboratory using routine automated techniques.

An MACCE was defined as the composite of any myocardial infarction (MI), stroke, or any ischemia-driven revascularization of target and non-target vessels. The target vessel was defined as the vessel in which the stent was placed during the first angiography. All patients were treated according to clinical guideline recommendations at the time of discharge. The occurrence of MACCEs within 1 year was recorded by telephone follow-up and medical record queries.

Statistical Analysis

Categorical variables were compared using the chi-square test or Fisher's exact test, and the results are presented as absolute frequencies and proportions. Continuous variables are expressed as the mean ± standard deviation for normally distributed data and as the median (interquartile range) for non-normally distributed data. They were compared using Student's *t*-test, Welch's *t*-test, or the Mann–Whitney *U*-test. Multivariate logistic regression analysis was employed to explore the relationship between LDL-C control and changes in QFR. For all analyses, a p-value of <0.05 was considered statistically significant. All statistical analyses were performed with SPSS 26.0 (IBM Inc., New York, NY, USA).

RESULTS

Baseline Characteristics

A total of 734 lesions in 606 patients who underwent PCI were collected, with 496 lesions in 432 patients examined for the final analysis. According to the study design, the enrolled patients were divided into a goal-achievement group ($n = 146$,

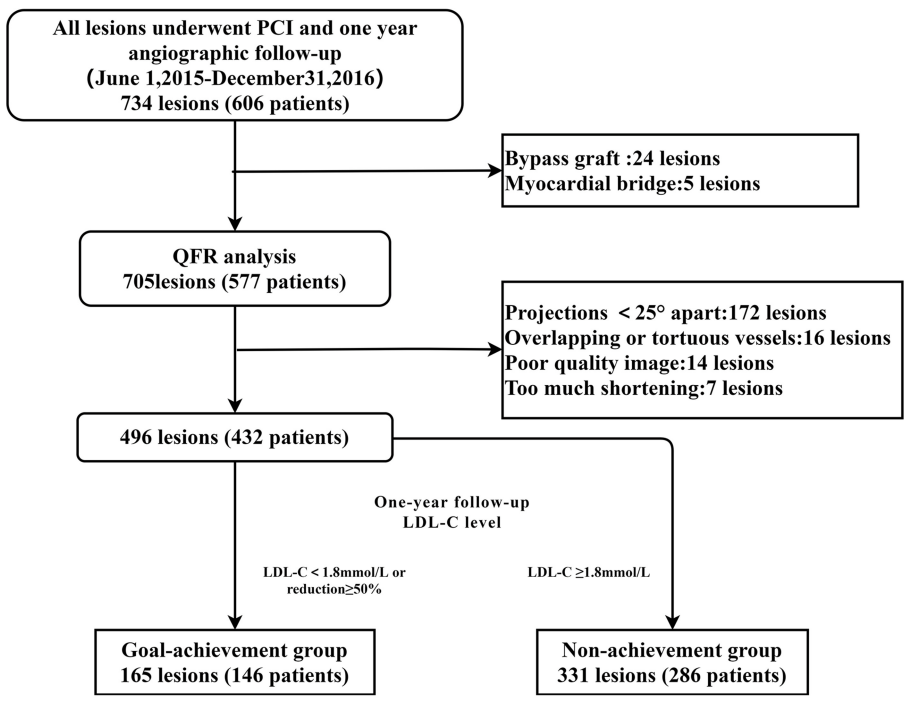

FIGURE 1 | Study flowchart. Among 734 lesions in 606 patients who underwent PCI, 705 lesions in 577 patients were analyzed by QFR. Of those, 172 lesions lacked two optimal angiographic projections at least 25° apart, 16 lesions were overlapping or tortuous, and 14 lesions in patients with poor-quality images were excluded. The other seven lesions were excluded due to excessive shortening lesions. Consequently, 496 lesions in 432 patients were analyzed in this study. According to the LDL-C level at the time of the 1-year follow-up, 165 lesions in 146 patients and 331 lesions in 286 patients were assigned to the goal-achievement and non-achievement groups, respectively. QFR, quantitative flow rate; PCI, percutaneous coronary intervention; LDL-C, low-density lipoprotein cholesterol.

lesion = 165) and non-achievement group (n = 286, lesion = 331) (**Figure 1**). The clinical, laboratory, and angiographic characteristics of the groups are summarized in **Table 1**. Based on comparison of baseline characteristics, the goal-achievement group showed a lower CRP level [1.71 (0.60–5.29) vs. 2.65 (0.89–8.52), $p = 0.033$] than the non-achievement group. No significant differences in age, sex, hypertension, diabetes mellitus, renal insufficiency, smoking, history of previous AMI or PCI, or type of CAD were found between the two groups. Levels of LDL-C, NT-proBNP, glucose, creatinine, and left ventricular ejection fraction (LVEF) were also similar. In addition, both groups had similar medical therapies.

One-Year Follow-Up Characteristics

The clinical and laboratory characteristics between the groups at the 1-year follow-up are summarized in **Table 2**. The goal-achievement group showed a lower LDL-C level (1.48 ± 0.31 vs. 2.69 ± 0.89, $p < 0.001$) than the non-achievement group. However, no significant differences in controlled hypertension and smoking cessation between the two groups were found, and levels of NT-proBNP, CRP, glucose, creatinine, and left ventricular ejection fraction (LVEF) were similar.

QCA and QFR Analysis Results

All QCA and QFR analysis data are summarized in **Table 3**. The goal-achievement group had a higher proportion of target lesions located in the right coronary artery (32.7% vs. 27.2%, $p = 0.034$) and similar proportions in the left anterior descending branch and left circumflex branch. There were no differences in QCA data or QFR between the groups post-PCI. However, the goal-achievement group showed a lower DS% (27.89 ± 10.16 vs. 30.93 ± 12.03, $p = 0.010$) and AS% (36.57 ± 16.12 vs. 41.68 ± 17.39, $p = 0.003$) at the 1-year follow-up. In addition, QFR was higher in the goal-achievement group than in the non-achievement group (0.96 ± 0.05 vs. 0.94 ± 0.09, $p = 0.005$), and the delta QFR in the goal-achievement group was better than that in non-achievement group (0.003 ± 0.068 vs. −0.018 ± 0.086, $p = 0.007$). To compare differences in physiological outcomes, the incidence of physiological restenosis (QFR ≤ 0.8) was recorded on the basis of the QFR value at the time of follow-up (**Table 4**). The goal-achievement group showed a lower incidence of physiological restenosis than the non-achievement group (2.1 vs. 8.4%, $p = 0.018$), though not all patients who were confirmed to have physiological restenosis received revascularization due to the lack of coronary physiological assessment at that time.

TABLE 1 | Baseline demographic characteristics.

	Goal-achievement group (n = 146)	Non-achievement group (n = 286)	*P*-value
Age, years	63.52 ± 10.62	62.47 ± 9.78	0.184
Male, *n* (%)	118 (80.8)	225 (78.7)	0.601
Hypertension, *n* (%)	98 (67.1)	173 (60.5)	0.319
Diabetes mellitus, *n* (%)	42 (28.8)	86 (30.1)	0.779
Renal insufficiency, *n* (%)	6 (4.1)	8 (2.8)	0.466
Current/past smoking, *n* (%)	82 (56.2)	156 (54.5)	0.749
Previous MI, *n* (%)	15 (10.3)	33 (11.5)	0.692
Previous PCI, *n* (%)	24 (16.4)	45 (15.7)	0.850
Medications			
Antiplatelet agent, *n* (%)	/	/	/
Statin, *n* (%)	/	/	/
ACE-inhibitor/ARB, *n* (%)	108 (74)	225 (78.7)	0.272
Type of coronary artery disease			
Unstable angina, *n* (%)	87 (59.6)	157 (54.9)	0.352
NSTEMI, *n* (%)	21 (14.4)	45 (15.7)	0.712
STEMI, *n* (%)	22 (15.1)	52 (18.2)	0.417
Stable angina, *n* (%)	16 (10.9)	32 (11.2)	0.943
Laboratory data			
NT-proBNP, pg/ml	121.00 (49.75–624.25)	172.50 (66.00–577.75)	0.114[a]
CRP, mg/L	1.71 (0.60–5.29)	2.65 (0.89–8.52)	0.033
Glucose, mmol/L	6.58 ± 2.64	6.57 ± 2.73	0.845
Creatinine, μmol/L	83.44 ± 54.94	78.42 ± 21.88	0.181
LDL-C, mmol/L	2.81 ± 1.07	2.93 ± 0.93	0.138
LVEF, %	61.83 ± 11.76	60.47 ± 10.71	0.194

Values are the mean ± standard deviation, median (interquartile range), or number (%).

[a] *The p-value was log transformed.*

MI, myocardial infarction; PCI, percutaneous coronary intervention; ACE-inhibitor, angiotensin-converting-enzyme inhibitor; ARB, angiotensin II receptor blocker; NSTEMI, non-ST segment elevation myocardial infarction; STEMI, ST segment elevation myocardial infarction; LDL-C, low-density lipoprotein cholesterol; NT-proBNP, N-terminal pro brain natriuretic peptide; CRP, C-reactive protein; LVEF, left ventricular ejection fraction.

TABLE 2 | One-year follow-up characteristics.

	Goal-achievement group (*n* = 146)	Non-achievement group (*n* = 286)	*P*-value
Controlled hypertension, *n* (%)	108 (74)	216 (75.5)	0.725
Smoking cessation, *n* (%)	37 (25.3)	53 (18.5)	0.099
Laboratory data			
NT-proBNP, pg/ml	82.5 (48.75–227)	96 (44–249.25)	0.801[a]
CRP, mg/L	0.74 (0.34–2.89)	1.09 (0.44–2.68)	0.142
Glucose, mmol/L	5.71 ± 1.61	6.16 ± 2.28	0.202
Creatinine, μmol/L	84.80 ± 52.25	84.33 ± 46.91	0.675
LDL-C, mmol/L	1.48 ± 0.31	2.69 ± 0.89	<0.001
LVEF, %	62.48 ± 10.13	61.68 ± 11.46	0.915

Values are the mean ± standard deviation, median (interquartile range), or number (%).
[a]The p-value was log transformed.
LDL-C, low-density lipoprotein cholesterol; NT-proBNP, N-terminal pro brain natriuretic peptide; CRP, C-reactive protein; LVEF, left ventricular ejection fraction.

TABLE 3 | QCA and QFR analysis results.

	Goal-achievement group (*n* = 165)	Non-achievement group (*n* = 331)	*P*-value
Target lesion location			
LAD, *n* (%)	89 (53.9)	186 (56.2)	0.354
LCX, *n* (%)	22 (13.3)	55 (16.6)	0.668
RCA, *n* (%)	54 (32.7)	90 (27.2)	0.034
Post-PCI			
QFR	0.96 ± 0.07	0.96 ± 0.07	0.914
Diameter stenosis, %	27.26 ± 11.61	27.61 ± 11.20	0.766
Area stenosis, %	34.93 ± 16.83	36.22 ± 16.51	0.500
One-year follow-up			
QFR	0.96 ± 0.05	0.94 ± 0.09	0.005
Delta QFR[a]	0.003 ± 0.068	−0.018 ± 0.086	0.007
Diameter stenosis, %	27.89 ± 10.16	30.93 ± 12.03	0.010
Area stenosis, %	36.57 ± 16.12	41.68 ± 17.39	0.003
Late lumen loss, mm[b]	0.07 ± 0.50	0.16 ± 0.48	0.172

Values are the mean ± standard deviation or number (%).
QCA, quantitative coronary angiography; QFR, quantitative flow rate; LAD, left anterior descending branch; LCX, left circumflex branch; RCA, right coronary artery.
[a]Delta QFR = Follow-up QFR – Post-PCI QFR.
[b]Late lumen loss was defined as the difference in minimal lumen diameter between post-PCI and follow-up.

Clinical Outcomes

A comparison of clinical outcomes at the 1-year follow-up between the groups is shown in **Table 5**. A total of 44 patients (10.2%) developed MACCEs, 8 and 36 of whom were from the goal-achievement and non-achievement groups (5.4 vs. 12.6%, $p = 0.021$) (**Table 5**). Multivariate logistics regression analysis confirmed that optimal LDL-C control was independently associated with changes in QFR at 1 year (OR: 0.590; 95% CI: 0.399-0.873, $p = 0.008$) (**Table 6**).

TABLE 4 | Incidence of physiological restenosis.

Case No.	Age (years)/ gender	Target vessel	One-year follow-up LDL-C (mmol/L)	One-year follow-up QFR
Goal-achievement group				
1	71/F	LAD	1.36	0.67
2	64/M	LAD	1.69	0.71
3	79/M	RCA	1.27	0.78
Non-achievement group				
4	85/M	LAD	2.44	0.26
5	54/M	LAD	2.55	0.47
6	64/F	LAD	2.06	0.53
7	54/F	LAD	2.64	0.53
8	51/M	LAD	2.1	0.63
9	61/M	RCA	2.17	0.65
10	65/F	LAD	2.85	0.67
11	46/F	LAD	2.53	0.68
12	61/M	RCA	2.65	0.71
13	73/M	LAD	2.47	0.72
14	71/M	RCA	3.54	0.72
15	76/M	LAD	3.92	0.72
16	59/M	LCX	1.87	0.73
17	45/F	RCA	2.74	0.73
18	48/M	LAD	2.6	0.73
19	54/M	LCX	1.99	0.74
20	58/M	LAD	1.86	0.76
21	46/M	LAD	1.94	0.76
22	61/M	LAD	2.2	0.77
23	45/M	LAD	2.76	0.77
24	60/M	LAD	2.05	0.78
25	63/M	LAD	1.87	0.79
26	66/F	LAD	2.1	0.79
27	52/M	LAD	2.15	0.79

LDL-C, low-density lipoprotein cholesterol; QFR, quantitative flow rate; LAD, left anterior descending artery; LCX, left circumflex artery; RCA, right coronary artery; physiological restenosis means vessel QFR ≤ 0.8 at the time of 1-year angiographic follow-up.

Management of LDL-C

Reductions in LDL-C levels from baseline were found in both groups (**Figure 2A**). We also found that LDL-C levels of patients who reported MACCEs were higher than those of patients without MACCEs or all patients (**Figure 2B**). The proportions of patients who achieved LDL-C goals were 50 (11.6%) at baseline and 134 (31.0%) at follow-up.

DISCUSSION

The main findings of this study are as follows. (1) Patients who achieved an LDL-C goal had a better change in QFR value and a lower DS% or AS% at the 1-year follow-up, indicating a better improvement in coronary physiology. (2) A positive consistent tendency in coronary physiology assessment (higher QFR) and clinical outcome (lower incidence of MACCEs) was observed, which supports the LDL-C goal achievement recommendation from the perspective of multidisciplinary assessments.

TABLE 5 | Incidence of MACCEs.

	Goal-achievement group ($n = 146$)	Non-achievement group ($n = 286$)	*P*-value
MACCEs, *n* (%)	8 (5.4)	36 (12.6)	0.021
MI, *n* (%)	0	1	/
TVR, *n* (%)	5 (3.4)	17 (5.9)	0.266
Non-TVR, *n* (%)	4 (2.7)	20 (7.0)	0.109
Stroke, *n* (%)	0	0	/

Values are number (%).
MACCEs, major adverse cardiovascular and cerebrovascular events; MI, myocardial infarction; TVR, target vessel revascularization; non-TVR, non-target vessel revascularization.

TABLE 6 | Multivariable logistic regression analysis of factors for the changes in QFR.

	OR (95%CI)	*P*-value
Age > 60 years (yes/no)	0.623 (0.422-0.919)	0.017
Controlled hypertension (yes/no)		0.544
Diabetes mellitus (yes/no)		0.320
Smoking cessation (yes/no)	0.602 (0.386-0.939)	0.023
LDL-C achievement (yes/no)	0.590 (0.399-0.873)	0.008

QFR, quantitative flow rate; LDL-C, low-density lipoprotein cholesterol.

In view of coronary physiology, we found that patients with lower levels of LDL-C tended to have a better change in QFR at the time of follow-up. Hashikata et al. reported that a lower level of LDL-C is associated with a higher increase in FFR. The mechanism of these changes is speculated to be due to the improvement in plaque burden and endothelial function by LLT (10). In addition, Ito et al.'s study showed that the plaque burden of a stented segment affects the FFR value rather than the luminal area immediately after optimal drug-eluting stent implantation; thus, plaque burden contributes to the change in coronary physiology to some extent (15). Our study also confirmed the influence of lipid control on physiological changes. However, QFR in our research was measured both post-PCI and at the 1-year follow-up, and significant in-stent restenosis is a major contributor to an increased pressure gradient across the stented segment and lower QFR value at the time of follow-up. The study by Kolozsvári et al. suggested that both luminal narrowing and plaque burden may affect FFR derived from computed tomography (CT) (16). Other studies have demonstrated that endothelial function may also affect the FFR value, though the mechanism is not completely understood (17, 18). The computational formula for QFR is similar to that for FFR (19, 20). We hold the opinion that plaque burden and endothelial function are the main factors influencing the QFR value in addition to the lumen narrowing resulting from significant stenosis. Hence, a more satisfactory QFR value may reflect a better improvement in plaque burden or endothelial function in patients without significant stenosis.

Patients who achieved the LDL-C goal seemed to have a better result in coronary physiology assessment. Indeed, we found that the achievement group had a better result in delta QFR ($p = 0.007$), indicating that a slight decline or even improvement in coronary physiological function occurred in these patients. In addition, a previous study concerning non-culprit plaque suggested that DS% can increase by 2.2% even with routine LLT (21). Our study showed a 0.6% increase in patients who achieved an LDL-C goal and a 3.3% increase in those who did not. It seems that LDL-C goal achievement may alleviate the deterioration of non-culprit lesions. LLL is an index to evaluate the absolute degree of restenosis and the status of intimal hyperplasia in the coronary artery (22), and no significant difference in LLL was found between the two groups ($p = 0.172$) in the short follow-up. However, Natsuaki et al. found that statin therapy was able to reduce the risk of late in-stent restenosis (23). By reviewing the angiography of patients with physiological restenosis in our study, the incidence of physiological restenosis due to in-stent restenosis was found to be close to 50% in the non-achievement group. Because of the short follow-up time, there was no significant difference in LLL, and the difference in QFR value was small. In other words, we hypothesized that statin therapy reduces late in-stent restenosis and thus affects physiological restenosis. Furthermore, a lower incidence of physiological restenosis was recorded in the goal-achievement group. These QCA analysis results indicate that patients who achieve an LDL-C goal have better improvement in coronary physiology. From the perspective of vascular physiology, the potential benefit of LDL-C goal achievement was verified.

The incidence of MACCEs was significantly lower in the patients who achieved an LDL-C goal. Previous studies have demonstrated clinical benefit from LLT, namely, a greater cardiovascular risk reduction with a greater absolute LDL-C reduction (24, 25), and the incidence of MACCEs in our study was consistent with that in previous studies. Nevertheless, no statistically significant differences in stroke, target, or non-target vessel revascularization were found in our study, which may be due to the small numbers of patients in the subgroups. Although the goal-achievement group did not show a significant difference in revascularization, this group of patients still had a lower incidence of revascularization according to numerical results. Therefore, our findings suggest that LDL-C management is of significance in cardiovascular event prevention. In addition, a positive accordant tendency in coronary physiology and clinical outcome was observed, which provides new evidence to support the LDL-C goal achievement recommendation.

For patients at very high cardiovascular risk, either secondary prevention or in primary prevention, a more aggressive LDL-C reduction goal is recommended according to the ESC/EAS 2019 guidelines (3). However, the proportion of patients who achieve an LDL-C goal remains unsatisfactory. In our study, only 31.0% of enrolled patients achieved an LDL-C goal, even though statins were prescribed to all. This may be due to an underdose of statins or insufficient concomitant use of other hypolipidemic drugs. Hence, there is considerable potential to optimize LLT further through statin intensification and appropriate use of novel LLTs.

Our study has some limitations. First, this was a retrospective observational study conducted at a single center with a

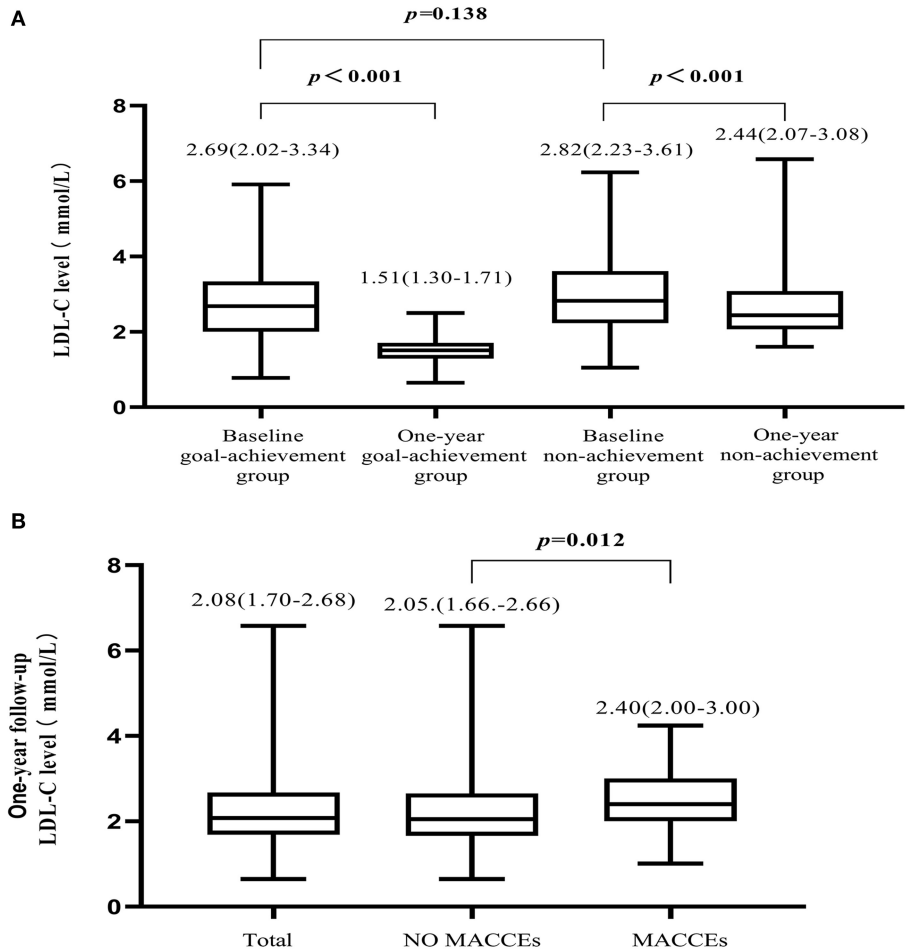

FIGURE 2 | Variation in LDL-C level. **(A)** Compared to baseline, LDL-C levels were reduced in both the goal-achievement and non-achievement groups at the 1-year follow-up. **(B)** LDL-C levels at the 1-year follow-up in all patients, patients with MACCEs, and patients without MACCEs.

short follow-up time and small sample size, and the findings need to be verified by further prospective multicenter cohort studies. Second, other treatment risk factors may affect the incidence of MACCEs, but they were not explored in detail in our study. Third, not all patients underwent a regular check, even though a 1-year angiographic follow-up strategy at first discharge was recommended to all. In addition, not all angiographic images were suitable for QFR analysis because of the lack of training in QFR operations at that time. These considerations may affect the selection process of patients.

CONCLUSIONS

As evaluated by QFR, patients who achieve an LDL-C goal appear to have a greater coronary physiological benefit. This group of patients also has a better clinical outcome, which is in agreement with physiological assessment results. This study provides new evidence to support LDL-C goal achievement recommendations from the perspective of multidisciplinary assessments.

DATA AVAILABILITY STATEMENT

The raw data supporting the conclusions of this article will be made available by the authors, without undue reservation.

AUTHOR CONTRIBUTIONS

QC and YL conceptualized and designed the project. LoC, JZ, and ZY collected the clinical data. LoC, YL, QC, and JZ analyzed data. LoC and JZ wrote the first draft of the manuscript. QC, YL, and LiC reviewed the article. YL is the guarantor for this article. All authors contributed to the article and approved the final version.

ACKNOWLEDGMENTS

We thank the staff and patients for their support to this study.

REFERENCES

1. Anderson L, Thompson DR, Oldridge N, Zwisler AD, Rees K, Martin N, et al. Exercise-based cardiac rehabilitation for coronary heart disease. *Cochrane Database Sys Rev.* (2016) 2016:Cd001800. doi: 10.1002/14651858.CD001800
2. Neumann FJ, Sousa-Uva M, Ahlsson A, Alfonso F, Banning AP, Benedetto U, et al. 2018 ESC/EACTS Guidelines on myocardial revascularization. *Eur Heart J.* (2019) 40:87–165. doi: 10.1093/eurheartj/ehy855
3. ESC/EAS guidelines for the management of dyslipidaemias: lipid modification to reduce cardiovascular risk. *Atherosclerosis.* (2019) 290:140–205. doi: 10.1093/eurheartj/ehz455
4. Baigent C, Blackwell L, Emberson J, Holland LE, Reith C, Bhala N, et al. Efficacy and safety of more intensive lowering of LDL cholesterol: a meta-analysis of data from 170,000 participants in 26 randomised trials. *Lancet.* (2010) 376:1670–81. doi: 10.1016/S0140-6736(10)61350-5
5. Boekholdt SM, Hovingh GK, Mora S, Arsenault BJ, Amarenco P, Pedersen TR, et al. Very low levels of atherogenic lipoproteins and the risk for cardiovascular events: a meta-analysis of statin trials. *J Am Coll Cardiol.* (2014) 64:485–94. doi: 10.1016/j.jacc.2014.02.615
6. Catapano AL, Graham I, De Backer G, Wiklund O, Chapman MJ, Drexel H, et al. 2016 ESC/EAS Guidelines for the Management of Dyslipidaemias. *Rev Esp Cardiol.* (2017) 70:115. doi: 10.1016/j.rec.2017.01.002
7. Heart Protection Study Collaborative G. Effects on 11-year mortality and morbidity of lowering LDL cholesterol with simvastatin for about 5 years in 20,536 high-risk individuals: a randomised controlled trial. *Lancet.* (2011) 378:2013–20. doi: 10.1016/S0140-6736(11)61125-2
8. Weintraub WS, Daniels SR, Burke LE, Franklin BA, Goff DC, Jr., Hayman LL, et al. Value of primordial and primary prevention for cardiovascular disease: a policy statement from the American Heart Association. *Circulation.* (2011) 124:967–90. doi: 10.1161/CIR.0b013e3182285a81
9. Schönbeck U, Libby P. Inflammation, immunity, and HMG-CoA reductase inhibitors: statins as antiinflammatory agents? *Circulation.* (2004) 109(21 Suppl 1):Ii18–26. doi: 10.1161/01.CIR.0000129505.34151.23
10. Hashikata T, Tojo T, Muramatsu Y, Sato T, Kakizaki R, Nemoto T, et al. Lower level of low density lipoprotein cholesterol is associated with a higher increase in the fractional flow reserve in patients with fixed-dose Rosuvastatin. *J Atheroscler Thromb.* (2018) 25:233–43. doi: 10.5551/jat.39560
11. Tu S, Westra J, Yang J, von Birgelen C, Ferrara A, Pellicano M, et al. Diagnostic accuracy of fast computational approaches to derive fractional flow reserve from diagnostic coronary angiography: the international multicenter FAVOR pilot study. *JACC Cardiovasc Interv.* (2016) 9:2024–35. doi: 10.1016/j.jcin.2016.07.013
12. Song L, Tu S, Sun Z, Wang Y, Ding D, Guan C, et al. Quantitative flow ratio-guided strategy versus angiography-guided strategy for percutaneous coronary intervention: rationale and design of the FAVOR III China trial. *Am Heart J.* (2020) 223:72–80. doi: 10.1016/j.ahj.2020.02.015
13. Westra J, Andersen BK, Campo G, Matsuo H, Koltowski L, Eftekhari A, et al. Diagnostic performance of in-procedure angiography-derived quantitative flow reserve compared to pressure-derived fractional flow reserve: the FAVOR II Europe-Japan Study. *J Am Heart Assoc.* (2018) 7:e009603. doi: 10.1161/JAHA.118.009603
14. Tu S, Barbato E, Köszegi Z, Yang J, Sun Z, Holm NR, et al. Fractional flow reserve calculation from 3-dimensional quantitative coronary angiography and TIMI frame count: a fast computer model to quantify the functional significance of moderately obstructed coronary arteries. *JACC Cardiovasc Interv.* (2014) 7:768–77. doi: 10.1016/j.jcin.2014.03.004
15. Ito T, Tani T, Fujita H, Ohte N. Relationship between fractional flow reserve and residual plaque volume and clinical outcomes after optimal drug-eluting stent implantation: insight from intravascular ultrasound volumetric analysis. *Int J Cardiol.* (2014) 176:399–404. doi: 10.1016/j.ijcard.2014.07.115
16. Kolozsvári R, Tar B, Lugosi P, Sánta J, Béres Z, Ungvári T, et al. Plaque volume derived from three-dimensional reconstruction of coronary angiography predicts the fractional flow reserve. *Int J Cardiol.* (2012) 160:140–4. doi: 10.1016/j.ijcard.2011.04.010
17. Yoshino S, Cassar A, Matsuo Y, Herrmann J, Gulati R, Prasad A, et al. Fractional flow reserve with dobutamine challenge and coronary microvascular endothelial dysfunction in symptomatic myocardial bridging. *Circ J.* (2014) 78:685–92. doi: 10.1253/circj.CJ-13-0846
18. Takase S, Matoba T, Nakashiro S, Mukai Y, Inoue S, Oi K, et al. Ezetimibe in combination with statins ameliorates endothelial dysfunction in coronary arteries after stenting: the CuVIC trial (Effect of Cholesterol Absorption Inhibitor Usage on Target Vessel Dysfunction After Coronary Stenting), a Multicenter Randomized Controlled Trial. *Arterioscler Thromb Vasc Biol.* (2017) 37:350–8. doi: 10.1161/ATVBAHA.117.309301
19. Lansky AJ, Pietras C. Fractional flow reserve from 3-dimensional quantitative coronary angiography: fresh light through an old window. *JACC Cardiovasc Interv.* (2014) 7:778–80. doi: 10.1016/j.jcin.2014.05.002
20. Pijls NH, Fearon WF, Tonino PA, Siebert U, Ikeno F, Bornschein B, et al. Fractional flow reserve versus angiography for guiding percutaneous coronary intervention in patients with multivessel coronary artery disease: 2-year follow-up of the FAME (Fractional Flow Reserve Versus Angiography for Multivessel Evaluation) study. *J Am Coll Cardiol.* (2010) 56:177–84. doi: 10.1016/j.jacc.2010.04.012
21. Kang J, Park KW, Lee MS, Zheng C, Han JK, Yang HM, et al. The natural course of nonculprit coronary artery lesions; analysis by serial quantitative coronary angiography. *BMC Cardiovasc Disord.* (2018) 18:130. doi: 10.1186/s12872-018-0870-9
22. Popma JJ, Leon MB, Moses JW, Holmes DR, Jr., Cox N, Fitzpatrick M, et al. Quantitative assessment of angiographic restenosis after sirolimus-eluting stent implantation in native coronary arteries. *Circulation.* (2004) 110:3773–80. doi: 10.1161/01.CIR.0000150331.14687.4B
23. Natsuaki M, Nakagawa Y, Morimoto T, Ono K, Shizuta S, Furukawa Y, et al. Impact of statin therapy on late target lesion revascularization after sirolimus-eluting stent implantation (from the CREDO-Kyoto Registry Cohort-2). *AM J Cardiol.* (2012) 109:1387–96. doi: 10.1016/j.amjcard.2012.01.350
24. Fulcher J, O'Connell R, Voysey M, Emberson J, Blackwell L, Mihaylova B, et al. Efficacy and safety of LDL-lowering therapy among men and women: meta-analysis of individual data from 174,000 participants in 27 randomised trials. *Lancet.* (2015) 385:1397–405. doi: 10.1016/S0140-6736(14)61368-4
25. Navarese EP, Robinson JG, Kowalewski M, Kolodziejczak M, Andreotti F, Bliden K, et al. Association between baseline LDL-C level and total and cardiovascular mortality after LDL-C lowering: a systematic review and meta-analysis. *JAMA.* (2018) 319:1566–79. doi: 10.1001/jama.2018.2525

Conflict of Interest: The authors declare that the research was conducted in the absence of any commercial or financial relationships that could be construed as a potential conflict of interest.

frontiers in Cardiovascular Medicine

ORIGINAL RESEARCH
published: 17 August 2021
doi: 10.3389/fcvm.2021.714471

SmartFFR, a New Functional Index of Coronary Stenosis: Comparison With Invasive FFR Data

Panagiotis K. Siogkas[1,2], Lampros Lakkas[3], Antonis I. Sakellarios[1], George Rigas[1], Savvas Kyriakidis[1], Kostas A. Stefanou[1], Constantinos D. Anagnostopoulos[4], Alberto Clemente[5], Silvia Rocchiccioli[5], Gualtiero Pelosi[5], Oberdan Parodi[5,6], Michail I. Papafaklis[3], Katerina K. Naka[3], Lampros K. Michalis[3], Danilo Neglia[5] and Dimitrios I. Fotiadis[1,2]

[1] Biomedical Research Institute, Foundation for Research and Technology Hellas, Ioannina, Greece, [2] Materials Science and Engineering, University of Ioannina, Ioannina, Greece, [3] Faculty of Medicine, School of Health Sciences, University of Ioannina, Ioannina, Greece, [4] PET-CT Department & Preclinical Imaging Unit, Center for Experimental Surgery, Clinical & Translational Research, Biomedical Research Foundation Academy of Athens, Athens, Greece, [5] Fondazione Toscana G. Monasterio and Institute of Clinical Physiology, Consiglio Nazionale delle Ricerche, Pisa, Italy, [6] Institute of Clinical Physiology, CNR, Pisa, Italy

OPEN ACCESS

Edited by:
Christos Bourantas,
University College London,
United Kingdom

Reviewed by:
Eric Poon,
St Vincent's Hospital (Melbourne), Australia
Peter Stone,
Brigham and Women's Hospital and Harvard Medical School, United States

***Correspondence:**
Dimitrios I. Fotiadis
fotiadis@uoi.gr

Specialty section:
This article was submitted to Cardiovascular Imaging, a section of the journal Frontiers in Cardiovascular Medicine

Received: 25 May 2021
Accepted: 27 July 2021
Published: 17 August 2021

Citation:
Siogkas PK, Lakkas L, Sakellarios AI, Rigas G, Kyriakidis S, Stefanou KA, Anagnostopoulos CD, Clemente A, Rocchiccioli S, Pelosi G, Parodi O, Papafaklis MI, Naka KK, Michalis LK, Neglia D and Fotiadis DI (2021) SmartFFR, a New Functional Index of Coronary Stenosis: Comparison With Invasive FFR Data. Front. Cardiovasc. Med. 8:714471. doi: 10.3389/fcvm.2021.714471

Aims: In this study, we evaluate the efficacy of SmartFFR, a new functional index of coronary stenosis severity compared with gold standard invasive measurement of fractional flow reserve (FFR). We also assess the influence of the type of simulation employed on smartFFR (i.e. Fluid Structure Interaction vs. rigid wall assumption).

Methods and Results: In a dataset of 167 patients undergoing either computed tomography coronary angiography (CTCA) and invasive coronary angiography or only invasive coronary angiography (ICA), as well as invasive FFR measurement, SmartFFR was computed after the 3D reconstruction of the vessels of interest and the subsequent blood flow simulations. 202 vessels were analyzed with a mean total computational time of seven minutes. SmartFFR was used to process all models reconstructed by either method. The mean FFR value of the examined dataset was 0.846 ± 0.089 with 95% CI for the mean of 0.833–0.858, whereas the mean SmartFFR value was 0.853 ± 0.095 with 95% CI for the mean of 0.84–0.866. SmartFFR was significantly correlated with invasive FFR values ($R_{CCTA} = 0.86$, $p_{CCTA} < 0.0001$, $R_{ICA} = 0.84$, $p_{ICA} < 0.0001$, $R_{overall} = 0.833$, $p_{overall} < 0.0001$), showing good agreement as depicted by the Bland-Altman method of analysis. The optimal SmartFFR threshold to diagnose ischemia was ≤0.83 for the overall dataset, ≤0.83 for the CTCA-derived dataset and ≤0.81 for the ICA-derived dataset, as defined by a ROC analysis ($AUC_{overall} = 0.956$, $p < 0.001$, $AUC_{ICA} = 0.975$, $p < 0.001$, $AUC_{CCTA} = 0.952$, $p < 0.001$).

Conclusion: SmartFFR is a fast and accurate on-site index of hemodynamic significance of coronary stenosis both at single coronary segment and at two or more branches level simultaneously, which can be applied to all CTCA or ICA sequences of acceptable quality.

Keywords: cardiovascular diseases, coronary stenosis, functional assessment, smartFFR, atherosclerosis

INTRODUCTION

Fractional flow reserve (FFR) is considered the gold standard for the assessment of the severity of coronary stenoses in patients undergoing invasive coronary angiography (ICA). It can reliably recognize hemodynamically significant lesions, thus providing an excellent tool for percutaneous coronary intervention (PCI) guidance (1, 2). However, FFR is not widely used in the clinical settings probably due to its increased total procedural cost (>$1,000 average cost per patient, including the dedicated pressure wire and the vasodilator adenosine administered i.v. to induce hyperemia), as well as the added discomfort of the patient. In fact, in the evaluation of intermediate stenoses (i.e. 40–70%) prior to intervention, FFR is measured only in 6.1% of the cases (3).

Accordingly, alternative invasive and non-invasive coronary functional assessment methods based on computational models have been proposed not requiring pressure measurements and vasodilator administration. During the past decade, computed tomography coronary angiography (CTCA) has gained increasing attention in the clinical setting as a non-invasive substitute of coronary angiography, thanks to the remarkable improvement of its imaging quality (4). CTCA is now considered as an accurate diagnostic tool for the assessment of CAD severity. It has been demonstrated that the combination of CTCA-derived 3D arterial models with the application of computational fluid dynamics (CFD) can offer a non-invasive assessment of the hemodynamic status of the artery of interest with an acceptable accuracy when compared to the invasively measured FFR (5–13). The existing approaches follow the rationale that since flow and pressure are not known *a priori*, lumped parameter models of several factors such as the pressure of the systemic circulation and the resistance of the coronary microcirculation need to be coupled with the fluid domain of the epicardial arteries, resulting to laborious virtual FFR calculations that require a large computational time. Recently, the virtual functional assessment index (vFAI) has been introduced as one amongst several valid computational FFR surrogates [i.e. such as QFR (14), DEEPVESSEL-FFR (15), FFRangio (16) as well as the aforementioned functional assessment indices given above] in patients undergoing ICA (17) or CTCA (18, 19), being able to determine the functional severity of a coronary lesion in an arterial segment. The non-invasive FFR computation by CFD on CTCA images currently adopted in clinical practice (5) is an off-site assessment with a relatively long computational time and no substantial advantages compared to alternative on-site CTCA assessment approaches as recently reported (12).

In this study, we present a new approach for a really on-site and real-time, geometrically derived functional assessment of coronary stenosis, which can be performed both with CCTA or ICA datasets and both in case of stenosis involving a single coronary segment as well as a coronary bifurcation (excluding the common trunk and the common trunk bifurcation). One of the main advantages of the proposed method is its speed and the ability to perform it on-site. The overall diagnostic performance of the proposed method was tested in a CTCA patient dataset as well as in an ICA patient dataset and compared with traditional pressure-wire derived FFR measurements available in both datasets. Furthermore, we also examined the optimal simulation type for the SmartFFR calculation by comparing rigid wall simulations against fluid structure interaction simulations.

MATERIALS AND METHODS

Study Population

To obtain a suitable CTCA-derived dataset, data from the multicenter EVINCI (EValuation of INtegrated Cardiac Imaging for the Detection and Characterization of Ischemic Heart Disease) project, as well as from the SMARTool (Simulation Modeling of coronary ARTery disease: a tool for clinical decision support) project were used. The aforementioned projects complied with the Declaration of Helsinki. In the context of the EVINCI study (20), ethical approval was provided by each participating center and all subjects gave written informed consent. For the present study investigating anonymized imaging data, informed consent was waived. From the EVINCI and SMARTool populations, we chose 69 patients with intermediate (20–90%) pre-test probability of CAD (21) who underwent CTCA and ICA exams and had invasive FFR assessed in at least one major vessel. The exclusion criteria were previous acute coronary syndrome, left ventricular ejection fraction <35%, cardiomyopathy, known CAD and more than moderate valve disease. An additional exclusion criterion was poor CTCA scan quality evaluated in a four levels scale (poor, satisfactory, good and excellent). Poor quality scans were excluded from our study. The final CTCA-derived dataset consisted of 88 major coronary arteries (**Figure 1**).

Regarding the ICA-derived dataset, a study population of 98 patients with stable or unstable angina or non-ST elevation myocardial infarction undergoing ICA and invasive FFR measurement at the University Hospital of Ioannina was retrospectively included in this study. The final ICA-derived dataset consisted of 114 major coronary arteries. Details on the coronary artery type distribution and patient demographics are presented in **Table 3**.

CTCA Acquisition

CTCA was performed in all patients using ≥64-slice scanners. All the arteries which were used in the present study were reconstructed at mean diastole (70%-80% of R-R interval) (22). The slice increment was 0.6 mm, whereas the average slice thickness was 0.625 mm. The pixel spacing values varied due to the different scanners that were used throughout the multi-center EVINCI study. Nitrates were used to enhance the CTCA quality, whereas beta-blockers were used when necessary to reduce the heart rate in order to perform good quality examinations and nitrates were always used as described in the international guidelines (23).

Invasive Coronary Angiography and FFR Acquisition

Standard techniques were used for the ICA acquisition with multiple projections. FFR was invasively measured after the intravenous administration of 140 μg/kg/min of adenosine,

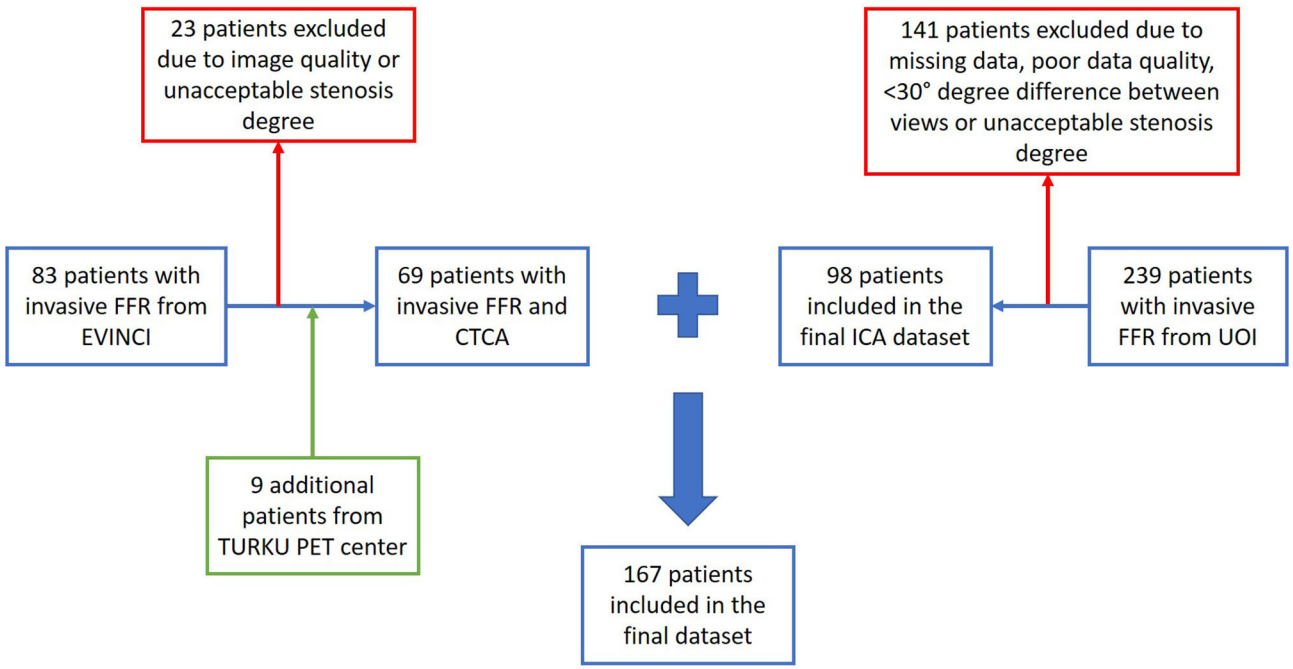

FIGURE 1 | Enrollment and diagnostic procedures.

using a combo-wire (Volcano Corporation). Arterial segments stenoses with FFR values lower than 0.80 were defined as hemodynamically relevant. The ICA dataset was provided by the University hospital of Ioannina which included all the FFR measurements that were performed during a period of 4 years. The main reasons for the exclusion of ICA cases were the following: a) poor image resolution, b) $<30^{\circ}$ angle difference between two ICA projections, c) presence of only one ICA projection, d) stenosis degree either <30 or $>90\%$.

3D Reconstruction

The reconstruction of the arterial models was performed with our in-house developed algorithms for the CTCA-derived dataset (24, 25) and for the ICA-derived dataset (26) and are both described in detail in the online **Supplementary Material** section. An expert interventional cardiologist (LL) performed the segmentation of the vessels of interest using the ICA images that contained the FFR wire within the vessel, in order to ensure the co-alignment of the FFR measured segment with the respective 3D reconstructed one.

SmartFFR Calculation

In order to calculate SmartFFR, blood flow simulations are carried out on the reconstructed 3D models of the arteries of interest using the finite element method. The arterial lumen is discretized into tetrahedral finite elements of face size that ranges from 0.09–0.12 mm, as defined by a mesh sensitivity analysis, and the respective Navier-Stokes and continuity equations are then solved using ANSYS® CFX 16.2. The SmartFFR index is primarily based on the virtual functional assessment index (17) as an outcome, but it has some key points of deviation regarding the process with which the index is calculated, constituting the method more robust, faster and able to be applied on more than one segment at a time. A transient blood flow simulation is performed on the 3D reconstructed artery for which the boundary conditions which are applied in single-segment simulations are the following:

Inlet: an average static pressure of 100 mmHg is applied as inlet boundary condition.
Outlet: an increasing transient flow profile is applied as an outlet boundary condition. It consists of 4 timesteps of a duration of 0.25 s each and flow rate values are increasing from 1 to 4 ml/s with a step of 1 ml/s (**Figure 2**).
Wall: a no-slip and no-penetration boundary condition is applied at the arterial wall.

For each timestep, the P_d/P_a value is calculated in order to construct the P_d/P_a vs. flow curve. The calculated P_d/P_a values for every timestep are then connected to create the appropriate patient-specific curve, using a smooth spline approximation with a total of 100 interpolation points using a dedicated script in MATLAB. The patient-specific curve is constructed for a flow range of 0–4 ml/s and the SmartFFR value is calculated by dividing the area under the patient-specific curve to the respective area under the curve of the respective healthy arterial segment (i.e. AUC = 4), following the vFAI rationale by Papafaklis et al. (17).

In the ICA-derived dataset, only the main vessel was reconstructed, whereas in the CTCA-derived dataset, when the simulation was performed in the left coronary artery system, the

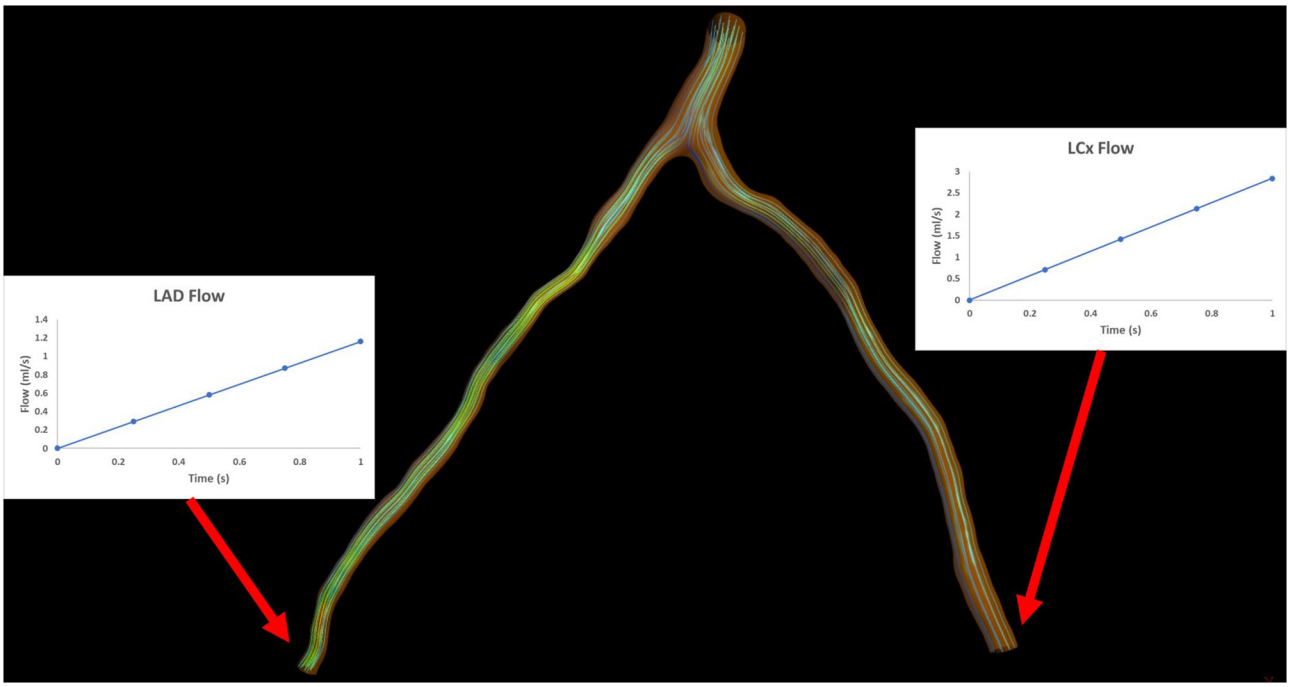

FIGURE 2 | Illustration depicting the outlet boundary conditions for an arterial bifurcation.

two main coronary arteries (LAD and LCx) were reconstructed. In order to calculate the SmartFFR in bifurcating arterial models, we first have to determine the flow ratio that enters each branch. The left descending and circumflex coronary arteries were evaluated by 3D reconstructed models and the flow ratio of each branch was determined at the level of the bifurcation involved. For the left vasculature, we assume a flow rate of 2 ml/s during rest that might be evenly distributed in the two main branches if we have an equal area at the inlet of the two branches (27). However, the patient-specific flow that enters each branch needs to be defined for every case. In order to do that, we apply Murray's law after having calculated the diameters and the areas of the two branches. Murray's law correlates the flow ratio that passes through the two branches with the respective diameters of the two branches. The aforementioned relation is given by:

$$\frac{q_{D2}}{q_{D1}} = \left(\frac{d_{D2}}{d_{D1}}\right)^3, \quad (1)$$

where q_{D1} and q_{D2} are the flows of branches 1 and 2 and d_{D1} and d_{D2}, their respective diameters (**Figure 3**).

After having calculated the ratio, we then perform a transient blood flow simulation in the entire model with the following outlet boundary conditions:

Outlets: an increasing transient flow profile is applied as a boundary condition. However, in this case, we need to calculate the flow of each branch for each time step. The left main branch of the coronary vasculature has a total flow of around 2 ml/s during rest as it has been calculated through PET quantitative measurements. This is expected since both left main branches (i.e. Left Anterior Descending and Left Circumflex) average a mere 1 ml/s during rest (i.e. approximately equal to the respective flow during rest of the Right Coronary Artery). We assume that in a totally healthy left vasculature, we will have a peak hyperemic flow of 8 ml/s (i.e. 4 ml/s per branch) entering the left main stem [i.e. following the rationale of (28) stating that it is equal to the mean ± 2SD hyperemic flow increase in a normal artery] (29). Having this in mind, we create a transient flow of 4 timesteps of 0.25 s each with a total flow for each timestep from 0 to 8 ml/s. The outlet flow of each branch is calculated using the previously computed flow ratio and is applied for each timestep, respectively.

The inlet and wall boundary conditions were the same as in the single segment smartFFR calculation process. Flow is considered laminar, and blood is treated as a Newtonian fluid with density 1050 kg/m^3 and dynamic viscosity 0.0035 Pa·s.

In order for the SmartFFR value to be calculated for each branch, we need to calculate the P_d/P_a values for each time step at each branch. In order to do that, we first have to find the computed pressure at the inlet of each of the two branches, since this is the inlet pressure for each branch and not the overall inlet pressure at the left main stem. After having the P_d/P_a values calculated for each timestep, we then build the respective P_d/P_a vs. flow curves for each branch. In order to have a balanced universal value for each branch, we have to interpolate the curve of the branch with the higher flow up to a flow of 4 ml/s and extrapolate the respective curve of the second branch up that had the lower flow to the same value. The flow division is performed in order to apply physically valid boundary conditions on the two branches regarding the outlet, since the two branches cannot

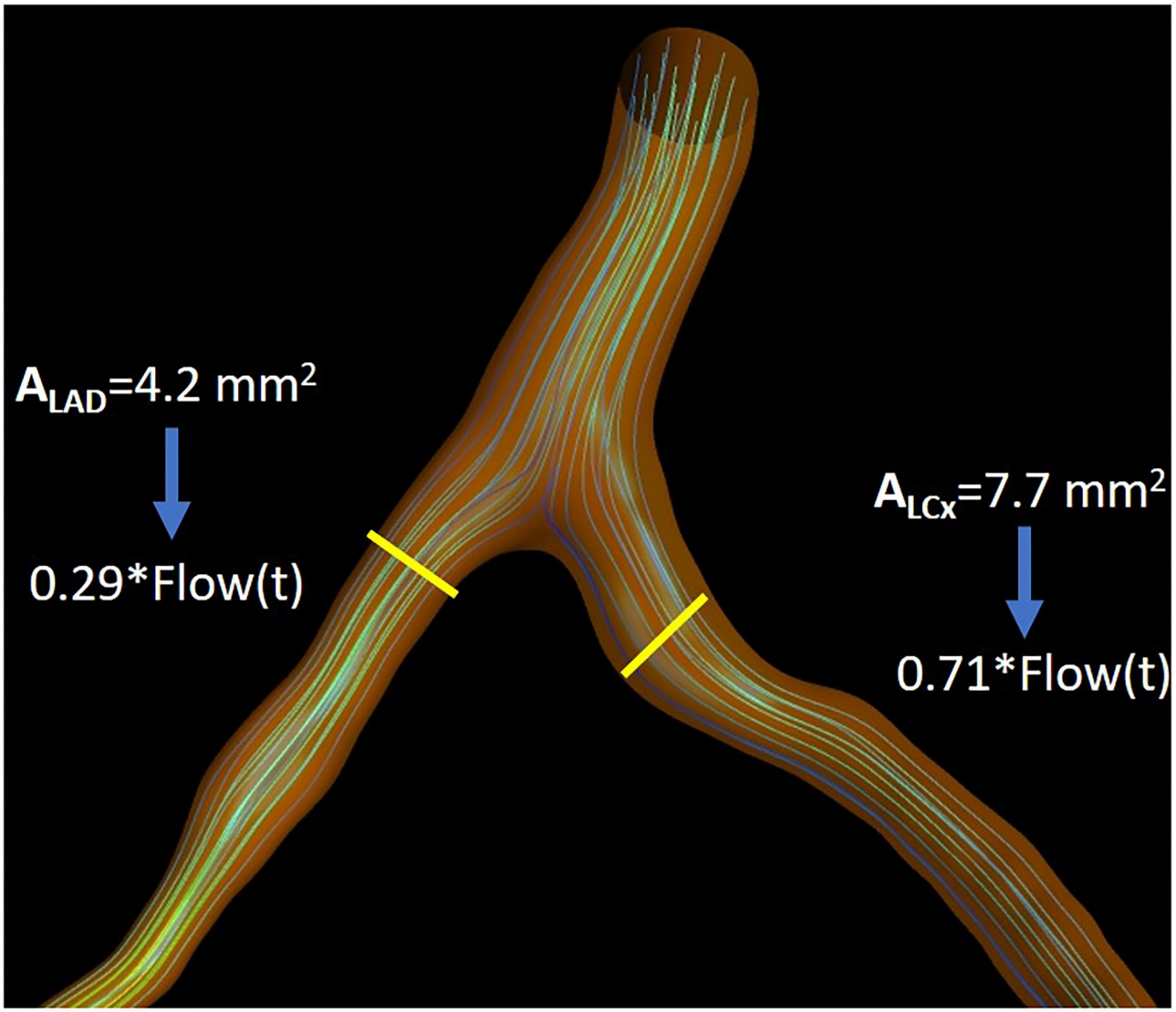

FIGURE 3 | Illustration depicting the flow separation ratio as calculated for an indicative case, as calculated by Murray's law.

have an equal division of flow. SmartFFR is then calculated as the ratio of the area under the patient-specific curve divided by area under the curve of the respective healthy arterial segment for each branch (**Figure 4**). The SmartFFR values were calculated in a blind fashion from the actual FFR values.

Effect of Fluid Structure Interaction (FSI) on SmartFFR

We have investigated the effect of different simulation methods on the calculated SmartFFR values. The whole process is described in detail in the online **Supplementary Material**.

Statistical Analysis

The relationship between FFR and SmartFFR was quantified by calculating the Pearson's correlation coefficient. In order to assess the agreement between the two methods, the Bland–Altman plots and the corresponding 95% limits of agreement were used. A Receiver Operator Curve (ROC) analysis was performed to identify the cut-off values of the examined variables. The categorization of FFR and SmartFFR values was made using the cut-off value of 0.8 and the calculated cut-off from ROC curve for the FFR and SmartFFR (for each dataset separately), respectively. Sensitivity (SE), specificity (SP), positive predictive value (PPV), negative predictive value (NPV), and diagnostic accuracy (the percentage of patients correctly diagnosed by SmartFFR) were used to assess the performance of SmartFFR. P values < 0.05 were considered statistically significant. The comparison between the ROC curves was based on the DeLong method (MedCalc software).

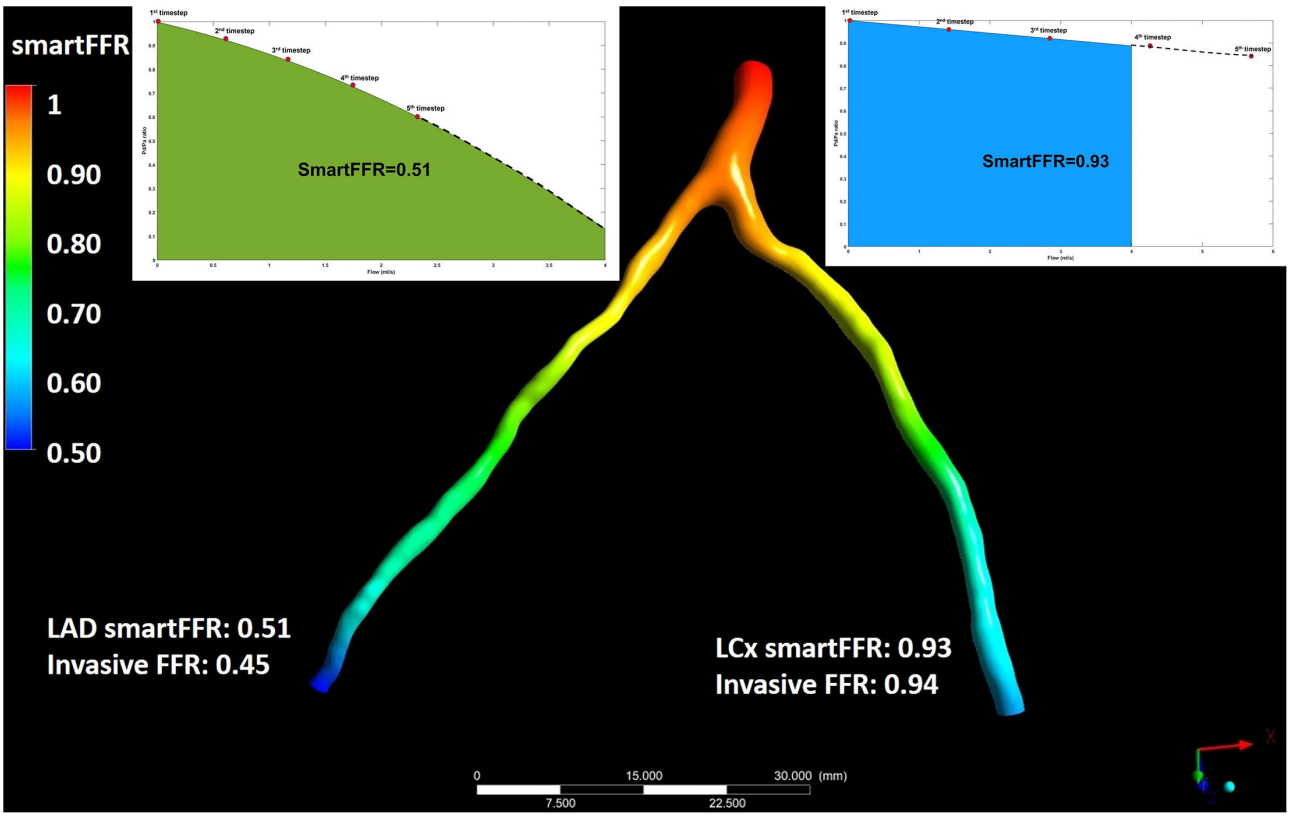

FIGURE 4 | Illustration depicting the simultaneous SmartFFR calculation process for the two main branches of the left coronary vasculature (i.e. LAD and LCx). The dashed line after the last simulation timestep at the LAD branch was used to extrapolate the curve to reach the 4 ml/s mark, whereas for the LCx branch, the curve was interpolated to limit the curve to the 4 ml/s mark, respectively.

RESULTS

From the CTCA-derived and ICA-derived datasets, 202 major coronary arteries (i.e. stenosis degree ranging between 30–90%), in which invasive FFR had been measured, were used to compute and validate the SmartFFR index. The ICA-derived dataset consisted of 114 major coronary vessels from 98 patients. Among the 114 arteries, 81 were LAD segments, 18 were LCx segments and the remaining 15 were RCA segments. 29 vessels (i.e. 25.4%) presented with a pathologic FFR value (i.e. FFR $\leq$ 0.80) and among these, sixteen arteries had FFR values within the so-called "gray zone" (i.e. FFR 0.75–0.80) (30).

In order to validate the efficacy of the bifurcation-based SmartFFR, we used the CTCA-derived dataset. The dataset consisted of 88 major coronary arteries. However, we must here state that the cases for which FFR measurements of both LAD and LCx branches (i.e. simultaneous SmartFFR calculation for two branches) were available were very few (i.e. nine cases). Twenty-seven cases (i.e. 30.7%) exhibited an ischemic FFR value (i.e. FFR $\leq$ 0.80) and from these, eleven cases were within the "gray zone". In order to tackle this issue, we validated the method by comparing the SmartFFR value with the respective invasively measured FFR value of the branch that was available.

Strong correlation was observed between the two methods for the three (i.e. CCTA-derived dataset, ICA-derived dataset and overall dataset) datasets ($R_{CCTA} = 0.86$, $p_{CCTA} < 0.0001$, $R_{ICA} = 0.84$, $p_{ICA} < 0.0001$ and $R_{overall} = 0.833$, $p_{overall} < 0.0001$, respectively) and good agreement was observed by the Bland-Altman method of analysis (**Figure 6**). For the ICA-derived dataset there was a slight overestimation of FFR by SmartFFR in this case with a mean difference of 0.024 ± 0.051 ($p < 0.0001$). The corresponding limits of agreement were -0.012 to 0.08 with 95% confidence intervals -0.14 to -0.11 for the lower limit and 0.06 to 0.09 for the upper limit, respectively. For the CCTA-derived dataset there was a slight underestimation of FFR by SmartFFR with a mean difference of 0.006 ± 0.053 ($p = 0.26$). The corresponding limits of agreement were from-0.098 to 0.11 with 95% confidence intervals -0.1150 to -0.08135 for the lower limit and -0.1150 to -0.08135 for the upper limit, respectively. Finally, for the overall dataset, there was a slight overestimation of FFR by SmartFFR in this case with a mean difference of 0.007 ± 0.053 ($p < 0.0001$). The corresponding limits of agreement were -0.0147 to 0.00016 with 95% confidence intervals -0.1251 to-0.09966 for the lower limit and 0.085 to 0.11 for the upper limit, respectively.

The interobserver agreement for SmartFFR measurements was tested in 20 randomly selected coronary vessels reconstructed

from ICA (12 LAD, 4 LCx and 4 RCA, respectively) and 20 vessels reconstructed by CTCA (13 LAD, 3 LCx and 4 RCA, respectively). Strong agreement was found between the two observers for the CTCA dataset (mean difference = −0.007 ± 0.01, $p = 0.0068$), as well as for the ICA dataset (mean difference = −0.009 ± 0.018, $p = 0.04$). The intraobserver agreement for SmartFFR measurements was tested in the same randomly selected set of 40 vessels (20 vessels reconstructed from ICA and 20 vessels reconstructed from CTCA, respectively). Excellent agreement was observed in the intraobserver variability analysis for the CTCA-derived dataset (mean difference = -0.002 ± 0.006, $p = 0.16$), as well as for the ICA-derived dataset, respectively (mean difference = -0.0035 ± 0.006, $p = 0.15$).

Diagnostic Accuracy of SmartFFR (Overall Dataset)

The optimal SmartFFR cutoff value for identifying a functionally significant stenotic segment with an FFR value ≤0.80 was ≤0.83 from receiver operator curve (ROC) analysis (**Figure 5**). The overall diagnostic performance of SmartFFR using the calculated optimal threshold but also the established FFR threshold of 0.80 is presented in **Table 1** (AUC = 0.956, $p < 0.001$).

Diagnostic Accuracy of SmartFFR (ICA Dataset)

In the ICA-derived dataset, the optimal SmartFFR cutoff value for identifying a functionally significant stenotic segment with an FFR value ≤0.80 was ≤0.81, deriving from the receiver operator curve (ROC) analysis (**Figure 5**). The overall diagnostic performance of SmartFFR using the calculated optimal threshold but also the established FFR threshold of 0.80 is presented in **Table 1** (AUC = 0.975, $p < 0.001$).

Diagnostic Accuracy of SmartFFR (CTCA Dataset)

In the CTCA-derived SmartFFR analysis, the optimal SmartFFR threshold to identify a functionally significant stenotic segment with FFR ≤ 0.80 was SmartFFR ≤ 0.83, as dictated by the receiver operator curve (ROC) analysis (**Figure 5**). The overall diagnostic performance of SmartFFR is presented in **Table 1** (AUC = 0.952, $p < 0.001$).

SmartFFR and Type of Simulation

To assess the possible effect of the simulation type on SmartFFR, a rigid wall or a FSI simulation model were used to compute SmartFFR in 25 coronary segments. The average SmartFFR for the rigid wall simulations for the 25 segments was 0.838 ± 0.19 whereas, for the FSI simulations the average SmartFFR was 0.848 ± 0.19, respectively. Strong correlation was found between the two simulation methods presenting with almost identical SmartFFR values (r = 0.99, $p < 0.0001$) (**Figure 6**).

Excellent agreement was also found for the two methods of simulation with a mean difference of −0.010000 ± 0.012 as calculated by the Bland-Altman method of analysis (**Figure 7**). The upper limit was 0.0133 with 95% CI from 0.0048 to 0.022, whereas the lower limit was −0.033 with 95% CI from −0.042 to −0.025.

DISCUSSION

In this study, we have demonstrated the efficacy of our newly proposed SmartFFR index in assessing the hemodynamic significance of coronary stenoses within a matter of minutes, using either the most well-known non-invasive cardiac imaging modality (i.e. CTCA), or the most-commonly used invasive coronary imaging modality (i.e. ICA) (**Figure 8**). We observed that SmartFFR values from the ICA-derived dataset had a slightly inferior correlation to the invasively measured FFR than those from the CTCA-derived dataset, but had slightly increased accuracy and sensitivity, possibly due to the higher spatial resolution of ICA. More specifically, in the overall dataset, SmartFFR matched the values of the invasively measured FFR closely, having sensitivity and specificity of 94.6 and 85.6%, respectively, using the computed cutoff value of ≤0.83 to identify stenoses of FFR ≤ 0.80 (**Table 1**).

Several studies have already demonstrated the efficacy of CTCA-derived or ICA-derived functional indices to identify ischemic lesions with the aid of CFD simulations (8, 31). In the first studies investigating the possible application of CTCA-derived computational FFR measurements, the agreement between FFR_{CT} and the invasively measured FFR was rather modest (32). However, by gaining the ability to create far more complex models of the coronary vasculature that included vascular microcirculation, the accuracy of FFR_{CT} was significantly improved over the past years and many studies demonstrated the efficacy of the method. The results of the present study indicate the efficacy of a new method, SmartFFR, to identify hemodynamically significant stenoses. Compared to the previously validated virtual Functional Assessment Index (17) which is the foundation for SmartFFR, SmartFFR required a lower total computational time, since only one blood flow simulation is needed (**Table 2**). Furthermore, SmartFFR allows for the simultaneous functional assessment of at least two vessels and could even allow for the assessment of more than two branches. When compared to other virtual indices, SmartFFR exhibits similar or even superior diagnostic performance having a diagnostic accuracy, sensitivity, specificity, PPV and NPV of 88.1, 94.6, 85.4, 71.6, and 97.7%, regarding the overall dataset (**Table 1**). Furthermore, SmartFFR can be calculated on a simple personal computer on-site, without the need of a dedicated core-laboratory and the total process time, along with the required 3D reconstruction time does not exceed an average of 10 minutes, depending on the available imaging modality (**Table 2**).

Study Limitations

Our study included a retrospective analysis of two imaging datasets including either invasive or non-invasive coronary angiographies. The rather limited number of patients included in the CTCA-derived dataset is a limitation. We tested the efficacy of the multi-vessel SmartFFR only on the left coronary system of the CTCA patients that had invasive FFR measurements available for the LAD, the LCx or both, since this was the only way to validate the efficacy of the method. Unfortunately, there was a lack of simultaneous invasive FFR

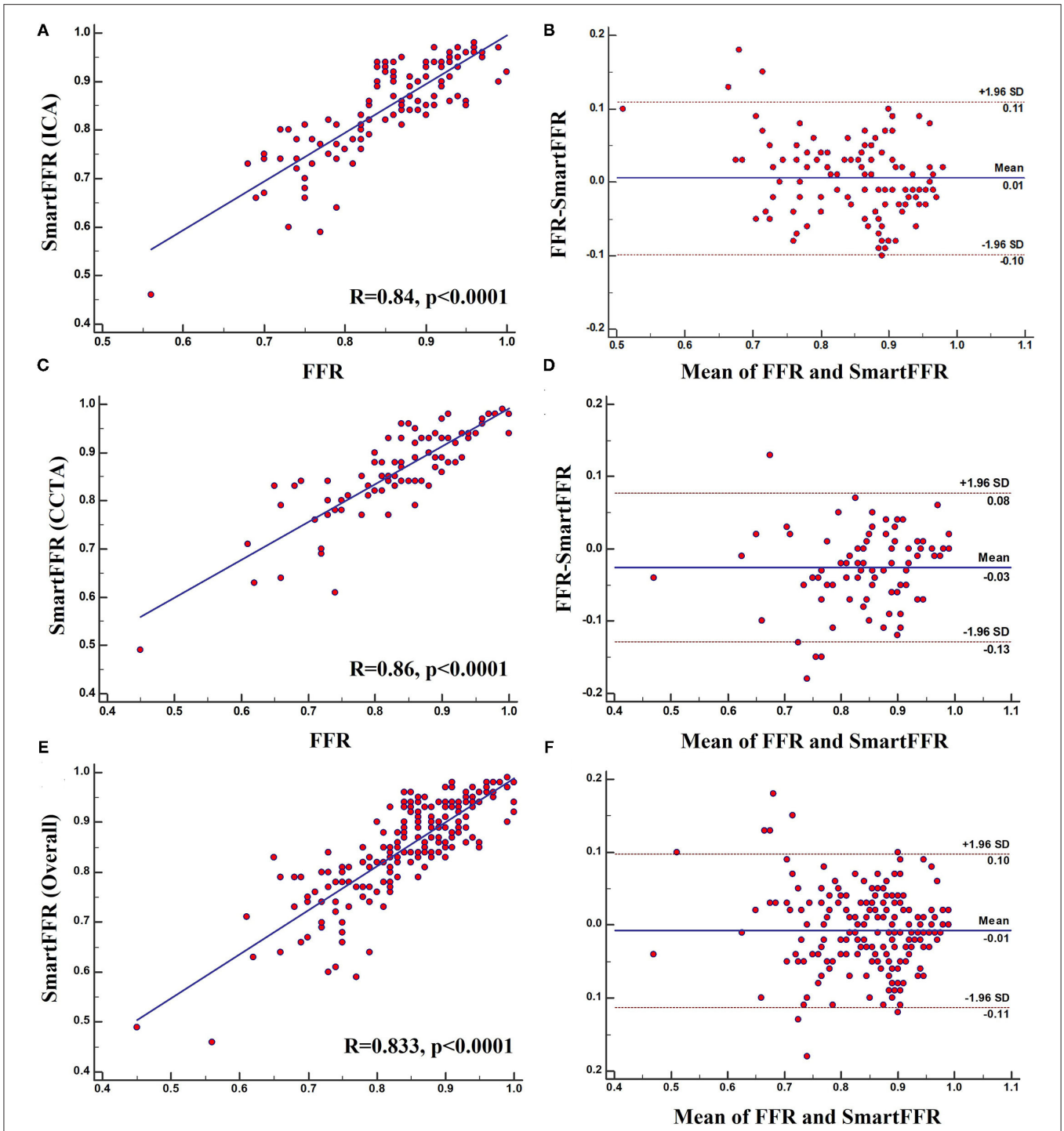

FIGURE 5 | (A) Regression plot and **(B)** Bland-Altman plot comparing SmartFFR to the invasively measured FFR (ICA Dataset). **(C)** Regression plot and **(D)** Bland-Altman plot comparing SmartFFR to the invasively measured FFR (CTCA Dataset). **(E)** Regression plot and **(F)** Bland-Altman plot comparing SmartFFR to the invasively measured FFR (Overall dataset).

measurements in two branches (only 9 cases had simultaneous invasive FFR measurements for the LAD and the LCx branch, respectively), which constitutes a limitation of our study. Even in this rather modest sample though, SmartFFR matched the invasively measured FFR values rather well, discriminating the hemodynamically significant stenoses with good accuracy. We should also mention that SmartFFR was tested also in a single-vessel manner in the CTCA dataset for the RCA cases that

TABLE 1 | Diagnostic performance of SmartFFR for the overall dataset, the ICA-derived dataset and the CCTA-derived dataset, for the optimal thresholds as calculated by the Youden index and for the established FFR threshold of 0.80.

	FFR ≤ 0.80								
	Accuracy (%)	**Sensitivity (%)**	**Specificity (%)**	**PPV (%)**	**NPV (%)**	**TP**	**TN**	**FP**	**FN**
SmartFFR ≤ 0.83 Overall dataset	88.1	94.6	85.6	71.6	97.7	53	125	21	3
SmartFFR ≤ 0.80 (Overall dataset)	89.1	76.8	93.8	82.7	91.3	43	137	9	13
SmartFFR ≤ 0.81 (ICA dataset)	91.2	96.6	89.4	75.7	98.7	28	76	9	1
SmartFFR ≤ 0.80 (ICA dataset)	91.2	89.7	91.8	78.8	96.3	26	78	7	3
SmartFFR ≤ 0.83 (CTCA Dataset)	90.9	88.9	91.8	82.8	94.9	24	56	5	3
SmartFFR ≤ 0.80 (CTCA Dataset)	86.4	63	96.7	89.5	85.5	17	59	2	10

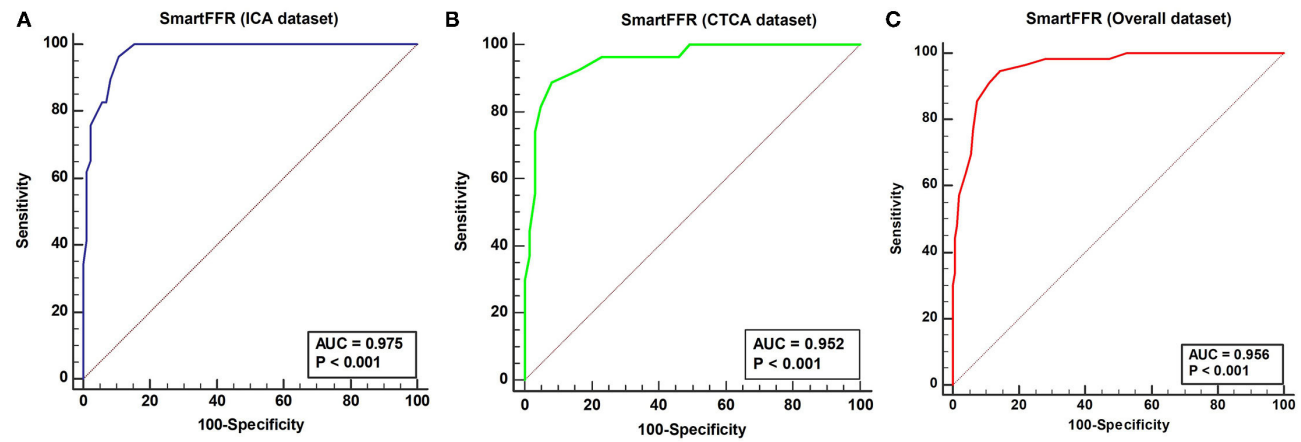

FIGURE 6 | ROC curve depicting the diagnostic performance of SmartFFR for **(A)** ICA dataset (95% CI 0.91–0.98), **(B)** CTCA dataset (95% CI 0.88–0.99) and **(C)** Overall dataset (95% CI: 0.92 to 0.98).

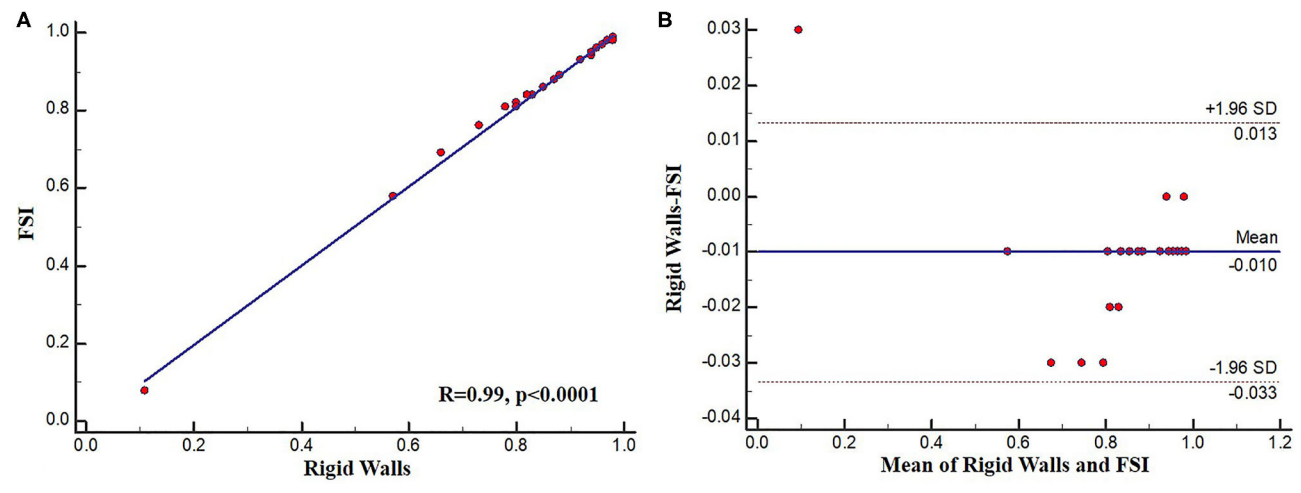

FIGURE 7 | (A) Regression plot and **(B)** Bland-Altman plot comparing FSI and rigid wall SmartFFR calculations.

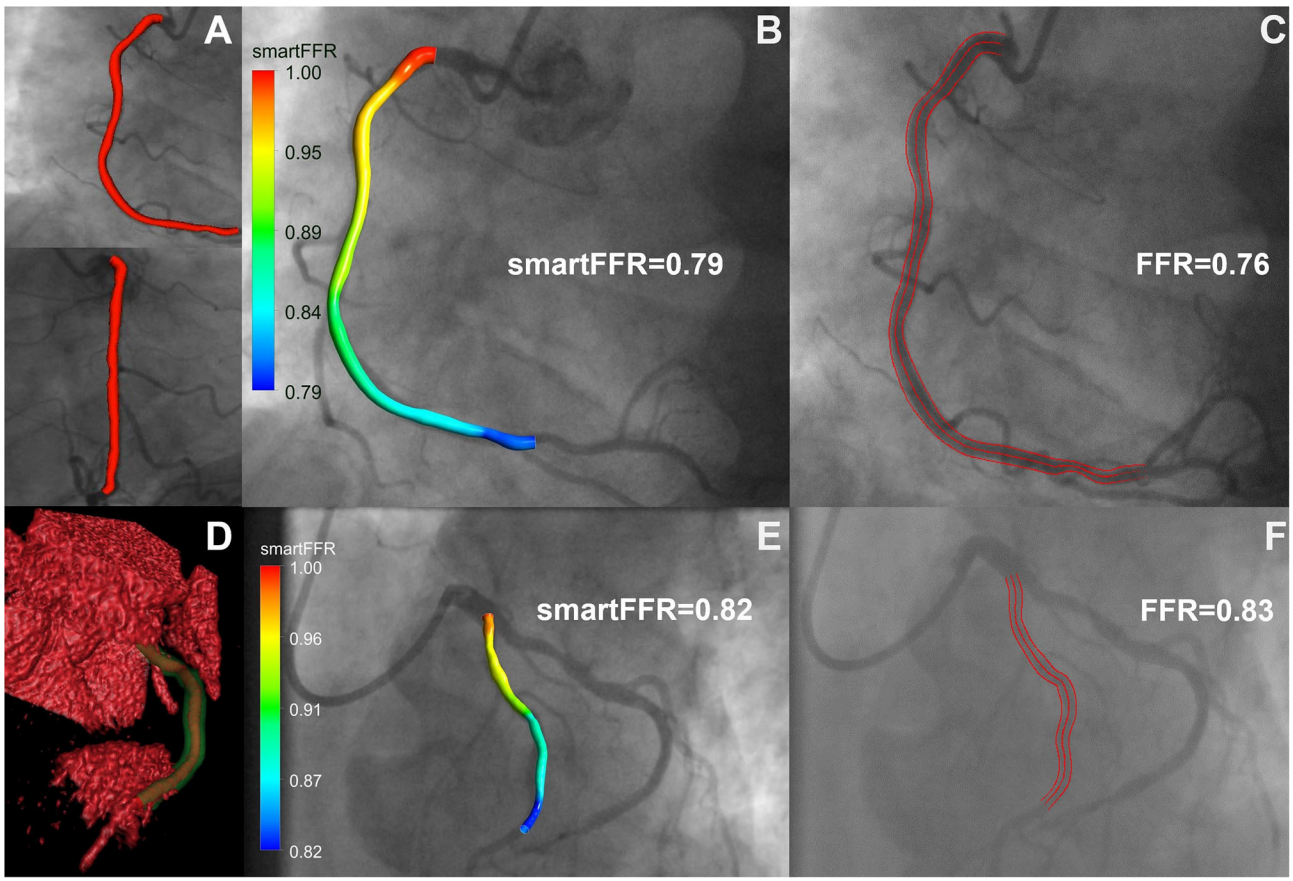

FIGURE 8 | Top row: ICA-derived model, Bottom row: CCTA-derived model. **(A)** 3D reconstructed ICA-derived model back-projected on the two utilized angiographic views using our in-house developed software platform. **(B)** ICA-derived 3D model with smartFFR value, back-projected on the respective angiographic image, **(C)** ICA image with respective invasively measured FFR value and delineation of the segment of interest, **(D)** Volume rendered 3D reconstructed model with our in-house developed software platform. The outer wall is depicted in transparent green and the lumen in orange. **(E)** CCTA-derived 3D model with smartFFR value, back-projected on the respective angiographic image **(F)** ICA image of the CCTA model with respective invasively measured FFR value and delineation of the segment of interest.

TABLE 2 | Average required time for SmartFFR and vFAI.

Imaging modality	Reconstruction time	Mesh generation	SmartFFR (per bifurcation)	vFAI (per segment)
ICA	∼3 min	∼3 min	∼3 min	∼7 min
CTCA	∼1-2 min	∼3 min	∼3 min	∼7 min

were examined. However, the majority of the lesions were located at the left coronary vasculature (i.e. ∼80%) which is also a limitation of the examined dataset. Furthermore, the lack of diastolic blood pressure data did not allow us to substitute the universal inlet pressure value with a patient-specific blood pressure value, a methodological step that will further enhance the SmartFFR methodology. Moreover, Murray's law is generally used for idealized laminar flows and in cases of severe stenoses it might not be most suitable. However, we used laminar flow assumptions throughout the entire dataset in order to preserve consistency through the simulations. Finally, we must also mention the rather limited number of marginal cases (i.e. within the so-called FFR "gray-zone"), cases that are usually most challenging in terms of accuracy, even for the invasive FFR measurement (**Table 3**). We are currently working on broadening our validation dataset for the multi-vessel SmartFFR analysis, a non-trivial task though, since multiple invasive FFR measurements are required in the left coronary vasculature.

CONCLUSIONS

We have demonstrated the efficacy of SmartFFR to discriminate hemodynamically significant stenoses in either CTCA-derived

TABLE 3 | Patient demographics and vessel characteristics.

Cardiovascular risk factors	
Age	63.1 (± 7.6)
Female	59 (29%)
Male	143 (71%)
BMI, kg/m^2	27.8 (± 4.7)
Body Mass, kg	82.1 (± 16.9)
Diabetes (*N*, %)	47 (23.2%)
Smoker during past year (*N*, %)	41 (20.3%)
Hypertension (*N*, %)	138 (68.3%)
Hypercholesterolemia (*N*, %)	138 (68.3%)
Coronary vessels (*N*, %)	
Right coronary artery	39 (19.3%)
Left anterior descending	131 (64.9%)
Left Circumflex	32 (15.8%)
Severity of coronary lesions at ICA (*N*, %)	
Stenosis 30–49%	89 (44.3%)
Stenosis 50–70%	69 (34.1%)
Stenosis 70–90%	44 (21.6%)
FFR categories (*N*, %)	
FFR $\leq$ 0.75	35 (17.3%)
FFR $>$ 0.75 and $\leq$ 0.8	21 (10.4%)
FFR $>$ 0.8	146 (72.3%)

or ICA-derived coronary 3-dimensional models on-site with relatively fast computational time and low computational cost. SmartFFR correlated well with the invasively measured FFR, which is the gold standard in the functional assessment of coronary stenoses.

DATA AVAILABILITY STATEMENT

The raw data supporting the conclusions of this article will be made available by the authors, without undue reservation. Requests to access data should be directed to Silvia Rocchiccioli, silvia.rocchiccioli@ifc.cnr.it, Lampros K. Michalis, lamprosmihalis@gmail.com.

ETHICS STATEMENT

The studies involving human participants were reviewed and approved by each participating center (National Research Council, University of Turku, University of Zurich, Fondazione Toscana Gabriele Monasterio, Warsaw National Institute of Cardiology) through the approval of the clinical study by the Ethics Committee Vast Area Northwest of Tuscany (CEAVNO), Pisa, Italy, and all subjects gave written informed consent. Our clinical study follows the declaration of Helsinki. The patients/participants provided their written informed consent to participate in this study.

AUTHOR CONTRIBUTIONS

PS performed the computational work, the concept of the method, and composed the manuscript. LL performed the annotation of the ICA dataset. AS contributed in the CCTA reconstruction and manuscript editing. GR, SK, and KS created the CCTA and the ICA reconstruction algorithms. CA and AC contributed in editing the manuscript. SR, GP, and OP contributed in the CCTA dataset. DN contributed in the CCTA dataset and the manuscript editing. KN and LM contributed in the ICA dataset. MP contributed with the initial vFAI methodology. DF contributed in the overall concept of the manuscript and the final editing of the manuscript. All authors contributed to the article and approved the submitted version.

FUNDING

This work is part-funded by the European Commission SMARTool simulation modeling in coronary artery disease: a tool for clinical decision support (GA 689068). This article reflects only the author's view. The Commission is not responsible for any use that may be made of the information it contains.

SUPPLEMENTARY MATERIAL

The Supplementary Material for this article can be found online at: https://www.frontiersin.org/articles/10.3389/fcvm.2021.714471/full#supplementary-material

REFERENCES

1. De Bruyne B, Fearon WF, Juni P. Fractional flow reserve-guided PCI. *N Engl J Med.* (2015) 372:95. doi: 10.1056/NEJMc1412894
2. Tonino PA, De Bruyne B, Pijls NH, Siebert U, Ikeno F. van' t Veer M, et al. Fractional flow reserve versus angiography for guiding percutaneous coronary intervention. *N Engl J Med.* (2009) 360:213–24. doi: 10.1056/NEJMoa0807611
3. Coughlan JJ, MacDonnell C, Arnous S, Kiernan TJ. Fractional flow reserve in 2017: current data and everyday practice. *Expert Rev Cardiovasc Ther.* (2017) 15:457–72. doi: 10.1080/14779072.2017.1327810
4. Vorre MM, Abdulla J. Diagnostic accuracy and radiation dose of CT coronary angiography in atrial fibrillation: systematic review and meta-analysis. *Radiology.* (2013) 267:376–86. doi: 10.1148/radiol.13121224
5. Koo BK, Erglis A, Doh JH, Daniels DV, Jegere S, Kim HS, et al. Diagnosis of ischemia-causing coronary stenoses by noninvasive fractional flow reserve computed from coronary computed tomographic angiograms. Results from the prospective multicenter DISCOVER-FLOW (Diagnosis of Ischemia-Causing Stenoses Obtained Via Noninvasive Fractional Flow Reserve) study. *J Am Coll Cardiol.* (2011) 58:1989–97. doi: 10.1016/j.jacc.2011.06.066
6. Kruk M, Wardziak L, Demkow M, Pleban W, Pregowski J, Dzielinska Z, et al. Workstation-Based Calculation of CTA-Based FFR for Intermediate Stenosis. *Jacc-Cardiovascular Imaging.* (2016) 9:690–9. doi: 10.1016/j.jcmg.2015.09.019
7. Min JK, Koo BK, Erglis A, Doh JH, Daniels DV, Jegere S, et al. Effect of image quality on diagnostic accuracy of noninvasive fractional flow reserve: results from the prospective multicenter international DISCOVER-FLOW study. *J Cardiovasc Comput Tomogr.* (2012) 6:191–9. doi: 10.1016/j.jcct.2012.04.010
8. Norgaard BL, Leipsic J, Gaur S, Seneviratne S, Ko BS, Ito H, et al. Diagnostic performance of noninvasive fractional flow reserve derived from coronary computed tomography angiography in suspected coronary artery disease: the NXT trial (Analysis of Coronary Blood Flow Using CT Angiography: Next Steps). *J Am Coll Cardiol.* (2014) 63:1145–55. doi: 10.1016/j.jacc.2013.11.043

9. Gaur S, Taylor CA, Jensen JM, Botker HE, Christiansen EH, Kaltoft AK, et al. FFR derived from coronary CT angiography in nonculprit lesions of patients with recent STEMI. *JACC Cardiovasc Imaging.* (2017) 10:424–33. doi: 10.1016/j.jcmg.2016.05.019
10. Stahli BE, Erbay A, Steiner J, Klotsche J, Mochmann HC, Skurk C, et al. Comparison of resting distal to aortic coronary pressure with angiography-based quantitative flow ratio. *Int J Cardiol.* (2019) 279:12–7. doi: 10.1016/j.ijcard.2018.11.093
11. Ties D, van Dijk R, Pundziute G, Lipsic E, Vonck TE, van den Heuvel AFM, et al. Computational quantitative flow ratio to assess functional severity of coronary artery stenosis. *Int J Cardiol.* (2018) 271:36–41. doi: 10.1016/j.ijcard.2018.05.002
12. Bom MJ, Driessen RS, Kurata A, van Diemen PA, Everaars H, Schumacher SP, et al. Diagnostic value of comprehensive on-site and off-site coronary CT angiography for identifying hemodynamically obstructive coronary artery disease. *J Cardiovasc Comput Tomogr.* (2021) 15:37–45. doi: 10.1016/j.jcct.2020.05.002
13. Van Belle E, Raposo L, Bravo Baptista S, Vincent F, Porouchani S, Cosenza A, et al. Impact of an interactive CT/FFRCT interventional planner on coronary artery disease management decision making. *JACC Cardiovasc Imaging.* (2021) 14:1068–70. doi: 10.1016/j.jcmg.2020.09.040
14. Tu S, Westra J, Yang J, von Birgelen C, Ferrara A, Pellicano M, et al. Diagnostic accuracy of fast computational approaches to derive fractional flow reserve from diagnostic coronary angiography: the international multicenter FAVOR pilot study. *JACC Cardiovasc Interv.* (2016) 9:2024–35. doi: 10.1016/j.jcin.2016.07.013
15. Wang ZQ, Zhou YJ, Zhao YX, Shi DM, Liu YY, Liu W, et al. Diagnostic accuracy of a deep learning approach to calculate FFR from coronary CT angiography. *J Geriatr Cardiol.* (2019) 16:42–8. doi: 10.11909/j.issn.1671-5411.2019.01.010
16. Witberg G, De Bruyne B, Fearon WF, Achenbach S, Engstrom T, Matsuo H, et al. Diagnostic performance of angiogram-derived fractional flow reserve: a pooled analysis of 5 prospective cohort studies. *JACC Cardiovasc Interv.* (2020) 13:488–97. doi: 10.1016/j.jcin.2019.10.045
17. Papafaklis MI, Muramatsu T, Ishibashi Y, Lakkas LS, Nakatani S, Bourantas CV, et al. Fast virtual functional assessment of intermediate coronary lesions using routine angiographic data and blood flow simulation in humans: comparison with pressure wire - fractional flow reserve. *EuroIntervention.* (2014) 10:574–83. doi: 10.4244/EIJY14M07_01
18. Siogkas PK, Anagnostopoulos CD, Liga R, Exarchos TP, Sakellarios AI, Rigas G, et al. Noninvasive CT-based hemodynamic assessment of coronary lesions derived from fast computational analysis: a comparison against fractional flow reserve. *Eur Radiol.* (2018) 29:2117–26. doi: 10.1007/s00330-018-5781-8
19. Anagnostopoulos CD, Siogkas PK, Liga R, Benetos G, Maaniitty T, Sakellarios AI, et al. Characterization of functionally significant coronary artery disease by a coronary computed tomography angiography-based index: a comparison with positron emission tomography. *Eur Heart J Cardiovasc Imaging.* (2019) 20:897–905. doi: 10.1093/ehjci/jey199
20. Neglia D, Rovai D, Caselli C, Pietila M, Teresinska A, Aguade-Bruix S, et al. Detection of significant coronary artery disease by noninvasive anatomical and functional imaging. *Circ Cardiovasc Imaging.* (2015) 8:e002179. doi: 10.1161/CIRCIMAGING.114.002179
21. Diamond GA, Forrester JS. Analysis of probability as an aid in the clinical diagnosis of coronary-artery disease. *N Engl J Med.* (1979) 300:1350–8. doi: 10.1056/NEJM197906143002402
22. Isma'eel H, Hamirani YS, Mehrinfar R, Mao S, Ahmadi N, Larijani V, et al. Optimal phase for coronary interpretations and correlation of ejection fraction using late-diastole and end-diastole imaging in cardiac computed tomography angiography: implications for prospective triggering. *Int J Cardiovasc Imaging.* (2009) 25:739–49. doi: 10.1007/s10554-009-9481-y
23. Abbara S, Blanke P, Maroules CD, Cheezum M, Choi AD, Han BK, et al. SCCT guidelines for the performance and acquisition of coronary computed tomographic angiography: A report of the society of Cardiovascular Computed Tomography Guidelines Committee: Endorsed by the North American Society for Cardiovascular Imaging (NASCI). *J Cardiovasc Comput Tomogr.* (2016) 10:435–49. doi: 10.1016/j.jcct.2016.10.002
24. Sakellarios AI, Rigas G, Kigka V, Siogkas P, Tsompou P, Karanasiou G, et al. SMARTool: A tool for clinical decision support for the management of patients with coronary artery disease based on modeling of atherosclerotic plaque process. *Conf Proc IEEE Eng Med Biol Soc.* (2017) 2017:96–9. doi: 10.1109/EMBC.2017.8036771
25. Kigka VI, Rigas G, Sakellarios A, Siogkas P, Andrikos IO, Exarchos TP, et al. 3D reconstruction of coronary arteries and atherosclerotic plaques based on computed tomography angiography images. *Biomed Signal Process Control.* (2018) 40:286–94. doi: 10.1016/j.bspc.2017.09.009
26. Siogkas PK, Stefanou KA, Athanasiou LS, Papafaklis MI, Michalis LK, Fotiadis DI. Art care: A multi-modality coronary 3D reconstruction and hemodynamic status assessment software. *Technol Health Care.* (2018) 26:187–93. doi: 10.3233/THC-170881
27. Johnson K, Sharma P, Oshinski J. Coronary artery flow measurement using navigator echo gated phase contrast magnetic resonance velocity mapping at 3.0 T. *J Biomech.* (2008) 41:595–602. doi: 10.1016/j.jbiomech.2007.10.010
28. Kern MJ, Bach RG, Mechem CJ, Caracciolo EA, Aguirre FV, Miller LW, et al. Variations in normal coronary vasodilatory reserve stratified by artery, gender, heart transplantation and coronary artery disease. *J Am Coll Cardiol.* (1996) 28:1154–60. doi: 10.1016/S0735-1097(96)00327-0
29. Xaplanteris P, Fournier S, Keulards DCJ, Adjedj J, Ciccarelli G, Milkas A, et al. Catheter-based measurements of absolute coronary blood flow and microvascular resistance: feasibility, safety, and reproducibility in humans. *Circ Cardiovasc Interv.* (2018) 11:e006194. doi: 10.1161/CIRCINTERVENTIONS.117.006194
30. Petraco R, Sen S, Nijjer S, Echavarria-Pinto M, Escaned J, Francis DP, et al. Fractional flow reserve-guided revascularization: practical implications of a diagnostic gray zone and measurement variability on clinical decisions. *JACC Cardiovasc Interv.* (2013) 6:222–5. doi: 10.1016/j.jcin.2012.10.014
31. Min JK, Leipsic J, Pencina MJ, Berman DS, Koo BK, van Mieghem C, et al. Diagnostic accuracy of fractional flow reserve from anatomic CT angiography. *JAMA.* (2012) 308:1237–45. doi: 10.1001/2012.jama.11274
32. Morris PD, Ryan D, Morton AC, Lycett R, Lawford PV, Hose DR, et al. Virtual fractional flow reserve from coronary angiography: modeling the significance of coronary lesions: results from the VIRTU-1 (VIRTUal Fractional Flow Reserve From Coronary Angiography) study. *JACC Cardiovasc Interv.* (2013) 6:149–57. doi: 10.1016/j.jcin.2012.08.024

Conflict of Interest: The authors declare that the research was conducted in the absence of any commercial or financial relationships that could be construed as a potential conflict of interest.

Publisher's Note: All claims expressed in this article are solely those of the authors and do not necessarily represent those of their affiliated organizations, or those of the publisher, the editors and the reviewers. Any product that may be evaluated in this article, or claim that may be made by its manufacturer, is not guaranteed or endorsed by the publisher.

frontiers in Cardiovascular Medicine

ORIGINAL RESEARCH
published: 13 September 2021
doi: 10.3389/fcvm.2021.713835

Association Among Local Hemodynamic Parameters Derived From CT Angiography and Their Comparable Implications in Development of Acute Coronary Syndrome

*Seokhun Yang[1], Gilwoo Choi[2], Jinlong Zhang[3], Joo Myung Lee[4], Doyeon Hwang[1], Joon-Hyung Doh[5], Chang-Wook Nam[6], Eun-Seok Shin[7], Young-Seok Cho[8], Su-Yeon Choi[9], Eun Ju Chun[10], Bjarne L. Nørgaard[11], Koen Nieman[12], Hiromasa Otake[13], Martin Penicka[14], Bernard De Bruyne[14], Takashi Kubo[15], Takashi Akasaka[15], Charles A. Taylor[2,16] and Bon-Kwon Koo[1,17]**

[1] Department of Internal Medicine and Cardiovascular Center, Seoul National University, Seoul, South Korea, [2] HeartFlow Inc., Redwood City, CA, United States, [3] Department of Cardiology, The Second Affiliated Hospital, School of Medicine, Zhejiang University, Hangzhou, China, [4] Department of Internal Medicine and Cardiovascular Center, Samsung Medical Center, Sungkyunkwan University, Seoul, South Korea, [5] Department of Medicine, Inje University Ilsan Paik Hospital, Goyang, South Korea, [6] Department of Medicine, Dongsan Medical Center, Keimyung University, Daegu, South Korea, [7] Department of Cardiology, Ulsan Hospital, Ulsan, South Korea, [8] Cardiovascular Center, Sejong General Hospital, Incheon, South Korea, [9] Department of Medicine, Healthcare System Gangnam Center, Seoul National University, Seoul, South Korea, [10] Department of Radiology, Seoul National University Bundang Hospital, Seongnam, South Korea, [11] Department of Cardiology, Aarhus University Hospital, Aarhus, Denmark, [12] School of Medicine, Cardiovascular Institute, Stanford University, Stanford, CA, United States, [13] Division of Cardiovascular and Respiratory Medicine, Department of Internal Medicine, Graduate School of Medicine, Kobe University, Kobe, Japan, [14] Cardiovascular Center Aalst, OLV-Clinic, Aalst, Belgium, [15] Department of Cardiovascular Medicine, Wakayama Medical University, Wakayama, Japan, [16] Department of Bioengineering, Stanford University, Stanford, CA, United States, [17] Institute on Aging, Seoul National University, Seoul, South Korea

OPEN ACCESS

Edited by:
Christos Bourantas,
University College London,
United Kingdom

Reviewed by:
Ryo Torii,
University College London,
United Kingdom
Eric Poon,
St Vincent's Hospital
(Melbourne), Australia

***Correspondence:**
Bon-Kwon Koo
bkkoo@snu.ac.kr

Specialty section:
This article was submitted to Cardiovascular Imaging, a section of the journal Frontiers in Cardiovascular Medicine

Received: 24 May 2021
Accepted: 12 August 2021
Published: 13 September 2021

Citation:
Yang S, Choi G, Zhang J, Lee JM, Hwang D, Doh J-H, Nam C-W, Shin E-S, Cho Y-S, Choi S-Y, Chun EJ, Nørgaard BL, Nieman K, Otake H, Penicka M, Bruyne BD, Kubo T, Akasaka T, Taylor CA and Koo B-K (2021) Association Among Local Hemodynamic Parameters Derived From CT Angiography and Their Comparable Implications in Development of Acute Coronary Syndrome. Front. Cardiovasc. Med. 8:713835. doi: 10.3389/fcvm.2021.713835

Background: Association among local hemodynamic parameters and their implications in development of acute coronary syndrome (ACS) have not been fully investigated.

Methods: A total of 216 lesions in ACS patients undergoing coronary CT angiography (CCTA) before 1–24 months from ACS event were analyzed. High-risk plaque on CCTA was defined as a plaque with ≥2 of low-attenuation plaque, positive remodeling, spotty calcification, and napkin-ring sign. With the use of computational fluid dynamics analysis, fractional flow reserve (FFR) derived from CCTA (FFR_{CT}) and local hemodynamic parameters including wall shear stress (WSS), axial plaque stress (APS), pressure gradient (PG) across the lesion, and delta FFR_{CT} across the lesion (ΔFFR_{CT}) were obtained. The association among local hemodynamics and their discrimination ability for culprit lesions from non-culprit lesions were compared.

Results: A total of 66 culprit lesions for later ACS and 150 non-culprit lesions were identified. WSS, APS, PG, and ΔFFR_{CT} were strongly correlated with each other (all $p < 0.001$). This association was persistent in all lesion subtypes according to a vessel, lesion location, anatomical severity, high-risk plaque, or $FFR_{CT} \leq 0.80$.

In discrimination of culprit lesions causing ACS from non-culprit lesions, WSS, PG, APS, and ΔFFR_{CT} were independent predictors after adjustment for lesion characteristics, high-risk plaque, and $FFR_{CT} \leq 0.80$; and all local hemodynamic parameters significantly improved the predictive value for culprit lesions of high-risk plaque and $FFR_{CT} \leq 0.80$ (all $p < 0.05$). The risk prediction model for culprit lesions with $FFR_{CT} \leq 0.80$, high-risk plaque, and ΔFFR_{CT} had a similar or superior discrimination ability to that with $FFR_{CT} \leq 0.80$, high-risk plaque, and WSS, APS, or PG; and the addition of WSS, APS, or PG into ΔFFR_{CT} did not improve the model performance.

Conclusions: Local hemodynamic indices were significantly intercorrelated, and all indices similarly provided additive and independent predictive values for ACS risk over high-risk plaque and impaired FFR_{CT}.

Keywords: acute coronary syndrome, atherosclerosis, local hemodynamic parameters, coronary artery disease, coronary CT angiography

INTRODUCTION

Acute coronary syndrome (ACS) is one of the leading causes of death in most countries (1), and predicting ACS risk prior to fatal events has been a major challenge in patients with coronary artery disease. Pathological studies demonstrated the vulnerable plaque features closely related to ACS (2), and identification of high-risk plaque features on coronary imaging provided better risk prediction for future events (3, 4). However, coronary anatomy or plaque morphology-based evaluation has shown a low positive predictive value in predicting ACS (5). Coronary physiological assessment such as fractional flow reserve (FFR), a guiding tool for appropriate revascularization in a current guideline (6), has an excellent negative predictive value for ACS, but its low likelihood ratio of ACS has also been reported in major randomized controlled trials (7, 8).

Unfavorable local hemodynamic environment has a critical role in ACS development (9). Plaque rupture commonly occurs when external forces acting on a plaque exceed plaque strength, and these forces can be estimated by the pressure drop across a lesion (10). Wall shear stress (WSS), a tiny tangential force, is known as a proinflammatory stimulus leading to plaque formation, progression, and destabilization prone to rupture events (11). Therefore, it has been speculated that identification of local hemodynamic parameters displayed better prediction of plaque rupture risk (12). Nonetheless, their clinical utilization has still been limited in daily practice since it requires additional resources and is a time-consuming process (13, 14). Moreover, whether the assessment of all diverse local hemodynamic indices provides incremental value has not been fully understood. In this regard, we performed this study to investigate the relationship among various local hemodynamic parameters and their comparability in prediction of ACS risk.

METHODS

Study Participants

This study is a substudy of the EMERALD (Exploring the Mechanism of Plaque Rupture in Acute Coronary Syndrome Using Coronary CT Angiography and Computational Fluid Dynamic) study (12). Patients with ACS defined as acute myocardial infarction or unstable angina with evidence of plaque rupture at invasive coronary imaging at the time of ACS and who underwent coronary CT angiography (CCTA) from 1 month to 2 years before ACS event were included. All angiograms were reviewed at a core laboratory, Seoul National University Hospital; and the culprit lesions were selected in a blinded fashion. Those with ACS due to in-stent restenosis, secondary myocardial infarction due to other general medical conditions, previous history of coronary artery bypass graft surgery, or unanalyzable CCTA for computational fluid dynamics (CFD) analysis at a core laboratory were excluded. The study protocol was approved by the institutional review board of each site. The study was conducted in accordance with the Declaration of Helsinki (ClinicalTrials.gov Identifier: NCT02374775).

Plaque Analysis on Coronary CT Angiography

CCTA images were analyzed at a core laboratory (Seoul National University Bundang Hospital) by an independent observer in a blinded fashion. All lesions with percent diameter stenosis >30% were analyzed. Lesion starting and ending locations were visually determined on the basis of lumen geometry by an independent reviewer. The presence of low-attenuation plaque (LAP) was defined as a plaque with an average density of ≤30 Hounsfield units [HU]) (15), which was obtained by the mean value of HU randomly selected ≥5 points in the lesion. Positive remodeling (PR) was defined as a remodeling index ≥1.1 (15). The remodeling index was defined as the vessel diameter at the maximal stenotic site divided by the reference diameter. Spotty calcification was a lesion with averaged density >130 HU and diameter <3 mm in any direction, and napkin-ring sign was ring-like attenuation pattern with peripheral high and central lower-attenuation portion. High-risk plaque was defined as a plaque with ≥2 of LAP, PR, spotty calcification, and napkin-ring sign.

Hemodynamic Parameters From Coronary CT Angiography Images

Hemodynamic parameters were obtained by CFD analyses on CCTA in a blinded fashion at an independent core laboratory (Heart Flow, Inc.) (16, 17). CFD analyses were performed by the same process performed during FFR_{CT} computation. In brief, the individual anatomic model of coronary arteries was reconstructed from CCTA images, and segmentation of lumen boundary was performed. Blood flow and pressure in the coronary trees were predicted using the CFD technique by solving the Navier–Stokes equations with the assumptions of a rigid wall and a Newtonian fluid in a patient-specific coronary geometry (16). Myocardial mass, vessel sizes at each outlet, and the microvascular response to adenosine were used for defining the boundary conditions. Following the principles that coronary supply meets myocardial demand of each patient at rest, and microvascular resistance at rest has an inverse relationship linearly proportional to the size of the vessel (18), and microcirculatory reaction to maximal hyperemia in patients with the normal coronary flow is predictable (19), total coronary flow at rest and the total baseline resistance were computed. The total baseline resistance was distributed to coronary trees on the basis of vessel caliber and was reduced according to the effect of adenosine on the microvasculature in hyperemic conditions. The inflow condition was determined by the patient-specific myocardial mass and functional relationships between flow and mass based on the allometric scaling law. The simulations were conducted under the steady flow assumption, and all hemodynamic parameters were calculated in hyperemic conditions. We obtained FFR_{CT}, change in FFR_{CT} across the lesion (ΔFFR_{CT}), WSS, axial plaque stress (APS), and pressure gradient (PG) across the lesion. Over the entire coronary tress, the hemodynamic quantities can be achieved by FFR_{CT} tracing. Whole coronary artery tree was sliced by a unit of a thin strip with 2-mm thickness with 0.5-mm intervals between strips. Then, the averaged values of hemodynamic parameters of every strip could be obtained, and hemodynamic properties of the whole coronary artery were identified. The definitions of hemodynamic parameters were as follows. FFR_{CT} was defined as (mean pressure in downstream coronary vessels/mean pressure of the aorta) under simulated hyperemic conditions at the distal part of a vessel. WSS was defined as tangential stress resulting from the friction between blood flow and the surface of the vessel wall. PG was defined as the difference between the proximal and distal pressure divided by lesion length. Given that the pressure drop across the lesion mainly occurs along the axial direction, the axial component of the traction was separately defined as APS, a measure for the main driving force along the vessel length (10). To obtain the net resultant forces acting on the plaque, we used hemodynamic parameters averaged over the surface of each lesion in the current analysis. ΔFFR_{CT} was calculated as the difference between the FFR_{CT} value at a lesion start point (i.e., proximal FFR_{CT}) and the FFR_{CT} value at a lesion endpoint (i.e., distal FFR_{CT}). Sampling points for ΔFFR_{CT} were equal to those for PG. As a sensitivity analysis, averaged WSS was divided into proximal WSS and distal WSS based on the point of minimum lumen area; and their association with other hemodynamic parameters, prognostic implications, and the additive value for ΔFFR_{CT} was analyzed. Optimal cutoff based on receiver operating characteristic curve analysis in discrimination of culprit lesions from non-culprit lesions was used to define high WSS ($\geq$154.7 dyn/cm^2), high APS ($\geq$1,606.6 dyn/cm^2), high ΔFFR_{CT} ($\geq$0.06), and high PG ($\geq$5.8 mmHg/cm). The optimal cutoff providing the maximal value of the sum of sensitivity and specificity was chosen, and the same cutoff was used in the original EMERALD study (12).

Statistical Analysis

All analyses were performed using R language version 3.6.2 (R Foundation for Statistical Computing, Vienna, Austria). Continuous variables were expressed as means with standard deviations. Categorical variables were shown as numbers (percentages). Two or more groups were compared using Student's *t*-test test or ANOVA test for continuous variables and chi-square test for categorical variables, as appropriate. Pearson's correlation coefficient was used to assess the linear association among hemodynamic parameters and was estimated according to the lesion subtypes stratified by a vessel, lesion location, % diameter stenosis, high-risk plaque, FFR_{CT}, and the number of lesions in a vessel. Global chi-square estimates were used to evaluate the additive predictive value of local hemodynamics over the presence of high-risk plaque and FFR_{CT} $\leq$0.80. The cumulative event rates were assessed by the Kaplan–Meier censoring estimates. Cox proportional hazard regression was used to estimate the hazard ratio (HR) and the corresponding 95% confidence interval (CI). For adjustment of intra-patient variability in the same patient, the marginal Cox model was used. In the multivariate analysis, lesion characteristics significantly different between culprit and non-culprit lesions (i.e., vessel location, % diameter stenosis, and lesion length), FFR_{CT} $\leq$0.80, high-risk plaque, and each local hemodynamic parameter were included in the Cox model. The discrimination ability for culprit lesions from non-culprit lesions was compared to assess comparability among local hemodynamics using the area under the receiver operating characteristic curve (AUC) based on logistic regression. A generalized estimating equation was used for the adjustment of intra-patient variability. All statistical tests were two-tailed, and a p-value $<$0.05 was considered statistically significant.

RESULTS

Baseline Characteristics of Patients and Lesions

Among 72 patients with ACS, the mean age of the study population was 69.9 $\pm$ 12.7 years, and 54% were male; and the proportion of patients with diabetes mellitus, hypertension, and hypercholesterolemia was 51.4, 63.9, and 48.6%, respectively. Current smoker was 30.6%, and 6.9% had a previous history of myocardial infarction. The median ejection fraction was 58.6 (44.5–63.3%). The median interval from CCTA to ACS events was 338.0 (161.5–535.0) days, and ACS events were comprised

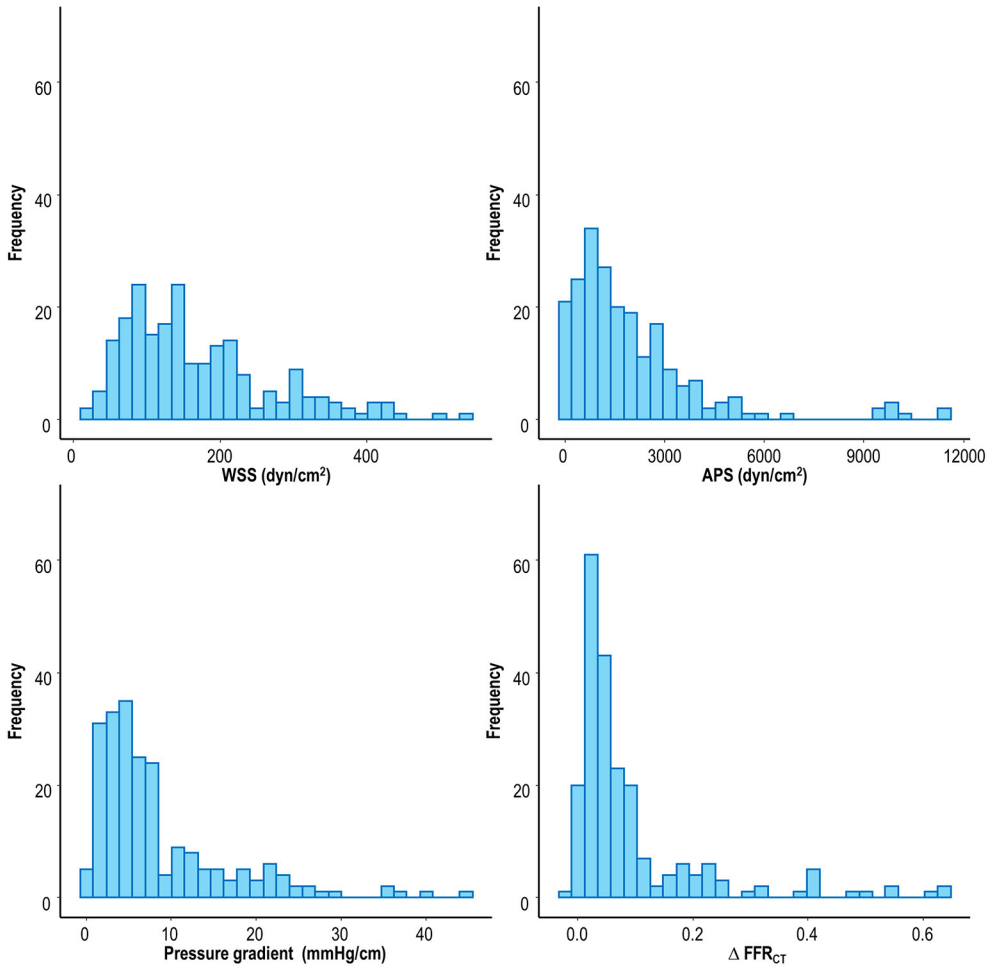

FIGURE 1 | Distribution of local hemodynamic parameters. APS, axial plaque stress; FFR_{CT}, coronary computed tomographic angiography-derived fractional flow reserve; WSS, wall shear stress.

by 93.1% of myocardial infarction and 6.9% of unstable angina. Of these patients, a total of 216 lesions were identified on CCTA taken prior to ACS, including 66 culprit lesions and 150 non-culprit lesions. Relative to non-culprit lesions, culprit lesions showed a higher % diameter stenosis (43.1 ± 15.0% vs. 55.5 ± 15.4%, $p < 0.001$), and lesion length (12.1 ± 7.4 mm vs. 15.8 ± 8.4 mm, $p = 0.002$). The proportion of located lesions on the left anterior descending artery, left circumflex artery, and right coronary artery was 59.1, 13.6, and 27.3%, respectively in culprit lesions; and 32.0, 26.0, and 42.0%, respectively, in non-culprit lesions ($p < 0.001$). Time between CCTA and ACS events was 271.5 [116.0–522.0] days in culprit lesions and 338.5 [164.0–535.0] days in non-culprit lesions ($p = 0.149$). The distributions of local hemodynamic parameters are presented in **Figure 1**. The value of local hemodynamic parameters by lesion characteristics is shown in **Table 1**; and the trends according to lesion characteristics are similar among WSS, APS, PG, and ΔFFR_{CT}.

Relationship Among Local Hemodynamic Parameters

Figure 2 describes the association among hemodynamic parameters. WSS, APS, and PG had a significant correlation among each other ($r = 0.917$, $p < 0.001$ for WSS and PG; $r = 0.384$, $p < 0.001$ for APS and PG; and $r = 0.269$, $p < 0.001$ for WSS and APS). ΔFFR_{CT} was significantly correlated with WSS, APS, and PG ($r = 0.581$, $p < 0.001$ for WSS and ΔFFR_{CT}; $r = 0.331$, $p < 0.001$ for APS and ΔFFR_{CT}; and $r = 0.752$, $p < 0.001$ for PG and ΔFFR_{CT}) (**Figure 2**). In regression of WSS, APS, or PG, the correlation coefficient of FFR_{CT} was lower than that of ΔFFR_{CT} with WSS, APS, or PG ($r = -0.349$, $p < 0.001$ for WSS and FFR_{CT}; $r = -0.131$, $p < 0.001$ for APS and FFR_{CT}; and $r = -0.526$, $p < 0.001$ for PG and FFR_{CT}) (**Supplementary Figure 1**). In various lesion subtypes stratified by a vessel, lesion location, % diameter stenosis, high-risk plaque, FFR_{CT}, and number of lesions in a vessel, local hemodynamic indices consistently correlated with each

TABLE 1 | Local hemodynamics according to lesion characteristics.

	WSS (dyn/cm^2)	*P*-value	APS (dyn/cm^2)	*P*-value	PG (mmHg/cm)	*P*-value	ΔFFR_{CT}	*P*-value
Total	168.8 ± 102.1	–	1,994.8 ± 2,095.5	–	8.3 ± 7.9	–	0.09 ± 0.12	–
Vessel location		<0.001		0.017		<0.001		0.016
LAD (n = 87)	208.8 ± 105.8		2,341.9 ± 2,266.9		10.9 ± 8.1		0.12 ± 0.13	
LCX (n = 48)	158.6 ± 99.6		2,083.2 ± 2,056.6		8.2 ± 9.4		0.08 ± 0.11	
RCA (n = 81)	131.9 ± 83.6		1,569.6 ± 1,863.7		5.6 ± 5.6		0.07 ± 0.11	
Lesion location		<0.001		0.033		<0.001		0.006
Proximal (n = 98)	201.9 ± 113.3		2,453.6 ± 2,418.2		10.5 ± 9.2		0.12 ± 0.14	
Middle (n = 81)	150.5 ± 90.0		1,482.6 ± 1,597.1		7.1 ± 6.7		0.08 ± 0.01	
Distal (n = 37)	121.2 ± 59.7		1,900.8 ± 1,904.5		5.3 ± 4.7		0.06 ± 0.08	
% Diameter stenosis		<0.001		0.001		<0.001		<0.001
≥50% (n = 84)	206.2 ± 121.7		2,656.8 ± 2,598.5		11.9 ± 10.1		0.15 ± 0.17	
<50% (n = 132)	145.0 ± 79.1		1,573.5 ± 1,571.2		6.0 ± 4.9		0.05 ± 0.05	
High-risk plaque		0.003		0.042		0.002		<0.001
Yes (n = 60)	201.4 ± 102.4		2,547.2 ± 2,641.4		11.3 ± 9.2		0.16 ± 0.18	
No (n = 156)	156.3 ± 99.5		1,782.3 ± 1,808.7		7.2 ± 7.0		0.07 ± 0.08	
FFR_{CT}		<0.001		0.097		<0.001		<0.001
≤0.80 (n = 66)	227.7 ± 127.1		2,351.8 ± 2,242.8		14.1 ± 10.5		0.19 ± 0.18	
>0.80 (n = 150)	142.9 ± 76.1		1,837.7 ± 2,015.0		5.8 ± 4.5		0.05 ± 0.04	
Number of lesions in a vessel		0.245		0.009		0.101		0.200
1 (n = 86)	158.9 ± 95.1		1,577.8 ± 1,482.9		7.3 ± 6.4		0.08 ± 0.09	
≥ 2 (n = 130)	175.4 ± 106.4		2,270.6 ± 2,382.6		9.0 ± 8.7		0.10 ± 0.14	

High-risk plaque was defined as a plaque with ≥2 of low-attenuation plaque, positive remodeling, spotty calcification, and napkin-ring sign.
APS, axial plaque stress; FFR_{CT}, coronary computed tomographic angiography-derived fractional flow reserve; LAD, left anterior descending artery; LAP, low-attenuation plaque; LCX, left circumflex artery; PG, pressure gradient; PR, positive remodeling; RCA, right coronary artery; WSS, wall shear stress.

other (**Table 2**), although the correlation of APS with other local hemodynamic parameters becomes weak in lesions with <50% diameter stenosis. FFR_{CT} showed a lower correlation coefficient with WSS, APS, or PG than that of ΔFFR_{CT} with WSS, APS, or PG in overall lesion types (**Supplementary Table 1**). In particular, FFR_{CT} did not correlate with local hemodynamics in lesions with FFR_{CT} ≤0.80, and the correlation of FFR_{CT} with local hemodynamics decreased in vessels with multiple lesions (**Supplementary Table 1**).

Comparable Implications of Each Local Hemodynamic Parameter in Prediction of Acute Coronary Syndrome

In prediction of culprit lesions of ACS, high WSS, high APS, high PG, or high ΔFFR_{CT} was significantly associated with an increased risk after adjustment for vessel location, % diameter stenosis, lesion length, FFR_{CT} ≤0.80, and high-risk plaque (adjusted HR 2.02, 95% CI 1.18–3.45, $p = 0.010$ for high WSS; adjusted HR 1.72, 95% CI 1.03–2.88, $p = 0.038$ for high APS; adjusted HR 2.21, 95% CI 1.34–3.67, $p = 0.002$ for high PG; and adjusted HR 2.29, 95% CI 1.35–3.86, $p = 0.002$ for high ΔFFR_{CT}) (**Table 3**). With FFR_{CT} ≤0.80 as a baseline model in prediction of culprit lesions, the presence of high-risk plaque had incremental predictability over FFR_{CT} ≤0.80; and high WSS, high APS, high PG, or high ΔFFR_{CT} similarly showed an additive predictive value over both FFR_{CT} ≤0.80 and high-risk plaque (**Figure 3**). High WSS, high APS, high PG, or high ΔFFR_{CT} was similar in their ability to discriminate culprit lesions from non-culprit lesions in lesions with and without FFR_{CT} ≤0.80 and high-risk plaque (**Figure 4**). The discrimination ability for culprit lesions of the model with FFR_{CT} ≤0.80, high-risk plaque, and ΔFFR_{CT} was similar to that with FFR_{CT} ≤0.80, high-risk plaque, and WSS (AUC 0.77 vs. 0.76, $p = 0.37$) or FFR_{CT} ≤0.80, high-risk plaque, and PG (0.77 vs. 0.77, $p = 0.63$); or superior to that with FFR_{CT} ≤0.80, high-risk plaque, and APS (AUC 0.77 vs. 0.71, $p = 0.03$). The addition of WSS, APS, or PG into ΔFFR_{CT} had no gain in predictive value for culprit lesions (**Table 4**). Overall results were similar when proximal WSS and distal WSS were separately analyzed in the sensitivity analysis.

DISCUSSION

The current study investigated the association among local hemodynamic parameters and their role in development of ACS. The main findings were as follows. First, local hemodynamic parameters (i.e., WSS, APS, PG, and ΔFFR_{CT}) were significantly correlated with each other. Second, all local hemodynamic indices similarly provided incremental and independent discrimination ability of culprit lesions causing ACS from non-culprit lesions over high-risk plaque and FFR_{CT} ≤0.80. Third, ΔFFR_{CT} showed a comparable predictive value for culprit lesions with that of WSS, APS, and PG.

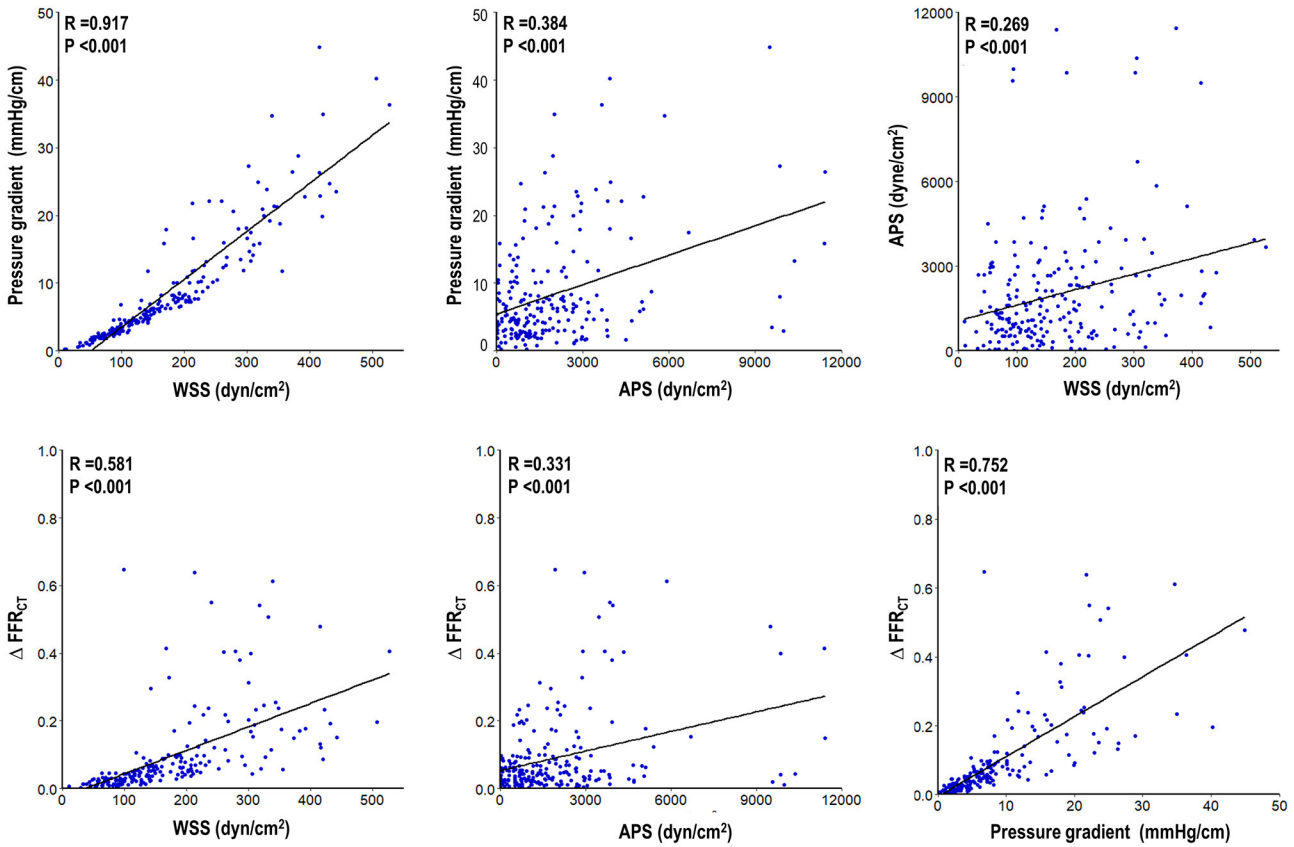

FIGURE 2 | Association among local hemodynamic parameters. Correlation among WSS, APS, PG, and ΔFFR_{CT} is presented. All local hemodynamic parameters were significantly correlated with each other. APS, axial plaque stress; FFR_{CT}, coronary computed tomographic angiography-derived fractional flow reserve; WSS, wall shear stress.

Components of Local Hemodynamic Environment and Their Association

A large body of evidence has supported the clinical relevance and prognostic value of physiological lesion characteristics in prediction of lesions causing future coronary events (9). It generally consists of endothelial shear stress (ESS) or WSS, a tangential component of force generated by friction between blood flow and vessel wall, which can be sensed by the endothelium leading to a biological process of atherosclerosis (11), and external mechanical force acting on a plaque, which can directly cause plaque rupture when it outpaces plaque strength (10). Although each component of local hemodynamic indices apparently appears to have a different role in a complex process of plaque formation, progression, and rupture events (20), their *in vivo* association and whether they have differential implications in prediction of ACS risk have not been fully understood. It is clinically relevant to investigate their association and compare their prognostic impact on ACS risk, since not all measurements can be obtained in daily practice. In the current study, we employed PG or APS as one of the indicative markers for the external hemodynamic force acting on a plaque, WSS as a local hemodynamic marker of biological signaling on the atherosclerosis process (11), and ΔFFR_{CT} as a clinically applicable marker derived from CFD analyses applied to CCTA taken prior to ACS events.

We demonstrated that WSS, APS, PG, and ΔFFR_{CT} had a significant association with each other (all $p < 0.001$). Moreover, this relationship was consistent, regardless of various lesion subtypes, which indicates that the nature of this firm association among physiological factors was not affected by lesion characteristics. Thus, ΔFFR_{CT} can be a marker of the level of WSS, APS, or PG of a target lesion. This finding may be expected in that each local hemodynamic parameter originates from the common interaction between blood flow, plaque, and vessel wall (20) and is in accordance with previous reports of the strong correlation between WSS and PG at resting ($r = 0.969$, $p < 0.001$) and hyperemic conditions ($r = 0.962$, $p < 0.001$) in CFD model from CCTA (17), and linear association between APS and PG in obstructive lesions (10). Of note, the degree of correlation of FFR_{CT} with local hemodynamics was lower than that of ΔFFR_{CT}, suggesting the importance of lesion-specific hemodynamic assessment than vessel-specific

TABLE 2 | Correlation among local hemodynamic parameters in various lesion subtypes.

Subgroups	Correlation between WSS and PG (coefficient, r)	*P*-value	Correlation between APS and PG (coefficient, r)	*P*-value	Correlation between WSS and APS (coefficient, r)	*P*-value	Correlation between ΔFFR_{CT} and WSS (coefficient, r)	*P*-value	Correlation between ΔFFR_{CT} and APS (coefficient, r)	*P*-value	Correlation between ΔFFR_{CT} and PG (coefficient, r)	*P*-value
Vessel location												
LAD ($n = 81$)	0.906	<0.001	0.287	0.007	0.159	0.142	0.541	<0.001	0.290	<0.001	0.762	<0.001
LCX ($n = 48$)	0.915	<0.001	0.596	<0.001	0.400	0.005	0.653	<0.001	0.621	<0.001	0.811	<0.001
RCA ($n = 81$)	0.941	<0.001	0.245	0.028	0.225	0.044	0.543	<0.001	0.152	0.177	0.703	<0.001
Lesion location												
Proximal ($n = 98$)	0.915	<0.001	0.299	0.003	0.173	0.088	0.548	<0.001	0.186	0.067	0.712	<0.001
Mid ($n = 81$)	0.910	<0.001	0.423	<0.001	0.306	0.006	0.566	<0.001	0.532	<0.001	0.777	<0.001
Distal ($n = 37$)	0.890	<0.001	0.638	<0.001	0.444	0.006	0.637	<0.001	0.579	<0.001	0.866	<0.001
% diameter stenosis												
≥50% ($n = 84$)	0.905	<0.001	0.453	<0.001	0.319	0.003	0.493	<0.001	0.377	<0.001	0.699	<0.001
<50% ($n = 132$)	0.948	<0.001	0.052	0.558	0.035	0.688	0.735	<0.001	−0.072	0.412	0.802	<0.001
High-risk plaque												
Yes ($n = 60$)	0.875	<0.001	0.295	0.022	0.111	0.398	0.492	<0.001	0.293	0.023	0.738	<0.001
No ($n = 156$)	0.943	<0.001	0.409	<0.001	0.326	<0.001	0.687	<0.001	0.316	<0.001	0.781	<0.001
FFR_{CT}												
≤0.80 ($n = 66$)	0.903	<0.001	0.559	<0.001	0.352	0.004	0.458	<0.001	0.544	<0.001	0.662	<0.001
>0.80 ($n = 150$)	0.941	<0.001	0.232	0.004	0.168	0.040	0.788	<0.001	0.073	0.374	0.819	<0.001
Number of lesions in a vessel												
1 ($n = 86$)	0.961	<0.001	0.128	0.242	0.058	0.596	0.735	<0.001	0.184	0.089	0.831	<0.001
≥2 ($n = 130$)	0.903	<0.001	0.449	<0.001	0.338	<0.001	0.526	<0.001	0.361	<0.001	0.725	<0.001

*The definition of high-risk plaque was the same as in **Table 1**.*

APS, axial plaque stress; FFR_{CT}, coronary computed tomographic angiography-derived fractional flow reserve; LAD, left anterior descending artery; LAP, low-attenuation plaque; LCX, left circumflex artery; PG, pressure gradient; PR, positive remodeling; RCA, right coronary artery; WSS, wall shear stress.

TABLE 3 | Univariate and multivariate analyses of local hemodynamics in prediction of culprit lesions causing acute coronary syndrome.

	Unadjusted HR (95% CI)	*P*-value	Adjusted HR* (95% CI)	*P*-value	Adjusted HR* (95% CI)	*P*-value	Adjusted HR* (95% CI)	*P*-value	Adjusted HR* (95% CI)	*P*-value
Predictors										
$FFR_{CT} \leq 0.80$	2.96 (1.79–4.91)	<0.001	1.51 (0.82–2.78)	0.182	1.78 (0.99–3.23)	0.056	1.47 (0.79–2.76)	0.227	1.27 (0.69–2.34)	0.446
High-risk plaque	3.46 (2.29–5.22)	<0.001	2.08 (1.22–3.56)	0.007	2.24 (1.34–3.73)	0.002	2.10 (1.23–3.58)	0.006	2.03 (1.78–3.51)	0.011
WSS ≥ 154.7 dyn/cm^2	2.93 (1.88–4.58)	<0.001	2.02 (1.18–3.45)	0.010						
APS ≥ 1,606.6 dyn/cm^2	2.20 (1.43–3.41)	<0.001			1.72 (1.03–2.88)	0.038				
PG ≥ 5.8 mmHg/cm	3.50 (2.16–5.68)	<0.001					2.21 (1.34–3.67)	0.002		
$\Delta FFR_{CT} \geq 0.06$	3.70 (2.38–5.76)	<0.001							2.29 (1.35–3.86)	0.002

The definition of high-risk plaque was the same as in ***Table 1****.*

**Adjusted for vessel location, % diameter stenosis, lesion length, $FFR_{CT} \leq 0.80$, high-risk plaque, and each local hemodynamic parameter.*

APS, axial plaque stress; CI, confidence interval; FFR_{CT}, coronary computed tomographic angiography-derived fractional flow reserve; HR, hazard ratio; PG, pressure gradient; WSS, wall shear stress.

indices to accurately estimate physiological lesion characteristics in clinical practice.

Additive Value of Local Hemodynamics Relative to High-Risk Plaque and Low FFR in Prediction of Acute Coronary Syndrome

While extensive studies have searched for vulnerable plaque features predictive of future rupture events, major clinical trials have shown that their positive predictive value is far from perfect (3, 21, 22), and the same is true for abnormal coronary physiology (i.e., FFR ≤0.80) (7, 8), currently the best indication of revascularization. In the current study, we confirmed the additive and independent predictive value for culprit lesions causing ACS over high-risk plaque and FFR_{CT} ≤0.80. High WSS, high APS, high PG, and high ΔFFR_{CT} were independent predictors for culprit lesions after adjustment for high-risk plaque and FFR_{CT} ≤0.80, and they all significantly improved the predictability for culprit lesions of the model with high-risk plaque and FFR_{CT} ≤0.80 (all $p < 0.001$). Of note, high WSS, high APS, high PG, and high ΔFFR_{CT} were still predictive of culprit lesions irrespective of the presence of high-risk plaque or FFR_{CT} ≤0.80. Our finding is in line with the previous report of a strong correlation between the shear stress concentration and plaque rupture site (kappa = 0.79) (23). Although plaque structural stress (PSS) was not estimated in the current study, prior observation of increased PSS or its variability in plaques with rupture (24) partially support our findings of the independent role of local hemodynamics in acute coronary events. *Post-hoc* analysis of FAME II also exhibited that the risk of myocardial infarction can be better predicted by high lesion-level shear stress relative to FFR in medically treated patients with FFR ≤0.80 (25). A recent report by Doradla et al. of the precise ability of a peak stress metric in locating the plaque rupture sites also aligns with the current findings (14). Thus, local hemodynamic parameters should be accounted for as one of the main determinants in predicting ACS risk, as they definitely can refine the current risk stratification for ACS with high-risk plaque and low FFR.

ΔFFR as a Local Hemodynamic Parameter Easily Applicable in Clinical Practice

Various CFD modeling strategies from multimodality imaging have been developed for precise evaluation of the local hemodynamic environment (26). Intravascular ultrasound (IVUS)-derived ESS or PSS has consistently predicted plaque progression, vulnerable plaque formation, and future coronary events (27–32). Recently proposed quantitative coronary angiography-derived ESS showed a correlation with IVUS-derived models ($r = 0.588$, $p < 0.001$) (33) and was an independent predictor of major adverse cardiovascular events at 5-year follow-up (13), suggesting a possibility of real-time assessment of local hemodynamic parameters in daily practice. A novel approach for computational tool (14) or hybrid multimodal imaging (34) has also broadened the clinical applicability of local hemodynamics. Nonetheless, there is no gold standard technique in identifying local hemodynamic

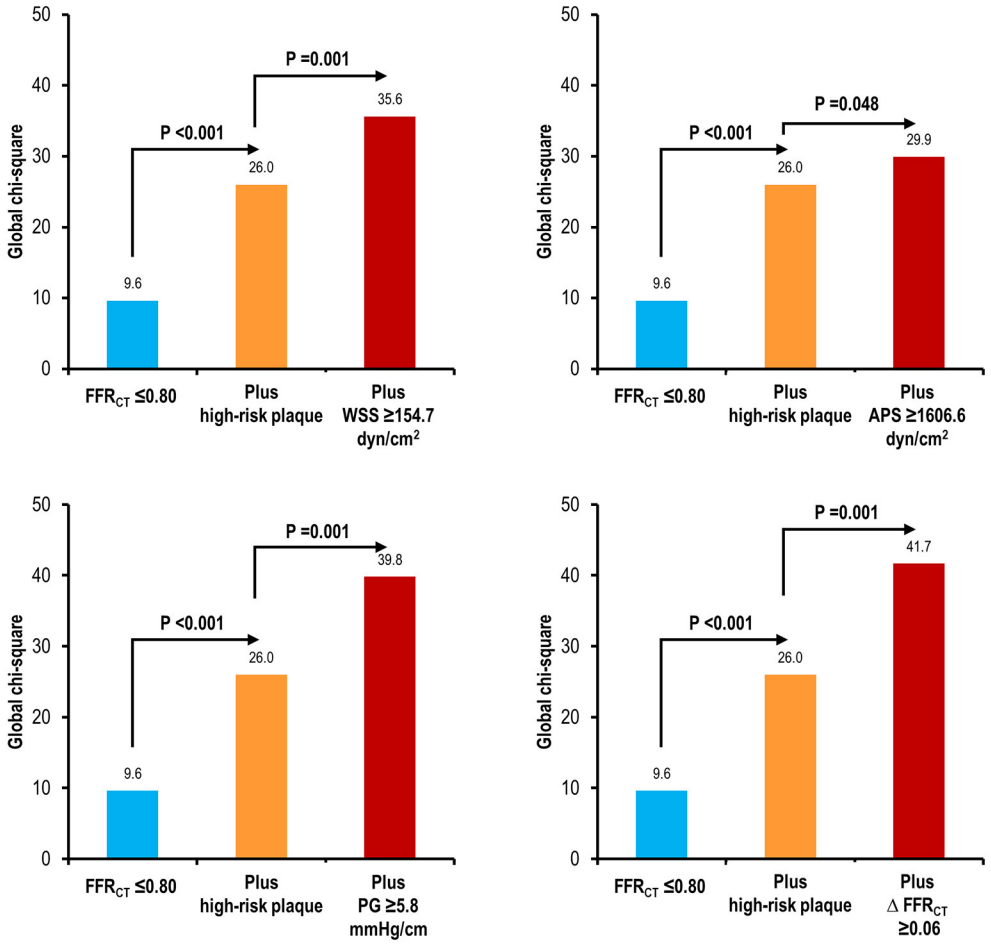

FIGURE 3 | Incremental predictive value of high WSS, high APS, high PG, or high ΔFFR_{CT} over high-risk plaque and FFR_{CT}. The predictability for culprit lesions causing ACS is compared with the model with FFR_{CT} ≤0.80; the model with FFR_{CT} ≤0.80 and high-risk plaque; and the model with FFR_{CT} ≤0.80, high-risk plaque, and local hemodynamic parameters. High WSS, high APS, high PG, or high ΔFFR_{CT} similarly improved the predictability for culprit lesions causing ACS of high-risk plaque and FFR_{CT} ≤0.80. High-risk plaque was defined as a plaque with ≥2 of low-attenuation plaque, positive remodeling, spotty calcification, and napkin-ring sign. APS, axial plaque stress; FFR_{CT}, coronary computed tomographic angiography-derived fractional flow reserve; PG, pressure gradient; WSS, wall shear stress.

parameters, and their definition and widely accepted consensus on clinical utilization still need to be determined in future studies. In view of physiological assessment in the cardiac catheterization laboratory, lesion-specific ischemia can be estimated by changes in the value of coronary physiological indices across the target lesion (i.e., ΔFFR), which are obtained by pressure-guide wire pullback measurement (35, 36). In our study, we aimed to compare the clinical implications of ΔFFR_{CT} with WSS, APS, and PG in prediction of ACS risk and demonstrated that ΔFFR_{CT} had comparable predictability for culprit lesions causing ACS with that of WSS, APS, and PG; and there was no significant benefit when WSS, APS, or PG was added into the risk prediction model with impaired FFR_{CT}, high-risk plaque, and ΔFFR_{CT}. Given that ΔFFR_{CT} can reflect the level of WSS, APS, or PG from the strong association among them, our finding postulates that the measurement of ΔFFR might provide equivalent prognostic information, which can be obtained by assessment of WSS, APS, or PG. Therefore, lesion-specific ΔFFR measurement through well-defined FFR pullback estimation in addition to vessel-specific FFR measurement for dichotomous decision-making for revascularization can better predict ACS risk, since it can depict local hemodynamic environments such as WSS, APS, or PG.

LIMITATIONS

The current study has several limitations. First, the comparison between culprit lesions and non-culprit lesions was performed based on intra-patient analysis. Second, the number of the study population is relatively small to generalize the comparability among local hemodynamic parameters. Subsequent large-scale studies are needed to validate the current findings. Third, the study design is retrospective, and there may be

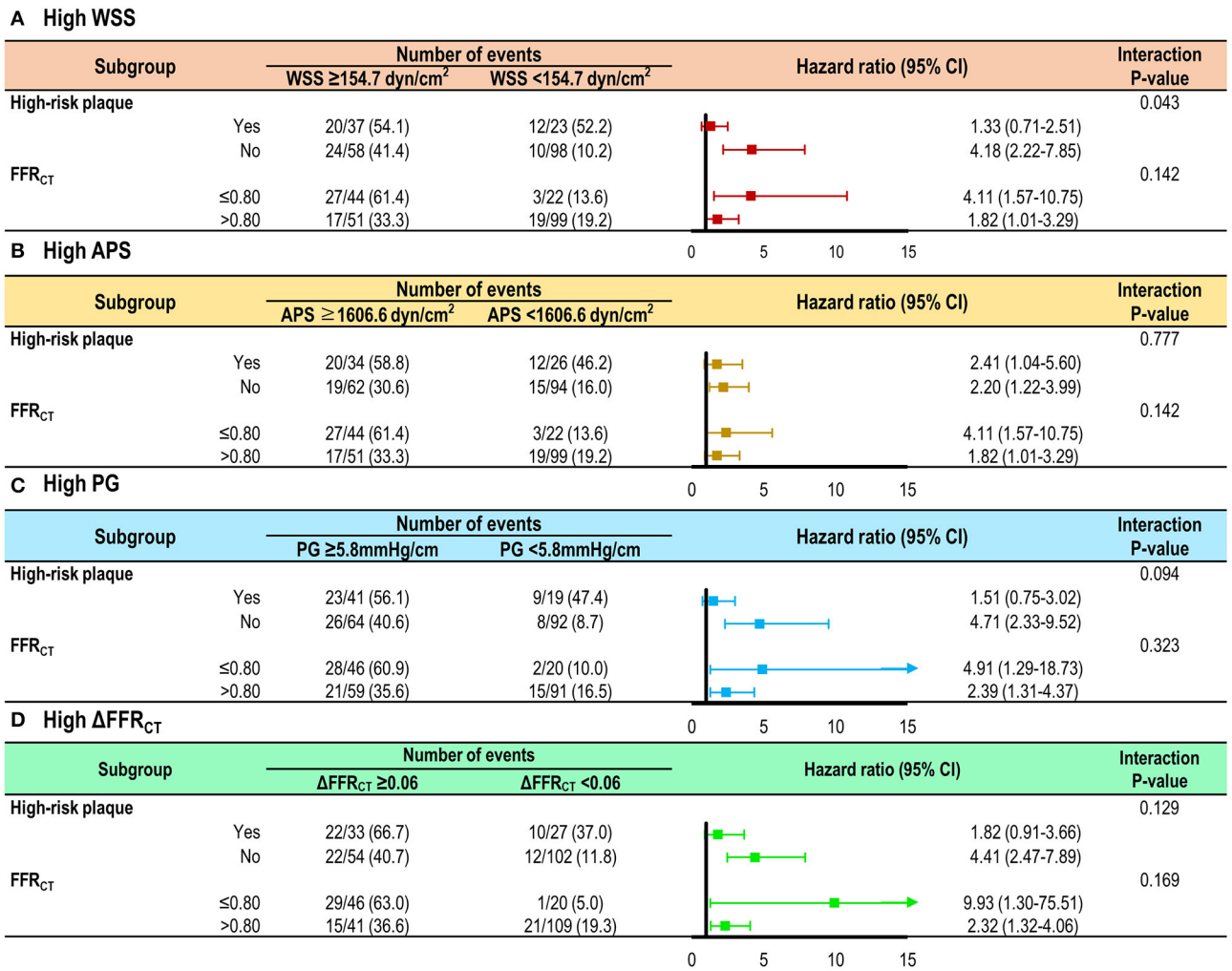

FIGURE 4 | Risk of culprit lesions according to local hemodynamic parameters in the subgroups by high-risk plaque or FFR_{CT}. The risk of culprit lesions according to **(A)** high WSS, **(B)** high APS, **(C)** high PG, or **(D)** high ΔFFR_{CT} is shown in lesions with and without high-risk plaque and FFR_{CT} ≤0.80. A trend toward an increased risk of culprit lesions was consistently observed in lesions with high WSS, high APS, high PG, or high ΔFFR_{CT}, independent of the presence of high-risk plaque and FFR_{CT} ≤0.80. The definition of high-risk plaque was the same as in **Figure 3**. APS, axial plaque stress; FFR_{CT}, coronary computed tomographic angiography-derived fractional flow reserve; PG, pressure gradient; WSS, wall shear stress.

selection bias on lesion progression or vulnerability. Fourth, the well-correlated relationship among local hemodynamic parameters is not a new finding given that those variables are mathematically associated with each other during the estimation process, and dependency among hemodynamic parameters might result in an insignificant increase in clinical value when they were used in the same prediction model. Nonetheless, we showed this relationship comprehensively using *in vivo* data, and we suggested a more accessible metric for estimation of local hemodynamic environment. Fifth, the blood rheology of an individual patient was not incorporated into the calculation of hemodynamic parameters. This might affect the accuracy of estimation of local hemodynamic environment because WSS can be generally estimated as the product of the blood dynamic viscosity and the gradient of the axial velocity of the vessel wall. Sixth, resting local hemodynamic parameters were not available for the current analysis, and future studies are needed to compare the prognostic implications between resting and hyperemic indices.

CONCLUSIONS

Local hemodynamic parameters are significantly correlated with each other, and all indices have a prognostic role in prediction of ACS risk. ΔFFR_{CT} or ΔFFR, easily measurable indices in clinical practice, can reflect local hemodynamics

TABLE 4 | ΔFFR_{CT} as a representative marker of local hemodynamic parameters in prediction of culprit lesions causing acute coronary syndrome.

Model	AUC	*P*-value
$FFR_{CT} \leq 0.80$ + high-risk plaque	0.68	<0.01
$FFR_{CT} \leq 0.80$ + high-risk plaque + ΔFFR_{CT} (ref)	0.77	NA
$FFR_{CT} \leq 0.80$ + high-risk plaque + WSS	0.76	0.37
$FFR_{CT} \leq 0.80$ + high-risk plaque + APS	0.71	0.03
$FFR_{CT} \leq 0.80$ + high-risk plaque + PG	0.77	0.63
$FFR_{CT} \leq 0.80$ + high-risk plaque + ΔFFR_{CT} + WSS	0.78	0.84
$FFR_{CT} \leq 0.80$ + high-risk plaque + ΔFFR_{CT} + APS	0.78	0.58
$FFR_{CT} \leq 0.80$ + high-risk plaque + ΔFFR_{CT} + PG	0.78	0.72

The definition of high-risk plaque was the same as in ***Table 1****.*
APS, axial plaque stress; AUC, area under curve; FFR_{CT}, coronary computed tomographic angiography-derived fractional flow reserve; PG, pressure gradient; WSS, wall shear stress; NA, not applicable.

including shear stress or plaque force acting on a plaque, and its use in clinical practice can optimize risk stratification for ACS.

DATA AVAILABILITY STATEMENT

The datasets presented in this article are not readily available because data cannot be shared publicly due to the privacy of individuals that participated in the study. The data will be shared on reasonable request to the corresponding author. Requests to access the datasets should be directed to Bon-Kwon Koo, bkkoo@snu.ac.kr.

ETHICS STATEMENT

The studies involving human participants were reviewed and approved by Seoul National University Hospital. Written informed consent for participation was not required for this study in accordance with the national legislation and the institutional requirements.

AUTHOR CONTRIBUTIONS

SY and B-KK: conception, design, analysis, and interpretation of data, drafting and revising of manuscript, and final approval of the manuscript submitted. GC, JZ, JL, DH, J-HD, C-WN, E-SS, Y-SC, S-YC, EC, BN, KN, HO, MP, BB, TK, TA, and CT: interpretation of data, revising of manuscript, and final approval of the manuscript submitted. All authors contributed to the article and approved the submitted version.

FUNDING

This study received funding from HeartFlow, Inc. The company performed the CFD analysis, but the funder was not involved in the study design, collection, analysis, interpretation of data, the writing of this article, or the decision to submit it for publication.

SUPPLEMENTARY MATERIAL

The Supplementary Material for this article can be found online at: https://www.frontiersin.org/articles/10.3389/fcvm.2021.713835/full#supplementary-material

REFERENCES

1. Go AS, Mozaffarian D, Roger VL, Benjamin EJ, Berry JD, Borden WB, et al. Heart disease and stroke statistics-−2013 update: a report from the American Heart Association. *Circulation.* (2013) 127:e6–e245. doi: 10.1161/CIR.0b013e31828124ad
2. Narula J, Nakano M, Virmani R, Kolodgie FD, Petersen R, Newcomb R, et al. Histopathologic characteristics of atherosclerotic coronary disease and implications of the findings for the invasive and noninvasive detection of vulnerable plaques. *J Am Coll Cardiol.* (2013) 61:1041–51. doi: 10.1016/j.jacc.2012.10.054
3. Stone GW, Maehara A, Lansky AJ, de Bruyne B, Cristea E, Mintz GS, et al. A prospective natural-history study of coronary atherosclerosis. *N Engl J Med.* (2011) 364:226–35. doi: 10.1056/NEJMoa1002358
4. Motoyama S, Ito H, Sarai M, Kondo T, Kawai H, Nagahara Y, et al. Plaque characterization by coronary computed tomography angiography and the likelihood of acute coronary events in mid-term follow-up. *J Am Coll Cardiol.* (2015) 66:337–46. doi: 10.1016/j.jacc.2015.05.069
5. Kaul S, Narula J. In search of the vulnerable plaque: is there any light at the end of the catheter? *J Am Coll Cardiol.* (2014) 64:2519–24. doi: 10.1016/j.jacc.2014.10.017
6. Neumann FJ, Sousa-Uva M, Ahlsson A, Alfonso F, Banning AP, Benedetto U, et al. (2019) 2018 ESC/EACTS Guidelines on myocardial revascularization. *Eur Heart J* 40:87–165. doi: 10.1093/eurheartj/ehy394
7. Zimmermann FM, Ferrara A, Johnson NP, van Nunen LX, Escaned J, Albertsson P, et al. Deferral vs. performance of percutaneous coronary intervention of functionally non-significant coronary stenosis: 15-year follow-up of the DEFER trial. *Eur Heart J.* (2015) 36:3182–8. doi: 10.1093/eurheartj/ehv452
8. Xaplanteris P, Fournier S, Pijls NHJ, Fearon WF, Barbato E, Tonino PAL, et al. Five-year outcomes with PCI guided by fractional flow reserve. *N Engl J Med.* (2018) 379:250–9. doi: 10.1056/NEJMoa1803538
9. Ford TJ, Berry C, De Bruyne B, Yong ASC, Barlis P, Fearon WF, et al. Physiological predictors of acute coronary syndromes. *JACC: Cardiovasc Interv.* (2017) 10:2539–47. doi: 10.1016/j.jcin.2017.08.059
10. Choi G, Lee JM, Kim HJ, Park JB, Sankaran S, Otake H, et al. Coronary artery axial plaque stress and its relationship with lesion geometry: application of computational fluid dynamics to coronary CT angiography. *JACC Cardiovasc Imaging.* (2015) 8:1156–66. doi: 10.1016/j.jcmg.2015.04.024
11. Gijsen F, Katagiri Y, Barlis P, Bourantas C, Collet C, Coskun U, et al. Expert recommendations on the assessment of wall shear stress in human coronary arteries: existing methodologies, technical considerations, clinical applications. *Eur Heart J.* (2019) 40:3421–33. doi: 10.1093/eurheartj/ehz551
12. Lee JM, Choi G, Koo BK, Hwang D, Park J, Zhang J, et al. Identification of high-risk plaques destined to cause acute coronary syndrome using coronary computed tomographic angiography and computational fluid dynamics. *JACC Cardiovasc Imaging.* (2019) 12:1032–43. doi: 10.1016/j.jcmg.2018.01.023
13. Bourantas CV, Zanchin T, Torii R, Serruys PW, Karagiannis A, Ramasamy A, et al. Shear stress estimated by quantitative coronary angiography predicts plaques prone to progress and cause events. *JACC Cardiovasc Imaging.* (2020) 13:2206–19. doi: 10.1016/j.jcmg.2020.02.028
14. Doradla P, Otsuka K, Nadkarni A, Villiger M, Karanasos A, Zandvoort L, et al. Biomechanical stress profiling of coronary atherosclerosis: identifying a multifactorial metric to evaluate plaque rupture risk. *JACC Cardiovasc Imaging.* (2020) 13:804–16. doi: 10.1016/j.jcmg.2019.01.033
15. Maurovich-Horvat P, Ferencik M, Voros S, Merkely B, Hoffmann U. Comprehensive plaque assessment by coronary CT angiography. *Nat Rev Cardiol.* (2014) 11:390–402. doi: 10.1038/nrcardio.2014.60

16. Taylor CA, Fonte TA, Min JK. Computational fluid dynamics applied to cardiac computed tomography for noninvasive quantification of fractional flow reserve: scientific basis. *J Am Coll Cardiol.* (2013) 61:2233–41. doi: 10.1016/j.jacc.2012.11.083
17. Park JB, Choi G, Chun EJ, Kim HJ, Park J, Jung JH, et al. Computational fluid dynamic measures of wall shear stress are related to coronary lesion characteristics. *Heart.* (2016) 102:1655–61. doi: 10.1136/heartjnl-2016-309299
18. Knaapen P, Camici PG, Marques KM, Nijveldt R, Bax JJ, Westerhof N, et al. Coronary microvascular resistance: methods for its quantification in humans. *Basic Res Cardiol.* (2009) 104:485–98. doi: 10.1007/s00395-009-0037-z
19. Wilson RF, Wyche K, Christensen BV, Zimmer S, Laxson DD. Effects of adenosine on human coronary arterial circulation. *Circulation.* (1990) 82:1595–606. doi: 10.1161/01.CIR.82.5.1595
20. Cameron JN, Mehta OH, Michail M, Chan J, Nicholls SJ, Bennett MR, et al. Exploring the relationship between biomechanical stresses and coronary atherosclerosis. *Atherosclerosis.* (2020) 302:43–51. doi: 10.1016/j.atherosclerosis.2020.04.011
21. Calvert PA, Obaid DR, O'Sullivan M, Shapiro LM, McNab D, Densem CG, et al. Association between IVUS findings and adverse outcomes in patients with coronary artery disease: the VIVA (VH-IVUS in Vulnerable Atherosclerosis) Study. *JACC Cardiovasc Imaging.* (2011) 4:894–901. doi: 10.1016/j.jcmg.2011.05.005
22. Cheng JM, Garcia-Garcia HM, de Boer SP, Kardys I, Heo JH, Akkerhuis KM, et al. In vivo detection of high-risk coronary plaques by radiofrequency intravascular ultrasound and cardiovascular outcome: results of the ATHEROREMO-IVUS study. *Eur Heart J.* (2014) 35:639–47. doi: 10.1093/eurheartj/eht484
23. Fukumoto Y, Hiro T, Fujii T, Hashimoto G, Fujimura T, Yamada J, et al. Localized elevation of shear stress is related to coronary plaque rupture: a 3-dimensional intravascular ultrasound study with in-vivo color mapping of shear stress distribution. *J Am Coll Cardiol.* (2008) 51:645–50. doi: 10.1016/j.jacc.2007.10.030
24. Costopoulos C, Huang Y, Brown AJ, Calvert PA, Hoole SP, West NEJ, et al. Plaque rupture in coronary atherosclerosis is associated with increased plaque structural stress. *JACC Cardiovasc Imaging.* (2017) 10:1472–83. doi: 10.1016/j.jcmg.2017.04.017
25. Kumar A, Thompson EW, Lefieux A, Molony DS, Davis EL, Chand N, et al. High coronary shear stress in patients with coronary artery disease predicts myocardial infarction. *J Am Coll Cardiol.* (2018) 72:1926–35. doi: 10.1016/j.jacc.2018.07.075
26. Thondapu V, Bourantas CV, Foin N, Jang IK, Serruys PW, Barlis P. Biomechanical stress in coronary atherosclerosis: emerging insights from computational modelling. *Eur Heart J.* (2017) 38:81–92. doi: 10.1093/eurheartj/ehv689
27. Samady H, Eshtehardi P, McDaniel MC, Suo J, Dhawan SS, Maynard C, et al. Coronary artery wall shear stress is associated with progression and transformation of atherosclerotic plaque and arterial remodeling in patients with coronary artery disease. *Circulation.* (2011) 124:779–88. doi: 10.1161/CIRCULATIONAHA.111.021824
28. Stone PH, Saito S, Takahashi S, Makita Y, Nakamura S, Kawasaki T, et al. Prediction of progression of coronary artery disease and clinical outcomes using vascular profiling of endothelial shear stress and arterial plaque characteristics: the PREDICTION study. *Circulation.* (2012) 126:172–81. doi: 10.1161/CIRCULATIONAHA.112.096438
29. Stone PH, Maehara A, Coskun AU, Maynard CC, Zaromytidou M, Siasos G, et al. Role of low endothelial shear stress and plaque characteristics in the prediction of nonculprit major adverse cardiac events: the PROSPECT study. *JACC Cardiovasc Imaging.* (2018) 11:462–71. doi: 10.1016/j.jcmg.2017.01.031
30. Bourantas CV, Zanchin T, Sakellarios A, Karagiannis A, Ramasamy A, Yamaji K, et al. Implications of the local haemodynamic forces on the phenotype of coronary plaques. *Heart.* (2019) 105:1078–86. doi: 10.1136/heartjnl-2018-314086
31. Costopoulos C, Timmins LH, Huang Y, Hung OY, Molony DS, Brown AJ, et al. Impact of combined plaque structural stress and wall shear stress on coronary plaque progression, regression, and changes in composition. *Eur Heart J.* (2019) 40:1411–22. doi: 10.1093/eurheartj/ehz132
32. Costopoulos C, Maehara A, Huang Y, Brown AJ, Gillard JH, Teng Z, et al. Heterogeneity of plaque structural stress is increased in plaques leading to mace: insights from the PROSPECT study. *JACC Cardiovasc Imaging.* (2020) 13:1206–18. doi: 10.1016/j.jcmg.2019.05.024
33. Bourantas CV, Ramasamy A, Karagiannis A, Sakellarios A, Zanchin T, Yamaji K, et al. Angiographic derived endothelial shear stress: a new predictor of atherosclerotic disease progression. *Eur Heart J Cardiovasc Imaging.* (2019) 20:314–22. doi: 10.1093/ehjci/jey091
34. Bourantas CV, Jaffer FA, Gijsen FJ, van Soest G, Madden SP, Courtney BK, et al. Hybrid intravascular imaging: recent advances, technical considerations, and current applications in the study of plaque pathophysiology. *Eur Heart J.* (2017) 38:400–12. doi: 10.1093/eurheartj/ehw097
35. Kikuta Y, Cook CM, Sharp ASP, Salinas P, Kawase Y, Shiono Y, et al. Pre-angioplasty instantaneous wave-free ratio pullback predicts hemodynamic outcome in humans with coronary artery disease: primary results of the international multicenter iFR GRADIENT registry. *JACC Cardiovasc Interv.* (2018) 11:757–67. doi: 10.1016/j.jcin.2018.03.005
36. Collet C, Sonck J, Vandeloo B, Mizukami T, Roosens B, Lochy S, et al. Measurement of hyperemic pullback pressure gradients to characterize patterns of coronary atherosclerosis. *J Am Coll Cardiol.* (2019) 74:1772–84. doi: 10.1016/j.jacc.2019.07.072

Conflict of Interest: GC and CT are employees and shareholders of HeartFlow, Inc. BN has received institutional unrestricted research grants from Siemens and HeartFlow, Inc. BB has received institutional unrestricted research grants from Abbott, Boston Scientific, and Biotronik; has received consulting fees from Abbott, Opsens, and Boston Scientific; and is a shareholder for Siemens, GE, Bayer, Philips, HeartFlow, Inc., Edwards Life Sciences, Sanofi, and Omega Pharma. KN has received support from HeartFlow, Inc., Siemens Healthineers, and Bayer Healthcare. JL received a Research Grant from Abbott and Philips. J-HD received a Research Grant from Philips. B-KK received an Institutional Research Grant from Abbott, Philips, and HeartFlow, Inc.

The remaining authors declare that the research was conducted in the absence of any commercial or financial relationships that could be construed as a potential conflict of interest.

Publisher's Note: All claims expressed in this article are solely those of the authors and do not necessarily represent those of their affiliated organizations, or those of the publisher, the editors and the reviewers. Any product that may be evaluated in this article, or claim that may be made by its manufacturer, is not guaranteed or endorsed by the publisher.

frontiers in Cardiovascular Medicine

ORIGINAL RESEARCH
published: 12 October 2021
doi: 10.3389/fcvm.2021.714077

Diagnostic Performance of Angiography-Based Fractional Flow Reserve for Functional Evaluation of Coronary Artery Stenosis

Changling Li[1], Xiaochang Leng[2], Jingsong He[2], Yongqing Xia[2], Wenbing Jiang[3], Yibin Pan[4], Liang Dong[1], Yong Sun[1], Xinyang Hu[1], Jian'an Wang[1], Jianping Xiang[2] and Jun Jiang[1]**

[1] Department of Cardiology, The Second Affiliated Hospital, Zhejiang University School of Medicine, Hangzhou, China, [2] ArteryFlow Technology Co., Ltd., Hangzhou, China, [3] Department of Cardiology, The Third Clinical Institute Affiliated to Wenzhou Medical University, Wenzhou, China, [4] Department of Cardiology, Affiliated Jinhua Hospital, Zhejiang University School of Medicine, Jinhua, China

OPEN ACCESS

Edited by:
Sebastian Kelle,
Deutsches Herzzentrum
Berlin, Germany

Reviewed by:
Jan Brüning,
Charité—Universitätsmedizin
Berlin, Germany
Haikun Qi,
ShanghaiTech University, China
Masafumi Ono,
Cardialysis, Netherlands

***Correspondence:**
Jun Jiang
jiang-jun@zju.edu.cn
Jianping Xiang
jianping.xiang@arteryflow.com

Specialty section:
This article was submitted to Cardiovascular Imaging, a section of the journal Frontiers in Cardiovascular Medicine

Received: 24 May 2021
Accepted: 15 September 2021
Published: 12 October 2021

Citation:
Li C, Leng X, He J, Xia Y, Jiang W, Pan Y, Dong L, Sun Y, Hu X, Wang J, Xiang J and Jiang J (2021) Diagnostic Performance of Angiography-Based Fractional Flow Reserve for Functional Evaluation of Coronary Artery Stenosis. Front. Cardiovasc. Med. 8:714077. doi: 10.3389/fcvm.2021.714077

Background: A new method for calculating fraction flow reserve (FFR) without pressure-wire (angiography-derived FFR) based on invasive coronary angiography (ICA) images can be used to evaluate the functional problems of coronary stenosis.

Objective: The aim of this study was to assess the diagnostic performance of a novel method of calculating the FFR compared to wire-based FFR using retrospectively collected data from patients with stable angina.

Methods: Three hundred patients with stable angina pectoris who underwent ICA and FFR measurement were included in this study. Two ICA images with projections $>25^{\circ}$ apart at the end-diastolic frame were selected for 3D reconstruction. Then, the contrast frame count was performed in an angiographic run to calculate the flow velocity. Based on the segmented vessel, calculated velocity, and aortic pressure, AccuFFRangio distribution was calculated through the pressure drop equation.

Results: Using FFR ≤ 0.8 as a reference, we evaluated AccuFFRangio performance for 300 patients with its accuracy, sensitivity, specificity, positive predictive value (PPV), and negative predictive value (NPV). Comparison of AccuFFRangio with wire-measured FFR resulted in an area under the curve (AUC) of 0.954 (per-vessel, $p < 0.0001$). Accuracy for AccuFFRangio was 93.7% for Pa set from measurement and 87% for Pa = 100 mmHg in this clinical study. Overall sensitivity, specificity, PPV, and NPV for per-vessel were 90, 95, 86.7, 96.3, and 57.5, 97.7, 90.2, 86.3%, respectively. Overall accuracy, sensitivity, specificity, PPV, and NPV for 2-dimensional (2D) quantitative coronary angiography (QCA) were 63.3, 42.5, 70.9, 34.7, and 77.2%, respectively. The average processing time of AccuFFRangio was 4.30 ± 1.87 min.

Conclusions: AccuFFRangio computed from coronary ICA images can be an accurate and time-efficient computational tool for detecting lesion-specific ischemia of coronary artery stenosis.

Keywords: fractional flow reserve, invasive coronary angiography, coronary artery, ischemia, stenosis

INTRODUCTION

Compared with the anatomical stenosis of the coronary artery, functional assessment can more accurately evaluate and predict the progression of coronary heart disease (1). In the catheterization laboratory, invasive coronary angiography (ICA) images can only qualitatively assess the degree of stenosis but cannot evaluate the physiological function of coronary arteries. Therefore, it may overestimate or underestimate the severity of the disease, leading to the untreated or over-treatment of lesions (2). Fractional flow reserve (FFR) has become a recognized index for the functional evaluation of coronary stenosis, which is defined as a ratio of the pressure of the distal end of the stenosis and the cardiac aorta at hyperemia (1). The current method of measuring FFR requires a pressure wire inserted into the distal end of the stenosis, which will bring additional procedure-related risks causing adverse effects to the blood vessel and increase the treatment time and cost (3, 4). A new method of non-pressure wire FFR (angio-based FFR) calculation method based on ICA images can reflect functional problems of coronary stenosis (5–7). By using two angiograms greater than 25° through independent 3D vessel reconstruction and numerical calculation of pressure drop, angio-based FFR enables interventional cardiologists and researchers to obtain accurate anatomical quantifications of one or more lesions in the analyzed coronary segment, to determine the functional significance of the individual and consecutive multiple lesions. These methods can be helpful for optimal percutaneous coronary intervention (PCI) treatment of the lesion of coronary disease. Several studies have shown that angio-based FFR is highly correlated with invasive FFR compared to coronary computed tomography angiography (CTA) and ICA assessment (4, 8–10). It is also more advantageous in formulating treatment strategies for coronary artery disease under circumstances that screening people with suspected chest pain for the presence of myocardial ischemia.

In this study, coronary angiography was used to calculate the average volume flow using TIMI (thrombolysis in myocardial infarction) frame count combined with three-dimensional quantitative coronary angiography (QCA). Subsequently, applying computational fluid dynamics theory, a new angiography-based FFR calculation method AccuFFRangio was proposed. The FFR measured by the pressure-wire was used as a reference standard to evaluate the diagnostic performance of AccuFFRangio.

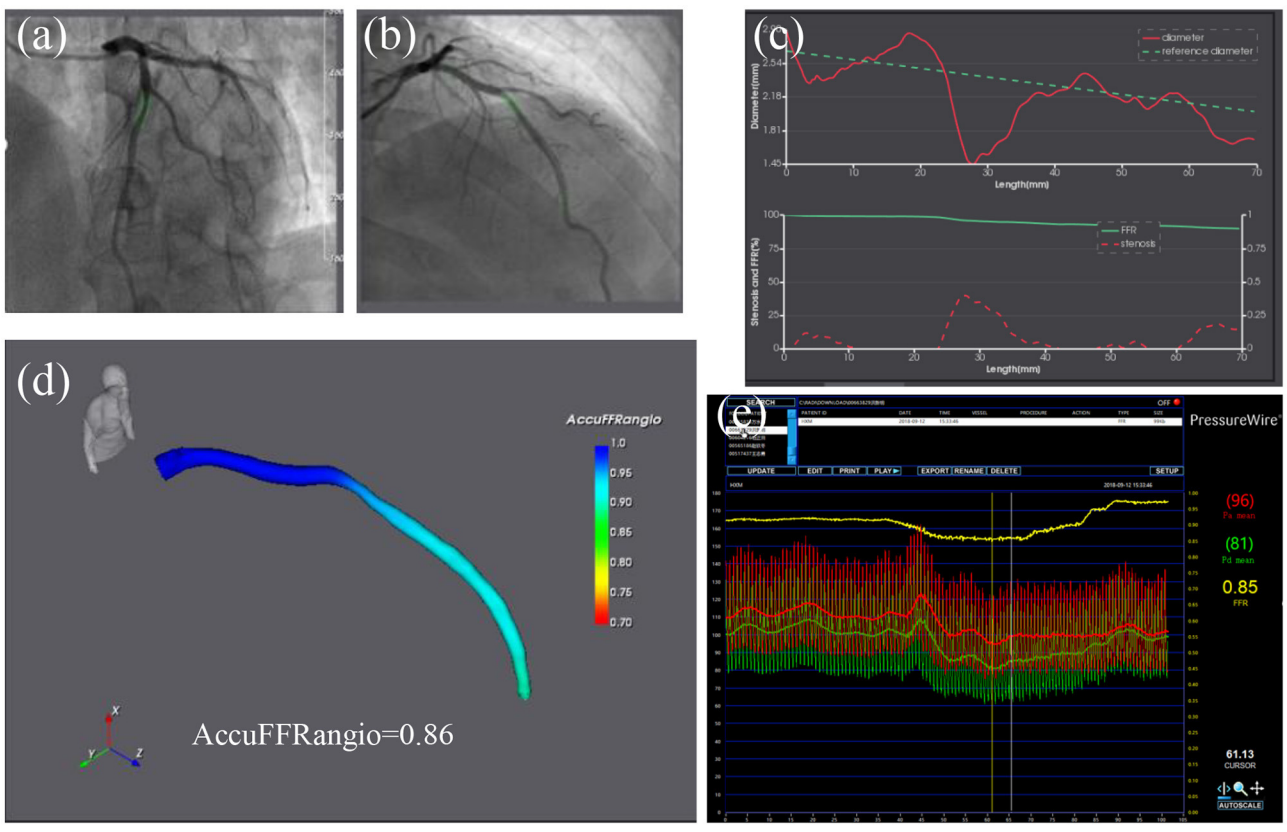

FIGURE 1 | AccuFFRangio analysis of intermediate stenosis of a left anterior descending artery (LAD). **(a,b)** Coronary angiography images from two different angles of view. **(c)** The above chart shows the change of lumen diameter (red) along LAD with the computed reference diameter (green); the chart below shows the diameter stenosis (red) and AccuFFRangio pullback (green). **(d)** Computed AccuFFRangio distribution; the AccuFFRangio value was 0.86. **(e)** The FFR measured by pressure wire was 0.85.

MATERIALS AND METHODS

Study Design

The present study is a retrospective, single-center, observational study performed at The Second Affiliated Hospital, Zhejiang University School of Medicine. This study aims to evaluate the diagnostic accuracy, sensitivity, and specificity of AccuFFRangio in identifying functionally significant stenosis by using pressure wire-based FFR as the reference. AccuFFRangio and 2D-QCA were analyzed and compared in the core laboratory of the Department of Cardiology at The Second Affiliated Hospital, Zhejiang University School of Medicine. After receiving ethics approval from the institutional review board, this study was conducted with a written informed consent form waived.

Patient Population

Since this was a retrospective study, consecutive patients with stable angina pectoris who underwent ICA and FFR measurement were eligible for enrollment. Angiographic inclusion criteria were (1) percentage diameter stenosis of the coronary artery between 30% and 90% in a vessel $\geq$2 mm by visual estimation; (2) angiographic projections $\geq$25° apart were recorded. Exclusion criteria include (1) overlapping interrogated vessels with too much shortening without preferred references in proximal or distal vessels; (2) insufficient injected contrast for QCA analysis; (3) location of the target lesion at the ostium of the left or right coronary artery; (4) wire-position not documented. Exclusion criteria on patient level contain (1) acute myocardial infarction within 72 h; (2) severe asthma or severe chronic obstructive pulmonary disease; (3) allergy to contrast media or adenosine; or (4) atrial fibrillation.

Invasive Coronary Angiography and 2D-QCA Analysis

ICA was performed using the X-ray system (Allura Xper FD20/10; PHILIPS Medical Systems, the Netherlands). These angiographic images were recorded at 15 frames/s. The contrast medium was injected manually with a forceful and stable injection or by the pump at a rate of ∼4 ml/s. 2D-QCA was conducted by using angiogram vendor-integrated QCA software (Allura Xper FD20/10; PHILIPS Medical Systems, the Netherlands).

Wire-Based FFR Measurement

FFR was measured in all patients using coronary pressure wire (St. Jude Medical, St. Paul, MN, USA). After calibration and equalization, the pressure wire was advanced distally to the stenosis. Maximum hyperemia was induced with i.v. adenosine triphosphate at a concentration of 180 μg/kg/min. Both the distal coronary pressure at the pressure sensor and the proximal pressure at the coronary artery ostium were recorded simultaneously. The FFR measurement was performed by physicians in The Second Affiliated Hospital, Zhejiang University School of Medicine (Y.P., L.D., W.J., Y.S.). Pressure sensor was pulled back to the catheter tip to check or correct the pressure drift (**Figure 1e**).

AccuFFRangio Computation

AccuFFRagnio was computed with the AccuFFRangio V1.0 software (ArteryFlow Technology, Hangzhou, China) by participating physicians and technicians (F.M., Y.Z., M.H.) blinded to FFR. Two angiographic images with projections

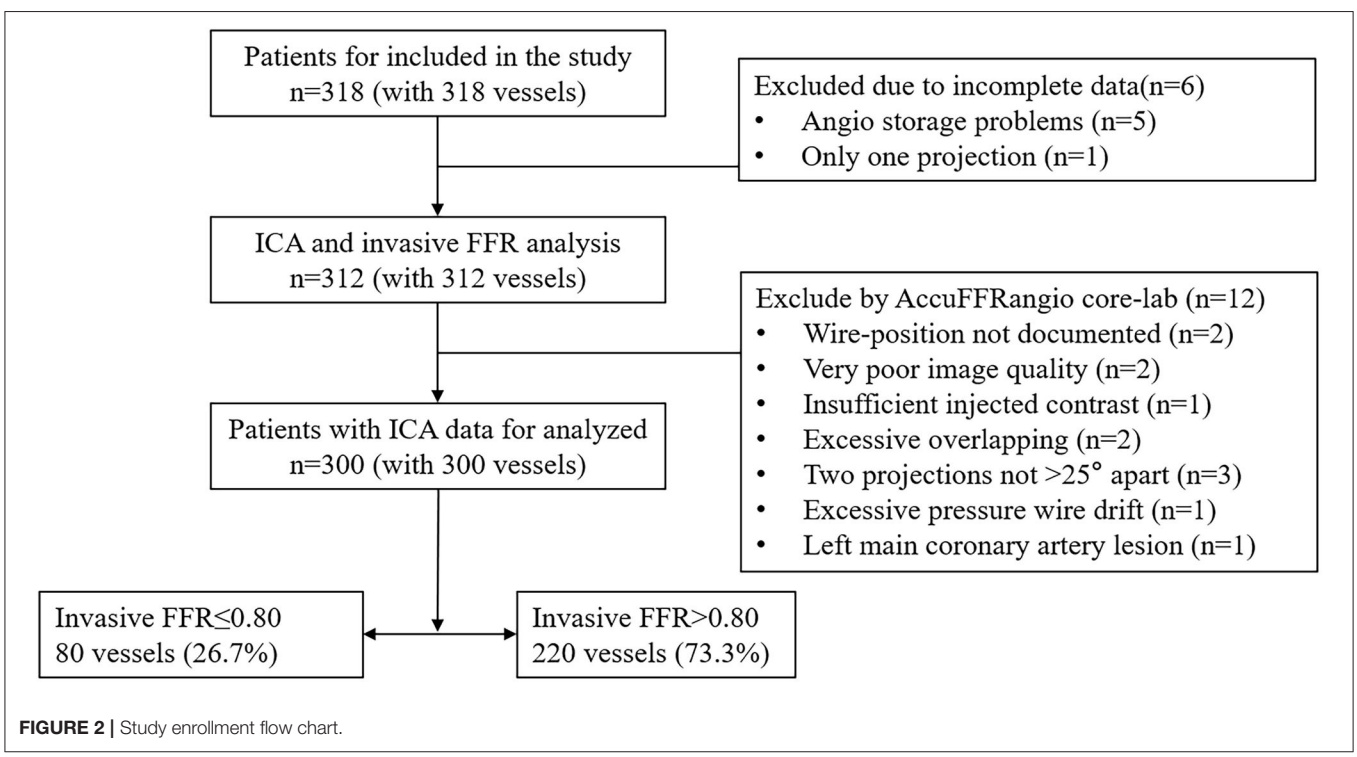

FIGURE 2 | Study enrollment flow chart.

>25° apart at the end-diastolic frame were selected for three-dimensional (3D) reconstruction (6, 7, 11). To simplify the geometry calibration procedure and achieve a reliable correspondence in centerline points for 3D reconstruction, we have implemented three pairs of reference points to eliminate the isocenter offset and rotational angle parameter errors. Since the pressure drop has a positive relationship with the coronary vessel flow rate, the frame count method is a relatively feasible solution (12). This method hypothesizes that the blood flow velocity is proportional to the vessel cross-section diameter dimension. Typically, the pressure drop from proximal to distal stenosis is caused by two factors. The first is the viscous pressure drop associated with friction. The second is the expansion pressure drop due to the rapid change in radius, which is usually characterized by narrowing. Pressure drop P_R is related to viscosity loss coefficient C_{Vis}, expansion loss coefficient C_{Expan}, and flow rate Q: $P_R = (C_{Vis} + C_{Expan} \bullet Q) \bullet Q$. More detail of the derived equations can be seen in our previous study (11).

Contrast flow rate velocity for FFR computation was derived from the TIMI frame counting method for the segmented vessel. With the calculated velocity and input aortic pressure from the measurement of the pressure at the coronary ostium, AccuFFRangio distribution can be calculated (**Figure 1**). AccuFFRangio value was taken at the same position of wire-based FFR using angiography images as a reference. To compare the diagnostic accuracy of AccuFFRangio by using a fixed value of aortic pressure and to study the influence of fixed value on the performance of our approach in case some patient-specific pressures cannot be obtained, Pa = 100 mmHg was set for each calculation of angio-based FFR (13, 14).

Statistical Analysis

Continuous variables with normally distributed were expressed as mean ± standard deviation (SD) and non-normal distributed variables as the median. Categorical variables were expressed as percentages and data were analyzed on a per vessel basis. Pearson

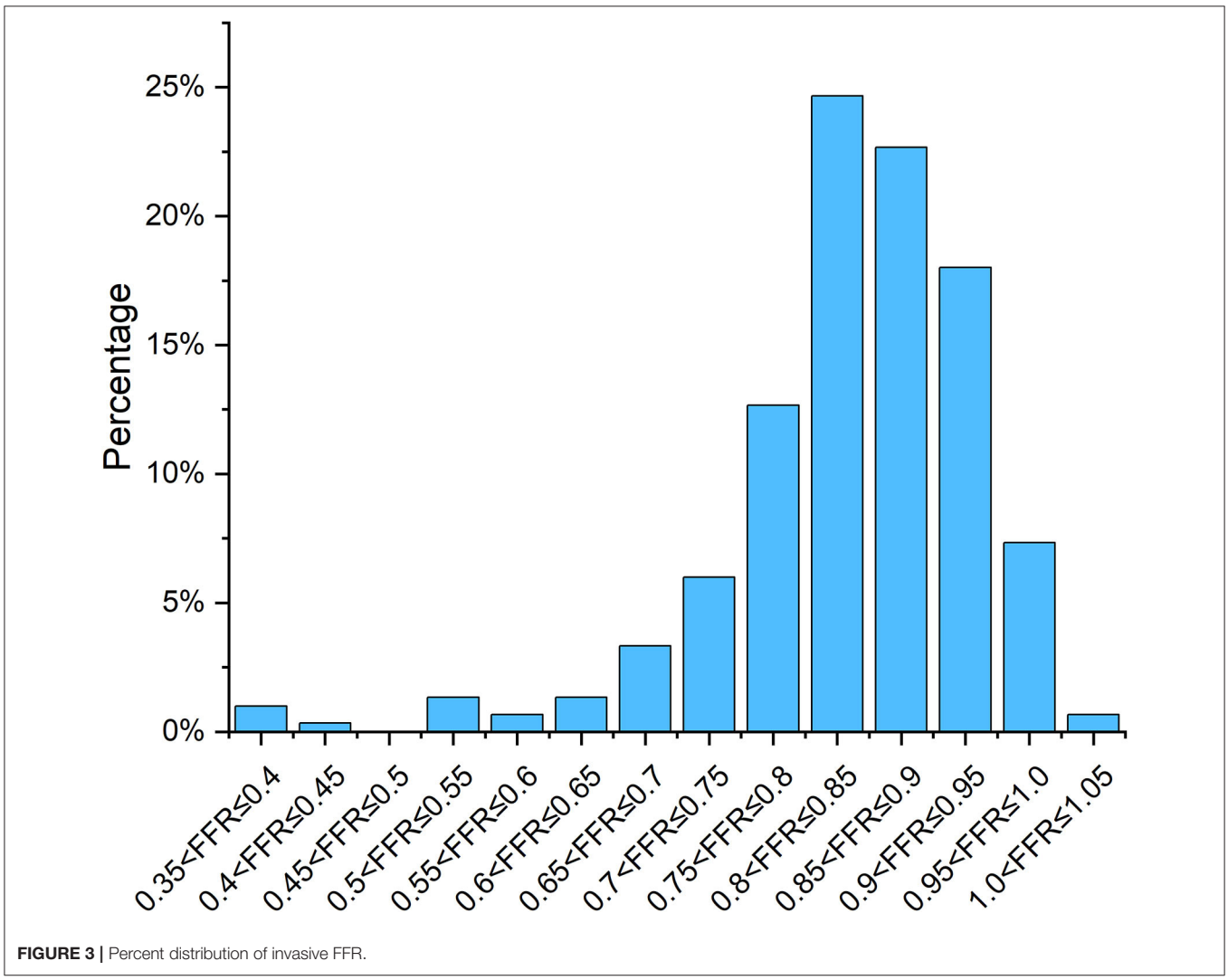

FIGURE 3 | Percent distribution of invasive FFR.

correlation was used to quantify the correlation between FFR and AccuFFRangio. Agreement between FFR and AccuFFRangio was assessed on the Bland-Altman plot. Using FFR $\leq$ 0.8 as the reference standard, the performance of AccuFFRangio for predicting functionally significant stenosis was evaluated by diagnostic accuracy, sensitivity, specificity, positive predictive value (PPV), and negative predictive value (NPV). The area under the curve (AUC) of receiver operating characteristic (ROC) analysis was used to assess the diagnostic accuracy of AccuFFRangio. All the statistical analyses were performed by using MedCalc (MedCalc Software Inc., Belgium).

RESULTS

Patient Characteristics

Figure 2 presents the study enrollment flow chart. Three hundred eighteen patients with 318 vessels were included in this clinical study from May 2016 to July 2019. Due to the incomplete data from six patients, 312 patients underwent ICA procedure and wire-FFR waveform analysis. Among them, 12 patients were excluded due to predefined exclusion criteria, including undocumented wire-position, poor image quality, excessive vessel overlap, insufficient contrast, projections <25 degrees, excessive pressure wire drift, and left main coronary artery lesions. In the end, 300 patients with 300 vessels were included in the final analysis.

Mean FFR was 0.84 $\pm$ 0.10, as shown in **Figure 3**, and mean percentage diameter stenosis (%DS) form 2D-QCA was 44 $\pm$ 12%. FFR $\leq$ 0.80 was found in 80 (26.7%) vessels and the mean contrast flow rate velocity was 0.17 $\pm$ 0.05 m/s. Baseline patient and procedural characteristics are listed in **Tables 1**, **2**.

TABLE 1 | Baseline patient characteristics (n = 300).

Age, y	64.1 ± 9.6
Male	67% (201)
Weight (kg)	68.5 ± 34.5
Height (cm)	165 ± 7.3
BMI, kg/m^2	25.2 ± 13.9
Systolic blood pressure (mm Hg)	130 ± 20
Diastolic blood pressure (mm Hg)	78 ± 15
Diabetes	21% (64)
Hypertension	45% (135)
Hyperlipidemia	13% (40)

TABLE 2 | Vessel characteristics (n = 300).

Vessels	
LAD	61.7% (185)
LCX	7.3% (22)
RCA	29.7% (89)
Anatomy	
Diameter stenosis, %	44 ± 12%
<50%	67.3% (202)
≥50%	32.7% (98)
Physiology	
FFR (per vessel)	0.84 ± 0.10
Vessels with FFR ≤ 0.8	26.7% (80)
Vessels with FFR > 0.8	73.3% (220)
Diffuse or serial lesions	32.3% (97)
Bifurcation lesions	2.7% (8)
Calcified lesions	2% (6)
Myocardial bridge	5.7% (17)

Correlation and Agreement Between AccuFFRangio and FFR

Good correlations were observed in **Figure 4** with a correlation coefficient of $r = 0.83$ ($p < 0.001$). There were good agreements between AccuFFRangio and FFR in the Bland-Altman plot with a mean difference value of −0.001 (limits of agreement: −0.124 to 0.122) when Pa measured at the coronary ostium and −0.030 (limits of agreement: −0.155 to 0.095) when Pa = 100 mmHg was used, as shown in **Figure 5**. The number of patients with the absolute difference between AccuFFRangio and FFR falling out of the 95% CI was 9 (3%) when Pa was set according to the patients and 18 (6%) when Pa was set equal to a fixed value.

Diagnostic Performance of AccuFFRangio and 2D-QCA

Accuracy for AccuFFRangio was 93.7% in this clinical study. Overall sensitivity, specificity, PPV, and NPV were 90, 95, 86.7, and 96.3%, respectively (**Table 3**). Meanwhile, these values for AccuFFRangio, when Pa = 100 mmHg was implemented in the calculation, were 87, 57.5, 97.7, 90.2, and 86.3%. Comparison of AccuFFRangio and 2D-QCA with pressure wire measured FFR as reference resulted in an AUC for AccuFFRangio of 0.954 (95%CI: 0.924–0.975) and 0.934 (95%CI: 0.900–0.960, when Pa = 100 mmHg) and 2D-QCA of 0.567 (95% CI: 0.509–0.624), as shown in **Figure 6**.

In addition, the mean processing time of AccuFFRangio assessment was 4.30 $\pm$ 1.87 min including the 3D anatomic model reconstruction and AccuFFRangio calculation for each patient.

DISCUSSION

Wire-based FFR has potential risks in measurement procedures and vasodilator complications, and the complexity of the operation is also a challenge. In this situation, this study had demonstrated a reliable and efficient computational method AccuFFRangio for the functional evaluation of lesion-specific ischemia of coronary artery stenosis based on ICA images without injecting vasodilators. Thus, instead of using invasive wire-based FFR for evaluating the severity of suspected coronary heart disease, AccuFFRangio uses a combination of the 3D structure of the coronary vessel and computational fluid dynamics (CFD)-based equations on account of TIMI frame count to analyze the functional performance in a short time of 5 min. The diagnostic accuracy of AccuFFRangio was 93.7%

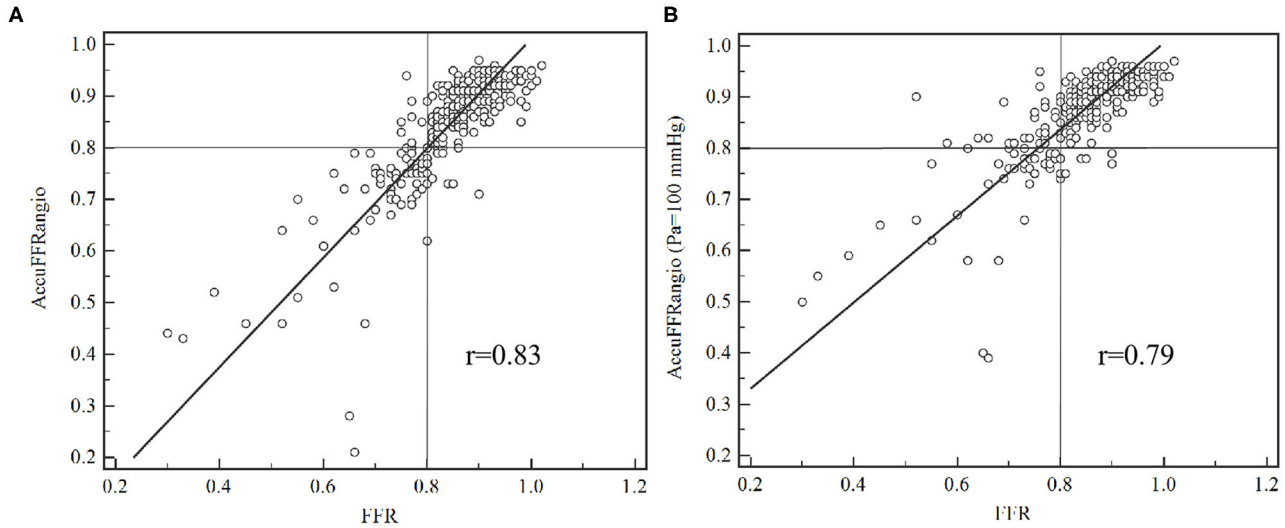

FIGURE 4 | Correlation between AccuFFRangio computation and conventional pressure wired measured FFR. **(A)** Pa from the measurement of the pressure at the coronary ostium; **(B)** Pa set as equal to 100 mmHg.

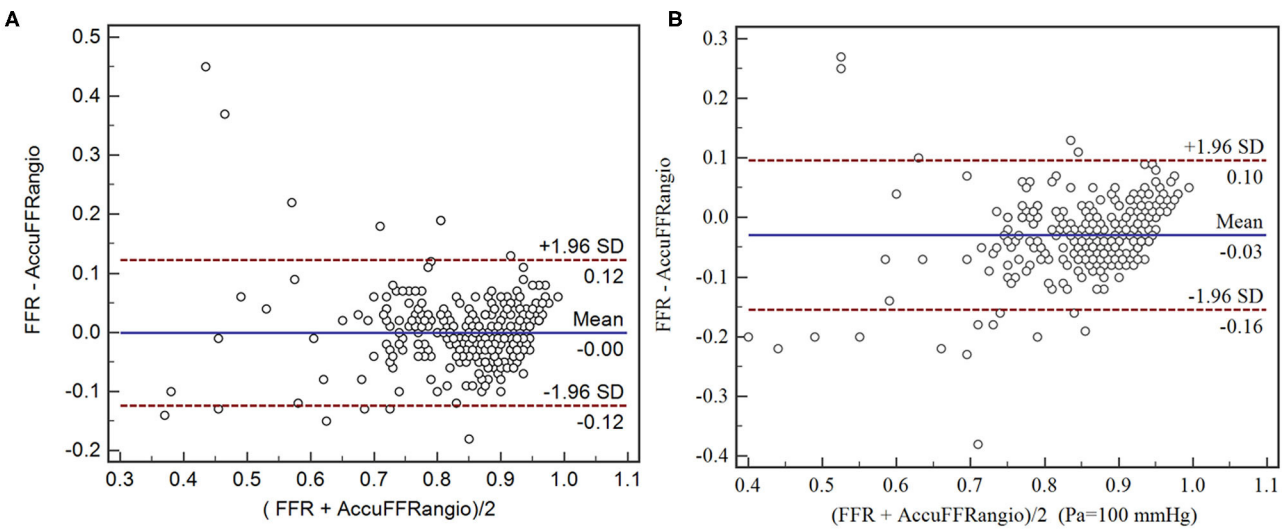

FIGURE 5 | Agreement between AccuFFRangio computation and conventional pressure wired measured FFR. **(A)** Pa from the measurement of the pressure at the coronary ostium; **(B)** Pa set as equal to 100 mmHg.

compared to pressure wire-derived FFR, which shows a higher accuracy compared to 2D-QCA with an accuracy of 63.3%.

For assessment of FFR without pressure-wire, many research groups have made significant efforts and developed different angiography-based FFR methods. Morris et al. (15) described that the construction of arteries was based on two projections from similar phases of the cardiac cycle with good vessel opacification and contrast. Meanwhile, the virtual FFR was calculated from CFD simulations with generic downstream boundary conditions applied to the arterial outlet with a Windkessel model (16). With a 3D coronary tree construction based on the geometry of two or more projections with a minimum separation of 30° and application of an automatic resistance-based lumped model of the entire coronary tree, FFR_{angio} (17–19) showed a high concordance between pressure-wire measured FFR. By reconstructing a 3D QCA model of the target vessel using two angiographic projections recorded at least 25° intervals, the QFR was computed through mathematic equations incorporated with contrast flow velocity determined using frame count analysis (6, 20). It represented a high diagnostic accuracy with FFR, reducing the number of patients for pressure-wire

TABLE 3 | Diagnostic performance of AccuFFRangio for per-vessel.

	AccuFFRangio ≤ 0.8	AccuFFRangio ≤ 0.8 (Pa = 100 mmHg)	Diameter stenosis by QCA ≥ 50%
Accuracy	93.7% (89.9–95.9%)	87% (81.9–90.0%)	63.3% (57.94–69.1%)
Sensitivity	90.0% (84.6–97.2%)	57.5% (45.3–67.8%)	42.5% (33.8–56.5%)
Specificity	95.0% (89.5–96.5%)	97.7% (94.1–99.0%)	70.9% (63.9–76.4%)
PPV	86.7% (76.3–89.9%)	90.2% (77.3–94.5%)	34.7% (28.8–43.2%)
NPV	96.3% (94.1–98.7%)	86.3% (82.6–88.7%)	77.2% (73.9–81.4%)

Data are shown in percentage with 95% confidence interval in brackets.

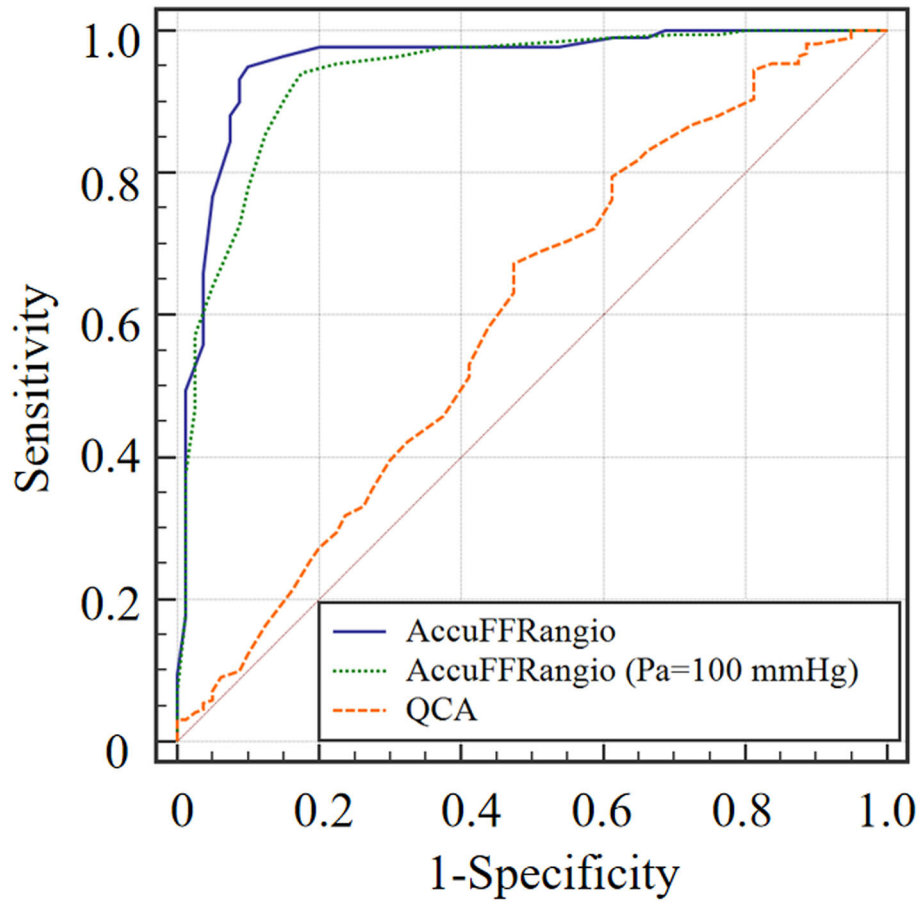

FIGURE 6 | ROC Curve between AccuFFRangio and QCA.

measurements. In the current study of AccuFFRangio, the 3D geometry model construction and calculation of FFR were different from the methods described above. We used three physiological points to do the vessel calibration to eliminate the error during the reprojection procedure, as the same processes in our previous studies (11). Moreover, the velocity of the inlet of the blood vessel was set according to the TIMI frame count. The blood pressure at the aorta was chosen equal to the value from measuring the pressure at the coronary ostium.

The accuracy of AccuFFRangio in the present study was 93.7% for per-vessel bias, which is comparable to the clinical trials with patients over 200, such as 83% for WIFI II Study (21), 86.8% for FAVOR II Europe-Japan Study (7), 92.7% for FAVOR II China Study (4), and 93.5% for FAST-FFR Study (18). The sensitivity, specificity, and AUC for the four clinical trials were 86, 77%, and 0.86 for WIFI II Study (21), 86.5, 86.9%, and 0.92 for FAVOR II Europe-Japan Study (7), 94.6, 91.7%, and 0.96 for FAVOR II China Study (4), and 91.2, 92.2%, and 0.944 for FAST-FFR Study (18). Those for AccuFFRangio were 90, 95%,

and 0.954. Compared to Pa taken from the measurement at the coronary ostium, as Pa set equal to a fixed value of 100 mmHg, the diagnostic performance decreased to 87% for accuracy and 57.5% for sensitivity, respectively. Angiography-based FFR can improve the low sensitivity of 2D-QCA in evaluating hemodynamically significant of coronary stenosis, from about 42.5–62.5–86.5–94.6% (4, 7, 21–23). Similarly, this method will also increase the specificity from the original 58.1–76.5–86.9–92.2% (4, 7, 21–23). Thus, the implementation of angiography-based FFR can avoid unnecessary revascularization of many interrogated vessels when performed coronary angiography. It is also useful to optimize the strategies of percutaneous coronary intervention (PCI) to reduce the number of the implanted stents and improve the clinical outcome for patients who plan to perform PCI.

The time for calculating angiography-based FFR is also essential for evaluating superiority when there is only limited time during the PCI operation. For vFFR (15), it took ∼ 24 h for the CFD simulation of one case, which cannot be implemented in the condition during PCI performance. Another method FFR_{angio} took nearly 10 min for the whole procedure, including reconstruction of the 3D geometry model of the entire coronary tree and calculation of the FFR values based on lumped model (17, 18, 24, 25). But, it only took 4.3 ± 3.4 min to perform an analysis for one lesion (24). By constructing the 3D geometry model for only the target vessel and CFD-based equations on account of TIMI frame count to calculate the FFR values, the entire procedure was completed in a short time of 5 min 59 s on average (6), which can be used during the PCI operation. In addition, the entire process of calculating FFR with a similar algorithm used in this paper took about 5 min, which met the requirement of clinical application in PCI surgery.

It is worth noting the limitations of this clinical study. Firstly, this was a retrospective study at one single center. Secondly, the study may have selection bias because of the relatively small number of positive cases (80 vessels, 26.7%) compared with the negative ones (220 vessels, 73.3%). Third, this study was an observational study. In the future, prospective, multi-center, and follow-up studies will be performed in the post-market clinical researches. Fourth, abnormal pressure curves such as wave form distortion or ventricularization were not found in this study due to the nature of our study population, while this could influence the measurement of FFR; thus, further assessment should be considered.

CONCLUSIONS

This clinical study demonstrates that AccuFFRangio is clinically feasible. The performance is superior to angiographic assessment by 2D-QCA for evaluating coronary artery stenosis when using FFR as a reference. The accuracy, sensitivity, and specificity of AccuFFRangio in identifying hemodynamically significant of coronary stenosis using 300 patient data were 93.7, 90, and 95%, respectively. Those were better than the diagnostic performance of AccuFFRangio calculated based on Pa setting equal to 100 mmHg. AccuFFRangio bears the potential of improving angiography-based identification of functionally significant stenosis during coronary angiography procedure.

Impact on Daily Practice

AccuFFRangio can quickly and accurately calculate FFR values based on coronary angiography images and can be used for functional assessment of patients with coronary heart disease, avoiding unnecessary PCI treatment.

DATA AVAILABILITY STATEMENT

The original contributions presented in the study are included in the article/supplementary material, further inquiries can be directed to the corresponding authors.

ETHICS STATEMENT

The studies involving human participants were reviewed and approved by Department of Cardiology, Second Affiliated Hospital of Zhejiang University School of Medicine. Written informed consent for participation was not required for this study in accordance with the national legislation and the institutional requirements.

AUTHOR CONTRIBUTIONS

CL and XL: concept and design of the study, analysis of the data, and drafting of the manuscript. JH: case calculation and drafting of the manuscript. CL, LD, and XH: image annotation of ICA and critical review of the manuscript. YX and JH: implementation of the algorithm and drafting of the manuscript. JW and JX: conception and design of the study, analysis of the data, drafting of the manuscript, and final approval of the manuscript submitted. WJ, YP, YS, and JJ: have contributed to the submitted work. All authors contributed to the article and approved the submitted version.

FUNDING

This work was supported by the National Natural Science Foundation of China (Nos. 82170332, 81320108003, 31371498, 81100141, and 81570322), Zhejiang Provincial Public Welfare Technology Research Project (No. LGF20H020012), Zhejiang Provincial key research and development plan (No. 2020C03016), the Major projects in Wenzhou of China (No. 2019ZG0107), the Major projects in Jinhua of China (No. 2020A31003), Scientific research project of Zhejiang Education Department (No. Y201330290), and Major medical and health science and technology plan of Zhejiang Province (No. WKJ-ZJ-1913).

REFERENCES

1. Kern MJ, Samady H. Current concepts of integrated coronary physiology in the catheterization laboratory. *J Am Coll Cardiol.* (2010) 55:173–85. doi: 10.1016/j.jacc.2009.06.062
2. Lindstaedt M, Spiecker M, Perings C, Lawo T, Yazar A, Holland-Letz T, et al. How good are experienced interventional cardiologists at predicting the functional significance of intermediate or equivocal left main coronary artery stenoses? *Int J Cardiol.* (2007) 120:254–61. doi: 10.1016/j.ijcard.2006.11.220
3. Douglas PS, Pontone G, Hlatky MA, Patel MR, Norgaard BL, Byrne RA, et al. Clinical outcomes of fractional flow reserve by computed tomographic angiography-guided diagnostic strategies vs. usual care in patients with suspected coronary artery disease: the prospective longitudinal trial of FFRCT: outcome and resource impacts study. *Eur Heart J.* (2015) 36:3359–67. doi: 10.1093/eurheartj/ehv444
4. Xu B, Tu S, Qiao S, Qu X, Chen Y, Yang J, et al. Diagnostic accuracy of angiography-based quantitative flow ratio measurements for online assessment of coronary stenosis. *J Am Coll Cardiol.* (2017) 70:3077–87. doi: 10.1016/j.jacc.2017.10.035
5. Zhou J, Yang J-J, Yang X, Chen Z-Y, He B, Du L-S, et al. Impact of clinical guideline recommendations on the application of coronary computed tomographic angiography in patients with suspected stable coronary artery disease. *Chin Med J (Engl).* (2016) 129:135–41. doi: 10.4103/0366-6999.173434
6. Koltowski L, Zaleska M, Maksym J, Tomaniak M, Solinski M, Puchta D, et al. Quantitative flow ratio derived from diagnostic coronary angiography in assessment of patients with intermediate coronary stenosis: a wire-free fractional flow reserve study. *Clin Res Cardiol.* (2018) 107:858–67. doi: 10.1007/s00392-018-1258-7
7. Westra J, Andersen BK, Campo G, Matsuo H, Koltowski L, Eftekhari A, et al. Diagnostic performance of in-procedure angiography-derived quantitative flow reserve compared to pressure-derived fractional flow reserve: The FAVOR II Europe-Japan study. *J Am Heart Assoc.* (2018) 7:e009603. doi: 10.1161/JAHA.118.009603
8. Min JK, Koo BK, Erglis A, Doh JH, Daniels DV, Jegere S, et al. Usefulness of noninvasive fractional flow reserve computed from coronary computed tomographic angiograms for intermediate stenoses confirmed by quantitative coronary angiography. *Am J Cardiol.* (2012) 110:971–6. doi: 10.1016/j.amjcard.2012.05.033
9. Min JK, Koo B-K, Erglis A, Doh J-H, Daniels DV, Jegere S, et al. Effect of image quality on diagnostic accuracy of noninvasive fractional flow reserve: Results from the prospective multicenter international DISCOVER-FLOW study. *J Cardiovasc Comput Tomogr.* (2012) 6:191–9. doi: 10.1016/j.jcct.2012.04.010
10. Nørgaard BL, Leipsic J, Gaur S, Seneviratne S, Ko BS, Ito H, et al. Diagnostic performance of noninvasive fractional flow reserve derived from coronary computed tomography angiography in suspected coronary artery disease: the NXT trial (Analysis of Coronary Blood Flow Using CT Angiography: Next Steps). *J Am Coll Cardiol.* (2014) 63:1145–55. doi: 10.1016/j.jacc.2013.11.043
11. Jiang J, Feng L, Li C, Xia Y, He J, Leng X, et al. Fractional flow reserve for coronary stenosis assessment derived from fusion of intravascular ultrasound and X-ray angiography. *Quant Imaging Med Surg.* (2021) 11:4543–55. doi: 10.21037/qims-20-1324
12. Gibson CM, Cannon CP, Daley WL, Dodge JT. Jr, Alexander B, Jr, Marble SJ, et al. TIMI frame count: a quantitative method of assessing coronary artery flow. *Circulation.* (1996) 93:879–88. doi: 10.1161/01.CIR.93.5.879
13. Papafaklis MI, Muramatsu T, Ishibashi Y, Lakkas LS, Nakatani S, Bourantas CV, et al. Fast virtual functional assessment of intermediate coronary lesions using routine angiographic data and blood flow simulation in humans: comparison with pressure wire - fractional flow reserve. *EuroIntervention.* (2014) 10:574–83. doi: 10.4244/EIJY14M07_01
14. Tu S, Bourantas CV, Norgaard BL, Kassab GS, Koo BK, Reiber JH. Image-based assessment of fractional flow reserve. *EuroIntervention.* (2015) 11:V50–4. doi: 10.4244/EIJV11SVA11
15. Morris PD, Ryan D, Morton AC, Lycett R, Lawford PV, Hose DR, et al. Virtual fractional flow reserve from coronary angiography: modeling the significance of coronary lesions: results from the VIRTU-1 (VIRTUal Fractional Flow Reserve From Coronary Angiography) study. *JACC Cardiovascular Interventions.* (2013) 6:149–57. doi: 10.1016/j.jcin.2012.08.024
16. Westerhof N, Lankhaar J-W, Westerhof BE. The arterial Windkessel. *Med Biol Eng Comput.* (2009) 47:131–41. doi: 10.1007/s11517-008-0359-2
17. Pellicano M, Lavi I, De Bruyne B, Vaknin-Assa H, Assali A, Valtzer O, et al. Validation study of image-based fractional flow reserve during coronary angiography. *Circ Cardiovasc Interv.* (2017) 10:e005259. doi: 10.1161/CIRCINTERVENTIONS.116.005259
18. Fearon WF, Achenbach S, Engstrom T, Assali A, Shlofmitz R, Jeremias A, et al. Accuracy of fractional flow reserve derived from coronary angiography. *Circulation.* (2019) 139:477–84. doi: 10.1161/CIRCULATIONAHA.118.037350
19. Kornowski R, Lavi I, Pellicano M, Xaplanteris P, Vaknin-Assa H, Assali A, et al. Fractional Flow Reserve Derived From Routine Coronary Angiograms. *J Am Coll Cardiol.* (2016) 68:2235–7. doi: 10.1016/j.jacc.2016.08.051
20. Smit JM, Koning G, van Rosendael AR, El Mahdiui M, Mertens BJ, Schalij MJ, et al. Referral of patients for fractional flow reserve using quantitative flow ratio. *Eur Heart J Cardiovasc Imaging.* (2018). doi: 10.1093/eurheartj/ehy563.P4635
21. Westra J, Tu S, Winther S, Nissen L, Vestergaard MB, Andersen BK, et al. Evaluation of coronary artery stenosis by quantitative flow ratio during invasive coronary angiography: The WIFI II study (wire-free functional imaging II). *Circulation Cardiovascular Imaging.* (2018) 11:e007107. doi: 10.1161/CIRCIMAGING.117.007107
22. Tu S, Westra J, Yang J, von Birgelen C, Ferrara A, Pellicano M, et al. Diagnostic accuracy of fast computational approaches to derive fractional flow reserve from diagnostic coronary angiography: the international multicenter FAVOR pilot study. *JACC Cardiovascular Interventions.* (2016) 9:2024–35. doi: 10.1016/j.jcin.2016.07.013
23. Asano T, Katagiri Y, Collet C, Tenekecioglu E, Miyazaki Y, Sotomi Y, et al. Functional comparison between the BuMA Supreme biodegradable polymer sirolimus-eluting stent and a durable polymer zotarolimus-eluting coronary stent using quantitative flow ratio: PIONEER QFR substudy. *EuroIntervention.* (2018) 14:e570–e9. doi: 10.4244/EIJ-D-17-00461
24. Omori H, Witberg G, Kawase Y, Tanigaki T, Okamoto S, Hirata T, et al. Angiogram based fractional flow reserve in patients with dual/triple vessel coronary artery disease. *Int J Cardiol.* (2019) 283:17–22. doi: 10.1016/j.ijcard.2019.01.072
25. Kornowski R, Vaknin-Assa H, Assali A, Greenberg G, Valtzer O, Lavi I. Online angiography image-based FFR assessment during coronary catheterization: a single-center study. *J Invasive Cardiol.* (2018) 30:224–9.

Conflict of Interest: XL is employed by ArteryFlow Technology and receives grants from National Natural Science Foundation of China (No. 11802113). JH and YX was employed by ArteryFlow Technology. JX is the CEO of ArteryFlow Technology and receives grants from National Natural Science Foundation of China (No. 81771242).

The remaining authors declare that the research was conducted in the absence of any commercial or financial relationships that could be construed as a potential conflict of interest.

frontiers in Cardiovascular Medicine

ORIGINAL RESEARCH
published: 15 October 2021
doi: 10.3389/fcvm.2021.735743

Diagnostic Value of Angiography-Derived IMR for Coronary Microcirculation and Its Prognostic Implication After PCI

Neng Dai[1,2†], Wenliang Che[3†], Lu Liu[3†], Wen Zhang[3], Guoqing Yin[3], Bin Xu[3], Yawei Xu[3], Shaofeng Duan[4], Haojun Yu[5], Chenguang Li[1,2], Kang Yao[1,2], Dong Huang[1,2] and Junbo Ge[1,2]*

[1] Department of Cardiology, Shanghai Institute of Cardiovascular Diseases, Zhongshan Hospital, Fudan University, Shanghai, China, [2] National Clinical Research Center for Interventional Medicine, Shanghai, China, [3] Department of Cardiology, Shanghai Institute of Cardiovascular Diseases, Shanghai Tenth People's Hospital, Tongji University, Shanghai, China, [4] GE Healthcare China, Shanghai, China, [5] Department of Nuclear Medicine, Zhongshan Hospital, Fudan University, Shanghai, China

OPEN ACCESS

Edited by:
Sebastian Kelle,
Deutsches Herzzentrum
Berlin, Germany

Reviewed by:
Krishnaraj Sinhji Rathod,
Queen Mary University of London,
United Kingdom
Arnold Seto,
VA Long Beach Healthcare System,
United States

***Correspondence:**
Junbo Ge
jbge@zs-hospital.sh.cn

[†]These authors have contributed equally to this work

Specialty section:
This article was submitted to Cardiovascular Imaging, a section of the journal Frontiers in Cardiovascular Medicine

Received: 03 July 2021
Accepted: 10 September 2021
Published: 15 October 2021

Citation:
Dai N, Che W, Liu L, Zhang W, Yin G, Xu B, Xu Y, Duan S, Yu H, Li C, Yao K, Huang D and Ge J (2021) Diagnostic Value of Angiography-Derived IMR for Coronary Microcirculation and Its Prognostic Implication After PCI. Front. Cardiovasc. Med. 8:735743. doi: 10.3389/fcvm.2021.735743

Background: Angiography-derived index of microcirculatory resistance (angio-IMR) is an emerging pressure-wire-free index to assess coronary microvascular function, but its diagnostic and prognostic value remains to be elucidated.

Methods and Results: The study population consisted of three independent cohorts. The internal diagnostic cohort enrolled 53 patients with available hyperemic microcirculatory resistance (HMR) calculated from myocardial blood flow and pressure. The external diagnostic cohort included 35 ischemia and no obstructive coronary artery disease (INOCA) patients and 45 controls. The prognostic cohort included 138 coronary artery disease (CAD) patients who received PCI. Angio-IMR was calculated after the estimation of angiography-derived fractional flow reserve (angio-FFR) using the equation of angio-IMR = estimated hyperemic Pa × angio-FFR × [vessel length/(K × $V_{diastole}$)]. The primary outcome was a composite of cardiac death or readmission due to heart failure at 28 months after index procedure. Angio-IMR demonstrated a moderate correlation with HMR (R = 0.74, $p < 0.001$) and its diagnostic accuracy, sensitivity, specificity, and area under the curve to diagnose INOCA were 79.8, 83.1, 78.0, and 0.84, respectively, with a best cut-off of 25.1. Among prognostic cohort, patients with angio-IMR ≥25.1 showed a significantly higher risk of cardiac death or readmission due to heart failure than those with an angio-IMR <25.1 (18.6 vs. 5.4%, adjusted HR 9.66, 95% CI 2.04–45.65, $p = 0.004$). Angio-IMR ≥25.1 was an independent predictor for cardiac death or readmission due to heart failure (HR 11.15, 95% CI 1.76–70.42, $p = 0.010$).

Conclusions: Angio-IMR showed a moderate correlation with HMR and high accuracy to predict microcirculatory dysfunction. Angio-IMR measured after PCI predicts the risk of cardiac death or readmission due to heart failure in patients with CAD.

Clinical Trial Registration: Diagnostic and Prognostic Value of Angiography-derived IMR (CHART-MiCro), NCT04825028.

Keywords: coronary microcirculation, index of microcirculatory resistance, prognosis, INOCA, functional angiography

INTRODUCTION

Percutaneous coronary intervention (PCI) is one of the important treatments for coronary artery disease (CAD) and aims to increase myocardial blood flow (MBF). However, it has been reported that 20–60% of patients still experience recurrent angina after PCI (1), which was partly attributed to microcirculatory dysfunction. Several studies have shown that microvascular dysfunction is an important factor that is related with adverse outcomes in CAD patients. The first step to the successful management of such condition is early identification and diagnosis. Although non-invasive imaging modalities including positron emission tomography and cardiac magnetic resonance were optimal for microcirculatory dysfunction assessment, they are not available at the cardiac catheterization laboratory during PCI. Invasive assessments, such as the index of microcirculatory resistance (IMR) and hyperemic microvascular resistance (HMR), have been validated as good indices (2, 3) for the quantitative measurement of coronary microcirculatory dysfunction. However, additional procedural time/complexity, increased procedural cost, and the need for maximal hyperemia may prohibit their usage in clinical practice.

With the technical development, angiographic derivation of fractional flow reserve (FFR) or IMR (angio-IMR), which does not require pressure wire, hyperemic agents, or theromdilution method, is proposed recently as a potential alternative for pressure wire–derived FFR or IMR (4, 5).

In this regard, our study aimed to evaluate the diagnostic performance of angio-IMR for microcirculatory dysfunction and its prognostic implication after PCI in stable CAD.

METHODS

Study Population

The study population was composed of three independent cohorts (**Figure 1**). Patients in the internal diagnostic cohort were selected from Zhongshan Hospital, which consisted of 53 consecutive patients with available cadmium–zinc–telluride single-photon emission computed tomography (CZT-SPECT) within 7 days of FFR measurement in the left anterior descending coronary artery. External diagnostic cohort–enrolled patients received CZT-SPECT and invasive angiography examinations for conventional clinical practice from Shanghai Tenth People's Hospital, whose results were previously published (6). Among this cohort, 35 patients with ischemia and no obstructive coronary artery disease (INOCA) were included; 45 patients with no obstructive CAD and normal CZT-SPECT perfusion imaging were regarded as normal controls, while vessels with normal corresponding perfusion territory in INOCA patients were regarded as internal controls. The prognostic cohort included 138 consecutive CAD patients who received PCI with available angiograms and who were suitable for angiography-derived FFR (angio-FFR) and angio-IMR measurements. The primary clinical outcome was cardiac death or readmission due to heart failure at a median of 28 months after the index procedure.

The institutional review board or ethics committee at each participating center approved the current study protocol, which was in accordance with the Declaration of Helsinki. In addition, written informed consent was obtained from all participants.

CZT- SPECT Perfusion Imaging and Analysis

CZT-SPECT perfusion imaging was performed using a dedicated cardiac scanner (Spectrum Dynamics, Caesarea, Israel). The single-day rest/stress imaging protocol was applied as described before (7).

In the internal diagnostic cohort, full scanning was conducted after establishing the scanning region of interest (ROI). For stress imaging, adenosine triphosphate (ATP) disodium was intravenously administrated at a rate of 140 $\mu g \cdot kg^{-1} \cdot min^{-1}$ for 5 min to induce pharmacological stress, followed by dynamic image acquisition. Rest and stress dynamic images were reconstructed into 32 time frames (21×3, 1×9, 1×15, 1×21, 1×27, and 7×30 s) for dynamic perfusion analysis. Using the previously established Renkin–Crone equation for ^{99m}Tc-sestamibi (MIBI), the MBF can be extrapolated from time–activity curves by inputting uptake rate K1 (8). The global myocardial ROI was divided into three regional ROIs corresponding to coronary territories of the left anterior descending coronary artery, right coronary artery, and left circumflex coronary artery, respectively, and the regional MBF was extrapolated for each coronary territory.

In the external diagnostic cohort, visual assessment for the stress and rest perfusion images was performed using the 17-segment model of the left ventricle and a five-point scale (0 = normal, 1 = equivocal, 2 = moderate, 3 = severe reduction of radioisotope uptake, 4 = absence of detectable radiotracer activity in a segment) (9). The summed stress score (SSS) and summed rest score (SRS) are the sum of all defects on the stress and rest image, respectively. The summed difference score (SDS) is defined as the difference between SRS and SSS. Myocardial ischemia in individual coronary territories was defined when the SSS was $\geq$4 and SDS was $\geq$2 (10).

Two experienced nuclear physicians who were blinded to the clinical data and angiography or wire-derived physiologic indices analyzed the images using Corridor 4DM software (INVIA, Ann Arbor, MI, USA) and QPS software (Cedars-Sinai Medical Center, Los Angeles, CA, USA).

Coronary Angiography

Coronary angiography was performed with standard techniques. All angiograms from the internal and the external diagnostic cohorts were recorded at 15 frames per second and analyzed at core laboratory (Zhongshan Hospital, Fudan University, Shanghai Institute of Cardiovascular Diseases, Shanghai, China) in a blinded fashion. Anatomical parameters including minimal lumen diameter, reference vessel size, lesion length, and percent

Abbreviations: Angio-IMR, angiography-derived index of microcirculatory resistance; Angio-FFR, angiography-derived fractional flow reserve; CAD, coronary artery disease; CZT-SPECT, cadmium–zinc–telluride single-photon emission computed tomography; FFR, fractional flow reserve; HMR, hyperemic microvascular resistance; MBF, myocardial blood flow; IMR, index of microcirculatory resistance; INOCA, ischemia and no obstructive coronary artery disease; PCI, percutaneous coronary intervention.

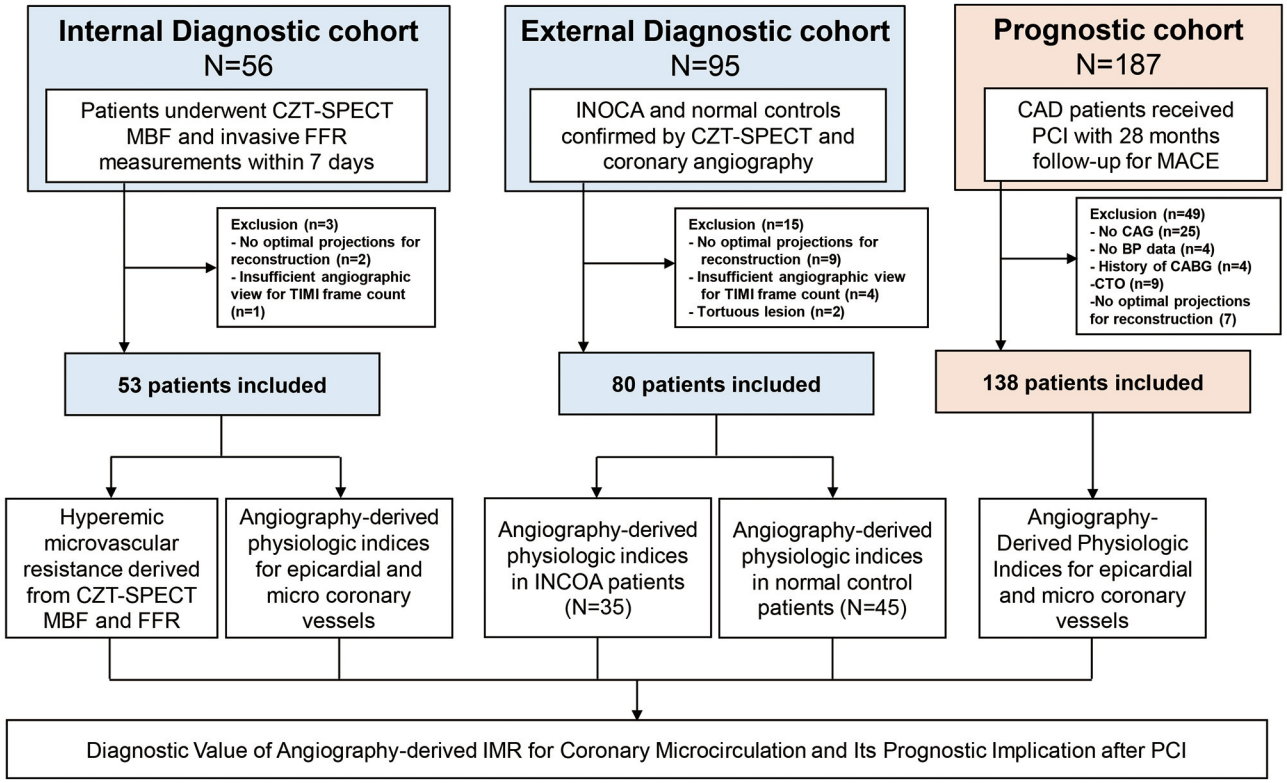

FIGURE 1 | Study flow. The study population was composed of internal and external diagnostic cohorts and prognostic cohort. Internal diagnostic cohort was used to evaluate the correlation between angio-IMR and HMR; external diagnostic cohort was used to evaluate the diagnostic performance of angio-IMR to diagnose INOCA. Prognostic cohort was used to evaluate the prognostic implication of angio-IMR in CAD patients after PCI. Angio-IMR, angiography-derived index of microcirculatory resistance; CAD, coronary artery disease; HMR, hyperemic microcirculatory resistance; INOCA, ischemia and no obstructive coronary artery disease; PCI, percutaneous coronary intervention.

diameter stenosis were analyzed, on the basis of quantitative coronary angiography (QCA) using the QAngio XA software package (Medis Medical Imaging Systems, Leiden, Netherlands).

Coronary Physiological Measurements and Calculations

Five thousand international units of intravenous heparin and intracoronary nitroglycerin were administrated before invasive FFR measurements. A 0.014-in. coronary pressure wire (Pressure Wire X; Abbott Vascular, Santa Clara, CA, United States) equipped with pressure sensor was advanced to the distal segment of a target vessel after equalization. Maximal hyperemia was induced through intravenous ATP (140 $\mu g \cdot kg^{-1} \cdot min^{-1}$) administration. After measurements, the pressure wire was pulled back to the guide catheter to identify possible pressure drift. FFR was calculated as the mean distal coronary pressure (Pd) divided by the mean aortic pressure (Pa) during maximal hyperemia. FFR $\leq$0.8 was considered positive for ischemia.

HMR was calculated as the ratio of hyperemic Pd to hyperemic MBF (**Figure 2**) (11). The rate–pressure products did not differ significantly at the time point of CZT-SPECT and invasive FFR assessments (8,926.2 vs. 8,784.7 mmHg·bpm; $p = 0.375$), demonstrating no myocardial oxygen demand change over the gap between two examinations.

Angio-Derived FFR and IMR Measurements

The angio-IMR measurement was conducted as described before using commercialized software (FlashAngio, Rainmed Ltd., Suzhou, China) (12). In brief, a three-dimensional reconstruction of coronary arteries was firstly conducted for the target vessels, followed by the estimation of angio-FFR by computational pressure–flow dynamics with a validated method (5); the estimated hyperemic Pa (Pa_{hyp}) was assumed by mean arterial pressure (MAP) during the index procedure–MAP$\times$0.2 when MAP $\geq$95 mmHg or MAP-MAP $\times$ 0.15 when MAP $<$95 mmHg (5).

Thus, angio-IMR was calculated as

$$Angio - IMR = Pd_{hyp} \frac{L}{kV_{diastole}}$$

where L represents the length from the inlet to the distal position, Pd_{hyp} is the mean pressure (unit: mmHg) at the distal position at the maximal hyperemia, which is computed by the FlashAngio software as the product of Pa_{hyp} and angio-FFR, $V_{diastole}$ is the mean flow velocity (unit: mm/s) at the distal position at

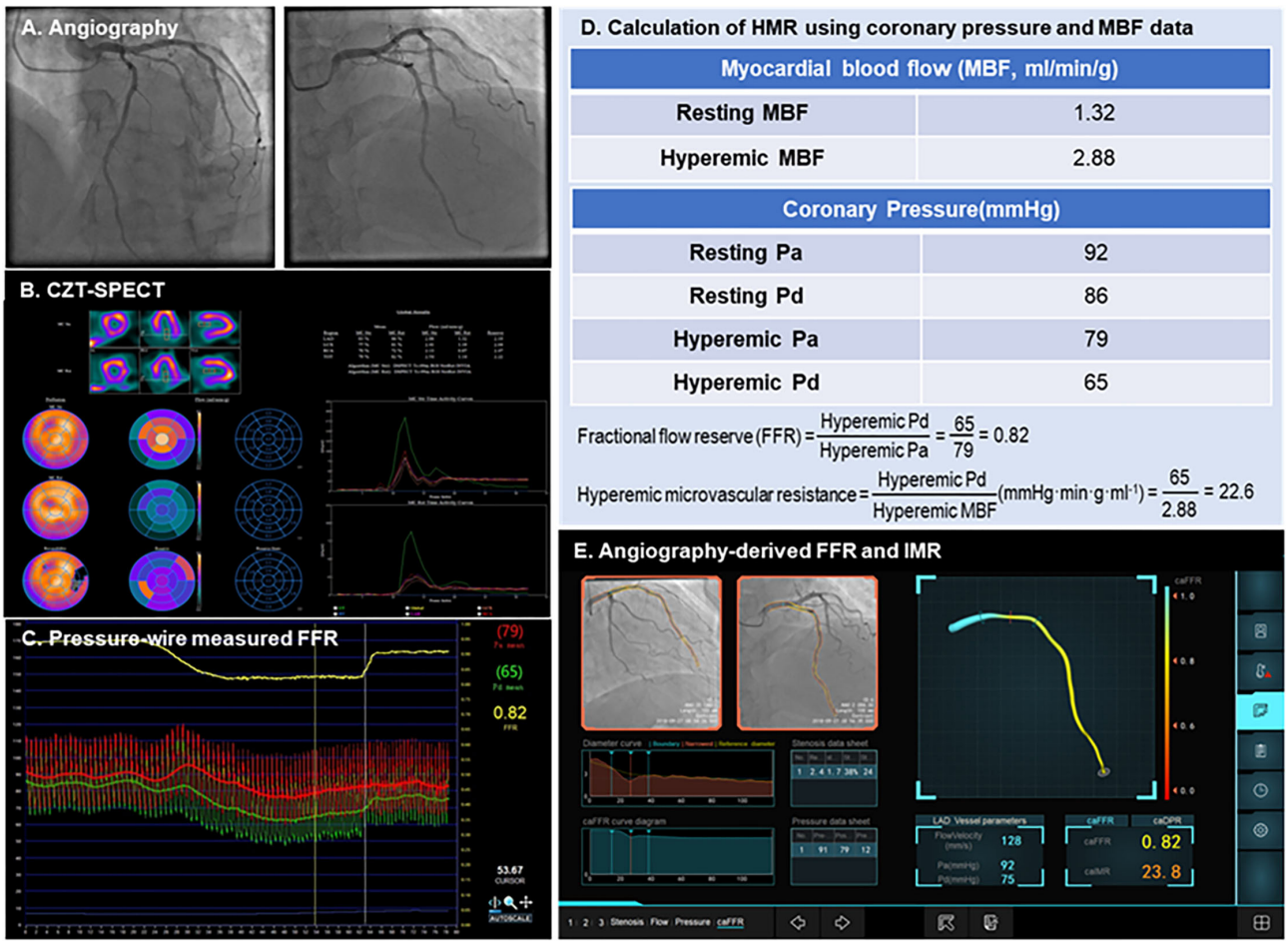

FIGURE 2 | Case examples of angiography-derived physiologic indices. A representative case of CZT-SPECT MBF, pressure wire FFR, and angio-IMR measurements, as well as how HMR are calculated from MBF and coronary pressure, are shown. **(A)** Coronary angiography; **(B)** CZT-SPECT MBF; **(C)** Pressure wire–measured FFR; **(D)** Calculation of HMR using coronary pressure and MBF data; **(E)** Angiography-derived FFR and IMR. CZT-SPECT, cadmium–zinc–telluride single-photon emission computed tomography; FFR, fractional flow reserve; HMR, hyperemic microcirculatory resistance; IMR, index of microcirculatory resistance; MBF, myocardial blood flow.

diastole, and K is a constant (K = 2.1) obtained from a previous literature (13).

The analysis of angio-IMR was performed by an independent core laboratory (Zhongshan Hospital, Fudan University, Shanghai Institute of Cardiovascular Diseases, Shanghai, China) in a blinded fashion for clinical data, CZT-SPECT, and wire-derived physiologic indices.

Data Collection, Follow-Up, and Outcomes

Demographic data and cardiovascular risk factors were retrospectively collected. Outpatient visits or telephone contacts were performed every 2 months. The median follow-up duration of the prognostic cohort was 28 months (Q1–Q3 10.3–36.0).

The primary outcome of the prognostic cohort was major adverse cardiac events (MACE) including cardiac death and readmission due to heart failure. All clinical outcomes were defined according to the Academic Research Consortium report (14). The secondary outcomes were a composite of cardiac death, readmission due to heart failure and angina, a composite of cardiac death, readmission due to heart failure, spontaneous myocardial infarction (MI), target vessel revascularization and readmission due to angina, and the individual components of these adverse outcomes. Cardiovascular death was defined as death due to myocardial infarction, significant cardiac arrhythmia, refractory heart failure, or cardiogenic shock. Readmission due to heart failure was defined as hospitalization due to new or worsening signs and symptoms of heart failure in conjunction with non-invasive imaging finding or increased N-terminal pro B-type natriuretic peptide concentrations and a discharge diagnosis of congestive heart failure. Readmission due to angina was defined according to the Braunwald Unstable Angina Classification and the Canadian Cardiovascular Society Angina Classification. Spontaneous MI was defined as an elevation of creatine kinase–myocardial band or a troponin level greater than the upper limit of normal with concomitant ischemic symptoms or electrocardiography findings indicative of ischemia

(15). Ischemia-driven target vessel revascularization was defined as a revascularization procedure with at least one of the following: (1) recurrence of angina; (2) positive non-invasive test; and (3) positive invasive physiological test. All events were adjudicated by an expert of interventional cardiology in a blinded fashion.

Statistical Analysis

Categorical variables are presented as numbers and relative frequencies (percentages); continuous variables are presented either as mean ± SD or median with interquartile range (IQR) according to their distributions, which were checked by using the Kolmogorov–Smirnov and Levene tests. In the internal diagnostic cohort, correlation coefficients were calculated to assess the relationship between angio-FFR and FFR or between angio-IMR and HMR (Pearson or Spearman according to the normality).

In the external diagnostic cohort, the diagnostic performances (including sensitivity, specificity, positive predictive value, negative predictive value, diagnostic accuracy, positive likelihood ratio, and negative likelihood ratio) of angio-IMR to predict INOCA were assessed. The area under curve (AUC) in the receiver-operator characteristic (ROC) curve was calculated for angio-IMR, and the optimal cutoff value of angio-IMR to predict INOCA was calculated to maximize the product of sensitivity and specificity using ROC curves. Intra-individual variability was assessed by two repeated measurements of angio-IMR and angio-FFR with time interval.

In the prognostic cohort, the cumulative incidence of clinical events was presented as Kaplan–Meier estimate and compared using a log-rank test. Multivariable Cox proportional hazard regression was used to calculate the adjusted hazard ratio (HR) and 95% confidence interval (CI) to compare the risk of clinical events according to angio-IMR. The adjusted covariables were age, sex, left ventricular ejection fraction (LVEF), and post-PCI angio-FFR values. The assumption of proportionality was assessed graphically by log-minus-log plot, and the Cox proportional hazard models for all clinical outcomes satisfied the proportional hazards assumption. The best cut-off value of angio-IMR to predict the risk of cardiac death or readmission due to heart failure was evaluated by the maximally selected log-rank statistics method. Independent predictors for cardiac death or readmission due to heart failure were evaluated by the multivariable Cox proportional hazard regression model, and the discriminant function of predictive model was evaluated with Harrell's c-statistics with 95% CI. The additive prognostic implications of angio-IMR into the model with clinical risk factors were evaluated by assessing improvement in the discriminant and reclassification ability of the models with angio-IMR compared with a reference model with clinical risk factors (age, sex, diabetes, hyperlipidemia, hypertension, LVEF, and post-PCI angio-FFR values), using the category-free net reclassification index (NRI) and integrated discrimination improvement (IDI).

All probability values were two-sided, and p-values <0.05 were considered statistically significant. All statistical analyses were performed using R version 4.0.2 (R Foundation for Statistical Computing, Vienna, Austria) and SPSS 25.0 for Windows (SPSS-PC, Chicago, IL, USA).

RESULTS

Characteristics of Patients and Lesions in Internal and External Diagnostic Cohort

Figure 1 shows the study flow. Patient and lesion characteristics of internal and external diagnostic cohorts were shown in **Supplementary Table 1**. In the internal diagnostic cohort, the mean age was 63.5 ± 9.4 and 90.6% were male. The mean angio-FFR in this cohort was 0.84 ± 0.06, and the mean angio-IMR was 24.7 ± 3.2. The pressure wire–measured FFR was 0.81 ± 0.06, and the CZT-SPECT-measured hyperemic MBF was 1.94 ± 0.43, leading to a mean calculated HMR of 40.29 ± 10.94.

In the external diagnostic cohort (**Supplementary Table 2**), the median SSS and SDS were 4 ± 2 and 3 ± 2, respectively, in INOCA patients. The mean angio-FFR and angio-IMR were 0.94 ± 0.03 and 35.83 ± 13.35 in INOCA patients and 0.93 ± 0.03 and 23.7 ± 9.0 in normal controls.

Diagnostic Performance of Angio-IMR

Figure 2 shows a case example whose CZT-SPECT MBF was measured within 7 days of pressure wire FFR measurement and summarizes how HMR was calculated from coronary pressures and absolute MBF and how angio-IMR was calculated from an angiogram.

As shown in **Figure 3**, there were significant correlations of angio-FFR with FFR ($R = 0.84$, $p < 0.001$) and angio-IMR with HMR ($R = 0.74$, $p < 0.001$) and two repeated measures of angio-FFR ($R = 0.99$, $p < 0.001$) and angio-IMR ($R = 0.92$, $p < 0.001$) were significantly correlated and nearly the same without significant differences (the differences between two angio-FFR and angio-IMR measurements were 0.002 ± 0.014 and 0.258 ± 2.141, respectively) (**Supplementary Figure 1**).

The angio-IMR in vessels with abnormal corresponding perfusion territory in INOCA patients was significantly higher than that in the normal corresponding perfusion territory (35.8 ± 13.3 vs. 22.0 ± 7.8, $p < 0.001$) in INOCA patients, as well as that in normal controls (35.8 ± 13.3 vs. 23.2 ± 7.3, $p < 0.001$). ROC analysis demonstrated that angio-IMR had a cut-off value of 25.1 to predict patients with microcirculatory dysfunction represented by normal coronary angiogram but abnormal CZT-SPECT perfusion imaging and showed an AUC of 0.839 (95% CI 0.781–0.898). Sensitivity, specificity, positive predictive value, negative predictive value, and the diagnostic accuracy of angio-IMR were 83.1, 78.0, 67.5, 89.3, and 79.8%, respectively (**Figure 4**).

Characteristics of Patients and Lesions in Prognostic Cohort

Table 1 shows patient and lesion characteristics of the prognostic cohort. Mean age was 65.0 ± 8.7, and 96 of the 138 included patients were male. Among these patients, the left anterior descending artery was the most frequent vessel that received PCI. Forty-five (32.6%) patients showed significant microcirculatory dysfunction by angio-IMR ≥25.1. There were no significant differences between angio-IMR <25.1 vs. ≥25.1 regarding patient, lesion, procedural characteristics, and discharge medications.

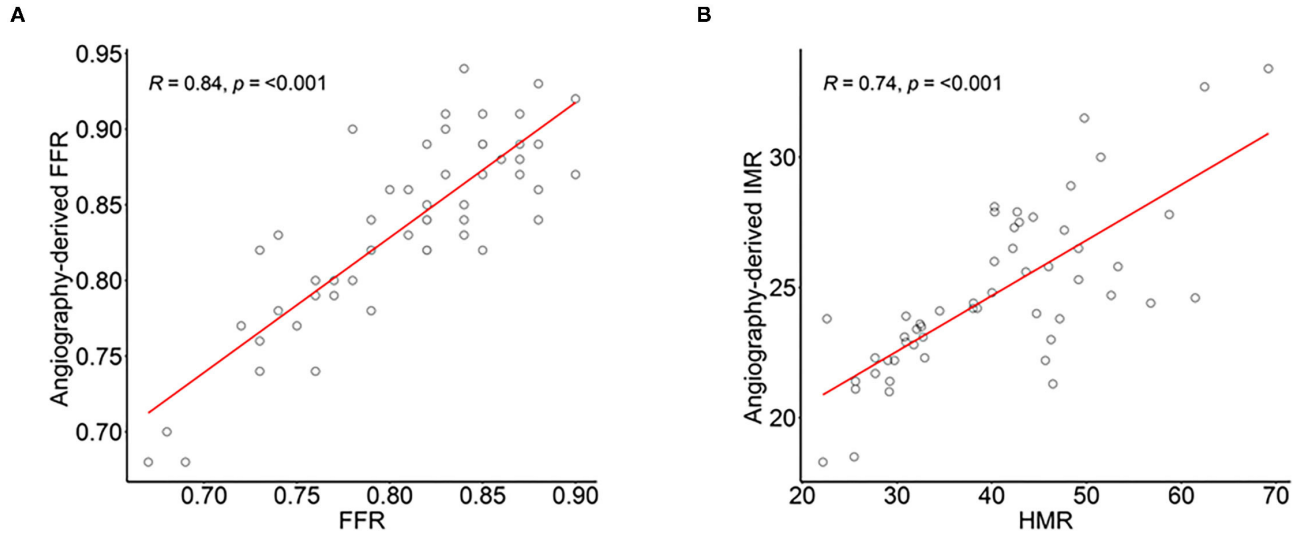

FIGURE 3 | Correlation of angiography-derived FFR with invasive FFR and angiography-derived IMR and HMR in diagnostic cohort. The correlation and agreement between **(A)** angio-FFR and pressure wire–derived FFR, and **(B)** angio-IMR and coronary pressure and myocardial blood flow calculated HMR. Abbreviations are listed in **Figures 1**, **2**.

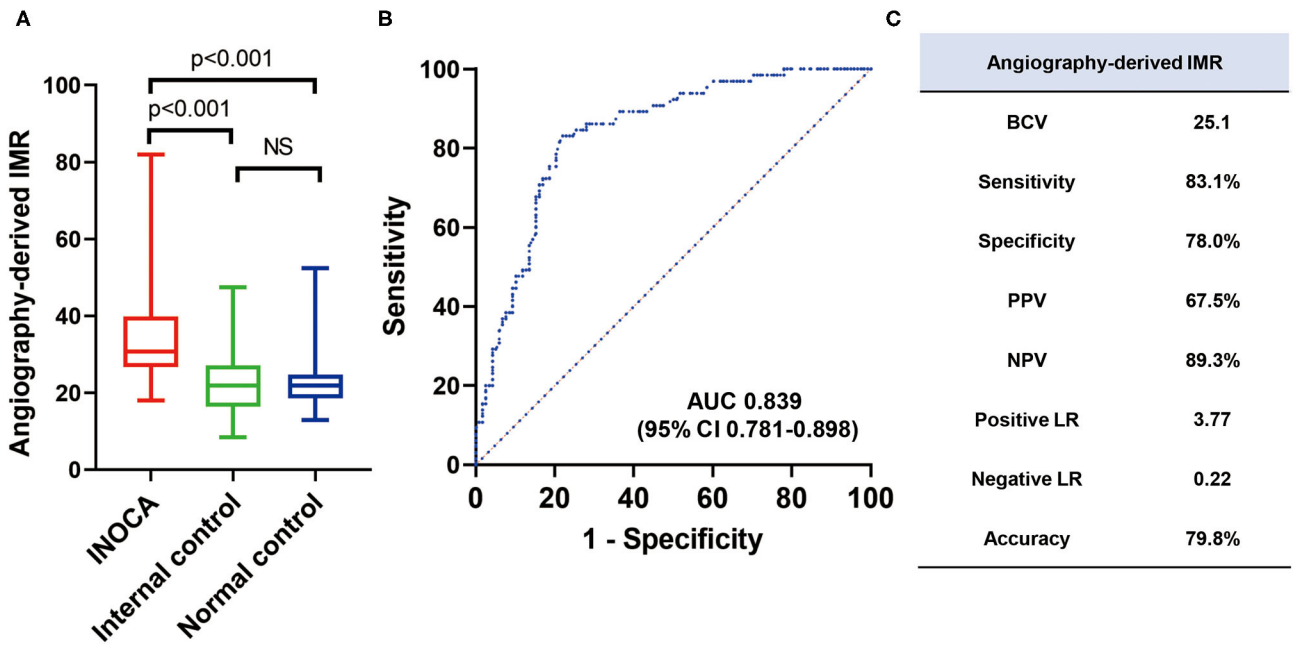

Angiography-derived IMR	
BCV	25.1
Sensitivity	83.1%
Specificity	78.0%
PPV	67.5%
NPV	89.3%
Positive LR	3.77
Negative LR	0.22
Accuracy	79.8%

FIGURE 4 | Diagnostic accuracy of angiography-derived IMR to diagnose INOCA in external validation cohort. **(A)** Mean angio-IMR values in vessels with abnormal (INOCA) and normal (internal controls) corresponding CZT-SPECT perfusion territory among INOCA patients and in vessels among patients with normal CZT-SPECT perfusion imaging and angiography (normal controls); **(B)** ROC of angio-IMR to diagnose INOCA and **(C)** diagnostic performances of angio-IMR to diagnose INOCA are shown. AUC, area under curve; BCV, best cut-off value; LR, likelihood ratio; NPV, negative predictive value; PPV, positive predictive value; others are with **Figure 1**.

Prognostic Implication of Angio-IMR in CAD Patients Received PCI

During a median of 28-month follow-up after index procedure, patients with angio-IMR ≥25.1 demonstrated a significantly higher incidence of cardiac death or readmission due to heart failure than those with angio-IMR <25.1 (18.6 vs. 5.4%, adjusted HR 9.66, 95% CI 2.04–45.65, $p = 0.004$) (**Table 2** and **Figure 5**).

The significantly higher risk of cardiac death or readmission due to heart failure in the angio-IMR ≥25.1 group was mainly

TABLE 1 | Patient and lesion characteristics of prognostic cohort.

	Total	Angiography-derived IMR <25.1	Angiography-derived IMR ≥25.1	*p*-values
Patients' characteristics	138	93 (67.4%)	45 (32.6%)	
Demographics				
Age (years)	65.0 ± 8.7	64.9 ± 9.0	65.2 ± 8.1	0.85
Male	96 (69.6%)	69 (74.2%)	27 (60.0%)	0.09
Body mass index (kg/m^2)	24.6 ± 3.0	24.5 ± 2.8	25.0 ± 3.3	0.36
Ejection fraction (%)	59.7 ± 9.0	60.0 ± 9.0	59.1 ± 9.2	0.59
Cardiovascular risk factors				
Hypertension	100 (72.5%)	68 (73.1%)	32 (71.1%)	0.81
Diabetes mellitus	50 (36.2%)	31 (33.3%)	19 (42.2%)	0.31
Hyperlipidemia	11 (8.0%)	8 (8.6%)	3 (6.7%)	0.70
Current smoker	36 (26.1%)	25 (26.9%)	11 (24.4%)	0.75
Previous percutaneous coronary intervention	56 (40.6%)	35 (37.6%)	21 (46.7%)	0.30
Multivessel disease	84 (60.9%)	57 (61.3%)	27 (60.0%)	0.88
SYNTAX score	19.3 ± 8.9	19.7 ± 8.8	19.1 ± 9.2	0.71
Hemodynamic parameters				
Systolic blood pressure (mmHg)	130.1 ± 19.2	129.1 ± 19.2	132.3 ± 17.9	0.35
Diastolic blood pressure (mmHg)	78.6 ± 12.6	77.8 ± 12.4	79.3 ± 12.2	0.50
Discharge medication				
Aspirin	138 (100.0%)	93 (100.0%)	45 (100.0%)	NA
$P2Y_{12}$ inhibitor	138 (100.0%)	93 (100.0%)	45 (100.0%)	NA
Beta-blocker	88 (63.8%)	59 (63.4%)	29 (64.4%)	0.91
RAAS blockade	75 (54.3%)	53 (57.0%)	22 (48.9%)	0.37
Statin	138 (100.0%)	93 (100.0%)	45 (100.0%)	NA
Lesion characteristics				
Target vessel				
LAD	171 (55.3%)	126 (56.0%)	45 (53.6%)	0.79
LCX	50 (16.2%)	32 (14.2%)	18 (21.4%)	0.29
RCA	88 (28.5%)	67 (29.8%)	21 (25.0%)	0.56
Procedural characteristics				
Pre-PCI diameter stenosis	76.8 ± 9.7	77.2 ± 8.9	76.4 ± 10.0	0.64
Pre-PCI lesion length	26.7 ± 10.9	27.9 ± 10.2	26.0 ± 12.3	0.34
Post-PCI diameter stenosis	3.1 ± 9.3	2.8 ± 7.7	3.2 ± 9.6	0.79
Total number of stents	1.3 ± 1.0	1.3 ± 1.0	1.1 ± 0.9	0.26
Mean stent diameter	3.0 ± 0.4	3.0 ± 0.4	3.1 ± 0.3	0.14
Total length of stents	40.9 ± 24.6	42.5 ± 25.7	37.1 ± 21.9	0.23
Angiography-derived Physiologic Indices				
Angiography-derived FFR, Post-PCI	0.91 ± 0.06	0.89 ± 0.06	0.94 ± 0.03	<0.001
Angiography-derived IMR, U	22.8 ± 10.1	17.1 ± 4.2	34.4 ± 9.0	<0.001

Values are mean ± standard deviations or n (%).
FFR, fractional flow reserve; IMR, index of microcirculatory resistance; LAD, left anterior descending artery; LCX, left circumflex artery; PCI, percutaneous coronary intervention; RAAS, renin–angiotensin–aldosterone system; RCA, right coronary artery.

due to increased risk of readmission due to heart failure than the angio-IMR<25.1 group; in addition, a higher risk of readmission due to angina was observed in patients with IMR ≥25.1, while the risk of cardiac death, MI, and ischemia-driven revascularization was similar between the two groups (**Table 2**). In a multivariable model, angio-IMR ≥25.1 was an independent predictor for cardiac death or readmission due to heart failure (HR 11.15, 95% CI 1.76–70.42, $p = 0.010$) (**Table 3**). As for the discriminant ability for cardiac death or readmission due to heart failure, angio-IMR did not increase discriminant and reclassification indices when added to the model with clinical risk factors, while for the outcomes of cardiac death or readmission due to heart failure and angina, angio-IMR increased the discriminant ability (AUC 0.71 vs. 0.53, $p = 0.002$; IDI 0.16, $p = 0.01$; category-free NRI 0.46, $p = 0.010$) (**Supplementary Figure 2**).

The best cut-off value of angio-IMR to predict the risk of cardiac death or readmission due to heart failure was 27.3 (**Supplementary Figure 3**). When we apply 27.3 as the cut-off to define microcirculatory dysfunction, our primary result of cardiac death or readmission due to heart failure remains unchanged (**Supplementary Figure 4**).

TABLE 2 | Clinical outcomes at 28 months after index procedure according to angiography-derived IMR.

	Angiography-derived IMR < 25.1 (*N* = 93)	Angiography-derived IMR ≥ 25.1 (*N* = 45)	Univariable HR (95% CI)	Multivariable HR (95% CI)*	*p*-value
Cardiac death or readmission due to heart failure	5 (5.4%)	8 (18.6%)	5.24 (1.69–16.19)	9.66 (2.04–45.65)	0.004
Cardiac death	1 (1.1%)	2 (4.4%)	7.58 (0.67–86.23)	7.26 (0.55–95.57)	0.13
Readmission due to heart failure	6 (6.5%)	7 (15.6%)	4.28 (1.35–13.62)	5.93 (1.37–25.77)	0.02
Myocardial infarction	2 (2.2%)	2 (4.4%)	3.49 (0.48–25.65)	5.80 (0.49–68.99)	0.16
Ischemia-driven revascularization	7 (7.5%)	6 (13.3%)	2.46 (0.82–7.41)	3.20 (0.86–11.96)	0.08
Readmission due to angina	18 (19.4%)	21 (46.7%)	3.19 (1.61–6.29)	3.66 (1.68–7.97)	0.001

The cumulative incidences of clinical outcomes are presented as event number and Kaplan–Meier estimates at 28 months after index procedure. p values were log-rank p value in survival analysis.

**Covariables which were included in the multivariable adjusted Cox regression model were age, sex, left ventricular ejection fraction, and post-PCI angiography-derived FFR.*

CI, confidence intervals; HR, hazard ratios; others as in ***Table 1****.*

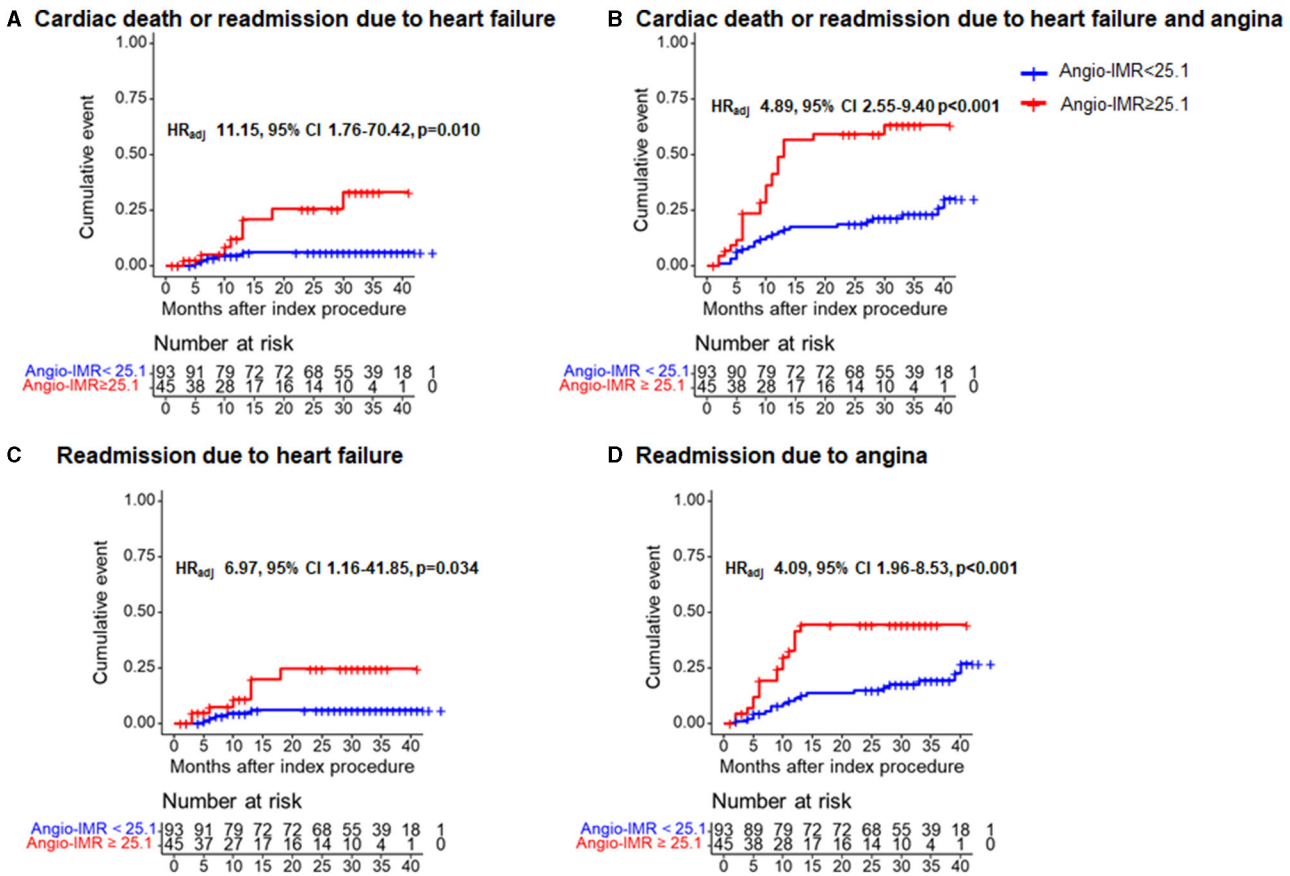

FIGURE 5 | Comparison of primary and secondary outcomes at 28 months after index procedure according to angiography-derived IMR. Cumulative incidences of cardiac death or readmission due to **(A)** heart failure; **(B)** cardiac death or readmission due to heart failure and angina; **(C)** readmission due to heart failure; and **(D)** readmission due to angina at 28 months are presented according to the best cut-off value of angio-IMR. CI, confidence intervals; HR_{adj}, multivariable adjusted hazard ratios; others are with **Figure 1**.

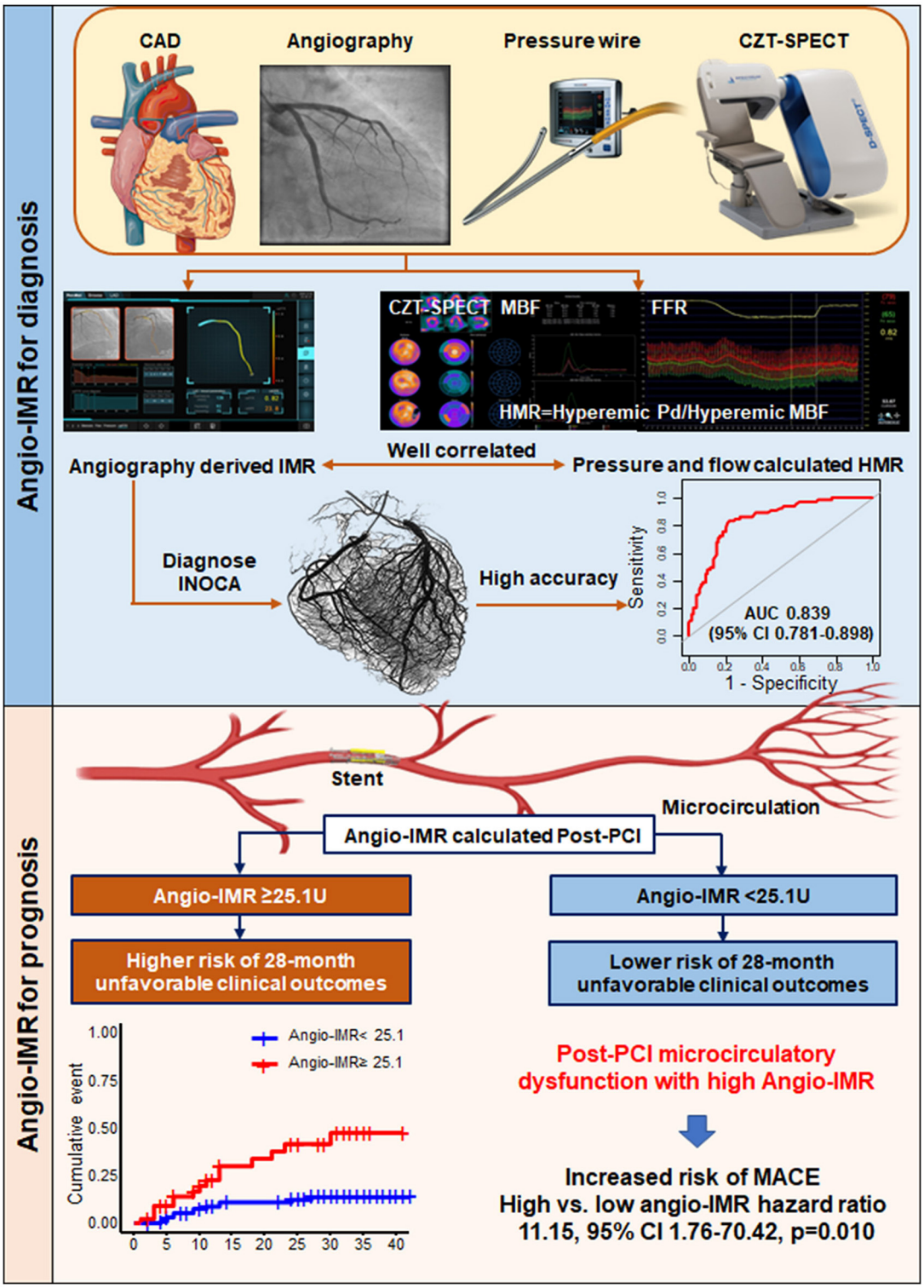

FIGURE 6 | Diagnostic Value of Angiography-derived Index of Microcirculatory Resistance for Coronary Microcirculation and Its Prognostic Implication after PCI in CAD Patients. The current study evaluated diagnostic and prognostic implications of angiography-derived IMR. In diagnostic cohorts, angio-IMR showed a close correlation with HMR calculated as the ratio of hyperemic coronary pressure to myocardial blood flow, and a high diagnostic accuracy to predict patients with microcirculatory dysfunction. In prognostic cohort, patients with post-PCI impaired microcirculatory function assessed by angio-IMR ≥ 25.1U showed significantly higher risk of cardiac death or readmission due to heart failure than those with preserved microcirculatory function assessed by angio-IMR < 25.1U. Angio-IMR ≥ 25.1U was independently associated with the occurrence of cardiac death or readmission due to heart failure. MACE, major adverse cardiac events; others are with **Figures 1**, **2**.

TABLE 3 | Independent predictors for cardiac death or readmission due to heart failure.

Variable	Univariable analysis		Multivariable analysis	
	HR (95% CI)	*p*-value	HR (95% CI)	*p*-value
Angio-IMR ≥25.1	5.00 (1.62–15.45)	0.005	11.15 (1.76–70.42)	0.01
Age (per 10 years)	1.01 (0.95–1.08)	0.69	1.08 (0.98–1.20)	0.14
Female	2.50 (0.56–11.29)	0.23	1.93 (0.29–13.07)	0.50
Diabetes mellitus	2.11 (0.71–6.27)	0.18	2.47 (0.65–9.38)	0.19
Hyperlipidemia	2.20 (0.49–9.93)	0.31	6.78 (0.90–51.35)	0.06
Hypertension	2.17 (0.48–9.77)	0.32	0.74 (0.09–6.01)	0.78
Left ventricular ejection fraction (per 10% increase)	0.86 (0.81–0.90)	<0.001	0.84 (0.79–0.90)	<0.001
Post-PCI angio-FFR in culprit vessel ≤0.80	0.30 (0.07–1.36)	0.12	0.25 (0.02–3.11)	0.28

*Abbreviations as in **Tables 1**, **2**.*

DISCUSSION

The current study evaluated the diagnostic and prognostic implications of angio-IMR in CAD patients (**Figure 6**). Our main findings are as follows. First, angio-IMR showed a moderate correlation with HMR derived from coronary pressure and MBF data; second, angio-IMR showed a high diagnostic accuracy for microcirculatory dysfunction determined by normal coronary angiography and perfusion defect by CZT-SPECT; and third, patients with post-PCI angio-IMR ≥25.1 showed a significantly higher risk of cardiac death or readmission due to heart failure than those with angio-IMR <25.

Post-PCI Microcirculatory Dysfunction in Patients With Stable CAD

Since the first PCI performed in 1977, it has been aimed to restore blood flow by relieving obstruction to the epicardial vessels. However, post-PCI angina and/or ischemia may recur or persist in a significant patient subset (16), with reported rates ranging from 15% to more than 50% (17, 18). As demonstrated in our study, 108 (78.3%) patients achieved post-PCI angio-FFR over 0.90, while there were 45 (32.6%) patients who demonstrated microcirculatory dysfunction with high angio-IMR. These findings have also been confirmed in other studies that adopted modern therapeutic strategies (19). Most importantly, symptom and/or ischemia recurrence is associated with adverse cardiovascular events (20). Accordingly, the current European Society of Cardiology guidelines on stable CAD have emphasized the importance of coronary vascular dysfunction in causing angina post-PCI (21).

Assessment of Microvascular Disease Using Angiography-Derived IMR as an Alternative to Wire-Derived IMR

The rationale for identifying microvascular dysfunction is to provide a definitive diagnosis; then, a possible treatment may be anticipated (22). Positron emission tomography remains the reference standard for assessing myocardial blood flow (23). Unfortunately, most patients who present to the cardiac catheterization laboratory did not evaluate their microcirculation. Angiographic techniques have their limitations considering the qualitative and subjective nature. Doppler wire–derived coronary flow reserve has been applied in research studies, but its clinical role has been limited by the technical issues.

IMR is a quantitative method for specifically assessing the microvascular function of the interrogated vessel (2). The emerging data demonstrate its role in evaluating patients with chest pain and non-obstructive coronary artery disease, as well as in predicting adverse events. However, it is hampered by the need of extra care to ensure maximal hyperemia (drug type, dose, infusion route, contraindication for drug, etc.) and continuous infusion of intravenous adenosine may raise potential safety concerns. HMR is also a quantitative index for microcirculatory dysfunction; however, measuring HMR is probably more challenging than measuring IMR, with higher failure rates related to the contemporary measurement of myocardial blood flow and coronary pressure. For these reasons, there is a need for an invasive technique to rapidly, reliably, and relatively easily assess for microcirculatory dysfunction in the cardiac catheterization laboratory.

With the technical development, angiographic derivation of IMR without pressure wire, hyperemic agents, or thermodilution method is available as a potential alternative for pressure wire–derived IMR. In the internal diagnostic cohort of our study, our analysis demonstrated that angio-IMR had a significant correlation with HMR ($R = 0.74$, $P < 0.001$). Furthermore, in the external diagnostic cohort, angio-IMR demonstrated a good diagnostic accuracy for microvascular disease with an AUC of 0.839 and a diagnostic accuracy of 79.8%. With no additional angiogram imaging acquisition or need for a hyperemic agent, angio-IMR may represent a promising measure as an alternative to wire-derived IMR and potentially increase the adoption of the physiological assessment of microvascular diseases in the cardiac catheterization lab.

Prognostic Implication of Microcirculatory Dysfunction in Patients Received PCI

Microvascular disease has been confirmed to be associated with a higher risk of cardiovascular events in patients without

obstructive epicardial stenosis (24, 25). In our study, the prognostic implication of angio-IMR in patients after PCI was evaluated. Increased angio-IMR was significantly associated with the higher risk of cardiac death or readmission due to heart failure and incidence of angina. In multivariable analysis, increased angio-IMR ≥25.1 remained as an independent predictor for cardiac death or readmission due to heart failure. These results are in line with the previous studies. Studies by Fearon et al. and Carrick et al. have shown that high IMR after primary percutaneous coronary intervention predicts adverse clinical outcomes in patients with myocardial infarction (26, 27). A recent study indicated that IMR measured immediately after PCI predicts adverse events in patients with stable CAD (28).

Our study provided a simple and convenient quantitative index to assess patients' microcirculatory status at the time of PCI. Further research is needed to assess whether angio-IMR-guided strategies might improve prognosis in patients with microcirculation dysfunction compared with standard care.

LIMITATIONS

There are some limitations that should be considered. First, because of the comprehensive study protocol, the number of patients included in our study was limited; our findings need to be verified in other cohorts with a larger sample size. Second, as a retrospective study, our included patients did not receive IMR assessment, which is a "gold standard" for microvascular dysfunction; third, though we observed a moderate correlation between angio-IMR and HMR, no definite normal range for HMR was reported yet. As a complementary, we investigated the diagnostic performance of angio-IMR in INOCA patients and angio-IMR showed a high accuracy for predicting microcirculatory dysfunction. Fourth, ROC analysis determined the best cut-off value for angio-IMR as 25.1, which is very close to that for pressure wire–measured IMR. Thus, we used this cut-off value to define post-PCI microcirculatory dysfunction. However, the underlying mechanism between INOCA and post-PCI patients may be different. We further used the maximally selected log-rank statistics method to derive the best cut-off value of angio-IMR to predict clinical outcomes as 27.3; when we used this value as a cut-off, our primary results remained unchanged.

CONCLUSIONS

In conclusion, this study demonstrated that angiography-derived IMR had a moderate correlation with HMR derived by CZT-SPECT and pressure-wire measurement and a good diagnostic accuracy to predict microcirculatory dysfunction. An elevated angio-IMR measured at the time of PCI predicts a higher risk of cardiac death or heart failure admission at 28 months.

DATA AVAILABILITY STATEMENT

The raw data supporting the conclusions of this article will be made available by the authors, without undue reservation.

ETHICS STATEMENT

The studies involving human participants were reviewed and approved by Zhongshan Hospital Fudan University and Shanghai Tenth People's Hospital. The patients/participants provided their written informed consent to participate in this study.

AUTHOR CONTRIBUTIONS

ND, WC, and LL drafted and revised the manuscript. WZ, GY, BX, YX, CL, KY, and DH collected the data and follow up the patients. SD and HY analyzed the data and did the statistical analysis. JG designed the study. All authors contributed to the article and approved the submitted version.

FUNDING

This study was partly supported by National Key R&D Program of China 2016YFC1301203 and 2016YFC1301200. ND was funded by project 81600279 from the National Natural Science Foundation of China and project 2019M650075 from China Postdoctoral Science Foundation.

SUPPLEMENTARY MATERIAL

The Supplementary Material for this article can be found online at: https://www.frontiersin.org/articles/10.3389/fcvm.2021.735743/full#supplementary-material

REFERENCES

1. Alexander KP, Weisz G, Prather K, James S, Mark DB, Anstrom KJ, et al. Effects of ranolazine on angina and quality of life after percutaneous coronary intervention with incomplete revascularization: results from the ranolazine for incomplete vessel revascularization (RIVER-PCI) trial. *Circulation.* (2016) 133:39–47. doi: 10.1161/CIRCULATIONAHA.115.019768
2. Fearon WF, Balsam LB, Farouque HM, Caffarelli AD, Robbins RC, Fitzgerald PJ, et al. Novel index for invasively assessing the coronary microcirculation. *Circulation.* (2003) 107:3129–32. doi: 10.1161/01.CIR.0000080700.98607.D1
3. Chamuleau SA, Siebes M, Meuwissen M, Koch KT, Spaan JA Piek JJ. Association between coronary lesion severity and distal microvascular resistance in patients with coronary artery disease. *Am J Physiol Heart Circ Physiol.* (2003) 285:H2194–200. doi: 10.1152/ajpheart.01021.2002
4. Collet C, Onuma Y, Sonck J, Asano T, Vandeloo B, Kornowski R, et al. Diagnostic performance of angiography-derived fractional flow reserve: a systematic review and Bayesian meta-analysis. *Eur Heart J.* (2018) 39:3314–21. doi: 10.1093/eurheartj/ehy445
5. Li J, Gong Y, Wang W, Yang Q, Liu B, Lu Y, et al. Accuracy of computational pressure-fluid dynamics applied to coronary angiography to derive fractional flow reserve: FLASH FFR. *Cardiovasc Res.* (2020) 116:1349–56. doi: 10.1093/cvr/cvz289
6. Liu L, Abdu FA, Yin G, Xu B, Mohammed AQ, Xu S, et al. Prognostic value of myocardial perfusion imaging with D-SPECT camera in patients with

ischemia and no obstructive coronary artery disease (INOCA). *J Nucl Cardiol*. (2020). doi: 10.1007/s12350-020-02252-8. [Epub ahead of print].
7. Li C, Xu R, Yao K, Zhang J, Chen S, Pang L, et al. Functional significance of intermediate coronary stenosis in patients with single-vessel coronary artery disease: a comparison of dynamic SPECT coronary flow reserve with intracoronary pressure-derived fractional flow reserve (FFR). *J Nucl Cardiol*. (2020). doi: 10.1007/s12350-020-02293-z. [Epub ahead of print].
8. Leppo JA Meerdink DJ. Comparison of the myocardial uptake of a technetium-labeled isonitrile analogue and thallium. *Circ Res*. (1989) 65:632–9. doi: 10.1161/01.RES.65.3.632
9. Henzlova MJ, Duvall WL, Einstein AJ, Travin MI Verberne HJ. Erratum to: ASNC imaging guidelines for SPECT nuclear cardiology procedures: stress, protocols, and tracers. *J Nucl Cardiol*. (2016) 23:640–42. doi: 10.1007/s12350-016-0463-x
10. Hachamovitch R, Berman DS, Shaw LJ, Kiat H, Cohen I, Cabico JA, et al. Incremental prognostic value of myocardial perfusion single photon emission computed tomography for the prediction of cardiac death: differential stratification for risk of cardiac death and myocardial infarction. *Circulation*. (1998) 97:535–43. doi: 10.1161/01.CIR.97.6.535
11. Lee JM, Hwang D, Park J, Zhang J, Tong Y, Kim CH, et al. Exploring coronary circulatory response to stenosis and its association with invasive physiologic indexes using absolute myocardial blood flow and coronary pressure. *Circulation*. (2017) 136:1798–808. doi: 10.1161/CIRCULATIONAHA.117.029911
12. Ai H, Feng Y, Gong Y, Zheng B, Jin Q, Zhang HP, et al. Coronary angiography-derived index of microvascular resistance. *Front Physiol*. (2020) 11:605356. doi: 10.3389/fphys.2020.605356
13. Johnson NP, Kirkeeide RL, Asrress KN, Fearon WF, Lockie T, Marques KM, et al. Does the instantaneous wave-free ratio approximate the fractional flow reserve? *J Am Coll Cardiol*. (2013) 61:1428–35. doi: 10.1016/j.jacc.2012.09.064
14. Garcia-Garcia HM, McFadden EP, Farb A, Mehran R, Stone GW, Spertus J, et al. Standardized end point definitions for coronary intervention trials: the academic research consortium-2 consensus document. *Circulation*. (2018) 137:2635–50. doi: 10.1161/CIRCULATIONAHA.117.029289
15. Thygesen K, Alpert JS, Jaffe AS, Simoons ML, Chaitman BR, White HD, et al. Third universal definition of myocardial infarction. *Circulation*. (2012) 126:2020–35. doi: 10.1161/CIR.0b013e31826e1058
16. Venkitachalam L, Kip KE, Mulukutla SR, Selzer F, Laskey W, Slater J, et al. Temporal trends in patient-reported angina at 1 year after percutaneous coronary revascularization in the stent era: a report from the National Heart, Lung, and Blood Institute-sponsored 1997-2006 dynamic registry. *Circ Cardiovasc Qual Outcomes*. (2009) 2:607–15. doi: 10.1161/CIRCOUTCOMES.109.869131
17. Pijls NH, Fearon WF, Tonino PA, Siebert U, Ikeno F, Bornschein B, et al. Fractional flow reserve versus angiography for guiding percutaneous coronary intervention in patients with multivessel coronary artery disease: 2-year follow-up of the FAME (fractional flow reserve versus angiography for multivessel evaluation) study. *J Am Coll Cardiol*. (2010) 56:177–84. doi: 10.1016/j.jacc.2010.04.012
18. Boden WE, O'Rourke RA, Teo KK, Hartigan PM, Maron DJ, Kostuk WJ, et al. Optimal medical therapy with or without PCI for stable coronary disease. *N Engl J Med*. (2007) 356:1503–16. doi: 10.1056/NEJMoa070829
19. Huqi A, Morrone D, Guarini G, Capozza P, Orsini E Marzilli M. Stress testing after complete and successful coronary revascularization. *Can J Cardiol*. (2016) 32:986 e23–9. doi: 10.1016/j.cjca.2015.12.025
20. Jespersen L, Hvelplund A, Abildstrom SZ, Pedersen F, Galatius S, Madsen JK, et al. Stable angina pectoris with no obstructive coronary artery disease is associated with increased risks of major adverse cardiovascular events. *Eur Heart J*. (2012) 33:734–44. doi: 10.1093/eurheartj/ehr331
21. Knuuti J, Wijns W, Saraste A, Capodanno D, Barbato E, Funck-Brentano C, et al. 2019 ESC Guidelines for the diagnosis and management of chronic coronary syndromes. *Eur Heart J*. (2020) 41:407–77. doi: 10.1093/eurheartj/ehz425
22. Lee BK, Lim HS, Fearon WF, Yong AS, Yamada R, Tanaka S, et al. Invasive evaluation of patients with angina in the absence of obstructive coronary artery disease. *Circulation*. (2015) 131:1054–60. doi: 10.1161/CIRCULATIONAHA.114.012636
23. Feher A Sinusas AJ. Quantitative assessment of coronary microvascular function: dynamic single-photon emission computed tomography, positron emission tomography, ultrasound, computed tomography, and magnetic resonance imaging. *Circ Cardiovasc Imaging*. (2017) 10:e006427. doi: 10.1161/CIRCIMAGING.117.006427
24. Dhawan SS, Corban MT, Nanjundappa RA, Eshtehardi P, McDaniel MC, Kwarteng CA, et al. Coronary microvascular dysfunction is associated with higher frequency of thin-cap fibroatheroma. *Atherosclerosis*. (2012) 223:384–8. doi: 10.1016/j.atherosclerosis.2012.05.034
25. Taqueti VR, Everett BM, Murthy VL, Gaber M, Foster CR, Hainer J, et al. Interaction of impaired coronary flow reserve and cardiomyocyte injury on adverse cardiovascular outcomes in patients without overt coronary artery disease. *Circulation*. (2015) 131:528–35. doi: 10.1161/CIRCULATIONAHA.114.009716
26. Carrick D, Haig C, Ahmed N, Carberry J, Yue May VT, McEntegart M, et al. Comparative prognostic utility of indexes of microvascular function alone or in combination in patients with an acute st-segment-elevation myocardial infarction. *Circulation*. (2016) 134:1833–1847. doi: 10.1161/CIRCULATIONAHA.116.022603
27. Fearon WF, Low AF, Yong AS, McGeoch R, Berry C, Shah MG, et al. Prognostic value of the Index of Microcirculatory Resistance measured after primary percutaneous coronary intervention. *Circulation*. (2013) 127:2436–41. doi: 10.1161/CIRCULATIONAHA.112.000298
28. Nishi T, Murai T, Ciccarelli G, Shah SV, Kobayashi Y, Derimay F, et al. Prognostic value of coronary microvascular function measured immediately after percutaneous coronary intervention in stable coronary artery disease: an international multicenter study. *Circ Cardiovasc Interv*. (2019) 12:e007889. doi: 10.1161/CIRCINTERVENTIONS.119.007889

Conflict of Interest: The authors declare that the research was conducted in the absence of any commercial or financial relationships that could be construed as a potential conflict of interest.

Publisher's Note: All claims expressed in this article are solely those of the authors and do not necessarily represent those of their affiliated organizations, or those of the publisher, the editors and the reviewers. Any product that may be evaluated in this article, or claim that may be made by its manufacturer, is not guaranteed or endorsed by the publisher.

frontiers in Cardiovascular Medicine

ORIGINAL RESEARCH
published: 04 November 2021
doi: 10.3389/fcvm.2021.715995

Optical Coherence Tomography-Derived Changes in Plaque Structural Stress Over the Cardiac Cycle: A New Method for Plaque Biomechanical Assessment

*Jiayue Huang[1,2], Fan Yang[1], Juan Luis Gutiérrez-Chico[3], Tianxiao Xu[1], Jigang Wu[4], Liang Wang[5], Rui Lv[5], Yan Lai[6], Xuebo Liu[6], Yoshinobu Onuma[2], Dalin Tang[5,7], Patrick W. Serruys[2], William Wijns[2] and Shengxian Tu[1]**

[1] School of Biomedical Engineering, Biomedical Instrument Institute, Shanghai Jiao Tong University, Shanghai, China, [2] The Lambe Institute for Translational Medicine and Curam, National University of Ireland Galway, Galway, Ireland, [3] Cardiology Department, Ruijin Hospital, Shanghai Jiao Tong University School of Medicine, Shanghai, China, [4] University of Michigan-Shanghai Jiao Tong University Joint Institute, Shanghai Jiao Tong University, Shanghai, China, [5] School of Biological Science and Medical Engineering, Southeast University, Nanjing, China, [6] Department of Cardiology, Tongji Hospital, Tongji University School of Medicine, Shanghai, China, [7] Mathematical Sciences Department, Worcester Polytechnic Institute, Worcester, MA, United States

OPEN ACCESS

Edited by:
Rene M. Botnar,
King's College London,
United Kingdom

Reviewed by:
Kenichiro Otsuka,
Massachusetts General Hospital,
United States
Yao-Jun Zhang,
Xuzhou Cancer Hospital, China

***Correspondence:**
Shengxian Tu
sxtu@sjtu.edu.cn

Specialty section:
This article was submitted to Cardiovascular Imaging, a section of the journal Frontiers in Cardiovascular Medicine

Received: 27 May 2021
Accepted: 04 October 2021
Published: 04 November 2021

Citation:
Huang J, Yang F, Gutiérrez-Chico JL, Xu T, Wu J, Wang L, Lv R, Lai Y, Liu X, Onuma Y, Tang D, Serruys PW, Wijns W and Tu S (2021) Optical Coherence Tomography-Derived Changes in Plaque Structural Stress Over the Cardiac Cycle: A New Method for Plaque Biomechanical Assessment. Front. Cardiovasc. Med. 8:715995. doi: 10.3389/fcvm.2021.715995

Introduction: Cyclic plaque structural stress has been hypothesized as a mechanism for plaque fatigue and eventually plaque rupture. A novel approach to derive cyclic plaque stress *in vivo* from optical coherence tomography (OCT) is hereby developed.

Materials and Methods: All intermediate lesions from a previous OCT study were enrolled. OCT cross-sections at representative positions within each lesion were selected for plaque stress analysis. Detailed plaque morphology, including plaque composition, lumen and internal elastic lamina contours, were automatically delineated. OCT-derived vessel and plaque morphology were included in a 2-dimensional finite element analysis, loaded with patient-specific intracoronary pressure tracing data, to calculate the changes in plaque structural stress (ΔPSS) on vessel wall over the cardiac cycle.

Results: A total of 50 lesions from 41 vessels were analyzed. A significant ΔPSS gradient was observed across the plaque, being maximal at the proximal shoulder (45.7 [32.3, 78.6] kPa), intermediate at minimal lumen area (MLA) (39.0 [30.8, 69.1] kPa) and minimal at the distal shoulder (35.1 [28.2, 72.3] kPa; $p = 0.046$). The presence of lipidic plaques were observed in 82% of the diseased segments. Larger relative lumen deformation and ΔPSS were observed in diseased segments, compared with normal segments (percent diameter change: 8.2 ± 4.2% vs. 6.3 ± 2.3%, $p = 0.04$; ΔPSS: 59.3 ± 48.2 kPa vs. 27.5 ± 8.2 kPa, $p < 0.001$). ΔPSS was positively correlated with plaque burden ($r = 0.37$, $p < 0.001$) and negatively correlated with fibrous cap thickness ($r = -0.25$, $p = 0.004$).

Conclusions: ΔPSS provides a feasible method for assessing plaque biomechanics *in vivo* from OCT images, consistent with previous biomechanical and clinical studies based on different methodologies. Larger ΔPSS at proximal shoulder and MLA indicates the critical sites for future biomechanical assessment.

Keywords: biomechanical assessment, finite element analysis, optical coherence tomography, plaque structural stress, plaque rupture

INTRODUCTION

Spontaneous plaque rupture and subsequent thrombosis are recognized as the leading pathogenic mechanism for acute coronary syndrome (ACS), one of the major causes of mortality worldwide (1–3). Thin cap fibroatheroma (TCFA) has been postulated as the phenotype responsible for plaque rupture (3–8). However, limited specificity was observed for TCFA in predicting future coronary events, urging the need to further define meaningful surrogates for rupture-prone plaque identification (9–12).

From a biomechanical point of view, long-term repetitive superficial stress, generated by the pulsatile coronary pressure wave, might weaken the fibrous cap and ultimately lead to its fatigue and rupture (13, 14). Thus, the evaluation of cyclic plaque structural stress might add prognostic value for future cardiac events and subsequently for ACS prevention. Although direct *in vivo* measurement of plaque structural stress is not currently feasible, finite element analysis (FEA) might provide a reliable estimation (15). The prerequisites for accurate FEA are precise plaque morphology and composition, known mechanical properties of the different materials and precise model loads. Optical coherence tomography (OCT) provides optimal image resolution, enabling detailed visualization and precise characterization of plaque composition (16). Meanwhile, intracoronary pressure tracing from pressure wire could serve as an accurate load for cyclic plaque stress evaluation using FEA. The aim of this study was to propose a novel method to derive the changes in plaque structural stress during the cardiac cycle *in vivo* using a combination of OCT images and intracoronary pressure recordings.

MATERIALS AND METHODS

All patients from a previous prospective optical flow ratio (OFR) study with both OCT and fractional flow reserve (FFR) interrogation were screened for *post-hoc* analysis (17). Inclusion criteria were intermediate coronary lesions, defined as a diameter stenosis 40–90% by visual estimation. Exclusion criteria for FEA were: 1) bifurcation lesions with a side-branch ≥2mm; 2) diffuse coronary disease in the target vessel; 3) stented lesions; 4) intracoronary thrombus; 5) guidewire artifact in the OCT images; 6) incomplete intracoronary pressure recording, with baseline aortic pressure or distal coronary pressure at rest missing. Detailed description of the OCT acquisition and intracoronary pressure measurement has been previously reported (17).

Representative Position Selection

Five OCT cross-sections were selected at representative positions for each lesion, whenever available (**Figures 1C1–C5**): 1) proximal and distal references (PR, DR): immediately adjacent cross-sections to the lesion, at the proximal and distal edges, respectively, where neither plaque nor remodeling were observed in OCT and angiography; 2) minimal lumen area (MLA): the cross-section with minimal lumen area in OCT; 3) proximal and distal shoulders (PS, DS): midpoints between PR and MLA or DR and MLA, respectively. In case the PR or DR are not present in certain lesion, the midpoint between proximal edge and MLA or distal edge and MLA will be used for PS or DS, respectively.

Geometric Model Reconstruction

The lumen contours of selected OCT cross-sections were automatically delineated using OctPlus software (Pulse Medical Imaging Technology, Shanghai, China). The contour of the internal elastic lamina (IEL) was then identified or extrapolated from adjacent cross-sections, according to a previously validated method (18). The plaque composition was then automatically analyzed at every cross-section in the region encompassed between IEL and the lumen contour, using artificial intelligence (18). The mechanical-relevant plaque components considered for the current FEA in the intima were lipids, calcium and fibrous tissue. Media and adventitia were also incorporated into the geometric model by measuring their thickness on OCT and offsetting the IEL contour uniformly (**Figures 1C1–C5,D1–D5**). In case media and adventitia were not visible at the cross-section, their thickness on adjacent OCT cross-section was selected.

Biomechanical Analysis

The simulation was performed with the commercially available FEA software ABAQUS (Version 6.13, Dassault Systemes Simulia Corp., Providence, RI, USA). Intimal lipidic plaque and calcific plaque were modeled as isotropic, hyperelastic materials as described by Mooney-Rivlin strain energy density function:

$$W = C_1 (I_1 - 3) + C_2 (I_2 - 3) + D_1 (\exp (D_2 (I_1 - 3)) - 1)$$

where I_1 and I_2 are the first and second strain invariants. C_1, C_2, D_1 and D_2 are material constants adapted from previous studies (19, 20).

Intimal fibrous tissue, media and adventitia were modeled as anisotropic, hyperelastic materials, according to Holzapfel model:

$$W = \mu (I_1 - 3) + \frac{k_1}{k_2} (\exp \left\{ k_2 \left[(1 - \rho) (I_1 - 3)^2 + \rho (I_4 - 1)^2 \right] \right\} - 1)$$

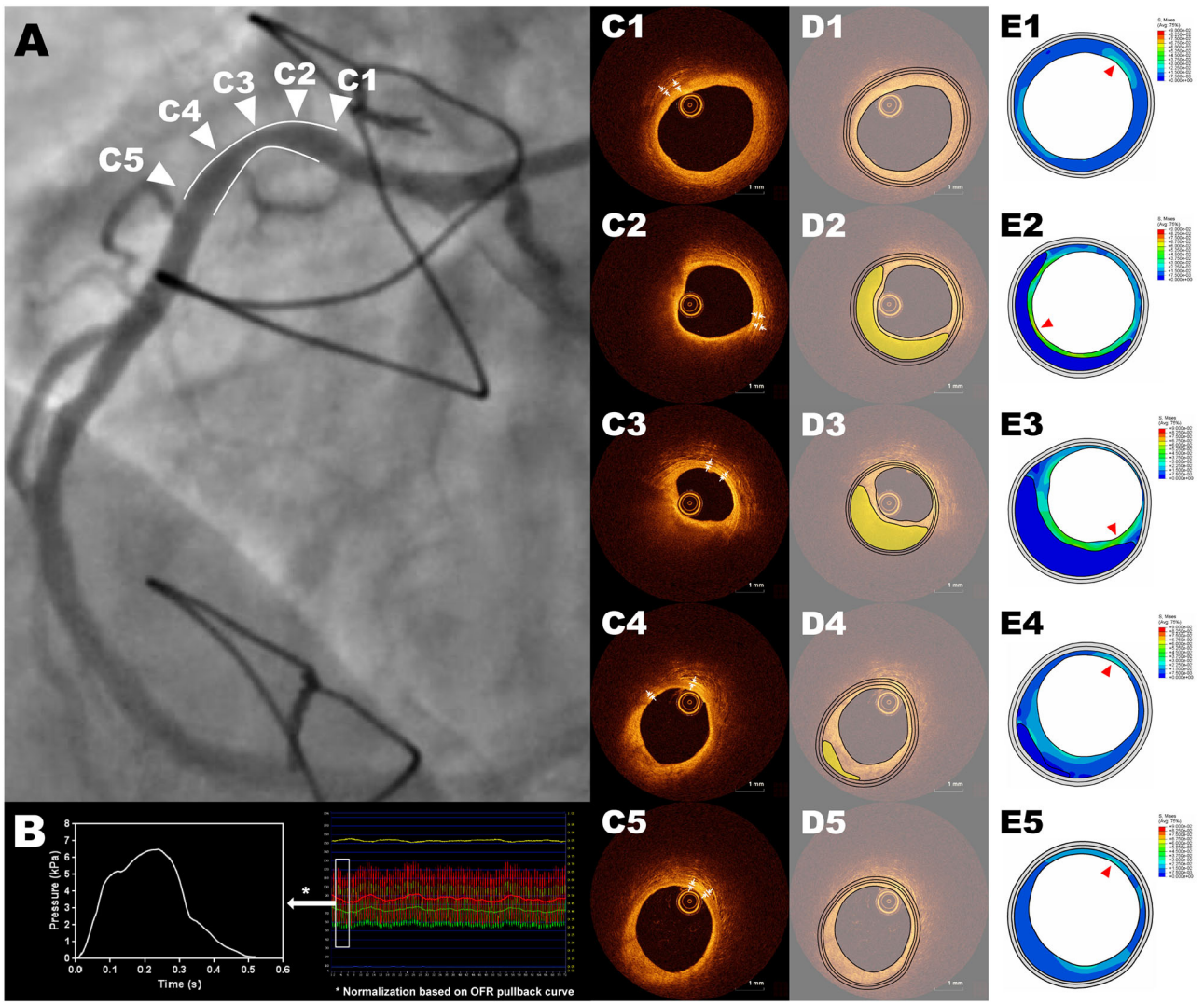

FIGURE 1 | Representative example of ΔPSS analysis of an intermediate RCA lesion. Cross-sections **(C1-C5)** correspond to the five representative positions in the angiography showed in panel **(A)**, with **(C1)** as the cross-section of proximal reference, **(C2)** as the cross-section of proximal shoulder, **(C3)** as the cross-section of minimal lumen area, **(C4)** as the cross-section of distal shoulder and **(C5)** as the cross-section of distal reference. The 2-dimensional FEA model is loaded with the position-specific intracoronary pressure derived from intracoronary tracing data, by normalizing the computed OFR pullback curve between the resting aortic pressure tracing data and distal coronary pressure tracing data **(B)**. The three-layer geometric models were reconstructed based on an automatic plaque delineation algorithm (18) **(D1–D5)**, where the lipidic plaque is shown in yellow. The thicknesses of media and adventitia were manually measured from OCT cross-sections **(C1–C5)**. **(E1–E5)** show the stress distribution with the red triangles pointing the positions with largest ΔPSS. FEA, finite element analysis; RCA, right coronary artery; OCT, optical coherence tomography; OFR, optical flow ratio; ΔPSS, delta plaque structural stress.

where μ, k_1 and k_2 are material constants adapted from previous studies (21–23).

Position-specific pressure condition derived from intracoronary tracing data was applied to the 2-dimensional (2D) FEA model for each cross-section. From OCT images the OFR pullback was firstly computed using a recently validated software package (OctPlus, Pulse medical imaging technology, Shanghai, China) (17, 24, 25). By normalizing the computed OFR pullback curve between the resting aortic pressure and distal coronary pressure tracing data, the position-specific intracoronary pressure at each OCT cross-section could be precisely estimated, also given the excellent agreement between OFR and FFR (17). The change in coronary pressure, i.e., the relative pressure, was then computed by subtracting the estimated diastolic pressure from the cyclic pressure (**Figure 1B**), which was used as the mechanical load for simulations. The 2D FEA models were then meshed with three-node or four-node linear, hybrid elements. Large deformation formulation and plane strain assumption were used for simulation. The rotational freedom was restricted to prevent the model from rolling while enabling its radial deformation. By submitting the FEA model to ABAQUS/Explicit Solver, the dynamic change of lumen and the plaque structural

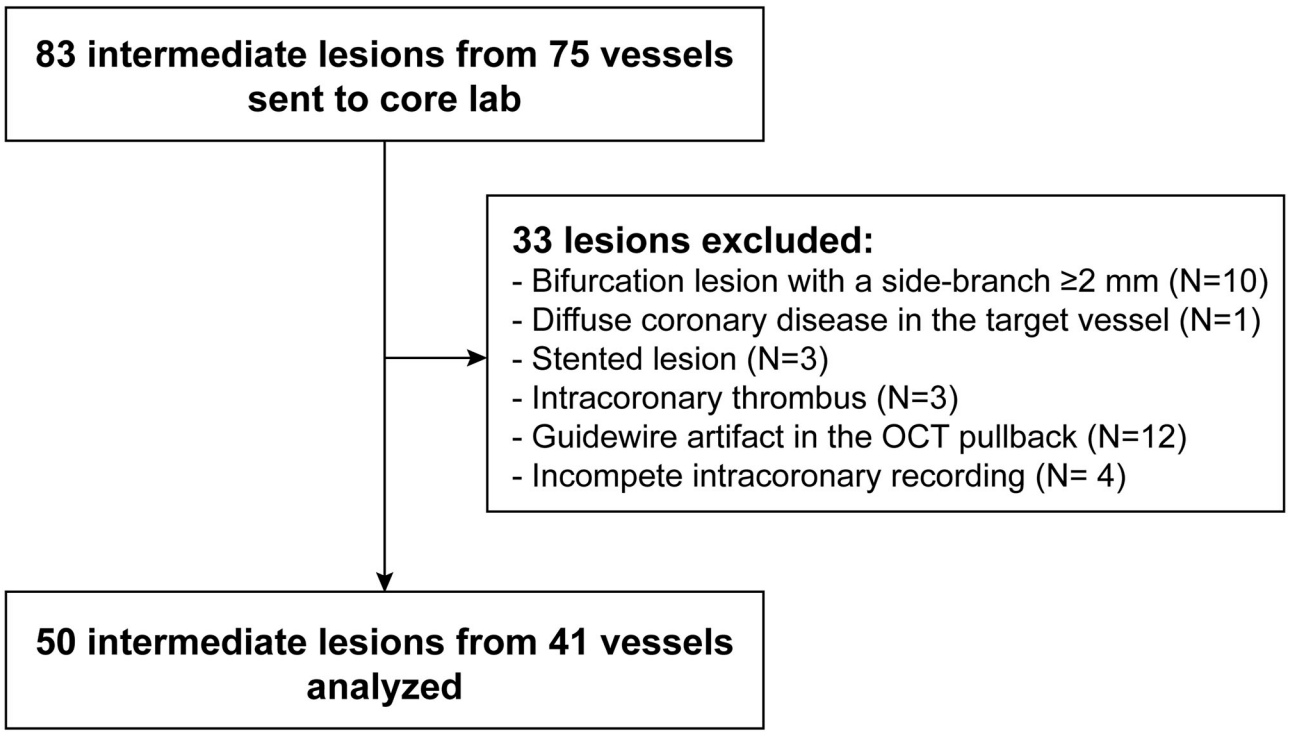

FIGURE 2 | Study flow chart. FFR, fractional flow reserve; OCT, optical coherence tomography.

stress distribution at each cross-section during the cardiac cycle could then be simulated (**Supplementary Video 1**).

After the simulation, the maximal superficial von Mises stress on the vessel wall at maximal pressure load moment was denoted as OCT-derived change in plaque structural stress (ΔPSS). The thickness of the superficial layer depends on the size of the meshes in the FEA model which was <50 μm. Lumen diameter change (LDC) and percent lumen diameter change (LDC%) during cardiac contraction were used for presenting lumen deformation and relative lumen deformation. The LDC equals to the maximal lumen diameter minus minimal lumen diameter over the cardiac cycle. The LDC% is computed by dividing LDC with the minimal lumen diameter.

Statistics

Descriptive statistics of continuous variables are reported as mean ± SD or median (quartiles) as appropriate, while those of categorical variables are presented as counts (percentages). The difference between groups was tested using independent sample *t*-test, Mann-Whitney test or One-way Analysis of Variance (ANOVA), as appropriate. Paired *t*-test, Wilcoxon signed-rank test or repeated measures ANOVA were used for pair-wise comparison, as appropriate. To evaluate the statistical differences of simulated lumen deformation and plaque structural stress at different locations of the lesion, the generalized estimation equation (GEE) analyses were performed. Statistical assessments were performed with MedCalc version 19.5.6 (MedCalc Software, Ostend, Belgium) and SPSS version 27.0.1.0 (SPSS Inc., Chicago, Illinois). A 2-sided value of $p < 0.05$ was considered to be statistically significant.

RESULTS

Baseline Clinical and Lesion Characteristics

A total of 83 intermediate lesions from 75 vessels were enrolled. Thirty-three lesions were excluded from FEA due to bifurcation ($n = 10$), diffuse disease ($n = 1$), stented lesion ($n = 3$), intracoronary thrombus ($n = 3$), guidewire artifact ($n = 12$) or incomplete intracoronary recording ($n = 4$), resulting in 50 lesions suitable for biomechanical analysis (**Figure 2**).

Baseline demographic and lesion characteristics are presented in **Tables 1**, **2**, respectively. The mean age of the patients was 63 ± 11 years. Half of the lesions (50.0%) were located at the proximal segment of the target vessel.

Plaque Morphology and Composition

Quantification of the OCT images was performed using the OctPlus software package (Pulse medical imaging technology, Shanghai, China). Automatic plaque characterization and delineation of the IEL from OCT images by the software was performed using artificial intelligence algorithm and recently validated with high accuracy (18). Average lumen diameter, plaque burden and fibrous cap thickness in the representative positions are presented in **Table 3**. MLA had the smallest lumen diameter (1.82 [1.60, 1.97] mm) and the largest plaque burden

TABLE 1 | Baseline demographic characteristics.

Patients (*N* = 37)	
Age, years	63 ± 11
Women	3 (8.1%)
BMI, kg/m^2	28.4 [25.4, 29.9]
Diabetes mellitus	12 (32.4%)
Hypertension	25 (67.6%)
Hyperlipidemia	17 (46.0%)
Current smoker	12 (32.4%)
Family history of CAD	3 (8.1%)
Previous PCI	29 (78.4%)
Previous CABG	1 (2.7%)
Previous MI	21 (56.8%)
Clinical presentation	
Stable Coronary Heart Disease	29 (78.4%)
Unstable Angina	4 (10.8%)
NSTEMI	4 (10.8%)

Data are presented as mean ± SD, median (quartiles), or n (%), as appropriate.
BMI, body mass index; CAD, coronary artery disease; CABG, coronary artery bypass surgery; NSTEMI, Non-ST-elevation myocardial infarction; MI, myocardial infarction; PCI, percutaneous coronary intervention.

TABLE 2 | Baseline lesion characteristics.

Vessels (*N* = 41)	
Interrogated vessel	
Left anterior descending	23 (56.1%)
Diagonal	4 (9.8%)
Left circumflex	0 (0.0%)
Obtuse marginal	2 (4.9%)
Ramus intermedius	1 (2.4)
Right coronary artery	11 (26.8%)
Lesions (*N* = 50)	
Lesion location	
Proximal segment	25 (50.0%)
Middle segment	19 (38.0%)
Distal segment	6 (12.0%)
Minimal Lumen Area, mm^2	2.70 [2.16, 3.11]

Data are presented as mean ± SD, median (quartiles), or n (%), as appropriate.

(69.11 ± 9.11%) of all the representative positions. Fibrous cap thickness was numerically smaller in PS than in MLA and DS, but it did not reach statistical significance (PS vs. MLA vs. DS: 154.1 [60.8, 242.2] μm vs. 168.9 [54.2, 264.7] μm vs. 212.4 [92.7, 253.2] μm, $p = 0.48$). The plaque composition and microfeatures of the lesions included in current study are presented in **Table 4**. Forty-one lesions (82.0%) have more than one plaque phenotypes. By using the predominant plaque phenotype for each lesion, a total of 28 fibroatheromas, 8 fibrotic plaques and 14 fibrocalcific plaques were included in the present study.

TABLE 3 | Plaque morphologies.

Position within the lesion	Lumen diameter (mm)	Plaque burden (%)	Cap thickness (μm)
PR (*N* = 10)	3.94 [2.92, 4.21]	32.47 ± 5.78	–
PS (*N* = 50)	2.46 [2.13, 2.95]	56.91 ± 5.67	154.1 [60.8, 242.2]*
MLA (*N* = 50)	1.82 [1.60, 1.97]	69.11 ± 9.11	168.9 [54.2, 264.7]*
DS (*N* = 50)	2.40 [2.15, 2.63]	53.82 ± 11.57	212.4 [92.7, 253.2]*
DR (*N* = 17)	2.91 [2.74, 3.18]	32.36 ± 8.70	–

**Cap thickness was not recorded in 3 PS, 2 MLA and 14 DS because only fibrous plaque was observed.*
PR, proximal reference; PS, proximal shoulder; MLA, minimal lumen area; DS, distal shoulder; DR, distal reference.

TABLE 4 | Plaque composition and microfeatures.

Position within the lesion	Number of lipidic plaques	Mean lipidic plaque area (mm^2)	Number of calcific plaques	Mean calcific plaque area (mm^2)
PS (*N* = 50)	49	2.18 [1.36, 3.22]	29	0.65 [0.39, 1.83]
MLA (*N* = 50)	51	2.28 [1.24, 3.85]	27	0.70 [0.31, 0.85]
DS (*N* = 50)	38	1.41 [0.87, 2.91]	22	0.48 [0.22, 0.89]

PS, proximal shoulder; MLA, minimal lumen area; DS, distal shoulder.

TABLE 5 | Biomechanical results.

Position within the lesion	LDC (mm)	LDC%	ΔPSS (kPa)
PR (*N* = 10)	0.19 [0.17, 0.26]	5.48 [4.75, 6.43]	25.2 [21.2, 32.3]
PS (*N* = 50)	0.20 [0.13, 0.31]	8.55 [6.13, 11.12]	45.7 [32.3, 78.6]
MLA (*N* = 50)	0.13 [0.08, 0.23]	7.56 [5.17, 11.28]	39.0 [30.8, 69.1]
DS (*N* = 50)	0.17 [0.13, 0.26]	6.26 [5.31, 9.85]	35.1 [28.2, 72.3]
DR (*N* = 17)	0.19 [0.12, 0.26]	6.84 [3.85, 8.39]	28.6 [20.8, 32.6]

PR, proximal reference; PS, proximal shoulder; MLA, minimal lumen area; DS, distal shoulder; DR, distal reference; LDC, lumen diameter change; ΔPSS, delta plaque structural stress.

Among all 177 interrogated cross-sections, more than half of them (92 cross-sections) have a good (external elastic lamina circumference ≥270°) or moderate visibility (270° > external elastic lamina circumference ≥ 180°) of the media (54 and 38 cross-sections, respectively). While the media were completely invisible in 14 (7.9%) cross-sections, where the artificial intelligence algorithm used their adjacent cross-sections for IEL delineation. In these cases, the mean number of skipped cross-sections for manual media and adventitia thicknesses measurement was 5.6 ± 6.8 frames.

Lumen Deformation and Plaque Structural Stress

A representative example of ΔPSS analysis is shown in **Figure 1** and **Supplementary Video 1**. The LDC, LDC% and ΔPSS across the lesion are presented in **Table 5** and **Figure 3**. Absolute LDC

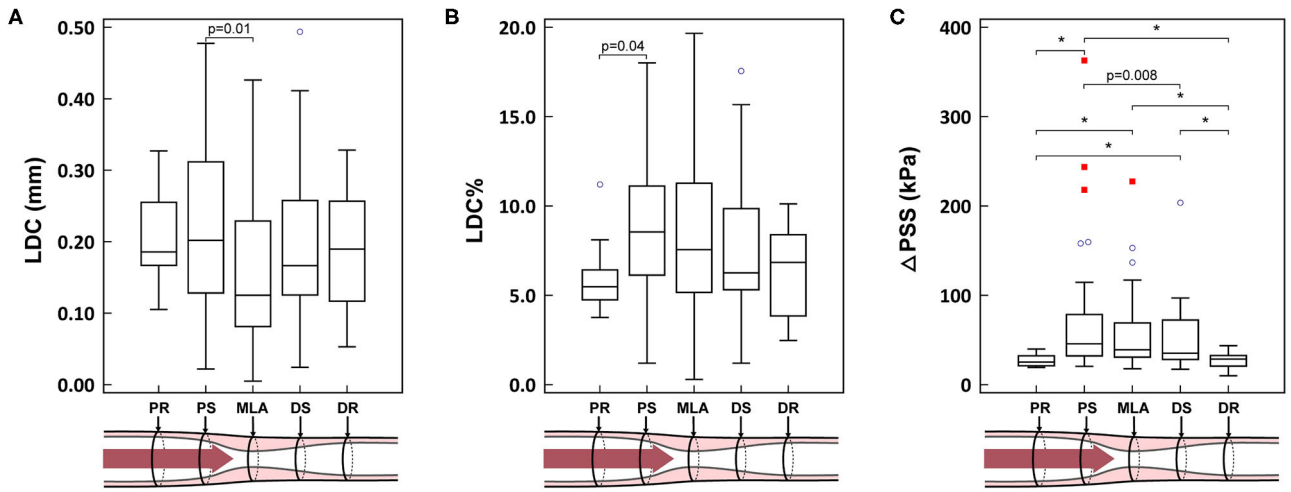

FIGURE 3 | (A–C) Biomechanical results in different locations of the lesion. *$p < 0.001$. PR, proximal reference; PS, proximal shoulder; MLA, minimal lumen area; DS, distal shoulder; DR, distal reference; LDC, lumen diameter change; LDC%, percent lumen diameter change; ΔPSS, delta plaque structural stress. The blue circles represent the mild outliers, and the red squares represent the extreme outliers.

was smaller at MLA than at both reference cross-sections (PR and DR), but LDC% was larger. Positive correlation was observed between LDC and lumen diameter ($r = 0.53$, $p < 0.01$). However, no correlation was observed between LDC% and lumen diameter.

ΔPSS was significantly smaller at the reference cross-sections than at MLA or at the shoulders (PR vs. PS, MLA and DS: 25.2 [21.2, 32.3] kPa vs. 45.7 [32.3, 78.6] kPa, 39.0 [30.8, 69.1] kPa and 35.1 [28.2, 72.3] kPa; $p < 0.001$, $p < 0.001$ and $p < 0.001$, respectively). In paired analysis per lesion, a significant ΔPSS gradient was observed across the plaque (PS-MLA-DS, $p = 0.046$; test for linear trend: $p = 0.012$). ΔPSS at PS was significantly larger than at DS ($p = 0.02$), while ΔPSS at MLA tended to have intermediate values between PS and DS (**Figure 3**). Within all 49 lesions with lipidic plaques, the highest ΔPSS occurred at the cross-sections with thinnest cap in 49.0% (24) of these lesions. While for 22 lesions (44.9%), the highest ΔPSS occurred at the cross-sections with lipidic plaques but thicker cap thickness. Three (6.1%) lesions were observed to have the highest ΔPSS at cross-sections without any lipidic plaque.

Normal vs. Diseased Segments

The analyzed OCT cross-sections were divided into two groups: 1) normal segments, comprising PR and DR; 2) diseased segments, comprising PS, MLA and DS. LDC was numerically smaller in diseased segments compared to normal segments, but statistically non-significant (0.17 [0.10, 0.27] mm vs. 0.19 [0.13, 0.25] mm, $p = 0.69$). While both LDC% and ΔPSS were significantly larger in diseased segments than in normal segments (LDC%: 7.57 [5.38, 10.64]% vs. 6.29 [4.44, 8.17]%, $p = 0.002$; ΔPSS: 41.8 [29.1, 74.6] kPa vs. 27.7 [21.2, 32.1] kPa, $p < 0.001$) (**Figure 4**).

In normal segments, a good correlation was observed between maximal pressure load and ΔPSS and ($r = 0.72$, $p < 0.001$). Nonetheless, this correlation was significantly worse in diseased segments ($r = 0.42$, $p < 0.001$; difference $p = 0.04$), wherein relatively low pressure loads often resulted in high ΔPSS.

Correlation of Stress Parameters With Morphological Features of Plaque Vulnerability

ΔPSS was positively correlated with plaque burden ($r = 0.37$, $p < 0.001$) while negatively correlated with fibrous cap thickness ($r = -0.25$, $p < 0.001$). Good correlation was observed between ΔPSS and LDC% ($r = 0.78$, $p < 0.001$).

Moderate correlation was observed between ΔPSS and lipidic plaque area (LPA) ($r = 0.44$, $p < 0.001$), while no significant correlation was observed between ΔPSS and calcific plaque area. LPA showed good correlation with both lumen deformation and relative lumen deformation (LPA-LDC: $r = 0.55$, $p < 0.001$; LPA-LDC%: $r = 0.88$, $p < 0.001$).

Computational Performance of ΔPSS Assessment

Using an off-the-shelf workstation with a quadcore Intel i7-4790 processor (Intel Corporation, Santa Clara, CA; 3.6 GHz) and 8GB of RAM, the average simulation time for analysis of each FEA model was 12.5 ± 10.2 min, and the estimated time for the whole FEA analysis process was <30 min.

DISCUSSION

In this study, we present for the first time a new methodology to calculate the changes in plaque structural stress within the cardiac cycle *in vivo* using OCT images and FEA simulation. The changes of superficial plaque structural stress on vessel wall are the main focus of our current study since it tends to be closely related to plaque rupture and subsequent acute coronary events (26–29).

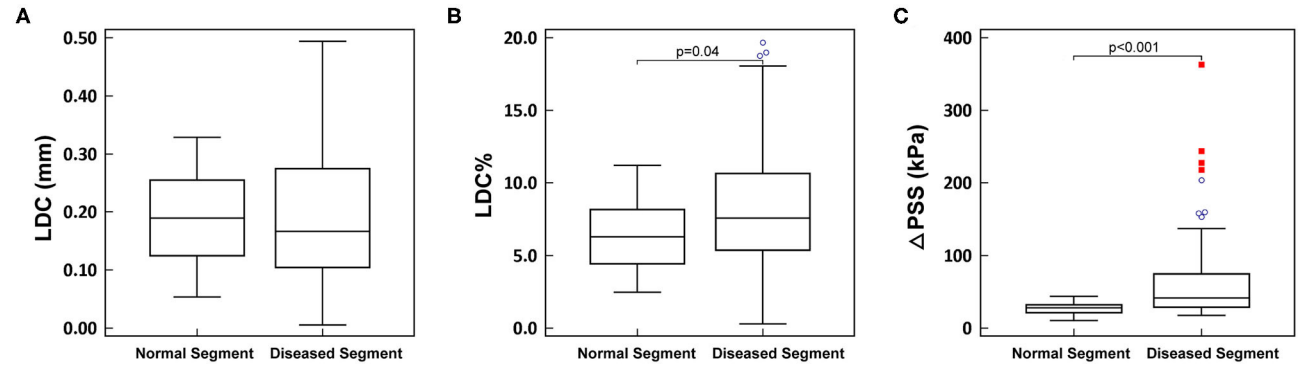

FIGURE 4 | (A–C) Comparison between normal segment and diseased segment. LDC, lumen diameter change; LDC%, percent lumen diameter change; ΔPSS, delta plaque structural stress. The blue circles represent the mild outliers, and the red boxes represent the extreme outliers.

The key findings of this study can be summarized as follows: 1) ΔPSS provides a feasible and reasonable approach for OCT-based biomechanical assessment; 2) diseased segments, especially the proximal shoulder and minimal lumen area of the lesion, bear the highest ΔPSS, thus highlighting the critical importance of these sites for future biomechanical studies of plaque vulnerability and prediction of event risk; 3) correlation between ΔPSS and plaque morphology is consistent with previous clinical and imaging studies, thus reassuring the rationale of our method.

This novel method is original in many aspects, including the automatic plaque characterization from OCT images using artificial intelligence, the incorporation of the three-layered structure of the vessel wall into 2D FEA model, the accurate position-specific load derived from intracoronary pressure tracing data. Previous studies performed coronary plaque stress simulation (27), but most of them were based on coronary angiography or intravascular ultrasound (IVUS), with inherent limitations in plaque characterization and inferior image resolution, as compared with OCT. Additionally, rigid-body assumption restricting all deformation was applied to most FEA models hitherto (20, 30, 31).

The first advantage of the current approach is the higher image resolution provided by OCT, enabling the detailed description of coronary lumen, plaque morphology and composition which are essential for FEA analysis. The significant lower correlation between load and ΔPSS in diseased segments than in normal segments ($r = 0.42$ vs. 0.72, $p < 0.001$) strongly suggests a crucial role of plaque morphology and composition in determining the actual plaque stress. Chau et al. have also proposed an FEA method to derive plaque stress from OCT images (32). However, a fixed pressure from 0 to 120 mmHg was applied to all models, which might not be realistic since the geometry of the vessel was not imaged under zero-pressure condition. In addition, the same isotropic material properties were applied to the whole artery wall, ignoring the anisotropy of media and adventitia and the mechanical differences between them. Although OCT has limited tissue penetration, as compared with IVUS, and notwithstanding the high attenuation of near-infrared waves in lipids, apparently precluding the imaging of media and adventitia in diseased segments (16), recent studies have proven that the external elastic lamina can be identified for ≥180° in most of the OCT cross-sections (33). Thus, the media contour could be extrapolated considering its circular or elliptical geometry. For OCT cross-sections with invisible IEL, which only accounts for 7.9% of the total cross-sections in this study, our artificial intelligence algorithm will refer to adjacent OCT cross-sections and estimate the contour of IEL. This principle was externally validated for the same specific software used in the current study, providing high diagnostic accuracy for delineation of the media contour and tissue characterization within the plaque, including lipids (90.5%) (18). In this study, we mainly focused on the superficial cyclic plaque structural stress on vessel wall, which is more likely to be affected by the different plaque components in near-lumen regions, as compared to outer layers as media and adventitia. During the analysis, we also observed that the slight deviation, i.e., thickness and contour, in media and adventitia have a relatively small impact on simulation results. While for superficial layers, even a tiny change, e.g., lumen contour and fibrous cap thickness, will cause great difference in ΔPSS. It has also been proven by previous studies that the most crucial impact on stress computation comes from the superficial wall adjacent to lumen, and that the vascular structure determined by OCT provides adequate basis for biomechanical analysis (23, 32). Nevertheless, when focusing on the stress distribution at deeper layer, e.g., behind the plaque or near the outer vessel boundary, more precise simulation results might be achieved by incorporating more accurate delineation of media and adventitia, especially for lesions with large lipidic plaque burden where the outer boundary is invisible due to light attenuation in OCT. In such cases, IVUS with higher tissue penetration could serve as a complemental modality (34). By combining detailed evaluation of plaque morphology provided by OCT and assessment of the entire vessel structure provided by IVUS, a more precise geometric model for FEA should become obtainable, leading to a more accurate biomechanical assessment especially for outer layers (35). In the future, with the development of automatic OCT-IVUS co-registration algorithm and/or hybrid intravascular imaging system with combined OCT

and IVUS probes (36), the accuracy of PSS assessment could be further improved with great efficiency.

A complete vessel architecture with three-layer structure was applied for simulation in this study. Very few studies have incorporated the three-layered structure of the vessel into the FEA simulation hitherto. This might be a potential limitation of previous studies because stress distribution heavily depends on the physical properties of the material and the layered arrangement of the vessel wall (21, 37–39). The different composition and stiffness of intima, media and adventitia determine their different roles during loading. The stiffness of intima widely varies depending on the different plaque components. Conversely, media and adventitia use to have more predictable mechanical properties: the structured arrangement of smooth muscle cells in the media confers this layer high resistance to load, while the helically arranged wavy collagen fibrils and elastic fibers in adventitia make it more compliant to pressure than media under normal load (40, 41).

Accurate model load using intracoronary pressure registration has been instrumental to render precise stress estimations. The model, however, was only loaded with the change in coronary pressure, instead of using the whole pressure recording, in order to simplify and expedite the calculation. The stress change over the cardiac cycle in atherosclerotic plaques has been proven to correlate with the incidence of major adverse cardiovascular events (42) and the general relation between plaque morphology and plaque stress remains intact irrespective of the inclusion or exclusion of the initial stress in the model (43). On this rationale, the decision of using only pressure change seems justified. Loading the model with the whole pressure recording might have added marginal accuracy to the estimations, but at the price of exponentially increasing the complexity of the analysis and subsequently the time required for it (43–45). For models to be loaded with the whole pressure recording, accurate computation of zero-pressure state is one of the prerequisites. Several methods have been proposed for the estimation of initial stress. A preshrinkage algorithm by Huang et al. iteratively shrinks the *in-vivo* plaque geometry before the whole pressure loading to estimate the zero-pressure state and initial stress (44, 45). However, manual adaptation was required in each iteration to compare the computed geometry with the image-derived real geometry and adjust the geometry for the next iteration, which might be too complicated for daily practice. Speelman et al. proposed a Backward Incremental method that requires no manual input (43). However, the vessel geometry under certain fixed intracoronary pressure is one of the prerequisites for the intimal stress estimation, making this method not suitable for *in vivo* assessment. Theoretically, zero-pressure state and initial stress could be accurately estimated from the geometrical models of the same cross-section at both diastole and systole, where the imaging catheter is required to be fixed at the same position for at least one cardiac cycle. However, this kind of relative stillness between catheter and vessel is technically difficult to achieve, considering the impact of cardiac motion and vessel contraction (46). Thus, the gain in incorporating whole pressure recording might be partly canceled by the relative displacement between the imaging catheter and the analyzed cross-section during cardiac cycle.

The consistency of the plaque stress calculated by this novel method with previous clinical findings and biomechanical studies is reassuring of the validity of our approach. Autopsy studies have linked high plaque stress with plaque rupture (13, 47). Likewise, imaging studies have associated high plaque stress with acute coronary syndromes (14). This evidence supports the biomechanical hypothesis for plaque rupture: the repetitive cyclic stress would end up breaking the plaque, like repetitively bending a paper leads to its weakening and fracture (1). In line with this evidence, normal coronary segments bear significantly lower ΔPSS than diseased segments in our study. Moreover, it is known that strain and plaque stress are higher upstream than downstream in the atherosclerotic plaque (48, 49), i.e., higher in the proximal segments than in the distal segments of the plaque, and that most plaque ruptures occur in these proximal segments of the lesion (30, 48, 50, 51). Our results, finding a plaque stress gradient from the PS to the MLA and ultimately to the DS, are in line with this preceding evidence. In addition, ΔPSS showed positive correlation with LPA and negative correlation with fibrous cap thickness, thus confirming a direct association between ΔPSS and morphologically rupture-prone plaque, i.e., TCFA. Nonetheless, both correlations were relatively weak ($r =$ 0.37 and−0.25, respectively) and only around half (49.0%) of the lesions with lipidic plaques have the highest ΔPSS located at the thinnest cap sites, thus suggesting a mismatch between the histological and biomechanical evaluation of vulnerability. This observation may at least partially account for the limited prognostic value of TCFA alone (9–12).

In this study, the mean LDC% in normal segment is 6.29%, slightly smaller than the range of 7–14% observed by several previous studies from groups of healthy people aged from 8 to 60 (52–54). Since the coronary artery stiffens with age and disease, the relatively smaller LDC% of 6.29% in this study seems reasonable considering that our material property for intimal fibrous tissue was adopted from patients with an average age of 66 (21). The LDC is larger in normal segments compared to the diseased segments, though statistically non-significant. This finding is in line with previous IVUS studies that normal segments are more compliant to deformation (55). Conversely, significantly larger LDC% in diseased segments were observed in the present study (7.57% vs. 6.29%, $p = 0.04$). A possible explanation for this phenomenon is that 82% of the diseased segments have lipidic plaques, which are softer and thus tend to have larger relative deformation. Good correlation between LPA and %LDC further elucidates this point ($r = 0.88$, $p < 0.001$).

Clinical Perspectives

TCFA is currently recognized as a precursor for plaque rupture. However, several issues regarding image-based TCFA detection remain unsolved, including modest interobserver agreement and inconsistent definitions between studies (56). In addition, most TCFAs do not cause symptomatic rupture (9–11), revealing the fact that histological assessment alone is not enough for ACS prevention.

Plaque stress evaluation based on FEA might serve as a supplementary strategy. The location of peak cyclic plaque stress might be helpful to predict the risk of rupture and hence for ACS prevention. However, the length of a focal lesion is 12–30 mm, with 60–150 OCT cross-sections at the highest pullback speed (57, 58). Therefore, plaque stress evaluation would be very time-consuming if the whole lesion were scanned. For future studies, limiting the analysis to high-risk locations, especially for lipid rich plaques which are at higher propensity to rupture, might be instrumental for fast and efficient risk stratification.

Interestingly, LDC% showed good correlation with both ΔPSS ($r = 0.78$, $p < 0.001$) and LPA ($r = 0.88$, $p < 0.001$) in our study. These findings invite us to explore the possibility of using angiography-derived lumen deformation for the estimation of lipidic burden and for simplified identification of high-risk sites for rupture. Considering the relatively short modeling and simulation time of ΔPSS, the hereby described method might also be integrated into the current OCT-based FFR computation system, where the morphological, histological and biomechanical assessments could be achieved efficiently within one single OCT pullback.

Limitations

The current study is limited by its *post-hoc* design and its relatively small sample size. Nevertheless, all intermediate lesions with both OCT and intracoronary pressure tracing were enrolled, following strictly predefined inclusion/exclusion criteria, thus minimizing the selection bias. Besides, not all interrogated lesions had PR and DR.

In this study, the FEA models were reconstructed in 2D without incorporating the shear stress and mechanical forces in the axial direction (59–61). The homogenous material property within lipidic and calcific plaque and the uniform assumption for media and adventitia might also introduce error into the simulation. Besides, the effect of residual stress was not considered since it was currently immeasurable. The lumen deformation might also be different from real situation depending on the prevailing diastolic blood pressure levels. In addition, for cross-sections with invisible IEL, the vessel boundaries estimated by the artificial intelligence might be less accurate and lead to imprecise simulation results. However, the impact of this limitation on superficial ΔPSS is negligible. Although the simulation results are in line with clinical findings, due to the complexity of our current approach combining OCT, FFR and FEA model together, there is no single "gold standard" for validation. Besides, only presentative positions were analyzed for each lesion in this feasibility study. We did not perform frame-by-frame analysis considering that the reliability in tissue characterization might be impaired for cross-sections with side branches. Future prospective studies with larger sample sizes are warranted to investigate the prognostic value and the clinical usefulness of ΔPSS and other ΔPSS-related parameters.

The current approach, using intracoronary pressure recordings, is exquisitely accurate, but it makes the method complex and expensive to routine clinical implementation. In addition, only OCT images without guidewire artifact were analyzed in this pilot study. Future simplifications of this approach might facilitate the applicability of this assessment in the cathlab, provided they rendered acceptable accuracy.

CONCLUSIONS

Plaque structural stress over the cardiac cycle can be estimated from OCT images, using automatic plaque characterization and FEA, on a feasible fully automated process aided by artificial intelligence. The results of this novel approach are consistent with previous clinical and biomechanical studies, showing higher plaque stress in diseased vs. normal segments. The highest stress at the proximal shoulder and MLA indicates the critical rupture-prone sites for efficient biomechanical assessment in the future.

DATA AVAILABILITY STATEMENT

The dataset can be shared upon reasonable request. Requests to access these datasets should be directed to the corresponding author.

ETHICS STATEMENT

The studies involving human participants were reviewed and approved by Local Ethic Committee of Campo de Gibraltar Health Trust. The patients/participants provided their written informed consent to participate in this study.

AUTHOR CONTRIBUTIONS

JH: analysis of the data and draft of the manuscript. WW and ST: concept design and draft of the manuscript. FY, TX, RL, JW, YL, and XL: analysis of the data. JG-C, PS, YO, LW, and DT: crucial revision of the manuscript. All authors contributed to the article and approved the submitted version.

FUNDING

This work was supported in part by grants from the National Natural Science Foundation of China [grant numbers 82020108015 and 81871460] to ST and [grant number 11972117] to LW, and by the Science Foundation Ireland Research Professorship grant RSF 1413 to WW, and by grants from the Science and Technology Committee of Shanghai Municipality (No. 19411963200) to YL.

SUPPLEMENTARY MATERIAL

The Supplementary Material for this article can be found online at: https://www.frontiersin.org/articles/10.3389/fcvm.2021.715995/full#supplementary-material

REFERENCES

1. Falk E, Shah PK, Fuster V. Coronary plaque disruption. *Circulation.* (1995) 92:657–71. doi: 10.1161/01.CIR.92.3.657
2. Burke AP, Farb A, Malcom GT, Liang Y, Smialek JE, Virmani R. Coronary risk factors and plaque morphology in men with coronary disease who died suddenly. *N Engl J Med.* (1997) 336: 1276–82. doi: 10.1056/NEJM199705013361802
3. Virmani R, Kolodgie FD, Burke AP, Farb A, Schwartz SM. Lessons from sudden coronary death: a comprehensive morphological classification scheme for atherosclerotic lesions. *Arterioscler Thromb Vasc Biol.* (2000) 20:1262–75. doi: 10.1161/01.ATV.20.5.1262
4. Cheruvu PK, Finn AV, Gardner C, Caplan J, Goldstein J, Stone GW, et al. Frequency and distribution of thin-cap fibroatheroma and ruptured plaques in human coronary arteries: a pathologic study. *J Am Coll Cardiol.* (2007) 50:940–9. doi: 10.1016/j.jacc.2007.04.086
5. Finn AV, Nakano M, Narula J, Kolodgie FD, Virmani R. Concept of vulnerable/unstable plaque. *Arterioscler Thromb Vasc Biol.* (2010) 30:1282–92. doi: 10.1161/ATVBAHA.108.179739
6. Kolodgie FD, Virmani R, Burke AP, Farb A, Weber DK, Kutys R, et al. Pathologic assessment of the vulnerable human coronary plaque. *Heart.* (2004) 90:1385–91. doi: 10.1136/hrt.2004.041798
7. Virmani R, Burke AP, Farb A, Kolodgie FD. Pathology of the vulnerable plaque. *J Am Coll Cardiol.* (2006) 47:C13–8. doi: 10.1016/j.jacc.2005.10.065
8. Naghavi M, Libby P, Falk E, Casscells SW, Litovsky S, Rumberger J, et al. From vulnerable plaque to vulnerable patient. *Circulation.* (2003) 108:1664–72. doi: 10.1161/01.CIR.0000087480.94275.97
9. Stone GW, Maehara A, Lansky AJ, de Bruyne B, Cristea E, Mintz GS, et al. A prospective natural-history study of coronary atherosclerosis. *N Engl J Med.* (2011) 364:226–35. PubMed PMID: 21247313. doi: 10.1056/NEJMoa1002358
10. Calvert PA, Obaid DR, Osullivan M, Shapiro LM, Mcnab DC, Densem CG, et al. Association between IVUS findings and adverse outcomes in patients with coronary artery disease: the VIVA (VH-IVUS in Vulnerable Atherosclerosis) study. *JACC-Cardiovasc Interv.* (2011) 4:894–901. doi: 10.1016/j.jcmg.2011.05.005
11. Cheng JM, Garcia-Garcia HM, de Boer SPM, Kardys I, Heo JH, Akkerhuis KM, et al. *In vivo* detection of high-risk coronary plaques by radiofrequency intravascular ultrasound and cardiovascular outcome: results of the ATHEROREMO-IVUS study. *Eur Heart J.* (2013) 35:639–47. doi: 10.1093/eurheartj/eht484
12. Prati F, Romagnoli E, Gatto L, La Manna A, Burzotta F, Ozaki Y, et al. Relationship between coronary plaque morphology of the left anterior descending artery and 12 months clinical outcome: the CLIMA study. *Eur Heart J.* (2019) 41:383–91. doi: 10.1093/eurheartj/ehz520
13. Cheng GC, Loree HM, Kamm RD, Fishbein MC, Lee RT. Distribution of circumferential stress in ruptured and stable atherosclerotic lesions. A structural analysis with histopathological correlation. *Circulation.* (1993) 87:1179–87. doi: 10.1161/01.cir.87.4.1179
14. Schaar JA, Regar E, Mastik F, McFadden EP, Saia F, Disco C, et al. Incidence of high-strain patterns in human coronary arteries. *Circulation.* (2004) 109:2716–9. doi: 10.1161/01.CIR.0000131887.65955.3B
15. Gutierrez-Chico JL. Superficial wall stress: the long awaited comprehensive biomechanical parameter to objectify and quantify our intuition. *Int J Cardiovasc Imaging.* (2018) 34:863–5. doi: 10.1007/s10554-018-1386-1
16. Gutiérrez-Chico JL, Alegría-Barrero E, Teijeiro-Mestre R, Chan PH, Tsujioka H, de Silva R, et al. Optical coherence tomography: from research to practice. *Eur Heart J-Cardiovasc Imaging.* (2012) 13:370–84. doi: 10.1093/ehjci/jes025
17. Gutierrez-Chico JL, Chen Y, Yu W, Ding D, Huang J, Huang P, et al. Diagnostic accuracy and reproducibility of optical flow ratio for functional evaluation of coronary stenosis in a prospective series. *Cardiology J.* (2020) 27:350–61. doi: 10.5603/CJ.a2020.0071
18. Chu M, Jia H, Gutiérrez-Chico JL, Maehara A, Ali ZA, Zeng X, et al. Automatic characterisation of human atherosclerotic plaque composition from intravascular optical coherence tomography using artificial intelligence. *EuroIntervention.* (2021) 17:41–50. doi: 10.4244/EIJ-D-20-01355
19. Huang H, Virmani R, Younis H, Burke AP, Kamm RD, Lee RT. The impact of calcification on the biomechanical stability of atherosclerotic plaques. *Circulation.* (2001) 103:1051–6. doi: 10.1161/01.CIR.103.8.1051
20. Teng Z, Brown AJ, Calvert PA, Parker RA, Obaid DR, Huang Y, et al. Coronary plaque structural stress is associated with plaque composition and subtype and higher in acute coronary syndrome: the BEACON I (Biomechanical Evaluation of Atheromatous Coronary Arteries) study. *Circ-Cardiovasc Imaging.* (2014) 7:461–70. doi: 10.1161/CIRCIMAGING.113.001526
21. Holzapfel GA, Sommer G, Gasser CT, Regitnig P. Determination of layer-specific mechanical properties of human coronary arteries with nonatherosclerotic intimal thickening and related constitutive modeling. *Am J Physiol-Heart Circul Physiol.* (2005) 289:H2048–58. doi: 10.1152/ajpheart.00934.2004
22. Hollander Y, Durban D, Lu X, Kassab GS, Lanir Y. Constitutive modeling of coronary arterial media—comparison of three model classes. *J Biomech Eng.* (2011) 133:061008. doi: 10.1115/1.4004249
23. Akyildiz AC, Speelman L, van Brummelen H, Gutiérrez MA, Virmani R, van der Lugt A, et al. Effects of intima stiffness and plaque morphology on peak cap stress. *BioMed Eng Online.* (2011) 10:25. doi: 10.1186/1475-925X-10-25
24. Yu W, Huang J, Jia D, Chen S, Raffel OC, Ding D, et al. Diagnostic accuracy of intracoronary optical coherence tomography-derived fractional flow reserve for assessment of coronary stenosis severity. *EuroIntervention.* (2019) 15:189–97. doi: 10.4244/EIJ-D-19-00182
25. Huang J, Emori H, Ding D, Kubo T, Yu W, Huang P, et al. Comparison of diagnostic performance of intracoronary optical coherence tomography-based and angiography-based fractional flow reserve for evaluation of coronary stenosis. *EuroIntervention.* (2020) 16:568–76. doi: 10.4244/EIJ-D-19-01034
26. Kwak BR, Bäck M, Bochaton-Piallat M-L, Caligiuri G, Daemen MJAP, Davies PF, et al. Biomechanical factors in atherosclerosis: mechanisms and clinical implications†. *Eur Heart J.* (2014) 35:3013–20. doi: 10.1093/eurheartj/ehu353
27. Brown AJ, Teng Z, Calvert PA, Rajani NK, Hennessy O, Nerlekar N, et al. Plaque structural stress estimations improve prediction of future major adverse cardiovascular events after intracoronary imaging. *Circ-Cardiovasc Imaging.* (2016) 9:e004172. doi: 10.1161/CIRCIMAGING.115.004172
28. Ohayon J, Finet G, Le Floc'h S, Cloutier G, Gharib AM, Heroux J, et al. Biomechanics of atherosclerotic coronary plaque: site, stability and *in vivo* elasticity modeling. *Ann Biomed Eng.* (2014) 42:269–79. doi: 10.1007/s10439-013-0888-1
29. Wu X, von Birgelen C, Zhang S, Ding D, Huang J, Tu S. Simultaneous evaluation of plaque stability and ischemic potential of coronary lesions in a fluid-structure interaction analysis. *Int J Cardiovasc Imaging.* (2019) 35:1563–72. doi: 10.1007/s10554-019-01611-y
30. Costopoulos C, Huang Y, Brown A, Calvert PA, Hoole SP, West N, et al. Plaque rupture in coronary atherosclerosis is associated with increased plaque structural stress. *JACC-Cardiovasc Interv.* (2017) 10:1472–83. doi: 10.1016/j.jcmg.2017.04.017
31. Akyildiz AC, Speelman L. Velzen Bv, Stevens RRF, Steen AFWvd, Huberts W, et al. Intima heterogeneity in stress assessment of atherosclerotic plaques. *Interface Focus.* (2018) 8:20170008. doi: 10.1098/rsfs.2017.0008
32. Chau AH, Chan R, Shishkov M, Macneill BD, Iftimia N, Tearney GJ, et al. Mechanical analysis of atherosclerotic plaques based on optical coherence tomography. *Ann Biomed Eng.* (2004) 32:1494–503. doi: 10.1114/B:ABME.0000049034.75368.4a
33. Ali ZA, Maehara A, Généreux P, Shlofmitz RA, Fabbiocchi F, Nazif TM, et al. Optical coherence tomography compared with intravascular ultrasound and with angiography to guide coronary stent implantation (ILUMIEN III: OPTIMIZE PCI): a randomised controlled trial. *Lancet.* (2016) 388:2618–28. doi: 10.1016/S0140-6736(16)31922-5
34. Fujii K, Hao H, Shibuya M, Imanaka T, Fukunaga M, Miki K, et al. Accuracy of OCT, grayscale IVUS, and their combination for the diagnosis of coronary TCFA: an *ex vivo* validation study. *JACC-Cardiovasc Imag.* (2015) 8:451–60. doi: 10.1016/j.jcmg.2014.10.015
35. Doradla P, Otsuka K, Nadkarni A, Villiger M, Karanasos A. Zandvoort LJv, et al. Biomechanical stress profiling of coronary atherosclerosis: Identifying a multifactorial metric to evaluate plaque rupture risk. *JACC-Cardiovasc Imag.* (2020) 13:804–16. doi: 10.1016/j.jcmg.2019.01.033
36. Ono M, Kawashima H, Hara H, Gao C, Wang R, Kogame N, et al. Advances in IVUS/OCT and future clinical perspective of novel hybrid catheter system in coronary imaging. *Front Cardiovasc Med.* (2020) 7:119. doi: 10.3389/fcvm.2020.00119

37. Lu X, Yang J, Zhao JB, Gregersen H, Kassab GS. Shear modulus of porcine coronary artery: contributions of media and adventitia. *Am J Physiol-Heart Circul Physiol.* (2003) 285:H1966–75. doi: 10.1152/ajpheart.00357
38. Thondapu V, Bourantas CV, Foin N, Jang I-K, Serruys PW, Barlis P. Biomechanical stress in coronary atherosclerosis: emerging insights from computational modelling. *Eur Heart J.* (2016) 38:81–92. doi: 10.1093/eurheartj/ehv689
39. Holzapfel GA, Sommer G, Regitnig P. Anisotropic mechanical properties of tissue components in human atherosclerotic plaques. *J Biomech Eng.* (2004) 126:657–65. doi: 10.1115/1.1800557
40. Holzapfel GA, Gasser TC, Ogden RW. A new constitutive framework for arterial wall mechanics and a comparative study of material models. *J Elast.* (2000) 61:1–48. doi: 10.1023/A:1010835316564
41. Baldewsing RA, de Korte CL, Schaar JA, Mastik F, van der Steen AFW. Finite element modeling and intravascular ultrasound elastography of vulnerable plaques: parameter variation. *Ultrasonics.* (2004) 42:723–9. doi: 10.1016/j.ultras.2003.11.017
42. Costopoulos C, Maehara A, Huang Y, Brown AJ, Gillard JH, Teng Z, et al. Heterogeneity of plaque structural stress Is increased in plaques leading to MACE: insights from the PROSPECT study. *JACC-Cardiovasc Imag.* (2020) 13:1206–18. doi: 10.1016/j.jcmg.2019.05.024
43. Speelman L, Akyildiz AC, den Adel B, Wentzel JJ, van der Steen AFW, Virmani R, et al. Initial stress in biomechanical models of atherosclerotic plaques. *J Biomech.* (2011) 44:2376–82. doi: 10.1016/j.jbiomech.2011.07.004
44. Huang X, Yang C, Yuan C, Liu F, Canton G, Zheng J, et al. Patient-specific artery shrinkage and 3D zero-stress state in multi-component 3D FSI models for carotid atherosclerotic plaques based on *in vivo* MRI data. *Mol Cell Biomech.* (2009) 6:121–34. doi: 10.3970/mcb.2009.006.121
45. Huang Y, Teng Z, Sadat U, Hilborne S, Young VE, Graves MJ, et al. Non-uniform shrinkage for obtaining computational start shape for in-vivo MRI-based plaque vulnerability assessment. *J Biomech.* (2011) 44:2316–9. doi: 10.1016/j.jbiomech.2011.06.014
46. Arbab-Zadeh A, DeMaria AN, Penny WF, Russo RJ, Kimura BJ, Bhargava V. Axial movement of the intravascular ultrasound probe during the cardiac cycle: implications for three-dimensional reconstruction and measurements of coronary dimensions. *Am Heart J.* (1999) 138:865–72. doi: 10.1016/S0002-8703(99)70011-6
47. Lee RT, Loree HM, Cheng GC, Lieberman EH, Jaramillo N, Schoen FJ. Computational structural analysis based on intravascular ultrasound imaging before *in vitro* angioplasty: prediction of plaque fracture locations. *J Am Coll Cardiol.* (1993) 21:777–82. doi: 10.1016/0735-1097(93)90112-E
48. Fukumoto Y, Hiro T, Fujii T, Hashimoto G, Fujimura T, Yamada J, et al. Localized elevation of shear stress is related to coronary plaque rupture. *J Am Coll Cardiol.* (2008) 51:645–50. doi: 10.1016/j.jacc.2007.10.030
49. Gijsen FJH, Wentzel JJ, Thury A, Mastik F, Schaar JA, Schuurbiers JCH, et al. Strain distribution over plaques in human coronary arteries relates to shear stress. *Am J Physiol-Heart Circul Physiol.* (2008) 295:H1608–14. PubMed PMID: 18621851. doi: 10.1152/ajpheart.01081.2007
50. Lee JM, Choi G, Hwang D, Park J, Kim HJ, Doh J-H, et al. Impact of longitudinal lesion geometry on location of plaque rupture and clinical presentations. *JACC-Cardiovasc Imag.* (2017) 10:677–88. doi: 10.1016/j.jcmg.2016.04.012
51. Wentzel JJ, Chatzizisis YS, Gijsen FJH, Giannoglou GD, Feldman CL, Stone PH. Endothelial shear stress in the evolution of coronary atherosclerotic plaque and vascular remodelling: current understanding and remaining questions. *Cardiovasc Res.* (2012) 96:234–43. doi: 10.1093/cvr/cvs217
52. Buntin CM, Silver FH. Noninvasive assessment of mechanical properties of peripheral arteries. *Ann Biomed Eng.* (1990) 18:549–66. doi: 10.1007/BF02364617
53. Lee RT, Kamm RD. Vascular mechanics for the cardiologist. *J Am Coll Cardiol.* (1994) 23:1289–95. doi: 10.1016/0735-1097(94)90369-7
54. Shimazu T, Hori M, Mishima M, Kitabatake A, Kodama K, Nanto S, et al. Clinical assessment of elastic properties of large coronary arteries: pressure-diameter relationship and dynamic incremental elastic modulus. *Int J Cardiovasc Imaging.* (1986) 13:27–45. doi: 10.1016/0167-5273(86)90077-X
55. Shaw JA, Kingwell BA, Walton AS, Cameron JD, Pillay P, Gatzka CD, et al. Determinants of coronary artery compliance in subjects with and without angiographic coronary artery disease. *J Am Coll Cardiol.* (2002) 39:1637–43. doi: 10.1016/S0735-1097(02)01842-9
56. Ali ZA, Karimi Galougahi K, Maehara A, Shlofmitz RA, Ben-Yehuda O, Mintz GS, et al. Intracoronary optical coherence tomography 2018: current status and future directions. *JACC-Cardiovasc Interv.* (2017) 10:2473–87. doi: 10.1016/j.jcin.2017.09.042
57. Smith SC, Dove JT, Jacobs AK, Ward Kennedy J, Kereiakes D, Kern MJ, et al. ACC/AHA guidelines for percutaneous coronary intervention (revision of the 1993 PTCA guidelines)—executive summary. *J Am Coll Cardiol.* (2001) 37:2215–38. doi: 10.1016/S0735-1097(01)01344-4
58. Antoniadis AP, Papafaklis MI, Takahashi S, Shishido K, Andreou I, Chatzizisis YS, et al. Arterial remodeling and endothelial shear stress exhibit significant longitudinal heterogeneity along the length of coronary plaques. *JACC-Cardiovasc Imag.* (2016) 9:1007–9. doi: 10.1016/j.jcmg.2016.04.003
59. Dobrin PB. Mechanical properties of arteries. *Physiol Rev.* (1978) 58:397–460. doi: 10.1152/physrev.1978.58.2.397
60. Pao YC, Lu JT, Ritman EL. Bending and twisting of an *in vivo* coronary artery at a bifurcation. *J Biomech.* (1992) 25:287–95. doi: 10.1016/0021-9290(92)90026-W
61. Waldman LK, Fung YC, Covell JW. Transmural myocardial deformation in the canine left ventricle. Normal *in vivo* three-dimensional finite strains. *Circ Res.* (1985) 57:152–63. doi: 10.1161/01.RES.57.1.152

Conflict of Interest: WW reports research grants and honoraria from MicroPort, medical advisor of Rede Optimus Research and co-founder of Argonauts, an innovation facilitator. ST reports research grants and consultancy from Pulse medical imaging technology. PS reports personal fees from Sino Medical Science Technology, Philips/Volcano, Xeltis, HeartFlow, and SMT, outside the submitted work.

The remaining authors declare that the research was conducted in the absence of any commercial or financial relationships that could be construed as a potential conflict of interest.

Publisher's Note: All claims expressed in this article are solely those of the authors and do not necessarily represent those of their affiliated organizations, or those of the publisher, the editors and the reviewers. Any product that may be evaluated in this article, or claim that may be made by its manufacturer, is not guaranteed or endorsed by the publisher.

frontiers in Cardiovascular Medicine

ORIGINAL RESEARCH
published: 18 November 2021
doi: 10.3389/fcvm.2021.732646

The Association Between Time-Varying Wall Shear Stress and the Development of Plaque Ulcerations in Carotid Arteries From the Plaque at Risk Study

*Kristine Dilba[1,2], Dianne H. K. van Dam-Nolen[2], Suze-Anne Korteland[1], Anja G. van der Kolk[3], Mohamed Kassem[4], Daniel Bos[2,5], Peter J. Koudstaal[6], Paul J. Nederkoorn[7], Jeroen Hendrikse[3], M. Eline Kooi[4], Frank J. H. Gijsen[1], Anton F. W. van der Steen[1], Aad van der Lugt[2] and Jolanda J. Wentzel[1]**

[1] Department of Cardiology, Erasmus MC, University Medical Center Rotterdam, Rotterdam, Netherlands, [2] Department of Radiology and Nuclear Medicine, Erasmus MC, University Medical Center Rotterdam, Rotterdam, Netherlands, [3] Department of Radiology, University Medical Center Utrecht, Utrecht, Netherlands, [4] Department of Radiology and Nuclear Medicine, CARIM School for Cardiovascular Diseases, Maastricht University Medical Center+, Maastricht, Netherlands, [5] Department of Epidemiology, Erasmus MC, University Medical Center Rotterdam, Rotterdam, Netherlands, [6] Department of Neurology, Erasmus MC, University Medical Center Rotterdam, Rotterdam, Netherlands, [7] Department of Neurology, University Medical Centers Amsterdam, Amsterdam, Netherlands

OPEN ACCESS

Edited by:
Christos Bourantas,
University College London,
United Kingdom

Reviewed by:
Antonis Sakellarios,
University of Ioannina, Greece
Vikas Thondapu,
Yale University, United States

***Correspondence:**
Jolanda J. Wentzel
j.wentzel@erasmusmc.nl

Specialty section:
This article was submitted to Cardiovascular Imaging, a section of the journal Frontiers in Cardiovascular Medicine

Received: 29 June 2021
Accepted: 06 October 2021
Published: 18 November 2021

Citation:
Dilba K, van Dam-Nolen DHK, Korteland S-A, van der Kolk AG, Kassem M, Bos D, Koudstaal PJ, Nederkoorn PJ, Hendrikse J, Kooi ME, Gijsen FJH, van der Steen AFW, van der Lugt A and Wentzel JJ (2021) The Association Between Time-Varying Wall Shear Stress and the Development of Plaque Ulcerations in Carotid Arteries From the Plaque at Risk Study. Front. Cardiovasc. Med. 8:732646. doi: 10.3389/fcvm.2021.732646

Background and Purpose: Shear stress (WSS) is involved in the pathophysiology of atherosclerotic disease and might affect plaque ulceration. In this case-control study, we compared carotid plaques that developed a *new* ulcer during follow-up and plaques that remained silent for their exposure to time-dependent oscillatory shear stress parameters at baseline.

Materials and Methods: Eighteen patients who underwent CTA and MRI of their carotid arteries at baseline and 2 years follow-up were included. These 18 patients consisted of six patients who demonstrated a new ulcer and 12 control patients selected from a larger cohort with similar MRI-based plaque characteristics as the ulcer group. (Oscillatory) WSS parameters [time average WSS, oscillatory shear index (OSI), and relative residence time (RRT)] were calculated using computational fluid dynamics applying the MRI-based geometry of the carotid arteries and compared among plaques (wall thickness>2 mm) with and without ulceration (Mann–Whitney *U* test) and ulcer-site vs. non-ulcer-site within the plaque (Wilcoxon signed rank test). More detailed analysis on ulcer cases was performed and the predictive value of oscillatory WSS parameters was calculated using linear and logistic mixed-effect regression models.

Results: The ulcer group demonstrated no difference in maximum WSS [9.9 (6.6–18.5) vs. 13.6 (9.7–17.7) Pa, $p = 0.349$], a lower maximum OSI [0.04 (0.01–0.10) vs. 0.12 (0.06–0.20) $p = 0.019$] and lower maximum RRT [1.25 (0.78–2.03) Pa^{-1} vs. 2.93 (2.03–5.28) Pa^{-1}, $p = 0.011$] compared to controls. The location of the ulcer (ulcer-site) within the plaque was not always at the maximal WSS, but demonstrated higher average WSS, lower average RRT and OSI at the ulcer-site compared to the non-ulcer-sites. High WSS (WSS>4.3 Pa) and low RRT (RRT < 0.25 Pa) were associated with ulceration with

an odds ratio of 3.6 [CI 2.1–6.3] and 2.6 [CI 1.54–4.44] respectively, which remained significant after adjustment for wall thickness.

Conclusion: In this explorative study, ulcers were not exclusively located at plaque regions exposed to the highest WSS, OSI, or RRT, but high WSS and low RRT regions had a significantly higher odds to present ulceration within the plaque even after adjustment for wall thickness.

Keywords: shear stress (fluid), carotid, ulceration, risk, atherosclerotic cardiovascular disease, MRI, computational fluid dynamics

INTRODUCTION

Carotid atherosclerotic plaque rupture with thrombus formation and artery-to-artery embolism remains one of the leading causes of ischemic stroke (1, 2). Currently, the decision to perform a carotid endarterectomy is determined by the clinical symptomatology and the presence of severe stenosis in the carotid artery (3). However, there is robust evidence that a substantial number of clinical events occur in patients who have a low degree of stenosis, showing that other characteristics of the plaque beyond stenosis may also play an important role (4, 5). Therefore, researchers started to investigate other markers of rupture-prone plaques beyond the degree of luminal stenosis, mainly focusing on plaque composition to identify vulnerable plaques (6). Vulnerable plaques are characterized by a large lipid rich necrotic core (LRNC) covered by a thin fibrous cap and the presence of intraplaque hemorrhage (IPH) (7–10). However, not all vulnerable plaques do rupture and cause symptoms (9).

Wall shear stress (WSS) is the frictional force that flowing blood exerts on endothelial cells and plays a substantial role in plaque initiation and growth (11, 12). Initially, atherosclerotic plaques develop at inner curvature regions or close to side branches, where WSS is low and oscillating (11, 13). WSS oscillations have been defined using the oscillatory shear index (OSI) and relative residence time (RRT) (14, 15). High OSI and RRT were associated with plaque growth in carotid bifurcations (13). Since ulcers were most frequently observed at the upstream part of the stenotic carotid plaques, where WSS is supposedly high, it was hypothesized that high WSS influences plaque destabilization and thus plaque ulceration (16, 17). Furthermore, in coronary arteries it was observed that plaque rupture was also associated with OSI and RRT (18).

Longitudinal studies that investigated the association between WSS and plaque rupture in carotid arteries have hardly been performed, since ulcerations are not frequently captured during the follow-up period. Up till now, only three case studies have been performed reporting controversial results (17, 19, 20). However, they did not evaluate the role of WSS oscillations in relation to plaque ulceration. Therefore, we investigated in a case-control study design the relation between WSS, OSI, and RRT at baseline and new ulceration formation during 2 years of follow-up in patients with mild-to-moderate carotid artery stenosis. Furthermore, a detailed analysis on the ulcer location within the plaque was performed.

METHODS

Study Population

This study is embedded within the Plaque At Risk (PARISK) study (clinicaltrials.gov NCT01208025) (21). Non-invasive plaque imaging [Ultrasound (US), MDCTA, MRI] was scheduled at baseline in all 240 included patients and in a predefined subset of patients at 2 years follow-up. For this study, we only selected patients that, in addition to baseline MDCTA and MRI, underwent MDCTA at 2 years follow-up.

Cases were defined as patients who developed new plaque ulceration during follow-up. In a previous study (22), we demonstrated that plaques presenting with newly formed ulceration during follow-up have a larger wall volume, percentage LRNC and IPH volume than the cases without ulceration. Moreover, since WSS is dependent on the luminal dimensions of the carotid arteries, the carotid arteries of the selected control patients were chosen to have similar lumen dimensions. The selection procedure was as follows: first, patients with carotid plaques presenting with LRNC and IPH were selected ($n = 21$). Those patients were ranked on minimal lumen diameter and by checking the percentage of IPH, LRNC, and wall volume two control cases were selected per ulcer case. Using this approach, WSS parameters could be compared between patients with (cases) and without new plaque ulceration, independent of known confounding factors. The study was approved by the institutional Medical Ethical Committees. Written informed consent was obtained from each participant before enrollment.

MDCTA Data Acquisition and Analysis

We performed MDCTA image acquisition by using a standardized protocol, as previously described in the study design article (21). All MDCTA images were transferred to a workstation equipped with dedicated 3D analysis software (Syngo. *via*; Siemens, Erlangen, Germany). This multiplanar reformatting application allowed analysis of carotid arteries in oblique, coronal, and sagittal planes.

The symptomatic carotid artery was analyzed. The degree of luminal stenosis in the carotid artery was measured according to the NASCET and ECST criteria (3, 23). Also, the minimal luminal diameter was established. Plaque surface morphology was evaluated and classified as either ulcerated or non-ulcerated. Plaque ulceration was defined as an extension of contrast material of >1 mm into the atherosclerotic plaque, being visible on at least two perpendicular planes (24).

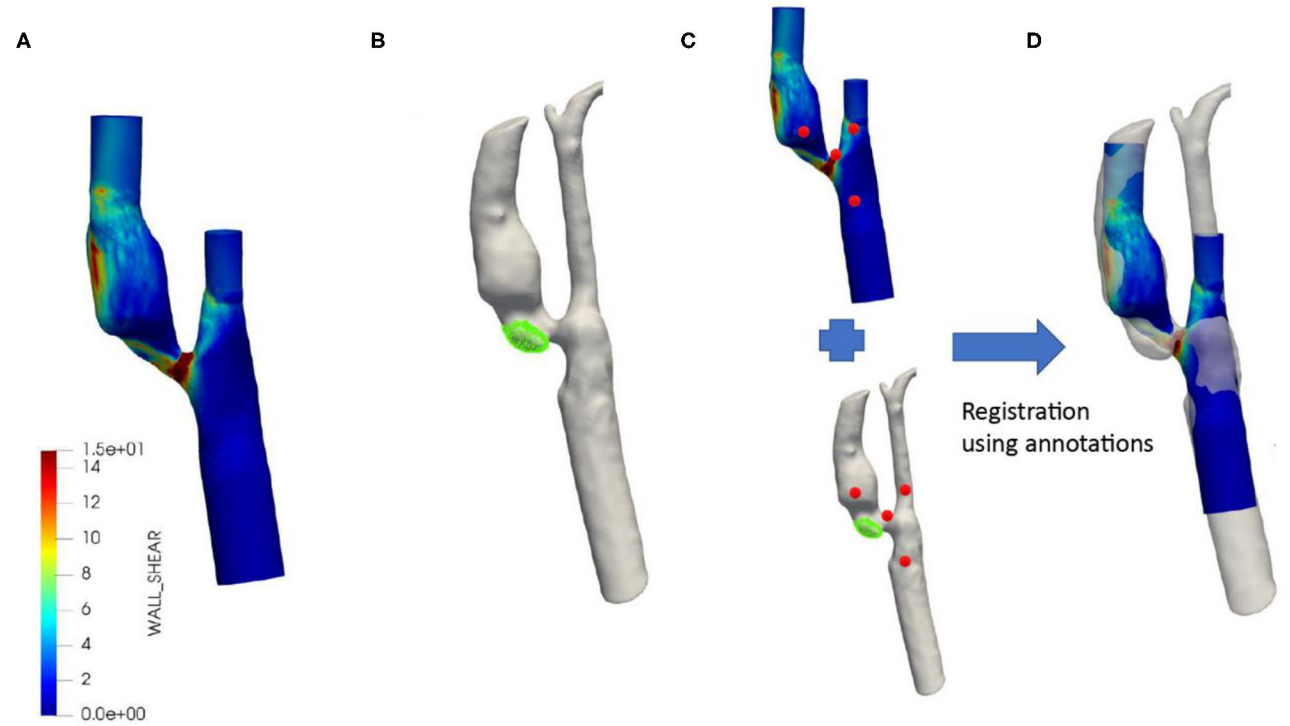

FIGURE 1 | Typical example of co-registered baseline wall shear stress distribution with follow-up MDCTA. WSS distribution over the symptomatic carotid artery based on MRI baseline contours and flow as measured by Duplex **(A)**. Segmented MDCTA follow-up lumen with the new ulcer shown in green **(B)**. Registration between MRI baseline and MDCTA follow-up using annotations (red) **(C)**. Final registration of baseline MRI including wall shear stress and MDCTA with new ulcer **(D)**.

Plaque surface morphology was evaluated by two trained readers at baseline (B.H. and A.C.v.D) and at follow-up (K.D. and D.v.D.N.). The trained readers (B.H., A.C.v.D., K.D., and D.v.D.N.) were physicians who were first trained on a training set to identify the presence of ulceration on MDCTA. They had to successfully complete this training set before they assessed the ulcerations on the PARISK data set. The third observer who was consulted for consensus in case of no-agreement is a neuroradiologist with $>$ 25 years of experience (A.v.d.L.). Temporal changes in plaque surface morphology were subsequently evaluated by two trained readers (K.D. and D.v.D.N.) by visual comparison of baseline and follow-up images in which a newly formed ulceration was detected.

MRI Data Acquisition and Analysis

All examinations were performed on 3.0 T whole body MRI scanners [Achieva, Philips Healthcare, Best, The Netherlands; or Discovery MR 750; General Electric (GE) Healthcare, Milwaukee, Wisconsin]. Imaging protocols included five sequences that were comparable between centers. A more detailed description of these sequences has previously been described in the study design article (21). Six observers evaluated the MR images of the symptomatic carotid artery with dedicated vessel wall analysis software (VesselMass; Department Radiology, Leiden University Medical Center, The Netherlands). Observers had to demonstrate good interobserver agreement for all parameters (intraclass correlation coefficient/ kappa values $\geq$ 0.6) on a validation set that was delineated by experts with $>$ 15 years of experience (M.E.K. and A.v.d.L.), before they could start with delineating the MR images. The observers were blinded to clinical data and other imaging examinations. Firstly, the different MRI sequences were registered, which allowed us to use multisequence imaging criteria to subsequently draw contours of vessel lumen, outer vessel wall and plaque components such as IPH, LRNC, and calcifications (25). The lumen and wall volume were calculated and since, for all patients, the same nine slices (five in the internal and four in the common carotid artery) were used, bias because of different scan ranges that may include different lengths of common carotid artery and internal carotid artery was prevented. Percentage wall volume was calculated as wall volume/(wall volume + lumen volume) $*$ 100%. The relative volume of plaque components to wall volume (outer vessel volume−lumen volume) was also calculated (e.g., percentage IPH = IPH volume/wall volume $*$ 100%).

Assessment of (Oscillatory) Wall Shear Stress Parameters

The commercial software MATLAB (The MathWorks, Massachusetts, USA) was used to generate the 3D geometry of the carotid bifurcation using MRI contours obtained from the VesselMass software. The Vascular Modeling ToolKit (VMTK, www.vmtk.org) was used to add flow extensions to the in and outflow boundaries and to smoothen the surface of the

bifurcation. The reconstructed geometry was loaded into ANSYS ICEM (version 17.1) to generate a tetrahedral volume mesh with five layers of prism elements at the vessel wall. This mesh was then imported into ANSYS Fluent (version 17.1) to calculate WSS by solving the Navier Stokes equations. The blood was modeled as an incompressible non-Newtonian fluid (Carreau model) with a density of 1,060 kg/m^3. The arterial wall was assumed to be rigid and a no-slip boundary condition at the wall was applied. At the inlet of the common carotid artery (CCA), a transient flow curve was applied based on the average flow curve (26). For each patient, the flow curve was scaled such that the average flow agreed with the measured flow in the CCA using color Doppler. The flow was obtained by combining the velocity data measured by color doppler with local measurements of the diameter of the artery. This approach was used to be less sensitive to measurement artifacts in the individual patient. A heartrate of 68 bpm was assumed. In addition, using these flows, a Womersley profile was prescribed over the surface of the CCA inlet (27). Outflow ratios for the internal carotid artery and external carotid artery were assumed to be 64 vs. 36%, since the vessels were not severely stenotic (28). The simulation was carried out over two full heart cycles. The first heart cycle was used for initialization, while the second heart cycle was used to compute the (oscillatory) WSS parameters. Each heart cycle was divided into 200-time steps (∼4.4 ms dependent on the heart rate). Post-processing of the computational fluid dynamics (CFD) simulation results was done in MATLAB (The MathWorks, Massachusetts, USA). Over the whole vessel, the time averaged WSS (WSS), oscillatory shear index (OSI), and relative residence time (RRT) were calculated (14, 15, 29, 30). The time-averaged WSS is the WSS averaged over the cardiac cycle. OSI represents a ratio between back-and forward going WSS. RRT represents the relative time that a blood particle resides at a certain location at the vessel wall. **Figure 1A** shows an example of a 3D WSS-map on the lumen surface of the carotid artery.

Ulcer Segmentation and Registration

In order to study the ulcer location at follow-up in detail with respect to the local oscillatory WSS parameters at baseline, we reconstructed the MDCTA-based lumen and ulcer at follow-up and co-registered this reconstructed 3D geometry to the baseline MRI-based 3D geometry *via* the following steps (**Figure 1**). First, based on the local Hounsfield Units the vessel lumen and ulcer (320–500 HU) were segmented on MDCTA follow-up images using the open source software *3D slicer* (4.10 version) (31, 32). Subsequently, a four-point rigid registration approach was applied using the *3D slicer* software to register the baseline (MRI) and follow-up geometry (MDCTA). The 1st fiducial point was placed as a landmark on the carina, the 2nd was on the ECA, the 3rd was on the ICA, and the 4th was on the CCA. Using these fiducial points, baseline MRI and follow-up MDCTA lumen geometries were aligned for maximum overlap of the carotid arteries. Finally, the ulcer surface location was projected on the WSS surface mesh using VMTK to determine the exact location of the ulcer within the plaque. This is called the ulcer-site in the plaque and the remainder of the plaque was considered the non-ulcer-site.

Statistical Analysis

First, clinical characteristics and plaque parameters in cases and controls were compared. Continuous variables were compared with Mann-Whitney U test and categorical data were evaluated using Fisher Exact test. The lumen surface was subdivided into regions (15° x 0.7 mm length) and the local wall thickness and average WSS, OSI, and RRT were calculated over these regions. The plaque regions were defined as the regions with wall thickness > 2 mm.

The analysis was performed at two levels: at patient level and at region level. The analysis was performed at the patient level to identify some extreme (oscillatory) WSS values and wall thickness information characteristic for plaques that develop an ulcer at follow up: the maximum WSS (maxWSS), minimum WSS (minWSS), maximum OSI (maxOSI), maximum RRT (maxRRT), and maximum wall thickness (maxWT). The maximum value was the 95th percentile of all the values. These values were compared for plaques with an ulcer and plaques without an ulcer (control cases). Using the Mann-Whitney *U* test. The same parameters were also determined at the ulcer-site within the plaque in comparison with the remainder of the plaque (non-ulcer-site). Therefore, the plaque surface (3-D surface) was divided into ulcer-site and non-ulcer-site. The methodology to register the ulcer location at follow-up with the (oscillatory) WSS values at baseline is described in detail above. The differences in minimum and maximum WSS, maximum OSI and maximum RRT, and maximum wall thickness between the ulcer-site and non-ulcer-site were compared with a one sample Wilcoxon signed rank test. For the plaques that developed an ulcer at follow-up, the analysis was also repeated at the region level to identify in even more detail the (oscillatory) WSS characteristics that are associated with the location of ulceration at follow-up. Therefore, the regions within the ulcer-site were identified and compared to the regions outside the ulcer site using linear mixed-effect regression models with the patient as a random factor to consider within patient clustering. To compute an odds ratio of oscillatory WSS parameters for the development of ulcer at follow up, the (oscillatory) WSS parameters were categorized in low, mid, and high based on the frequency distribution and logistics mixed-effect regression models with the patient as random factors were applied. The odds ratios are reported with their 95% confidence interval. A value of $p < 0.05$ was considered as significant (two sided). Continuous variables per patient are presented as median with interquartile range. The values presented based on the regional analysis are estimated means and standard error. All calculations were performed using SPSS version 21 (33).

RESULTS

Patient Characteristics

Figure 2 shows a flow diagram of patients included and excluded from the analyses, and the number of patients in the ulcer and control group. Seventy-three patients had good quality CTA

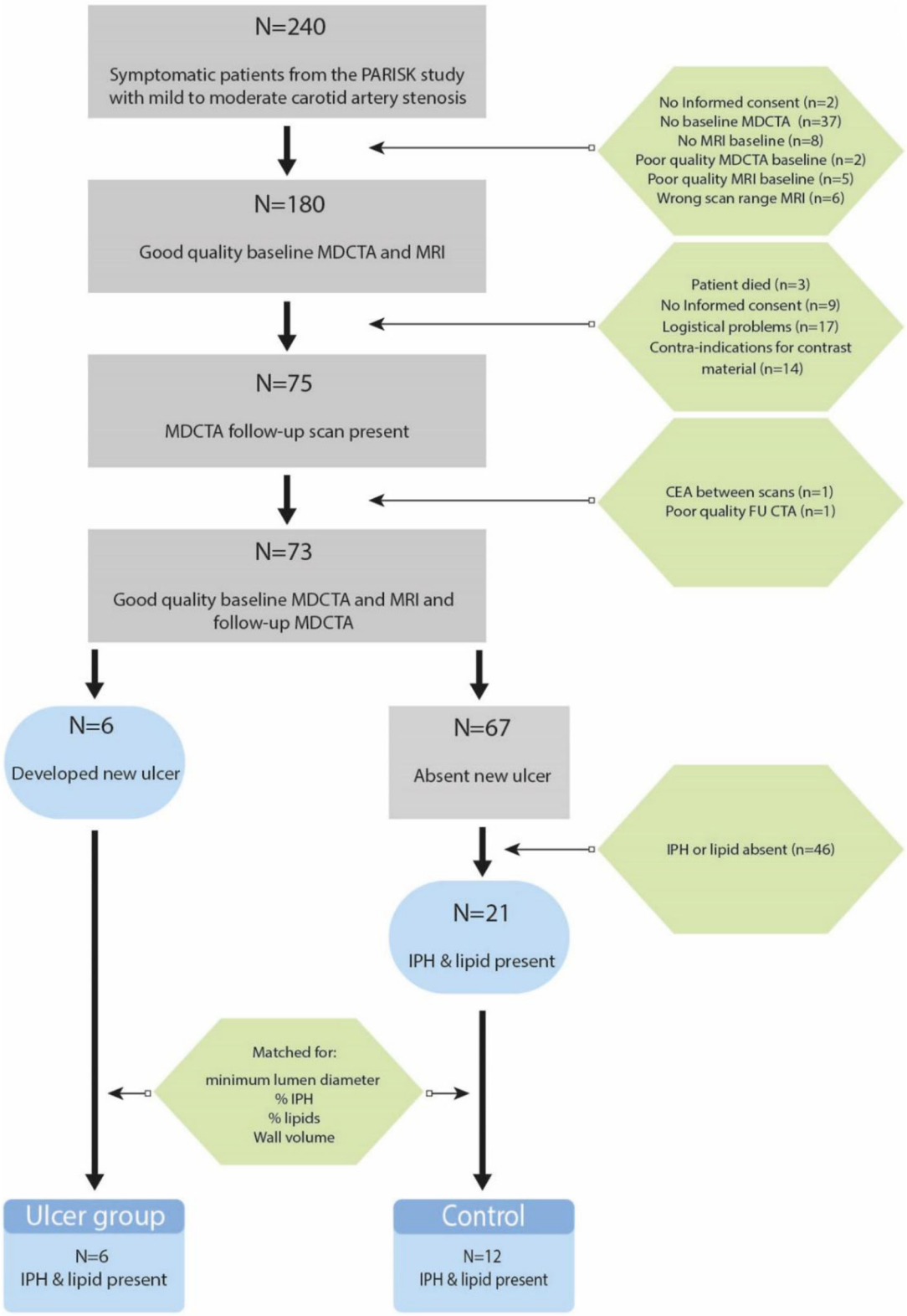

FIGURE 2 | Flow diagram of patients that are included and reasons for exclusion in the final data analysis.

TABLE 1 | Plaque characteristics in the symptomatic carotid artery with (cases) and without (controls) new ulcerations at follow-up.

	New ulceration present ($n = 6$)	New ulceration absent ($n = 12$)	*p* value
Total vessel volume (cm^3)	1.61 [1.53–1.87]	1.55 [1.30–1.86]	0.55
Wall volume (cm^3)	1.04 [0.97–1.16]	1.04 [0.88–1.15]	0.75
Lumen volume (cm^3)	0.59 [0.55–0.69]	0.53 [0.45–0.65]	0.25
% wall volume	64 [59–67]	66 [61–68]	0.39
% LRNC volume	23 [16–31]	15 [11–25]	0.15
% calcifications volume	6 [2–9]	7 [5–8]	0.75
% IPH volume	14 [8–24]	11 [7–19]	0.44
NASCET (%)	14 [0–39]	25 [12–35]	0.55
ECST (%)	62 [53–71]	66 [55–69]	0.82
Minimal lumen diameter (mm)	3.4 [2.9–4.8]	3.1 [2.8–4.4]	0.49
LRNC presence	100%	100%	
Calcifications presence	100%	100%	
IPH presence	100%	100%	
Maximal wall thickness (mm)	4.1 [3.6–4.3]	4.0 [3.6–4.5]	0.89
Mean wall thickness (mm)	2.8 [2.6–2.8]	2.7 [2.5–2.9]	0.96

LRNC, Lipid rich necrotic core; IPH, Intraplaque hemorrhage; NASCET, North American Symptomatic Carotid Endarterectomy Trial, definition of percentage lumen stenosis; ESCT, European symptomatic carotid endarterectomy trial: definition of percentage lumen stenosis.

TABLE 2 | Wall shear stress and wall thickness in the symptomatic carotid artery with (cases) and without (controls) new ulcerations at follow-up.

	New ulceration present ($n = 6$)	New ulceration absent ($n = 12$)	
Parameters	**Median [IQR]**	**Median [IQR]**	***P* value**
Minimum wall shear stress (Pa)	0.5 [0.4–0.8]	0.3 [0.2–0.4]	0.083
Maximum wall shear stress (Pa)	9.9 [6.6–18.5]	13.6 [9.7–17.7]	0.349
Maximum oscillatory shear index	0.04 [0.01–0.10]	0.12 [0.06–0.20]	0.019
Maximum relative residence time (Pa^{-1})	1.25 [0.78–2.03]	2.93 [2.03–5.28]	0.011
Maximum wall thickness (mm)	4.1 [3.6–4.25]	4.0 [3.55–4.52]	0.888

Maximum is the 95th percentile of the data except for wall thickness.

and MRI of their carotid arteries to assess atherosclerosis at baseline and 2 years follow-up. New ulcerations developed in six symptomatic atherosclerotic carotid plaques. The control group consisted of 12 patients with matched plaque characteristics. The median age of the study population ($n = 18$) was 70 (62–72) years and 89% of the participants was male. Sixty-one percent of the patients had hypertension, 83% had hypercholesterolemia, and 28% had diabetes mellitus. As anticipated, no differences in minimum lumen diameter, %IPH, %LRNC, and wall volume were observed between the group with and without new ulceration at follow-up (**Table 1**). However, the matched control cases also did not show differences in other plaque characteristics (**Table 1**).

Comparison Between Ulcer Cases and Controls

With the small number of plaques that developed a new ulceration after 2 years of follow-up, we could not demonstrate a significant difference in maxWSS compared to plaques that did not develop an ulceration (**Table 2**, **Figure 3**). The plaques that developed an ulceration tended to show a higher minWSS at baseline compared to the control group [0.5 Pa (0.4–0.8) vs. 0.3 (0.2–0.4); $p = 0.083$, **Figure 3**]. Interestingly, the maxOSI was lower for the ulceration group than for the control group [0.04 (0.01–0.10) vs. 0.12 (0.06–0.20); $p = 0.019$, **Figure 3**]. Regarding RRT, the ulceration group also showed lower maxRRT values compared to control group [1.25 (0.78–2.03) Pa^{-1} vs. 2.93 (2.03–5.28) Pa^{-1}; $p = 0.011$, **Figure 3**, **Table 2**]. No difference in maxWT was observed [4.1 (3.6–4.25) vs. 4.0 (3.55–4.52) mm, $p = 0.88$].

Comparison Within Ulcerated Plaques: Ulcer-Site vs. Non-ulcer-site

After registration, we noticed that in one case the ulceration on the follow-up MDCTA was partially located above the scan range on baseline MRI. Therefore, that case was excluded from further analysis. In the remaining five plaques, the minWSS at the ulcer-site was significantly higher than the minWSS at the non-ulcer-site within the plaque ($p = 0.04$) (**Table 3**, **Figure 4**). However, for maxWSS, no consistent difference between the ulcer and nonulcer site was observed: in three cases a higher maxWSS and in two cases a lower maxWSS was demonstrated at the ulcer site compared the rest of the plaque (**Table 3**). The maxOSI and maxRRT were significantly lower at the ulcer site compared to the non-ulcer site ($p = 0.043$ and $p = 0.043$). Furthermore, the maxWT at the ulcer site was not different comparted to the non-ulcer-site [3.8 (3.5–4.1) vs. 4.1 (3.7–4.3) mm, $p = 0.14$; **Table 3**].

Analysis at Region Level of Ulcer Cases

For the ulcer cases, the mean WSS at the ulcer-regions was significantly higher (6.9 ± 40.1 vs. 4.3 ± 40.1 Pa), the RRT was lower (0.37 ± 0.1 vs. 0.65 ± 0.0 Pa^{-1}), and WT was higher (3.3 ± 0.4 vs. 2.7 ± 0.4 mm) compared to the non-ulcer regions. For the OSI (0.013 vs. 0.009, $p = 0.14$), no significant differences were found. The odds ratio of low RRT compared to high RRT was 2.6 (CI 1.54–4.44), and high WSS compared to low WSS was 3.6 (CI 2.1–6.3) for the development of ulcers. After adjustment for wall thickness, high WSS and low RRT remained independently associated with ulceration with an odds of 1.59 (1.20–2.1) for high WSS and 1.5 (1.2–2.0) for low RRT. Low OSI was not associated at all with ulceration (**Figure 5**).

DISCUSSION

This case-control study investigated the difference in (oscillatory) WSS parameters among plaques that developed an ulcer during a follow-up period of 2 years, and matched control cases. Furthermore, we evaluated these parameters within the plaque comparing the ulcer-site from the non-ulcer site at the patient

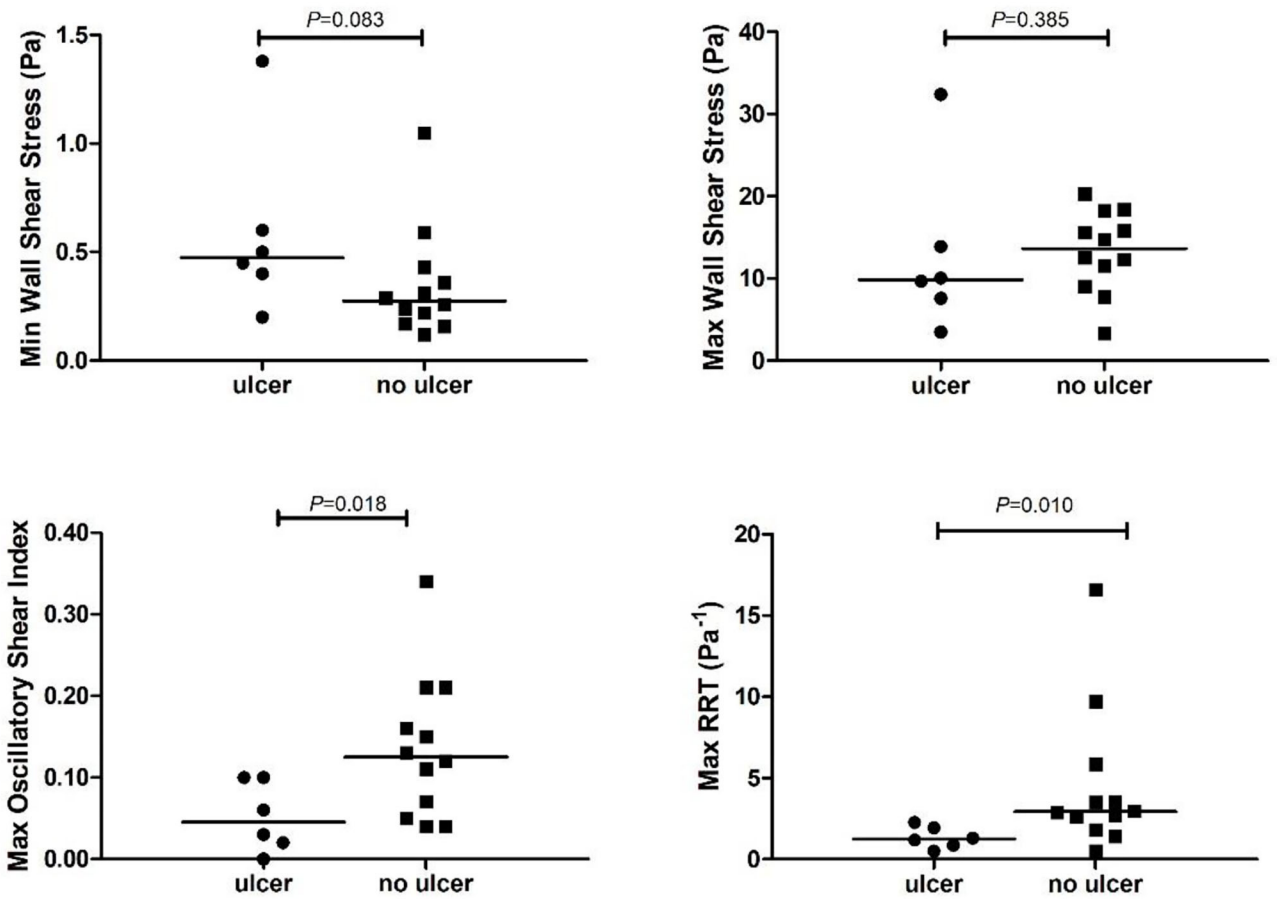

FIGURE 3 | Time varying wall shear stress at the plaque that developed an ulcer (ulcer) vs. the control plaques (no ulcer). RRT, relative residence time. Maximum or minimum time varying wall shear stress values are calculated at the plaque with ulcer or at the plaque without ulcer (no ulcer).

TABLE 3 | Comparison of wall shear stress and wall thickness measurements at ulcer site and non-ulcer site.

		Patient 1	Patient 2	Patient 3	Patient 4	Patient 5	Patient 6	Median	P value
Minimum wall shear stress (Pa)	Ulcer-site	1.8	0.7	0.8	2.3	0.9	NA	0.9 [0.7–2.1]	0.04
	Non-ulcer-site	0.6	0.4	0.2	0.5	0.5	NA	0.5 [0.3–0.6]	
Maximum wall shear stress (Pa)	Ulcer-site	6.7	1.4	15.1	9.6	19.3	NA	9.6 [4.1–17.2]	0.68
	Non-ulcer-site	32.5	3.5	9.5	7.0	11.8	NA	9.5 [5.2–22.1]	
Maximum oscillatory shear index	Ulcer-site	0.05	0.01	0.09	0.01	0.01	NA	0.01 [0.01–0.07]	0.04
	Non-ulcer-site	0.10	0.02	0.10	0.04	0.07	NA	0.07 [0.03–0.10]	
Maximum relative residence time (Pa^{-1})	Ulcer-site	0.61	1.30	1.48	0.37	0.53	NA	0.61 [0.45–1.39]	0.04
	Non-ulcer-site	0.92	1.97	2.39	1.24	1.45	NA	1.44 [1.08–2.18]	
	Non-ulcer-site	2.7	2.0	2.1	2.7	2.4	NA	2.7 [2.5–2.9]	
Maximum wall thickness (mm)	Ulcer-site	3.6	3.8	4.1	3.3	4.1	NA	3.8 [3.5–4.1]	0.14
	Non-ulcer-site	4.1	4.2	4.4	3.3	4.0	NA	4.1 [3.7–4.3]	

Maximum is 95th percentile, except for the wall thickness.

level and regional level. Our main findings were as follows: plaques that developed an ulcer could not be discriminated from control plaques based on the maximum WSS. However, plaques that developed an ulcer had significantly lower maximum values of OSI and RRT than plaques that did not develop an ulcer. More detailed analysis on (oscillatory) WSS parameters within the plaque demonstrated that at the ulcer location, compared to the non-ulcer-site, the average WSS was higher with higher odds to develop an ulcer at regions exposed to the highest WSS tertile. Moreover, the average RRT was lower, which was also reflected

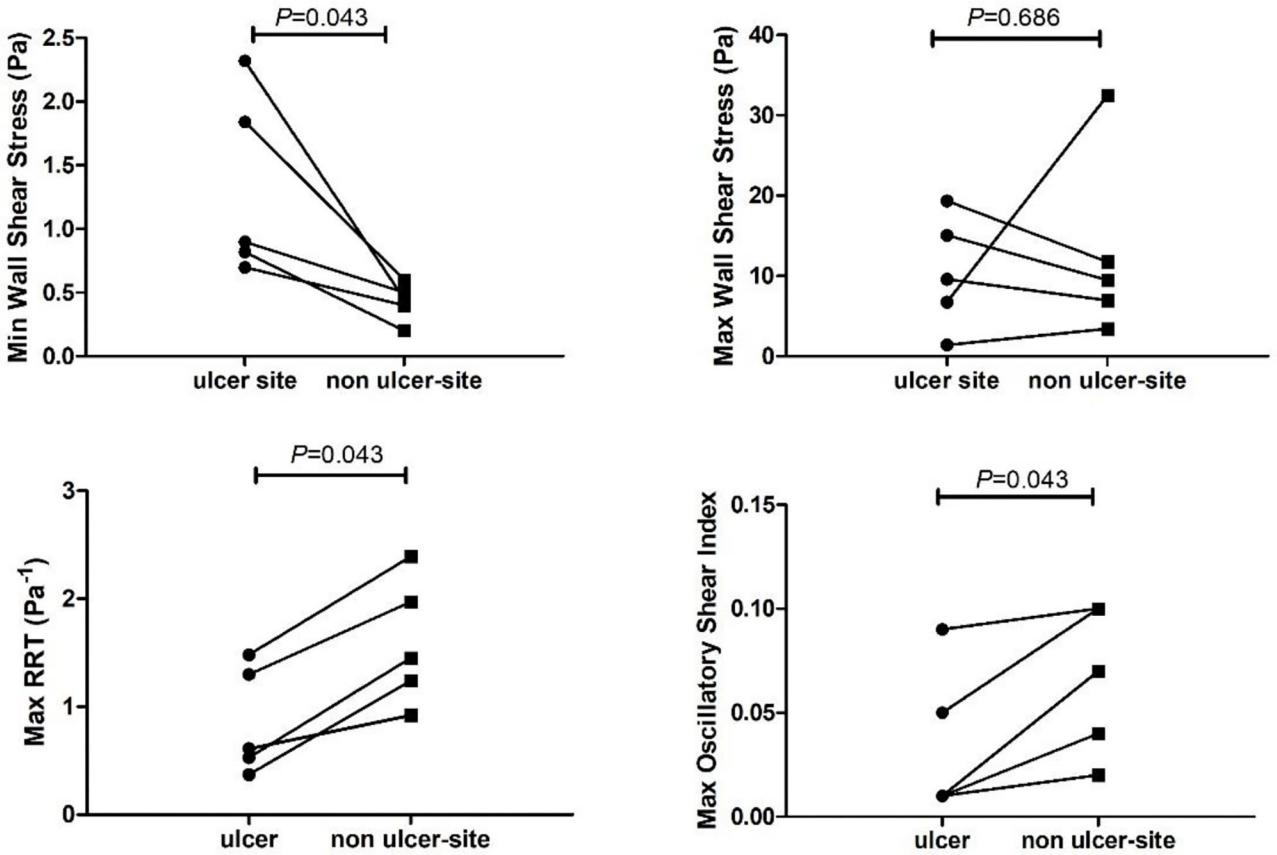

FIGURE 4 | Time varying wall shear stress at the ulcer-site (ulcer) vs. the non-ulcer site (remainder of the plaque) within a carotid artery. RRT, relative residence time.

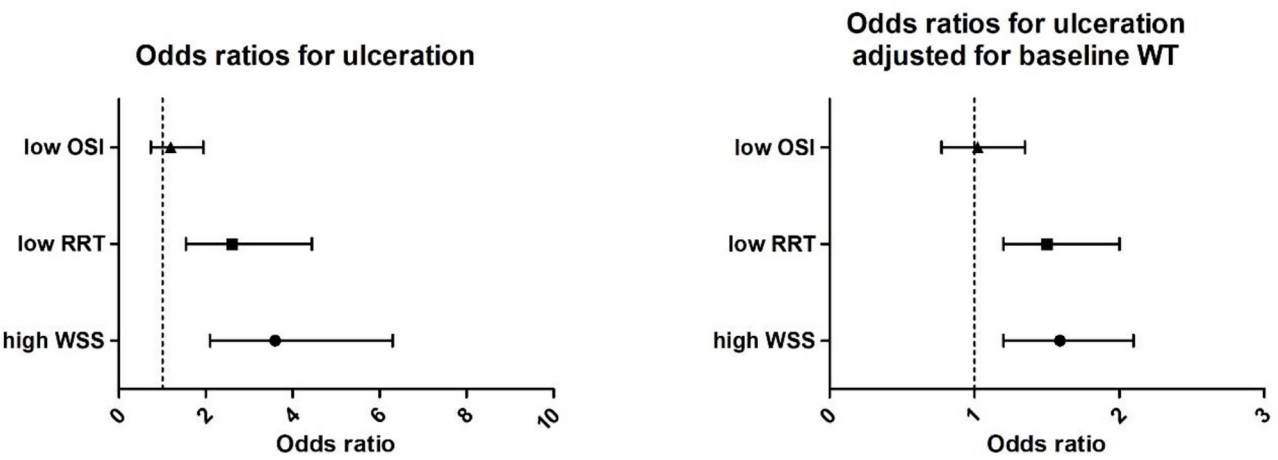

FIGURE 5 | (Left) Univariate correlation of high wall shear stress (WSS, > 4.2 Pa), low relative residence time (RRT, < 0.25 Pa^{-1}), and oscillatory shear index (OSI < 0.0006) with ulceration presented as odds ratios and **(right)** odd ratios adjusted for baseline wall thickness.

by the lower maximum values in RRT and OSI and higher odds to develop an ulcer at regions exposed to the lowest RRT tertile. Besides, ulcers developed at the thicker portion of the plaque. High WSS and low RRT remained significantly associated with ulceration after adjustment for wall thickness.

Several studies showed that carotid plaques containing IPH are associated with a high risk on future cardiovascular events (10). Furthermore, in an earlier study, we demonstrated that ulceration, a precursor of events, was not only associated with the presence of IPH but also with LRNC (22). Since plaques

that contain IPH are likely to be exposed to high WSS (34) and high WSS triggers molecular pathways involved in fibrous cap thinning (35), it was hypothesized that high WSS plays a role in plaque rupture. Therefore, to study the independent influence of WSS on plaque ulceration, we opted for a case control study design in which both plaques that developed an ulcer and control plaques contained IPH along with LRNC with similar lumen dimensions. By applying this study design, for this low number of plaques, we could not demonstrate significant differences in maximum values of WSS between plaques that developed an ulcer and those that did not. However, a more detailed analysis using the individual regions proved that the average WSS on the ulcer-site was higher compared to the remainder of the plaque. Also, the higher WSS tertile (>4.3 Pa) proved to be associated with ulceration. So, this might imply that even though ulcers do not always develop at the location exposed to the highest WSS within the artery at baseline, high WSS might still be instrumental in predicting ulcer location.

Three longitudinal case studies were performed that investigated the role of WSS in plaque ulceration within the ulcerated plaques (17, 19, 20). In the current study, we did not only study one case but had the possibility to investigate the development of five ulcers and their relation to baseline WSS. Interestingly, the three studies reported before described the same variation in WSS exposure at the ulcer site (**Table 3**). Groen et al. (17) and Wu et al. (19) reported higher WSS at the ulcer site compared to the non-ulcer site, whereas Leach et al. (20) reported lower WSS at the ulcer site. The predictive value of high WSS (>4.3 Pa) for ulceration is in agreement with a study in coronary arteries that also demonstrated that high WSS (>6.56 Pa) is associated with ulceration using univariate analysis (18). However, in that study multivariable analysis demonstrated that wall shear stress gradient is a stronger predictor than time average WSS (18). Other studies in coronary arteries already showed the association between high WSS (>4.71) and coronary events (36, 37).

Next to the observations on high WSS, we noticed that the minimal WSS was 1.7x−5x higher than the minimal WSS over the plaque. This observation implies that ulcers in our study population do not develop at the absolute minimum WSS at the plaque. Low WSS is known for its involvement in plaque progression (11) and lipid accumulation (12) and is therefore thought to potentially play a role in plaque destabilization and rupture. However, in this study low, WSS had lower odds compared to high WSS to develop an ulcer.

Our analysis also showed that plaque ulcerations particularly occur at the thicker part of the plaque. Although wall volume was shown to be a predictor for ulceration (38), no studies investigated the wall thickness as a predictor of the preferred site of plaque ulceration within the plaque. Therefore, we adjusted our analysis for local wall thickness and, accordingly, both wall thickness and high WSS were independently associated with ulceration (**Figure 5**).

A possible explanation for our findings could be that the thicker part of the plaque is more diseased since it more often contains plaque components such as IPH or LRNC that are known to be associated with plaque rupture (39). If the endothelial cells are exposed to high WSS but not necessarily the highest WSS, this leads to plaque destabilization and, finally, plaque rupture. Therefore, *local* plaque morphology in combination with hemodynamics parameters might be the key in identifying regions at risk for rupture.

Interestingly, while also exploring oscillatory WSS metrics known to be associated with plaque rupture in coronary arteries (18), potentially through regression of fibrous tissue (40), we found that the maximum RRT and OSI values were significantly lower in plaques that developed an ulcer compared to the control plaques. This means that high oscillations in the flow are not a prerequisite for plaque rupture. While studying the odds ratio for ulcer development, only low RRT and not OSI was associated with future ulceration. In a coronary artery study on ulceration, univariate analysis of plaque rupture proved that low OSI had a predictive value for ulceration. However, OSI was not any more significant in multivariate analysis with other oscillatory WSS parameters (18). Therefore, taking these observations together, it seems that OSI is not so strongly associated with ulceration. Future studies are needed to investigate which of the hemodynamic parameters is the strongest predictor.

We compared our data mostly to other work in coronary arteries. However, coronary arteries present with slightly different vulnerable plaque morphology, anatomy, and related hemodynamics (41) which might also explain some of the discrepancies with other studies. Vulnerable carotid plaques as compared to coronary plaques are characterized by a thicker fibrous cap, a higher prevalence of intraplaque hemorrhage, a lower prevalence of plaque erosion, and finally, a higher prevalence of calcified nodules. Furthermore, carotid arteries have a distinct anatomy with a bifurcation of two almost equally sized arteries and a bulb region. In particular, this bulb region is notorious for local oscillatory WSS behavior that is less present in coronary arteries (42).

The strength of this case control study is the longitudinal study design that allowed us to link the WSS at baseline to ulcer formation in the follow-up period. Previous cross-sectional studies showed that ruptured plaques were exposed to high WSS and wall shear stress gradient compared to non-ruptured plaques (18, 43, 44). While comparing our data with those studies, we have to be aware that in contrast to earlier cross-sectional studies in which the investigator tried to reconstruct pre-rupture lumen geometry and determine WSS on the reconstructed lumen, we used the true baseline 3D lumen geometry in our WSS analysis. In fact, in those cross-sectional studies, the 3D-reconstruction of the pre-rupture geometry might not be fully representative for the true baseline geometry since, at the ulcer site, a large part of plaque is washed out and plaques are perhaps smaller. Therefore, since WSS measures and ulcer location are studied in the pre-ulcer 3D geometry, these cross-sectional studies might serve in finding pathophysiological explanations for plaque ulceration rather than parameters to predict plaque ulceration in the future. Taken together, the association between WSS and plaque ulceration using a cross-sectional study design might

show different results from the ones obtained with a longitudinal study design. On top of that, we cannot rule out that the local WSS changed in the follow-up period so that it is still possible that the highest WSS in an artery are precursors of future plaque rupture.

This study has several limitations. Since only six ulcers developed in the studied patients, we were consequently restricted to those cases. However, the case-control study design allowed us to correct for multiple known risk factors along with the study of (oscillatory) WSS. Obviously, our findings on the association between WSS, OSI, and RRT should be confirmed in a larger cohort study. Another limitation is the registration of the (oscillatory) WSS based on MRI to the location of ulceration as assessed by MDCTA to study the WSS at the site of the ulceration. We opted for this approach to benefit from the advantages of both image modalities. Ulceration is proven to be the best identified using MDCTA (45, 46) whereas MRI delivers much more detailed information on plaque composition (47). Although we cannot rule out possible influence of misregistration in this detailed WSS analysis, the analysis comparing cases and controls that do not use this registration also resulted in significant differences and in the similar direction of maxRRT and maxOSI. Because of the careful registration, we revealed that one ulcer was partly located outside of the MRI range. Therefore, we included only five cases for the detailed analysis. However, for the whole plaque analysis, comparing time-dependent WSS parameters with control plaques, we did include that sixth case. Since the ulcer region, in that analysis was not included, the plaque analysis might not be fully representative for that plaque. Therefore, the plaque analysis was repeated for 5 cases with the 12 controls. Also, if we analyzed these 5 cases only, the baseline geometric parameters were similar to the 12 controls, and maxRRT and maxOSI remained significant (**Supplementary Table I**, **Supplementary Table II**).

CONCLUSION

In this study, symptomatic carotid artery plaques that developed a new ulcer during follow-up were investigated. These plaques were also compared to control cases. We demonstrated that plaques that undergo ulceration cannot be distinguished from the control cases based on the maximum WSS values. More detailed analysis on the ulcer location showed that ulcers do not exclusively develop at plaque regions exposed to the highest WSS, OSI, or RRT. However high WSS and low RRT had a significantly higher odds to present ulceration at 2 years follow up within the plaque even after wall thickness adjustment. These data might imply that high WSS and low RRT in combination with local, underlying morphology, and plaque composition predicts future ulcerations. More studies are needed to confirm our findings.

DATA AVAILABILITY STATEMENT

The datasets presented in this article are not readily available because the data is generated in a consortium. Approval by the consortium is needed before the data can be shared. Requests to access the datasets should be directed to j.wentzel@erasmusmc.nl.

ETHICS STATEMENT

The studies involving human participants were reviewed and approved by Institutional Medical Ethical Committee. The patients/participants provided their written informed consent to participate in this study.

AUTHOR CONTRIBUTIONS

JW, KD, and AL contributed to conception and design of the study. MK, DD-N, JH, PK, PN, AL, AS, AK, MEK, and KD organized the database and/or performed general analysis. S-AK performed the computational modeling. JW, FG, KD, and DB interpreted the data. KD and JW performed the statistical analysis and wrote the first draft of the manuscript. All authors contributed to manuscript revision, read, and approved the submitted version.

FUNDING

This research was performed within the framework of the Center for Translational Molecular Medicine (www.ctmm.nl), project PARISK (Plaque At RISK; Grant 01C-202) and supported by the Dutch Heart Foundation. KD was in part supported by STW project number 10813.

ACKNOWLEDGMENTS

We wish to thank Burhan Hussain and Anouk van Dijk for the plaque surface morphology score on MDCTA at baseline and Kim van Gaalen for the preparation of the figures.

SUPPLEMENTARY MATERIAL

The Supplementary Material for this article can be found online at: https://www.frontiersin.org/articles/10.3389/fcvm.2021.732646/full#supplementary-material

REFERENCES

1. Petty GW, Brown RD. Jr., Whisnant JP, Sicks JD, O'Fallon WM, Wiebers DO. Ischemic stroke subtypes: a population-based study of incidence and risk factors. *Stroke.* (1999) 30:2513–6. doi: 10.1161/01.STR.30.12.2513
2. Imbesi SG, Kerber CW. Why do ulcerated atherosclerotic carotid artery plaques embolize? A flow dynamics study. *AJNR Am J Neuroradiol.* (1998) 19:761–6.
3. North American Symptomatic Carotid Endarterectomy Trial C, Barnett HJM, Taylor DW, Haynes RB, Sackett DL, Peerless SJ, Ferguson GG,

et al. Beneficial effect of carotid endarterectomy in symptomatic patients with high-grade carotid stenosis. *N Engl J Med.* (1991) 325:445–53. doi: 10.1056/NEJM199108153250701
4. Rothwell PM, Gutnikov SA, Warlow CP. European Carotid Surgery Trialist's Collaboration. Reanalysis of the final results of the European Carotid Surgery Trial. *Stroke.* (2003) 34:514–23. doi: 10.1161/01.STR.0000054671.71777.C7
5. Rothwell PM, Eliasziw M, Gutnikov SA, Fox AJ, Taylor DW, Mayberg MR, et al. Analysis of pooled data from the randomised controlled trials of endarterectomy for symptomatic carotid stenosis. *Lancet.* (2003) 361:107–16. doi: 10.1016/S0140-6736(03)12228-3
6. Zhao H, Zhao X, Liu X, Cao Y, Hippe DS, Sun J, et al. Association of carotid atherosclerotic plaque features with acute ischemic stroke: a magnetic resonance imaging study. *Eur J Radiol.* (2013) 82:e465–470. doi: 10.1016/j.ejrad.2013.04.014
7. Yuan C, Zhang SX, Polissar NL, Echelard D, Ortiz G, Davis JW, et al. Identification of fibrous cap rupture with magnetic resonance imaging is highly associated with recent transient ischemic attack or stroke. *Circulation.* (2002) 105:181–5. doi: 10.1161/hc0202.102121
8. Takaya N, Yuan C, Chu B, Saam T, Underhill H, Cai J. *et al. Association between carotid plaque characteristics and subsequent ischemic cerebrovascular events: a prospective assessment with MRI–initial results Stroke.* (2006) 37:818–23. doi: 10.1161/01.STR.0000204638.91099.91
9. Altaf N, Daniels L, Morgan PS, Auer D, MacSweeny ST, Moody AR, et al. Detection of intraplaque hemorrhage by magnetic resonance imaging in symptomatic patients with mild to moderate carotid stenosis predicts recurrent neurological events. *J Vasc Surg.* (2008) 47:337–42. doi: 10.1016/j.jvs.2007.09.064
10. Schindler A, Schinner R, Altaf N, Hosseini AA, Simpson RJ, Esposito-Bauer L, et al. Prediction of Stroke Risk by Detection of Hemorrhage in Carotid Plaques: Meta-Analysis of Individual Patient Data. *JACC Cardiovasc Imaging.* (2020) 13:395–406. doi: 10.1016/j.jcmg.2019.03.028
11. Malek AM, Alper SL, Izumo S. Hemodynamic shear stress and its role in atherosclerosis. *JAMA.* (1999) 282:2035–42. doi: 10.1001/jama.282.21.2035
12. Samady H, Eshtehardi P, McDaniel MC, Suo J, Dhawan SS, Maynard C, et al. Coronary artery wall shear stress is associated with progression and transformation of atherosclerotic plaque and arterial remodeling in patients with coronary artery disease. *Circulation.* (2011) 124:779–88. doi: 10.1161/CIRCULATIONAHA.111.021824
13. Ku DN, Giddens DP, Zarins CK, Glagov S. Pulsatile flow and atherosclerosis in the human carotid bifurcation. Positive correlation between plaque location and low oscillating shear stress. *Arteriosclerosis.* (1985) 5:293–302. doi: 10.1161/01.ATV.5.3.293
14. Peiffer V, Sherwin SJ, Weinberg PD. Does low and oscillatory wall shear stress correlate spatially with early atherosclerosis? A systematic review. *Cardiovasc Res.* (2013) 99:242–50. doi: 10.1093/cvr/cvt044
15. Rikhtegar F, Knight JA, Olgac U, Saur SC, Poulikakos D, Marshall W. Jr., et al. Choosing the optimal wall shear parameter for the prediction of plaque location-A patient-specific computational study in human left coronary arteries. *Atherosclerosis.* (2012) 221:432–7. doi: 10.1016/j.atherosclerosis.2012.01.018
16. de Weert TT, Cretier S, Groen HC, Homburg P, Cakir H, Wentzel JJ, et al. Atherosclerotic plaque surface morphology in the carotid bifurcation assessed with multidetector computed tomography angiography. *Stroke.* (2009) 40:1334–40. doi: 10.1161/STROKEAHA.108.538439
17. Groen HC, Gijsen FJ, van der Lugt A, Ferguson MS, Hatsukami TS, van der Steen AFW, et al. Plaque rupture in the carotid artery is localized at the high shear stress region: a case report, *Stroke.* (2007) 38:2379–81. doi: 10.1161/STROKEAHA.107.484766
18. Thondapu V, Mamon C, Poon EKW, Kurihara O, Kin HO, Russo M, et al. High spatial endothelial shear stress gradient independently predicts site of acute coronary plaque rupture and erosion. *Cardiovasc Res.* (2021) 117:1974–85. doi: 10.1093/cvr/cvaa251
19. Wu Z, Yang C, Tang D. In vivo serial MRI-based models and statistical methods to quantify sensitivity and specificity of mechanical predictors for carotid plaque rupture: location and beyond. *Biomech Eng.* (2011) 133:064503. doi: 10.1115/1.4004189
20. Leach JR, Rayz VL, Soares B, Wintermark M, Mofrad MRK, Saloner D. Carotid atheroma rupture observed in vivo and FSI-predicted stress distribution based on pre-rupture imaging. *Ann Biomed Eng.* (2010) 38:2748–65. doi: 10.1007/s10439-010-0004-8
21. Truijman MT, Kooi ME, van Dijk AC, de Rotte AAJ, van der Kolk AG, Liem MI, et al. Plaque At RISK (PARISK): prospective multicenter study to improve diagnosis of high-risk carotid plaques. *Int J Stroke.* (2014) 9:747–54. doi: 10.1111/ijs.12167
22. Dilba K, van Dam-Nolen DHK, van Dijk AC, Kassem M, van der Steen AFW, Koudstaal PJ, et al. Plaque Composition as a Predictor of Plaque Ulceration in Carotid Artery ATherosclerosis: The Plaque at RISK Study. *AJNR Am J Neuroradiol.* (2021) 42:144–51 doi: 10.3174/ajnr.A6868
23. Randomised trial of endarterectomy for recently symptomatic carotid stenosis: final results of the MRC European Carotid Surgery Trial (ECST). *Lancet.* (1998) 351:1379–87 doi: 10.1016/S0140-6736(97)09292-1
24. Lovett JK, Gallagher PJ, Hands LJ, Walton J, Rothwell P M. Histological correlates of carotid plaque surface morphology on lumen contrast imaging. *Circulation.* (2004). 110:2190–7 doi: 10.1161/01.CIR.0000144307.82502.32
25. Kwee RM, Teule GJJ, van Oostenbrugge RJ, Mess WH, Prins MH, van der Geest RJ. et al. Multimodality imaging of carotid artery plaques: 18F-fluoro-2-deoxyglucose positron emission tomography, computed tomography, and magnetic resonance imaging. *Stroke.* (2009) 40:3718–24. doi: 10.1161/STROKEAHA.109.564088
26. Lee SW, Antiga L, Spence JD, Steinman DA. Geometry of the carotid bifurcation predicts its exposure to disturbed flow. *Stroke.* (2008) 39:2341–7. doi: 10.1161/STROKEAHA.107.510644
27. Womersley JR. Method for the calculation of velocity, rate of flow and viscous drag in arteries when the pressure gradient is known. *J Physiol.* (1955) 127:553–63. doi: 10.1113/jphysiol.1955.sp005276
28. Groen HC, Simons L, van den Bouwhuijsen QJA, Bosboom EMH, Gijsen FJH, van der Giessen AG, et al. MRI-based quantification of outflow boundary conditions for computational fluid dynamics of stenosed human carotid arteries. *J Biomech.* (2010) 43:2332–8. doi: 10.1016/j.jbiomech.2010.04.039
29. Wentzel JJ, Chatzizisis YS, Gijsen FJH, Giannoglou GD, Feldman CL, Stone PH. Endothelial shear stress in the evolution of coronary atherosclerotic plaque and vascular remodelling: current understanding and remaining questions. *Cardiovasc Res.* (2012) 96:234–43. doi: 10.1093/cvr/cvs217
30. Cunningham KS, Gotlieb AI. The role of shear stress in the pathogenesis of atherosclerosis. *Lab Invest.* (2005) 85:9–23. doi: 10.1038/labinvest.3700215
31. de Monye C, Cademartiri F, de Weert TT, Siepman DAM, Dippel DWJ, van Der Lugt A. Sixteen-detector row CT angiography of carotid arteries: comparison of different volumes of contrast material with and without a bolus chaser. *Radiology.* (2005) 237:555–62. doi: 10.1148/radiol.2372040653
32. de Weert TT, Cakir H, Rozie S, Cretier S, Meijering E, Dippel DWJ, et al. Intracranial internal carotid artery calcifications: association with vascular risk factors and ischemic cerebrovascular disease. *AJNR Am J Neuroradiol.* (2009) 30:177–84. doi: 10.3174/ajnr.A1301
33. IBM Corp. *IIBM SPSS Statistics, version 24, Release 24.0.0.0* (2012).
34. Tuenter A, Selwaness M, Arias Lorza A, Schuurbiers JCH, Speelman L, Cibis M, et al. High shear stress relates to intraplaque haemorrhage in asymptomatic carotid plaques. *Atherosclerosis.* (2016) 251:348–54. doi: 10.1016/j.atherosclerosis.2016.05.018
35. Slager CJ, Wentzel JJ, Gijsen FJH, Thury A, van der Wal AC, Schaar JA, et al. The role of shear stress in the destabilization of vulnerable plaques and related therapeutic implications. *Nat Clin Pract Cardiovasc Med.* (2005) 2:456–64. doi: 10.1038/ncpcardio0298
36. Kumar A, Thompson EW. Lefieux, A, Molongy DS, Davis EL, Chand N, et al. High Coronary Shear Stress in Patients With Coronary Artery Disease Predicts Myocardial Infarction. *J Am Coll Cardiol.* (2018) 72:1926–35. doi: 10.1016/j.jacc.2018.07.075
37. Tufaro V, Safi H, Torii R, Koo B, Kitslaar P, Ramasamy A, et al. Wall shear stress estima Wall shear stress estimated by 3D-QCA can predict cardiovascular events in lesions with borderline negative fractional flow reserve. *Atherosclerosis.* (2021) 322:24–30. doi: 10.1016/j.atherosclerosis.2021.02.018
38. Homburg PJ, Rozie S, van Gils MJ, van den Bouwhuijsen QJA, Niessen WJ, Dippel DWJ, et al. Association between carotid artery plaque ulceration and plaque composition evaluated with multidetector CT angiography. *Stroke.* (2011) 42:367–72. doi: 10.1161/STROKEAHA.110.597369

39. Underhill HR, Yuan C, Yarnykh VL, Chu B, Oikawa M, Dong L, et al. Predictors of surface disruption with MR imaging in asymptomatic carotid artery stenosis. *AJNR Am J Neuroradiol.* (2010) 31:487–93. doi: 10.3174/ajnr.A1842
40. Kok AM, Molony DS, Timmins LH, Ko Y, Boersma E, Eshtehardi P, et al. The influence of multidirectional shear stress on plaque progression and composition changes in human coronary arteries. *EuroIntervention.* (2019) 15:692–9. doi: 10.4244/EIJ-D-18-00529
41. Sigala F, Oikonomou E, Antonopoulos AS, Galyfos G, Tousoulis D. Coronary versus carotid artery plaques. Similarities and differences regarding biomarkers morphology and prognosis. *Current Opinion in Pharmacology.* (2018) 39:9–18. doi: 10.1016/j.coph.2017.11.010
42. Gallo D, Steinman DA. Morbiducci U. Insights into the co-localization of magnitude-based versus direction-based indicators of disturbed shear at the carotid bifurcation. *J Biomech.* (2016) 49:2413–9. doi: 10.1016/j.jbiomech.2016.02.010
43. Tang D, Teng Z, Canton G, Yang C, Ferguson M, Huang X, et al. Sites of rupture in human atherosclerotic carotid plaques are associated with high structural stresses: an in vivo MRI-based 3D fluid-structure interaction study. *Stroke.* (2009) 40:3258–63. doi: 10.1161/STROKEAHA.109.558676
44. Teng Z, Canton G, Yuan C, Ferguson M, Yang C, Huang X, et al. 3D critical plaque wall stress is a better predictor of carotid plaque rupture sites than flow shear stress: An in vivo MRI-based 3D FSI study. *J Biomech Eng.* (2010) 132:031007. doi: 10.1115/1.4001028
45. Rafailidis V, Chryssogonidis I, Tegos T, Kouskouras K, Charitanti-Kouridou A. Imaging of the ulcerated carotid atherosclerotic plaque: a review of the literature. *Insights Imaging.* (2017) 8:213–25. doi: 10.1007/s13244-017-0543-8
46. Anzidei M, Napoli A, Zaccagna F, Di Paolo P, Saba L, Cavallo Marincola B, et al. Diagnostic accuracy of colour Doppler ultrasonography, CT angiography and blood-pool-enhanced MR angiography in assessing carotid stenosis: a comparative study with DSA in 170 patients. *Radiol Med.* (2012) 117:54–71. doi: 10.1007/s11547-011-0651-3
47. Cai JM, Hatsukami TS, Ferguson MS, Small R, Polissar NL, Yuan C. Classification of human carotid atherosclerotic lesions with in vivo multicontrast magnetic resonance imaging. *Circulation.* (2002) 106:1368–13734. doi: 10.1161/01.CIR.0000028591.44554.F9

Conflict of Interest: The authors declare that the research was conducted in the absence of any commercial or financial relationships that could be construed as a potential conflict of interest.

frontiers in Cardiovascular Medicine

ORIGINAL RESEARCH
published: 24 December 2021
doi: 10.3389/fcvm.2021.744181

Comparison of Resting Full-Cycle Ratio and Fractional Flow Reserve in a German Real-World Cohort

*Hendrik Wienemann[1], Annika Meyer[1], Victor Mauri[1], Till Baar[2], Matti Adam[1], Stephan Baldus[1] and Marcel Halbach[1]**

[1] University of Cologne, Faculty of Medicine and University Hospital Cologne, Clinic III for Internal Medicine, Cologne, Germany, [2] Institute of Medical Statistics and Computational Biology, Faculty of Medicine, University of Cologne, Cologne, Germany

Objective: The aim of this study was to evaluate non-hyperemic resting pressure ratios (NHPRs), especially the novel "resting full-cycle ratio" (RFR; lowest pressure distal to the stenosis/aortic pressure during the entire cardiac cycle), compared to the gold standard fractional flow reserve (FFR) in a "real-world" setting.

Methods: The study included patients undergoing coronary pressure wire studies at one German University Hospital. No patients were excluded based on any baseline or procedural characteristics, except for insufficient quality of traces. The diagnostic performance of four NHPRs vs. FFR $\leq$ 0.80 was tested. Morphological characteristics of stenoses were analyzed by quantitative coronary angiography.

Results: 617 patients with 712 coronary lesions were included. RFR showed a significant correlation with FFR ($r = 0.766$, $p < 0.01$). Diagnostic accuracy, sensitivity, specificity, positive predictive value, and negative predictive value of RFR were 78% (95% confidence interval = 75; 81), 72% (65; 78), 81% (77; 84), 63% (57; 69), and 86% (83; 89). Relevant predictors for discordance of RFR $\leq$ 0.89/FFR $>$ 0.8 were LAD lesions, peripheral artery disease, age, female sex and non-focal stenoses. Predictors for discordance of RFR $>$ 0.89/FFR $\leq$ 0.8 included non-LCX lesions, percent diameter stenosis and previous percutaneous coronary intervention in the target vessel. RFR and all other NHPRs were highly correlated with each other.

Conclusion: All NHPRs have a similar correlation with the gold standard FFR and may facilitate the acceptance and implementation of physiological assessments of lesion severity. However, we found ~20% discordant results between NHPRs and FFR in our "all-comers" German cohort.

Keywords: coronary artery disease (CAD), fractional flow reserve (FFR), coronary physiology, invasive coronary angiography (ICA), resting full-cycle ratio (RFR)

OPEN ACCESS

Edited by:
Patrick W. Serruys, Imperial College London, United Kingdom

Reviewed by:
Riccardo Liga, Pisana University Hospital, Italy
Karl Jakob Weiß, Deutsches Herzzentrum Berlin, Germany

****Correspondence:***
Marcel Halbach
marcel.halbach@uk-koeln.de
orcid.org/0000-0002-6361-5825

Specialty section:
This article was submitted to Cardiovascular Imaging, a section of the journal Frontiers in Cardiovascular Medicine

Received: *19 July 2021*
Accepted: *30 November 2021*
Published: *24 December 2021*

Citation:
Wienemann H, Meyer A, Mauri V, Baar T, Adam M, Baldus S and Halbach M (2021) Comparison of Resting Full-Cycle Ratio and Fractional Flow Reserve in a German Real-World Cohort. Front. Cardiovasc. Med. 8:744181. doi: 10.3389/fcvm.2021.744181

INTRODUCTION

Despite great advances in the prevention and treatment of cardiovascular diseases, ischemic heart disease remains one of the main causes of morbidity and mortality worldwide (1). Fractional flow reserve (FFR) is the gold standard pressure-derived index for the assessment of the physiological severity of coronary artery stenosis, and several guidelines and studies have highlighted the

benefit of FFR-guided percutaneous coronary intervention (PCI) (2–6). FFR is derived from the ratio between the mean distal coronary artery pressure (Pd) to the mean aortic pressure (Pa) under maximum hyperemia and is considered to be significant with a threshold of ≤0.80 (7, 8). Administration of adenosine to achieve maximum hyperemia is associated with possible side effects (9), increased costs, and longer examination time, which may cause reservations against the application of FFR. Therefore, utilization remains low and heterogeneous between different hospitals in Germany (10).

The development of resting indices, referred to as non-hyperemic pressure ratio (NHPR), is therefore of great importance. Two large randomized clinical trials among patients with stable angina or acute coronary syndrome revealed that instantaneous wave-free ratio (iFR), which is calculated during the diastolic wave-free period and used by one of the leading manufacturers of pressure wires, is clinically non-inferior to FFR with regard to serious adverse events at one year (11, 12). Moreover, a previous study demonstrated that NHPRs have a comparable diagnostic quality for diagnosing positron emission tomography defined myocardial ischemia and show a comparable outcome with FFR at two years (13). Lately, it has been found that the resting full-cycle ratio (RFR), described as the lowest ratio of resting Pd/Pa during the entire cardiac cycle, which is used by another leading manufacturer, is diagnostically equivalent to iFR (13–15). Randomized trials comparing RFR and FFR are lacking. Although FFR ≤ 0.8 or NHPRs ≤ 0.89 can predict ischemia-inducing coronary stenoses with high accuracy, the correlation and agreement between FFR and NHPRs test results varies in clinical practice (13, 14, 16). Available data show that FFR and iFR test results are discordant in about 15–20% of cases, leading to uncertainty about revascularization decisions. This might be caused by limitations such as the assumption of maximal flow and minimal resistance occurring during the wave-free period of the diastole, which is the rationale of iFR (17, 18). Several clinical, angiographic, and hemodynamic factors contribute to iFR/FFR discordance (19–21). Available data do not represent a broader population in a real-world setting. Many patients were excluded from studies due to wide exclusion criteria such as vessels with a previous myocardial infarction, previous coronary artery bypass graft surgery, left main disease, chronic renal disease, bradycardia, atrial fibrillation or in-stent lesions (17, 22, 23). Furthermore, patients from Western Europe are underrepresented in most trials.

In the present retrospective, single-center study, we sought to investigate the diagnostic accuracy of FFR and NHPRs and the clinical utility of NHPRs and especially the relatively new non-hyperemic index RFR in a German "all-comers" population with intermediate coronary stenoses. The objective of this study is to assess the correlation of FFR and NHPRs in a real-world setting and evaluate predictors of discrepancies.

Abbreviations: %DS, percent diameter stenosis; CABG, coronary artery bypass surgery; CFR, coronary flow reserve; dPR[entire], diastolic pressure ratio during entire diastole; dPR[WFP], diastolic pressure ratio during wave-free period; FFR, fractional flow reserve; LAD, left anterior descending; LM, left main coronary artery; LCX, left circumflex artery; NHPRs, non-hyperemic pressure ratios; Pa, proximal aortic pressure; Pd, distal arterial pressure; PAD, peripheral artery disease; PCI, percutaneous coronary intervention; RCA, right coronary artery; RFR, resting full-cycle ratio; RIM, Ramus intermedius; QCA, quantitative coronary angiography; QFR, quantitative flow ratio.

MATERIALS AND METHODS

Study Population

From 9th of March 2015 until 15th of February 2019, a total of 696 adult patients underwent 869 pressure wire recordings of at least one intermediate coronary lesion (30–80%, determined visually by the treating physician) for standard clinical indications at the Heart Center of the University of Cologne. Pressure wire recordings were not performed in the following settings: (1) contraindication for adenosine, (2) cardiogenic shock (3), ST-segment elevation myocardial infarction, (4) culprit vessels in the setting of myocardial infarction (5), stenosis technically not suitable for analysis and (6) lesions without myocardial viability. All patients with FFR recordings in this period were included in this study, i.e., no patients were excluded from the analysis based on any baseline or procedural characteristics, except for insufficient quality of recorded traces, which impeded a reliable retrospective analysis (see pressure wire assessment). All collected patient data were anonymized before the analysis. The study design was approved by the local ethics committee and complied with the Declaration of Helsinki.

Invasive Coronary Angiography and Quantitative Coronary Angiography

Coronary angiography was executed according to current guidelines and institutional standards by a femoral or radial approach, using a diagnostic or guiding catheter and low-osmolar contrast agents. Angiographic views were obtained in multiple standard projections. Diameter stenosis percentage, minimal and reference lumen diameter, and lesion length were assessed retrospectively by quantitative coronary angiography with validated software (CAAS II, Pie Medical System, Maastricht, The Netherlands).

Pressure Wire Assessment

Interventional procedures and application of medication were performed according to current guidelines and manufacturer's and institutional standards. A pressure guidewire (Pressure Wire™ X Guidewire [Abbott Vascular Inc., Santa Clara, CA], or Verrata® [Philips, San Diego, CA]) was calibrated, equalized, and advanced distal to the target lesion, and intracoronary nitrate was administered. Then continuous intravenous adenosine (140 μg/kg per min) was applied through a peripheral vein to induce hyperemia in the target vessel for FFR measurement. In the majority of cases, a pullback recording was made to exclude pressure drift.

For this study, all analyses were performed retrospectively using the raw data of pressure wire recordings. Distal (Pd) and aortic pressure (Pa) traces at baseline, i.e., before application of adenosine, were used to determine NHPRs. FFR was calculated using the lowest Pd/Pa under hyperemic conditions. FFR, RFR, diastolic pressure ratio during wave-free period (dPR[WFP]),

diastolic pressure ratio during entire diastole (dPR[entire]), and Pd/Pa values (see **Figure 1** for exact definitions) were calculated by a fully automated offline software algorithm at an independent core laboratory (CoroLab; Coroventis Research AB, Uppsala, Sweden). The thresholds for a hemodynamically significant stenosis (FFR $\leq$ 0.80, RFR $\leq$ 0.89, dPR[WFP] $\leq$ 0.89, dPR[entire] $\leq$ 0.89, and Pd/Pa $\leq$ 0.92) were defined according to current guidelines and recommendations. One hundred and fifty seven of 869 (18.1%) pressure recordings had to be excluded from the analysis, since resting or hyperemic periods could not be reliably identified or pressure recordings were instable. Hence, 617 patients with 712 stenoses were finally included in the study to assess the correlation of FFR to NHPRs. For patients with multivessel disease and recordings at different timepoints, baseline characteristics at first presentation were used for per-patient analysis.

In principle, assessment of non-focal (serial, diffuse) stenoses was performed using a dedicated software for calculation of quantitative flow ratio (QFR) based on coronary angiography (QAngio XA 3D version 2.0, Medis Medical Imaging Systems) (24).

Statistical Analysis

Continuous variables are presented as mean ± standard deviation or median with interquartile range (IQR), while categorical variables are reported as frequencies and percentages. The differences were evaluated using Chi-square test or Fisher's exact test for categorical variables and Student's *t*-test or Mann-Whitney-*U* test for continuous variables, depending on their distribution. Kruskal–Wallis test was used to test for differences among >2 groups followed by *post-hoc* Mann-Whitney *U* tests with Bonferroni correction. Pearson's correlation coefficient was used to assess the relationship between several indices.

To assess the diagnostic value of NHPRs in comparison to FFR (≤0.80), the area under the curve (AUC) of the receiver-operating characteristic (ROC), as well as the accuracy metric were used. Diagnostic accuracy, sensitivity, specificity, negative, and positive predictive value, likelihood positive and negative ratio were calculated. Diagnostic agreement between the different indices was assessed by Bland-Altman plots with corresponding 95% limits of agreement.

Predictors of discordance between FFR and NHPRs were determined using a logistic regression model. The associated covariates with a p-value < 0.05 by forward selection in univariate analysis were included in the multivariable model after testing for multicollinearity. Backward stepwise selection was performed using a binary logistic model (backward elimination method: Wald). A two-tailed p-value of <0.05 was regarded as statistically significant. Statistical analysis was conducted in SPSS Statistics, version 28 (IBM, Armonk, New York) and R programming language version 4.1.2 (R Foundation for Statistical Computing, Vienna, Austria).

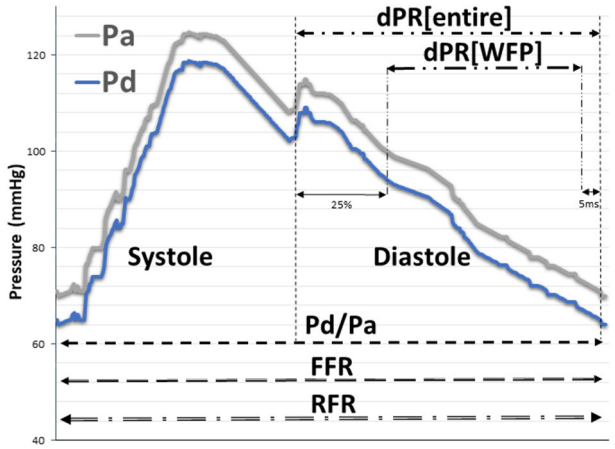

FIGURE 1 | Schematic explanation of the NHPRs and FFR. Diastole starts at the nadir of the dicrotic notch. The dPR[entire] is defined as mean Pd/Pa over the entire diastole. The dPR[WFP] is defined as the mean Pd/Pa value in the wave-free period for 5 heart cycles (from 25% of the entire diastole to 5 ms before the end of diastole; equivalent to the definition of iFR). Whole cycle resting Pd/Pa was calculated continuously throughout the entire cardiac cycle for three heart cycles. FFR is defined as the lowest, artifact-free Pd/Pa during maximal hyperemia over at least three heart cycles (Pd/Pa and FFR are calculated in the same way, just under different conditions, i.e. resting conditions vs hyperemic conditions). RFR is defined as the lowest Pd/Pa value in systole and diastole (mean of 5 consecutive cardiac cycles). dPR[entire], diastolic pressure ratio during entire diastole; dPR[WFP], diastolic pressure ratio during wave-free period; FFR, fractional flow reserve; NHPR, non-hyperemic pressure ratio; Pa, aortic pressure; Pd, distal coronary pressure; RFR, resting full-cycle ratio.

RESULTS

Patient and Vessel Characteristics

Clinical and angiographic characteristics are displayed in **Table 1**. The cohort consisted of patients with advanced age (median 69 years), with a high proportion of males (72.6%) and a high prevalence of comorbidities.

The lesions were located most often in the left anterior descending coronary artery (LAD; 424 vessels; 59.6%). The reference diameter showed sufficient size for PCI (2.98 ± 0.57 mm). The lesions had a minimum diameter of 1.42 ± 0.42 mm, the mean percent diameter stenosis (%DS) was 52.9 ± 8.7 %, and the mean lesion length 15.6 ± 9.54 mm. Two hundred and ninety (40.7%) lesions were non-focal.

Pressure Wire-Derived Indices

The median values of pressure wire-derived indices were 0.84 (IQR: 0.79 to 0.90) for FFR, 0.91 (IQR: 0.88 to 0.96) for RFR, 0.92 (IQR: 0.88 to 0.96) for dPR[entire], 0.92 (IQR: 0.88 to 0.96) for dPR[WFP] and 0.94 (IQR: 0.90 to 0.97) for Pd/Pa, respectively. Ischemia defined as FFR $\leq$ 0.80 was detected in 222 of 712 lesions (31.2%; 201 of 617 patients). Nineteen (3%) minor side effects [chest discomfort/dyspnea (1.4%) and transient atrioventricular block (0.5%)] occurred during adenosine infusion, but no serious adverse events were observed. Resting indices suggested ischemia in 253 lesions (35.5%) for RFR, 222 (31.2%) for dPR[entire], 238 (33.4%) for dPR[WFP], and 280 (39.3%) for Pd/Pa. The prevalence of ischemia, regarding the cut-off value of 0.89,

TABLE 1 | Patient demographics and vessel characteristics.

	All patients (n = 617)
Age (years)	69 (61–77)
Female gender	169 (27.4)
Hypertension	448 (72.6)
Dyslipidemia	322 (52.2)
Diabetes mellitus	168 (27.2)
Insulin dependent	61 (9.9)
Current or past smoker	216 (35.0)
Peripheral arterial disease	47 (7.6)
Atrial fibrillation	65 (10.5)
Previous stroke	55 (8.9)
Previous myocardial infarction	180 (29.2)
Previous coronary artery bypass surgery	41 (6.6)
Family history of coronary artery disease	95 (15.4)
β-Blocker use	417 (67.6)
Indication	
NSTEMI	28 (4.5)
Unstable angina	137 (22.2)
Stable angina	192 (31.1)
Atypical angina	63 (10.2)
Silent ischemia	197 (31.9)
Multi-vessel disease	444 (72.0)
Previous percutaneous coronary intervention in the target vessel	126 (20.4)
	All vessels (n=712)
Left main	6 (0.8)
Left anterior descending artery	424 (59.6)
Ramus intermedius	11 (1.5)
Right coronary artery	143 (20.1)
Left circumflex artery	124 (17.4)
Coronary artery bypass	4 (0.6)
Non-focal stenoses	290 (40.7)
Target segment	
Proximal	308 (43.3)
Mid	300 (42.1)
Distal	104 (14.6)

Data are given in n (%) or median (Q1–Q3).

between dPR[WFP] and RFR were not statistically significant ($p = 0.43$). FFR was correlated with NHPRs ($r = 0.766$ for RFR; $r = 0.763$ for dPR[WFP]; $r = 0.772$ for dPR[entire]; $r = 0.792$ for Pd/Pa, $p < 0.01$; see **Figure 2**). Bland-Altman plot showed the mean bias ± SD between FFR and NHPRs (**Figure 3**).

The diagnostic performance of NHPRs to predict FFR ≤ 0.80 is shown in **Table 2**. RFR and the other NHPRs were highly correlated ($r = 0.993$ for dPR[WFP]; $r = 0.992$ for dPR[entire]; $r = 0.943$ for Pd/Pa, all $p < 0.01$). Increasing the per-lesion threshold to RFR ≤ 0.93 resulted in higher sensitivity of 90% to predict FFR ≤ 0.80, RFR ≤ 0.97 had 100% sensitivity. ROC curve analysis was performed to examine diagnostic performance of NHPRs using FFR ≤ 0.80 as the reference standard (**Figure 4A**). As shown in **Figure 4B**, large AUC were observed for the NHPRs using RFR ≤ 0.89 as the reference standard.

The analysis yielded a total recording of 3,560 cardiac cycles in 712 lesions. The RFR values showed a high reproducibility within the 5 measurements. The lowest ratio of resting Pd/Pa, i.e., the RFR, was located within systole in at least one cardiac cycle in 295 (8.2%) pressure tracings; in 80 (2.2%) pressure tracings the lowest ratio of Pd/Pa was located within systole in all analyzed cycles. The RFR was more frequently located within systole, when left circumflex artery (LCX) and right coronary artery (RCA) were examined [CABG 0%, RIM 0%, LAD 4.9% (404 out of 424), LCX 12.8% (108 out of 124), RCA 15.4% (121 out of 143), left main 16.7% (1 out of 6)].

Discordance Between FFR and NHPRs

Concordant and discordant findings of FFR and NHPRs are summarized in **Figure 2**. One hundred and fifty seven lesions (22.1 %) in 138 patients (22.4%) showed discordant results of FFR and RFR, i.e., therapeutic decision would have differed. One hundred and forty eight lesions (20.8%) in 131 patients (21.2%) were discordant for FFR and dPR[WFP]. In the group with FFR ≤ 0.80 and RFR > 0.89, median FFR was 0.78 (IQR: 0.76–0.8) and median RFR 0.92 (0.91–0.93). In the group with FFR > 0.80 and RFR ≤ 0.89, median FFR was 0.84 (0.82–0.86) and median RFR 0.88 (0.85–0.89).

Patient and lesion characteristics of discordant and concordant RFR/FFR groups are shown in **Tables 3A,B**. In the univariate logistic regression analysis, age ($p < 0.01$), female sex ($p = 0.01$), peripheral artery disease ($p = 0.01$), LAD lesion ($p < 0.01$) und non-focal lesion ($p = 0.02$) were associated with discordance of RFR ≤ 0.89/FFR >0.8 (**Table 4A**). Previous PCI in target vessel ($p = 0.01$), % DS ($p < 0.01$) and non-LCX lesions ($p < 0.01$) were associated with discordance of RFR >0.89/FFR ≤ 0.8 (**Table 4B**). The multivariate analysis confirmed age (Odds Ratio [OR], 1.04; 95% confidence interval [CI], 1.02–1.07; $p = 0.01$), non-focal stenoses (OR, 1.84; 95% CI, 1.17–2.89; $p = 0.01$), female sex (OR, 1.70; 95% CI, 1.06–2.74; $p = 0.03$), peripheral artery disease (OR, 2.63; 95% CI, 1.36–5.09; p=0.01) and LAD lesion (OR, 3.22; 95% CI, 1.88–5.52; $p < 0.01$) as predictors of RFR ≤ 0.89/FFR > 0.8 (**Table 4A**). Previous PCI in target vessel (OR, 2.10; CI 1.15–3.85; $p = 0.02$), % DS (OR, 1.14; 95% CI, 1.1–1.19; $p < 0.01$) and non-LCX lesion (OR for LCX, 0.11; 95% CI, 0.02–0.52; $p = 0.01$) were confirmed as predictors of RFR > 0.89/FFR ≤ 0.8 in the multivariate analysis (**Table 4B**). The presence of acute coronary syndromes (ACS, mainly unstable angina) and the lesion location (proximal, medial or distal segment) did not predict discordance of RFR ≤ 0.89/FFR > 0.8 or RFR > 0.89/FFR ≤ 0.8 in the univariate analysis.

DISCUSSION

We validated NHPRs, with a special focus on RFR, vs. the gold standard FFR in patients with angiographically intermediate coronary stenoses in a German "all-comers"

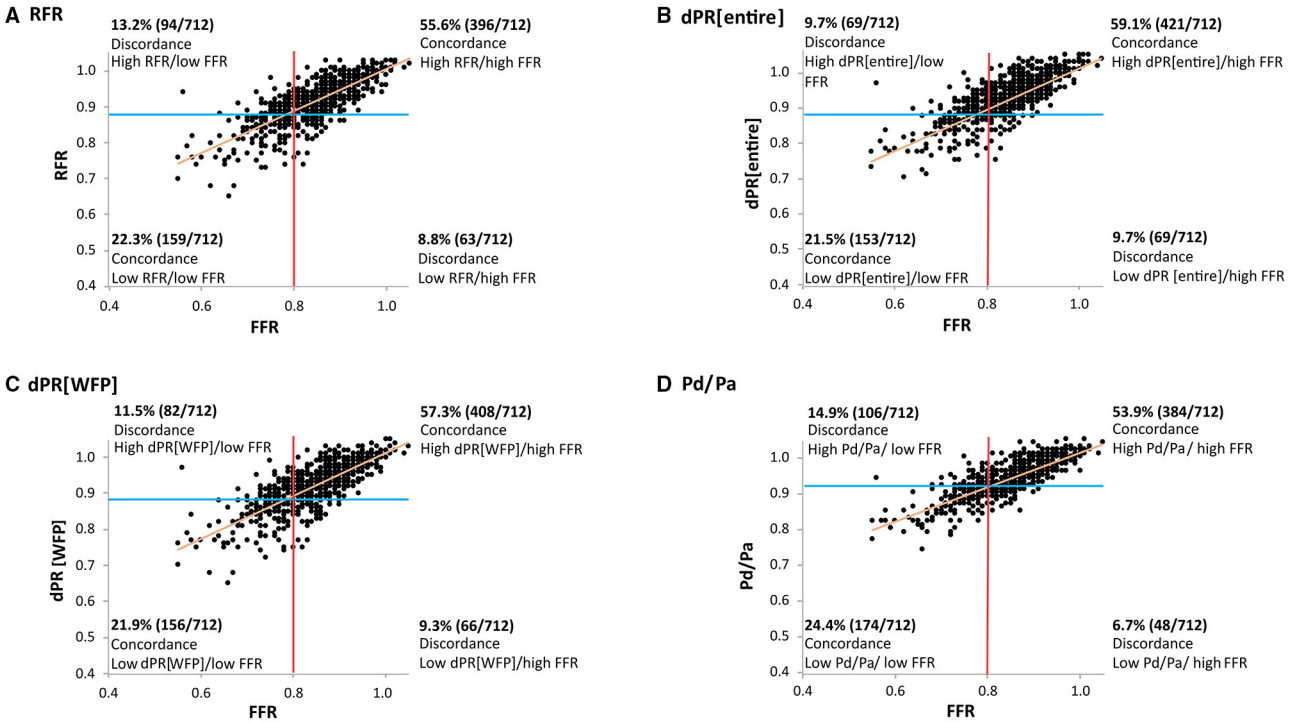

FIGURE 2 | Concordance and discordance among NHPRs and FFR. **(A)** FFR and RFR showed a significant correlation ($r = 0.766$; $p < 0.01$), but 21.0% of lesions showed discordant classifications with FFR and RFR cutoff values of ≤0.80 and ≤0.89, respectively. **(B–D)** The correlation of FFR and dPR[entire], dPR[WFP] and Pd/Pa was also significant with a similar correlation coefficient. The frequency of discordant indices was comparable, too. dPR[entire], diastolic pressure ratio during entire diastole; dPR[WFP], diastolic pressure ratio during wave-free period; FFR, fractional flow reserve; NHPR, non-hyperemic pressure ratio; Pa, aortic pressure; Pd, distal coronary pressure; RFR, resting full-cycle ratio.

population. All NHPRs correlated very well with each other and showed a diagnostic accuracy of 77–81% for FFR. Discrepancies between FFR and RFR were found in 22.0% of recordings, and a higher rate of ischemia was diagnosed by RFR compared to FFR. We identified several clinical parameters that may predict discordance of RFR and FFR.

FFR-guided revascularization is supported by several randomized trials (3–5) and recommended by European guidelines (2, 6). Despite convincing evidence and clear recommendations, the rate of FFR-guided revascularizations is low (e.g., ∼17% of interventions performed in Germany in 2019 were FFR-guided; unpublished survey of the German Society of Cardiology 2019, DGK). Reasons may include the costs and prolongation of procedures associated with administration of adenosine. Adenosine-free NHPRs may facilitate the acceptance and implementation of physiological assessments. Two randomized trials have demonstrated that iFR-guided treatment is non-inferior to FFR-guided treatment (11, 12), while other NHPRs were not yet validated in randomized trials. However, discrepancies between NHPRs and FFR have been reported, and literature about this topic is growing (17, 20, 25), but still limited by a small number of examined patients (26).

Our study represents a broad "all-comers" German population, which is one of the largest studied so far. Previous studies on NHPRs mostly enrolled Asian, American or Scandinavic patients, which may not be fully representative of the Central European population due to different patient characteristics and regional differences in the use of percutaneous coronary interventions (13–15). Furthermore, 26.7% of the patients presented with ACS in our study, which is more than in previous studies (23).

Diagnostic accuracy of NHPRs was between 78–81%, if the "gold standard" FFR is taken as reference, which must be rated as only moderate. This finding is in line with most prior studies (14, 16, 23). A slightly higher diagnostic accuracy of 86.6% for RFR and 87.5% for dPR[entire] was reported in the analysis of the 3V FFR-FRIENDS study (13), which included a population with less severe stenoses as indicated by a median FFR of 0.89 as compared to 0.84 in the present study. The moderate correlation of NHPRs and FFR justifies a carful interpretation of resting indices, e.g., adding FFR recordings in cases of borderline NHPRs may be considered, but it does not question the high value of resting indices, since the feasibility and costs are superior to FFR, which will facilitate the broad application of pressure-wire recordings and help to avoid clearly inferior angiography-based decision making.

To our knowledge, this is the largest study focusing on discordant findings of RFR and FFR. Discordant results were found in 22% of the lesions, which is more frequent compared

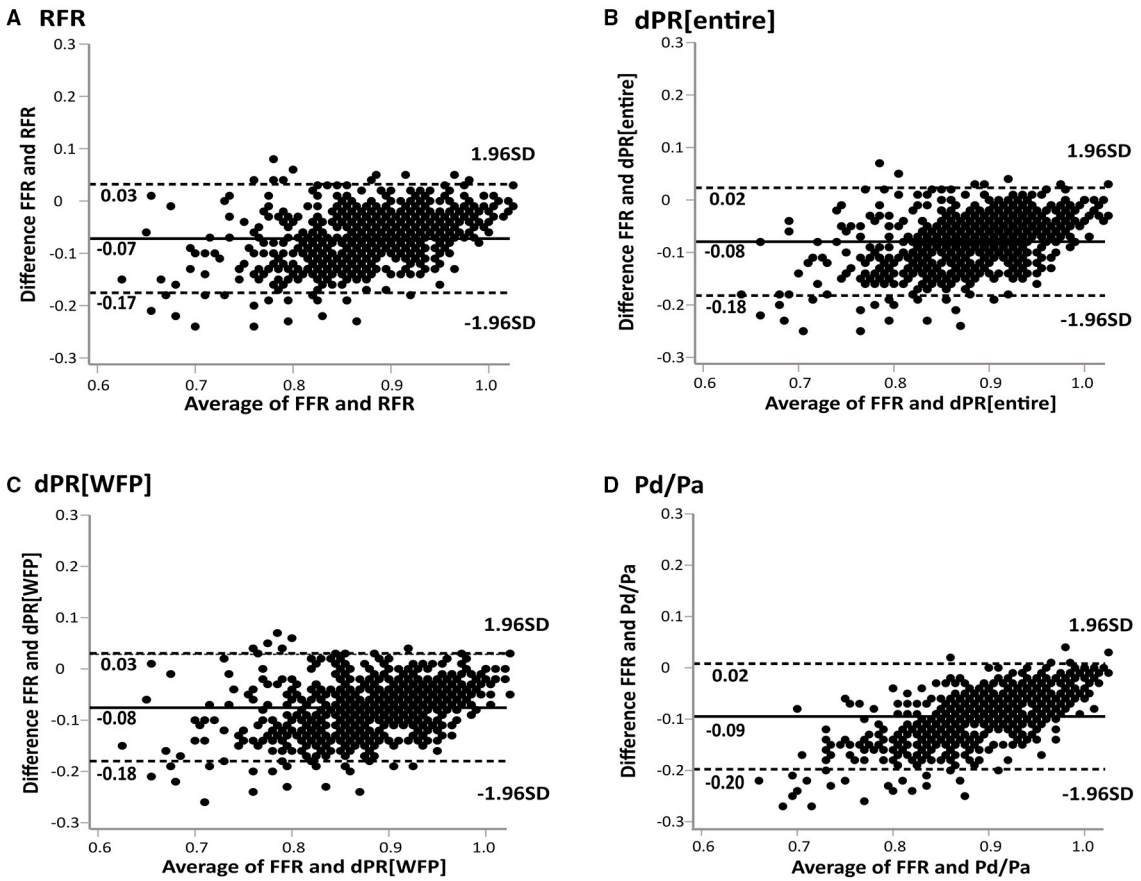

FIGURE 3 | Bland-Altman plots of differences against the means are displayed for RFR **(A)**, dPR[entire] **(B)**, dPR[WFP] **(C)** and Pd/Pa **(D)**. Solid lines represent the mean bias, enclosed by the limits of agreement (dashed lines). The Bland-Altman plots demonstrate a good agreement between FFR and NHPRs. dPR[entire], diastolic pressure ratio during entire diastole; dPR[WFP], diastolic pressure ratio during wave-free period; FFR, fractional flow reserve; NHPR, non-hyperemic pressure ratio; Pa, aortic pressure; Pd, distal coronary pressure; RFR, resting full-cycle ratio.

TABLE 2 | Diagnostic performance of non-hyperemic pressure ratios for predicting FFR ≤ 0.80 at vessel level.

	RFR ≤ 0.89	dPR[entire] ≤ 0.89	dPR[WFP] ≤ 0.89	Pd/Pa ≤ 0.92
True positive, n	159 (22.3)	153 (21.5)	156 (21.9)	174 (24.4)
True negative, n	396 (55.6)	421 (59.1)	408 (57.3)	384 (53.9)
False positive, n	94 (13.2)	69 (9.7)	82 (11.5)	106 (14.9)
False negative, n	63 (8.8)	69 (9.7)	66 (9.3)	48 (6.7)
Accuracy, %	77.9 (74.7–80.9)	80.6 (77.5–83.5)	79.2 (76.0–82.1)	78.4 (75.2–81.3)
Sensitivity, %	71.6 (65.2–77.5)	68.9 (62.4–74.9)	70.3 (63.8–76.2)	78.4 (72.4–83.6)
Specificity, %	80.8 (77.0–84.2)	85.9 (82.5–88.9)	83.3 (79.7–86.5)	78.4 (74.5–81.9)
Positive predictive value, %	62.8 (56.6–68.8)	68.9 (62.4–74.9)	65.5 (59.1–71.6)	62.1 (56.2–67.8)
Negative predictive value, %	86.3 (82.8–89.3)	85.9 (82.5–88.9)	86.1 (82.6–89.1)	88.9 (85.5–91.7)
Positive likelihood ratio	3.7 (3.2–4.6)	4.9 (3.9–6.2)	4.2 (3.4–5.2)	3.6 (3.0–4.4)
Negative likelihood ratio	0.4 (0.3–0.4)	0.4 (0.3–0.4)	0.4 (0.3–0.4)	0.3 (0.2–0.4)

Values are n (%) or n (95% confidence interval).

to previous smaller studies with a range from 7.2–19.7% (14, 22, 26–28). This may be attributed to the broad inclusion criteria, which may affect physiologic measurements and cause discrepancies (21). Discordant findings of NHPRs and FFR have been associated with worse prognosis as compared to concordant negative indices in previous trials (28). On the other hand, iFR-based revascularization was non-inferior to an FFR-based approach despite lower revascularization rates in

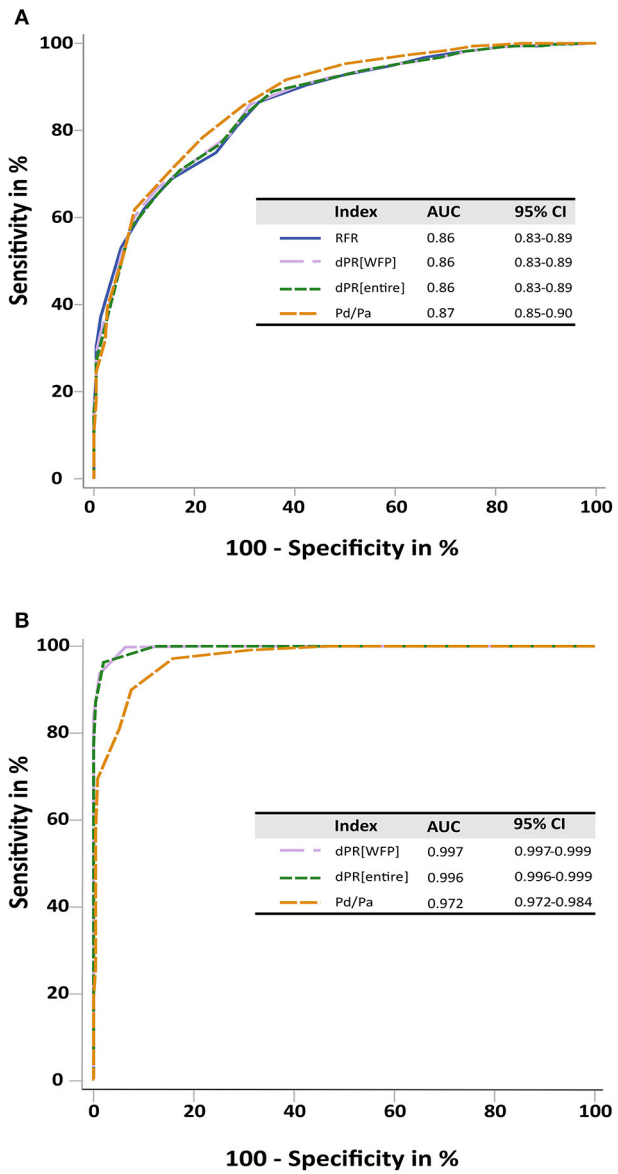

FIGURE 4 | ROC curves. **(A)** ROC curves for RFR, dPR[entire], dPR[WFP] and Pd/Pa showed a similar performance of all NHPRs tested against an FFR ≤ 0.80. **(B)** ROC curves for dPR[WFP], dPR[entire], and Pd/Pa tested against RFR ≤ 0.89. All three indexes showed an excellent prediction for RFR defined ischemia, supporting the similar performance of all NHPRs. dPR[entire], diastolic pressure ratio during entire diastole; dPR[WFP], diastolic pressure ratio during wave-free period; FFR, fractional flow reserve; NHPR, non-hyperemic pressure ratio; Pa, aortic pressure; Pd, distal coronary pressure; RFR, resting full-cycle ratio.

both randomized trials (11, 12). There is an ongoing debate, whether discordant lesions should be revascularized (20, 27, 28). Thus, there is a strong need for more data on the clinical impact of discordance on outcome as well as the indication for revascularization, which was beyond the scope of our study and encourages future - ideally randomized prospective—trials.

Since a single index is usually applied in clinical practice and determination of both resting and hyperemic indices is performed only in the minority of cases, discordance of results is usually inapparent, which increases the importance of potential predictors of discordant findings. Several clinical factors such as gender, anemia, LV diastolic dysfunction, diabetes mellitus and angiographic factors have been proposed as predictors of discordance of low NHPRs /high FFR (19, 20, 22, 26, 29), i.e., revascularization would be performed based on an NHPRs but deferred based on FFR. In our population, female sex, age, LAD lesion, PAD and non-focal lesion were predictors of RFR ≤ 0.89/FFR > 0.8.

Multivariate analysis revealed LAD lesions as a highly relevant predictor for RFR ≤ 0.89/FFR > 0.8 with an odds ratio of 3.17, confirming the findings of present studies of NHPRs (26, 29).

Kobayashi et al. speculated that the larger myocardial territory supplied by LM/LAD vs. non-LAD may cause larger coronary flow variation between resting and hyperemic conditions, which could be responsible for the difference (25).

PAD was a relevant predictor of discrepancy of RFR ≤ 0.89 /FFR > 0.8 with an odds ratio of 2.63. The same finding was reported by Goto et al. (26). Pellegrino et al. reported that the coronary flow reserve (CFR) was significantly lower in patients with PAD than in those without PAD (30), which could explain the discordance, since reduced flow may lead to an underestimation of stenosis severity by FFR. Also Cook et al. suggested that iFR ≤ 0.89 /FFR > 0.8 might be explained by differences in hyperemic coronary flow (17).

The odds ratio was 1.67 for female sex in the multivariate analysis. Two previous studies reported that female sex was significantly associated with NHPRs ≤ 0.89/FFR > 0.8 (20, 22), but not all studies confirmed this finding (26). A *post-hoc* analysis of the DEFINE-FLAIR study demonstrated that an FFR-guided strategy was associated with a higher rate of revascularization than an iFR-guided strategy in men, but not in women (31), so gender differences of pressure-derived indices appear to have a clinical impact. Kobayashi et al. speculated that women tend to have a higher coronary flow at rest leading to higher trans-stenotic pressure losses and lower NHPRs (32).

The odds ratio for age was only 1.04, so despite statistical significance in the multivariate analysis, the impact of age appears to be of minor relevance. Age was also not found as a predictor of discordance in most previous studies for FFR and NHPRs (19, 20, 22, 26). Just like described above for PAD, older age is associated with a decrease in CFR (33) and an increase in microvascular resistance under hyperemia, which may cause an underestimation of stenosis severity by FFR.

The presence of non-focal stenoses, i.e., serial stenoses or diffuse disease, was another predictor for discordance of RFR ≤ 0.89/FFR > 0.8. It has been described that the presence of serial stenoses increases the risk of discordance of FFR and iFR (34). In non-focal disease, downstream stenoses may impede hyperemic flow, thus FFR may underestimate the true physiological impact of analyzed stenoses. Therefore, NHPRs may be superior to FFR in the assessment of non-focal stenoses, although this hypothesis needs confirmation by further clinical trials.

TABLE 3A | Comparison of patient characteristics between concordant and discordant cases of RFR and FFR.

	RFR > 0.89 FFR > 0.8 Both negative	RFR ≤ 0.89 FFR > 0.8 Discordance	RFR ≤ 0.89 FFR ≤ 0.8 Both positive	RFR > 0.89 FFR ≤ 0.8 Discordance	*p* value	Concordance	Discordance	*p* value
Age	69 (61–77)	74 (69–80)	68 (61–74)	65 (56–74)	**< 0.01**	69 (61–79)	71 (63–78)	0.15
Female	104 (31.1)	31 (37.8)	25 (17.2)	9 (16.1)	**< 0.01**	129 (26.9)	40 (29.0)	0.63
Diabetes mellitus	89 (26.6)	22 (26.8)	46 (31.7)	11 (19.6)	0.37	135 (28.2)	33 (23.9)	0.32
Insulin dependent	34 (10.2)	9 (11.0)	15 (10.3)	3 (5.4)	0.69	49 (10.2)	12 (8.7)	0.60
Dyslipidemia	172 (51.5)	46 (56.1)	70 (48.3)	34 (60.7)	0.38	242 (50.5)	80 (58.0)	0.12
Hypertension	241 (72.2)	59 (72.0)	104 (71.7)	44 (78.6)	0.78	345 (72.0)	103 (74.6)	0.54
Peripheral arterial disease	22 (6.6)	13 (15.9)	10 (6.9)	2 (3.6)	**0.02**	32 (6.7)	15 (10.9)	0.10
Current or former smoking	107 (32.0)	35 (42.7)	53 (36.6)	21 (37.5)	0.29	160 (33.4)	56 (40.6)	0.12
β-Blocker use	226 (68.1)	57 (70.4)	106 (73.1)	30 (53.6)	0.06	332 (69.6)	87 (63.5)	0.18
Indication								
NSTEMI	14 (4.2)	5 (6.1)	3 (2.1)	6 (10.7)	0.06	17 (3.5)	11 (8.0)	**0.03**
Unstable angina	69 (20.7)	17 (20.7)	41 (28.3)	10 (17.9)	0.23	110 (23.0)	27 (19.6)	0.40
Stable angina	98 (29.3)	24 (29.3)	49 (33.8)	21 (37.5)	0.54	147 (30.7)	45 (32.6)	0.67
Atypical angina	39 (11.7)	10 (12.2)	12 (8.3)	2 (3.6)	0.22	51 (10.6)	12 (8.7)	0.51
Silent ischemia	114 (34.1)	26 (31.7)	40 (27.6)	17 (30.4)	0.56	154 (32.2)	43 (31.2)	0.83

Data are presented as n (%) or median (Q1–Q3). Bold numbers represent statistically significant p values.

Interestingly, RFR suggested ischemia more frequently than FFR (35.5% of patients had RFR≤ 0.89, 31.2% had FFR ≤ 0.80) in the present study, although most previous studies reported slightly higher rates of ischemia determination by FFR (22, 26). Both randomized studies of iFR- vs. FFR-guided revascularization demonstrated a lower number of revascularizations in the iFR group (12, 35).

Predictors of RFR > 0.89 /FFR ≤ 0.8 discordance, i.e., revascularization would be performed based on FFR but deferred based on an NHPR, were %DS, history of percutaneous coronary intervention in the target vessel, and non-LCX lesions in the multivariate analysis. The relevance of %DS was small with an odds ratio of 1.14. %DS was also a predictor of iFR > 0.90 /FFR ≤ 0.8 discordance in the work by Lee et al. (19). Other studies could not predict this type of discordance, maybe due to the small number of analyzed lesions (22, 26). History of percutaneous coronary intervention in the target vessel (odds ratio 2.10) and non-LCX lesions (odds ratio 0.11 for LCX) were stronger predictors of RFR > 0.89 /FFR ≤ 0.8 discordance in the present trial.

Lesion location (proximal, medial and distal segments) and multivessel disease had no significant effect on the concordance or discordance of indices. Due to the relatively high number of patients with ACS in our study, we could analyze the interaction between the presence of an ACS and the concordance or discordance of indices, which was not significant. This is an interesting finding, since microvascular function may be altered in patients with ACS, which may diminish the effect of adenosine and lead to false negative FFR values (36). Moreover, resting coronary flow in non-culprit ACS lesions may be higher than in stable coronary artery disease (37), which may also contribute to discordance of indices. Our finding of no relevant interaction between the presence of an ACS and the discordance of RFR and FFR is in line with a previous study on iFR and FFR (38).

A subgroup analysis of patients with and without prior myocardial infarction (irrespective of the location) revealed no interaction with the discordance of indices, too. However, we cannot exclude that an analysis of prior myocardial infarction in the territory of the examined vessel may have led to different findings. Unfortunately, information on the exact location of prior myocardial infarction was not available for our population.

It was speculated that coronary stenoses with iFR > 0.90 /FFR ≤ 0.75 show similar coronary flow properties as angiographically unobstructed vessels and, in cases with normal or high CFR and FFR ≤ 0.75, the low FFR may reflect high flow states in response to adenosine rather than significant stenoses, which would be associated with a good prognosis (39, 40). In line with this hypothesis, the randomized trials DEFINE-FLAIR and iFR-SWEDEHEART showed that the risk of coronary events was not increased, although more lesions were deferred for revascularization based on iFR compared to FFR (41).

In our study, all parameters of diagnostic performance were similar for all analyzed NHPRs, increasing the body of evidence that NHPRs are largely comparable among one another, as suggested by one previous trial (13). Thus, a special algorithm of any company has little advantage compared to the "open source" index Pd/Pa. One potential advantage may be that Pd/Pa shows a higher susceptibility to pressure-sensor drifts and to pressure-curves artifacts (42).

Since iFR is the only NHPR with evidence from randomized controlled trials, differences between iFR and other NHPRs are

TABLE 3B | Vessel and lesion characteristics between concordant and discordant cases of RFR and FFR.

	RFR > 0.89 FFR > 0.8 Both negative	RFR ≤ 0.89 FFR > 0.8 Discordance	RFR ≤ 0.89 FFR ≤ 0.8 Both positive	RFR > 0.89 FFR ≤ 0.8 Discordance	*p* value	Concordance	Discordance	*p* value
No. of vessels	396 (55.7)	94 (13.2)	159 (22.3)	63 (8.8)		555 (78.0)	157 (22.0)	
Target Vessel								
Left anterior descending	174 (43.9)	75 (79.8)	131 (82.4)	44 (69.8)	**< 0.01**	305 (55.0)	119 (75.8)	**< 0.01**
Ramus intermedius	7 (1.8)	2 (2.1)	2 (1.3)	0 (0)	0.70	9 (1.6)	2 (1.3)	0.76
Right coronary artery	108 (27.3)	8 (8.5)	10 (6.3)	17 (27)	**< 0.01**	118 (21.3)	25 (15.9)	0.14
Left circumflex artery	98 (24.7)	9 (9.6)	15 (9.4)	2 (3.2)	**< 0.01**	113 (20.4)	11 (7)	**< 0.01**
Number of diseased vessels total								
1	94 (23.7)	25 (26.6)	28 (17.6)	11 (17.5)	0.23	122 (22)	36 (22.9)	0.80
2	159 (40.2)	33 (35.1)	51 (32.1)	29 (46)	0.16	210 (37.8)	62 (39.5)	0.71
3	120 (30.3)	34 (36.2)	78 (49.1)	23 (36.5)	**< 0.01**	198 (35.7)	57 (36.3)	0.88
Lesion location								
Proximal	191 (48.2)	39 (41.5)	58 (36.5)	20 (31.7)	**0.02**	249 (44.9)	59 (37.6)	0.11
Mid	147 (37.1)	47 (50.0)	74 (46.5)	32 (50.8)	**0.03**	221 (39.8)	78 (49.7)	**0.03**
Distal	58 (14.6)	8 (8.5)	27 (17)	11 (17.5)	0.27	85 (15.3)	19 (12.1)	0.31
Non-focal lesion	136 (34.3)	49 (52.1)	81 (50.9)	24 (38.1)	**< 0.01**	217 (39.1)	73 (46.5)	0.10
QCA analysis								
Diameter stenosis, %	49.45 ± 7.26	51.69 ± 7.43	59.07 ± 8.1	61.04 ± 6.96	**< 0.01**	52.2 ± 8.68	55.44 ± 8.56	**< 0.01**
Reference diameter, mm	3.12 ± 0.61	2.9 ± 0.61	2.76 ± 0.57	2.79 ± 0.56	**< 0.01**	3.02 ± 0.62	2.86 ± 0.59	**0.01**
Minimal lumen diameter, mm	1.58 ± 0.39	1.41 ± 0.39	1.13 ± 0.31	1.12 ± 0.32	**< 0.01**	1.46 ± 0.42	1.3 ± 0.39	**< 0.01**
Lesion length, mm	14.27 ± 8.53	14.61 ± 9.17	18.07 ± 10.96	19.46 ± 10.25	**< 0.01**	15.36 ± 9.44	16.56 ± 9.88	0.17
Pressure wire-derived index								
FFR	0.89 (0.86–0.93)	0.84 (0.82–0.86)	0.75 (0.71–0.78)	0.78 (0.76–0.8)	**< 0.01**	0.86 (0.79–0.91)	0.82 (0.79–0.85)	**< 0.01**
RFR	0.95 (0.93–0.98)	0.88 (0.85–0.89)	0.85 (0.81–0.87)	0.92 (0.91–0.93)	**< 0.01**	0.93 (0.88–0.97)	0.89 (0.87–0.91)	**< 0.01**
dPR[WFP]	0.96 (0.93–0.98)	0.88 (0.86–0.89)	0.85 (0.81–0.87)	0.92 (0.91–0.94)	**< 0.01**	0.94 (0.88–0.97)	0.89 (0.87–0.91)	**< 0.01**
dPR[diastole]	0.96 (0.93–0.98)	0.88 (0.86–0.90)	0.86 (0.82–0.88)	0.92 (0.91–0.94)	**< 0.01**	0.94 (0.89–0.98)	0.90 (0.88–0.92)	**< 0.01**
Resting Pd/Pa	0.96 (0.95–0.99)	0.91 (0.9–0.92)	0.88 (0.85–0.9)	0.94 (0.92–0.95)	**< 0.01**	0.95 (0.91–0.98)	0.92 (0.9–0.94)	**< 0.01**

Data are presented as n (%), mean SD, or median (Q1–Q3); Abbreviations as in the text. Bold numbers represent statistically significant p values.

of particular interest. Van't Veer et al. reported that available diastolic resting indices calculated in the "wave-free period" are identical to iFR despite minor differences in algorithms (43), so we consider dPR[WFP] used in our study to be equal to iFR. We found a difference of only 2.2% for dPR[WFP] vs. RFR in the rate of ischemia determination, which was not statistically significant. So, an RFR-based approach would have led to the same treatment strategy as an iFR-based in the majority of cases.

Accordingly, only 2.2% of RFR measurements detected the lowest Pd/Pa in systole. This is much lower than reported in most previous studies with a range from 11.4–12.2% (13, 14). Flow profiles between LCA und RCA are different (44), which may be explained by differences in supplied myocardial mass (45) and may have an impact on the timing of lowest Pd/Pa. In the VALIDATE study, lowest Pd/Pa was detected in systole in 32.4% in the RCA (14). In the present study, lowest Pd/Pa was in systole in 15.4% of RCA analyses. In contrast, Hoshino et al. found only 2.4% of RFR values in systole in the RCA (23).

Limitations

Our trial has several limitations. It was an observational retrospective cohort study conducted at a single center. Revascularization of the target lesion was based on FFR values and operators' decision, and not on NHPRs. Patient selection for pressure-wire assessment was also within the discretion of the treating physician, which may have led to bias. However, we intended to study pressure wire-derived indices under real-life conditions. Another limitation is that we did not investigate

TABLE 4A | Independent predictors of disagreement between RFR and FFR.

	Discordance with RFR ≤0.89 and FFR >0.8					
	Univariate Analysis			Multivariate Analysis		
	Odds ratio	95% CI	*P*-value	Odds ratio	95% CI	*P*-value
Age, per 1-year increment	1.04	1.02–1.07	**< 0.01**	1.04	1.02–1.07	**0.01**
Female	1.86	1.19–2.92	**0.01**	1.70	1.06-2.74	**0.03**
Diabetes mellitus	0.99	0.6–1.61	0.96			
Hypertension	1.06	0.65–1.74	0.80			
Hyperlipidemia	1.24	0.8–1.92	0.33			
Current or former smoking	1.21	0.77–1.89	0.41			
Peripheral arterial disease	2.42	1.29–4.54	**0.01**	2.71	1.39–5.28	**0.01**
NSTEMI or unstable AP	0.97	0.59–1.59	0.91			
Previous PCI in target vessel	1.33	0.81–2.19	0.26			
Previous myocardial infarction	1.12	0.70–1.80	0.64			
Non-focal lesion	1.70	1.10–2.63	**0.02**	1.84	1.17–2.89	**0.01**
Multivessel disease	0.85	0.53–1.38	0.52			
Proximal or mid segment*	1.98	0.93–4.21	0.08			
Proximal segment	0.93	0.60–1.44	0.73			
Mid segment	1.38	0.90–2.14	0.14			
Distal segment	0.51	0.24–1.08	0.08			
% DS	0.98	0.96–1.01	0.14			
Minimal lumen diameter	0.96	0.58–1.62	0.89			
Lesion length	0.99	0.96–1.01	0.27			
Lesion location LAD	3.04	1.8–5.16	**< 0.01**	3.22	1.88–5.52	**< 0.01**
Lesion location RCA	0.33	0.16–0.7	**< 0.01**			
Lesion location LCX	0.46	0.23–0.95	**0.04**			

** Target lesion located in the proximal or mid segment of the target vessel. CI, confidence interval; other abbreviations as in the text. Bold numbers represent statistically significant p values.*

clinical outcomes after revascularization. Thus, the clinical impact of discrepancies between FFR and NHPRs could not be assessed.

Our cohort comprised patients with diabetes, CABG, and intake of beta-blockers. On the other side, we consider the broad "all-comers" population as one strength of the present study, since it probably better reflects the realities of care than previous studies with more extensive exclusion criteria.

No assessment of microvascular function or coronary flow was performed. A better understanding of microcirculation and coronary flow under baseline and hyperemic conditions would have improved the interpretation of discrepant findings of NHPRs and FFR.

A total of 157 out of 869 (18.1%) pressure tracings could not be analyzed. Previous studies have shown that even in the context of a prospective clinical trial, physiological assessments of stenosis severity may be limited by pressure tracings being unanalyzable due to artifacts and failure in up to 30% (16, 25). Patients were not excluded from our analysis based on any clinical parameters, but all non-analyzed recordings had to be excluded due to insufficient tracings (e.g., dampened aortic pressure, no stable resting or hyperemic recording, resting or hyperemic period not recorded at all). We did not collect clinical data of these patients, but we consider it very likely, that the technical shortcomings leading to exclusion of tracings from the analysis were not associated with any clinical characteristics.

The external analysis of pressure curves by an expert core lab is not fully representative for the real-life situation, however it reduces inter-observer variability and ensures reliability of the calculations. Moreover, due to the retrospective nature of our study and the incapability of commercially available systems to calculate all investigated resting indices online in the catheterization laboratory, an offline analysis was necessary.

CONCLUSIONS

All NHPRs have a similar correlation with the gold standard FFR and may facilitate the acceptance and implementation of physiological assessments of lesion severity. However, we found ∼20% discordant results between NHPRs and FFR in our "all-comers" German cohort. Most relevant predictors for discordance of RFR $\leq$ 0.89 /FFR $>$ 0.8 were LAD lesions, PAD, female sex and non-focal stenoses. Strong predictors for discordance of RFR $>$ 0.89/FFR $\leq$ 0.8 were non-LCX lesions and previous percutaneous coronary intervention in the target vessel. The impact of discrepant findings on outcome and the

TABLE 4B | Independent predictors of disagreement between RFR and FFR.

	Discordance with RFR >0.89 and FFR≤ 0.8					
	Univariate Analysis			Multivariate Analysis		
	Odds ratio	95% CI	*P*-value	Odds ratio	95% CI	*P*-value
Age, per 1-yr increment	0.97	0.95–1.00	**0.02**			
Female	0.50	0.26–0.99	**0.05**			
Diabetes mellitus	0.62	0.32–1.19	0.15			
Hypertension	1.37	0.74–2.55	0.31			
Hyperlipidemia	1.21	0.72–2.04	0.47			
Current or former smoking	1.10	0.64–1.88	0.73			
Peripheral arterial disease	0.33	0.08–1.4	0.13			
NSTEMI or unstable AP	1.38	0.80–2.41	0.25			
Previous PCI in target vessel	2.04	1.18–3.55	**0.01**	2.10	1.15–3.85	**0.02**
Previous myocardial infarction	0.99	0.56–1.75	0.97			
Non-focal lesion	0.89	0.52–1.51	0.87			
Multivessel disease	1.73	0.88–3.4	0.11			
Proximal or mid segment*	0.79	0.4–1.57	0.50			
Proximal segment	0.56	0.34–1.02	0.06			
Mid segment	1.48	0.89–2.48	0.14			
Distal segment	1.27	0.64–2.51	0.53			
% DS	1.14	1.1–1.18	**< 0.01**	1.14	1.10–1.19	**< 0.01**
Minimal lumen diameter	0.09	0.04–0.2	**< 0.01**			
Lesion length	1.04	1.02–1.06	**< 0.01**			
Lesion location LAD	1.64	0.94–2.87	0.08			
Lesion location RCA	1.53	0.85–2.77	0.16			
Lesion location LCX	0.14	0.03–0.59	**0.01**	0.11	0.02–0.52	**0.01**

** Target lesion located in the proximal or mid segment of the target vessel. CI confidence interval; other abbreviations as in the text. Bold numbers represent statistically significant p values.*

optimal treatment strategy needs to be further elucidated by future prospective trials.

DATA AVAILABILITY STATEMENT

The raw data supporting the conclusions of this article will be made available by the authors, without undue reservation.

ETHICS STATEMENT

The studies involving human participants were reviewed and approved by Ethics Committee Medical Faculty, University of Cologne. The Ethics Committee waived the requirement of written informed consent for participation.

AUTHOR CONTRIBUTIONS

HW, MH, and SB: study concept and design. HW, AM, VM, and TB: acquisition and analysis or interpretation of data. HW: writing and original draft preparation of the manuscript. HW, VM, MA, SB, and MH: discussion or critical revision of the interpretation for important intellectual content. MH: study supervision. All authors reviewed the manuscript.

FUNDING

The corelab analysis at Coroventis Research AB was supported by Abbott Vascular.

REFERENCES

1. Roth GA, Johnson C, Abajobir A, Abd-Allah F, Abera SF, Abyu G, et al. Global, regional, and national burden of cardiovascular diseases for 10 causes, 1990 to 2015. *J Am Coll Cardiol.* (2017) 70:1–25. doi: 10.1016/j.jacc.2017.04.052
2. Neumann F-J, Sousa-Uva M, Ahlsson A, Alfonso F, Banning AP, Benedetto U, et al. 2018 ESC/EACTS Guidelines on myocardial revascularization. *Eur Heart J.* (2019) 40:87–165. doi: 10.1093/eurheartj/ehy394
3. Xaplanteris P, Fournier S, Pijls NH, Fearon WF, Barbato E, Tonino PA, et al. Five-year outcomes with PCI guided by fractional flow reserve. *N Engl J Med.* (2018) 379:250–9. doi: 10.1056/NEJMoa1803538
4. Zimmermann FM, Ferrara A, Johnson NP, van Nunen LX, Escaned J, Albertsson P, et al. Deferral vs. performance of percutaneous coronary intervention of functionally non-significant coronary stenosis: 15-year follow-up of the DEFER trial. *Eur Heart J.* (2015) 36:3182–8. doi: 10.1093/eurheartj/ehv452

5. van Nunen LX, Zimmermann FM, Tonino PA, Barbato E, Baumbach A, Engstrøm T, et al. Fractional flow reserve versus angiography for guidance of PCI in patients with multivessel coronary artery disease (FAME): 5-year follow-up of a randomised controlled trial. *Lancet.* (2015) 386:1853–60. doi: 10.1016/S0140-6736(15)00057-4
6. Knuuti J, Wijns W, Saraste A, Capodanno D, Barbato E, Funck-Brentano C, et al. 2019 ESC guidelines for the diagnosis and management of chronic coronary syndromes. *Eur Heart J.* (2020) 41:407–77. doi: 10.1093/eurheartj/ehz425
7. Bruyne B de, Pijls NH, Kalesan B, Barbato E, Tonino PA, Piroth Z, et al. Fractional flow reserve-guided PCI versus medical therapy in stable coronary disease. *N Engl J Med.* (2012) 367:991–1001. doi: 10.1056/NEJMoa1205361
8. Pijls NH, Bruyne B, Peels K, Voort PH, Bonnier HJ, Bartunek J, et al. Measurement of fractional flow reserve to assess the functional severity of coronary-artery stenoses. *N Engl J Med.* (1996) 334:1703–8. doi: 10.1056/NEJM199606273342604
9. Röther J, Achenbach S, Tröbs M, Blachutzik F, Nef H, Marwan M, et al. Comparison of standard- and high-dose intracoronary adenosine for the measurement of coronary Fractional Flow Reserve (FFR). *Clin Res Cardiol.* (2016) 105:1003–10. doi: 10.1007/s00392-016-1010-0
10. Härle T, Zeymer U, Hochadel M, Zahn R, Kerber S, Zrenner B, et al. Real-world use of fractional flow reserve in Germany: results of the prospective ALKK coronary angiography and PCI registry. *Clin Res Cardiol.* (2017) 106:140–50. doi: 10.1007/s00392-016-1034-5
11. Götberg M, Christiansen EH, Gudmundsdottir IJ, Sandhall L, Danielewicz M, Jakobsen L, et al. Instantaneous wave-free ratio versus fractional flow reserve to guide PCI. *N Engl J Med.* (2017) 376:1813–23. doi: 10.1056/NEJMoa1616540
12. Davies JE, Sen S, Dehbi H-M, Al-Lamee R, Petraco R, Nijjer SS, et al. Use of the instantaneous wave-free ratio or fractional flow reserve in PCI. *N Engl J Med.* (2017) 376:1824–34. doi: 10.1056/NEJMoa1700445
13. Lee JM, Choi KH, Park J, Hwang D, Rhee T-M, Kim J, et al. Physiological and clinical assessment of resting physiological indexes. *Circulation.* (2019) 139:889–900. doi: 10.1161/CIRCULATIONAHA.118.037021
14. Svanerud J, Ahn J-M, Jeremias A, van 't Veer M, Gore A, Maehara A, et al. Validation of a novel non-hyperaemic index of coronary artery stenosis severity: the Resting Full-cycle Ratio (VALIDATE RFR) study. *EuroIntervention.* (2018) 14:806–14. doi: 10.4244/EIJ-D-18-00342
15. Kumar G, Desai R, Gore A, Rahim H, Maehara A, Matsumura M, et al. Real world validation of the nonhyperemic index of coronary artery stenosis severity-Resting full-cycle ratio-RE-VALIDATE. *Catheter Cardiovasc Interv.* (2020) 96:E53–8. doi: 10.1002/ccd.28523
16. Jeremias A, Maehara A, Généreux P, Asrress KN, Berry C, Bruyne Bde, et al. Multicenter core laboratory comparison of the instantaneous wave-free ratio and resting Pd/Pa with fractional flow reserve: the RESOLVE study. *J Am Coll Cardiol.* (2014) 63:1253–61. doi: 10.1016/j.jacc.2013.09.060
17. Cook CM, Jeremias A, Petraco R, Sen S, Nijjer S, Shun-Shin MJ, et al. Fractional flow reserve/instantaneous wave-free ratio discordance in angiographically intermediate coronary stenoses: an analysis using doppler-derived coronary flow measurements. *JACC Cardiovasc Interv.* (2017) 10:2514–24. doi: 10.1016/j.jcin.2017.09.021
18. Sen S, Escaned J, Malik IS, Mikhail GW, Foale RA, Mila R, et al. Development and validation of a new adenosine-independent index of stenosis severity from coronary wave-intensity analysis: results of the ADVISE (ADenosine Vasodilator Independent Stenosis Evaluation) study. *J Am Coll Cardiol.* (2012) 59:1392–402. doi: 10.1016/j.jacc.2011.11.003
19. Lee JM, Shin E-S, Nam C-W, Doh J-H, Hwang D, Park J, et al. Discrepancy between fractional flow reserve and instantaneous wave-free ratio: clinical and angiographic characteristics. *Int J Cardiol.* (2017) 245:63–8. doi: 10.1016/j.ijcard.2017.07.099
20. Arashi H, Satomi N, Ishida I, Soontorndhada K, Ebihara S, Tanaka K, et al. Hemodynamic and lesion characteristics associated with discordance between the instantaneous wave-free ratio and fractional flow reserve. *J Interv Cardiol.* (2019) 2019:3765282. doi: 10.1155/2019/3765282
21. Dérimay F, Johnson NP, Zimmermann FM, Adjedj J, Witt N, Hennigan B, et al. Predictive factors of discordance between the instantaneous wave-free ratio and fractional flow reserve. *Catheter Cardiovasc Interv.* (2019) 94:356–63. doi: 10.1002/ccd.28116
22. Muroya T, Kawano H, Hata S, Shinboku H, Sonoda K, Kusumoto S, et al. Relationship between resting full-cycle ratio and fractional flow reserve in assessments of coronary stenosis severity. *Catheter Cardiovasc Interv.* (2020) 96:E432–8. doi: 10.1002/ccd.28835
23. Hoshino M, Yonetsu T, Sugiyama T, Kanaji Y, Hamaya R, Kanno Y, et al. All resting physiological indices may not be equivalent - comparison between the diastolic pressure ratio and resting full-cycle ratio. *Circ J.* (2020) 84:1147–54. doi: 10.1253/circj.CJ-19-1110
24. Biscaglia S, Uretsky BF, Tebaldi M, Erriquez A, Brugaletta S, Cerrato E, et al. Angio-based fractional flow reserve, functional pattern of coronary artery disease, and prediction of percutaneous coronary intervention result: a proof-of-concept study. *Cardiovasc Drugs Ther.* (2021). doi: 10.1007/s10557-021-07162-6. [Epub ahead of print].
25. Kobayashi Y, Johnson NP, Berry C, Bruyne B de, Gould KL, Jeremias A, et al. The influence of lesion location on the diagnostic accuracy of adenosine-free coronary pressure wire measurements. *JACC Cardiovasc Interv.* (2016) 9:2390–9. doi: 10.1016/j.jcin.2016.08.041
26. Goto R, Takashima H, Ohashi H, Ando H, Suzuki A, Sakurai S, et al. Independent predictors of discordance between the resting full-cycle ratio and fractional flow reserve. *Heart Vessels.* (2021) 36:790–8. doi: 10.1007/s00380-020-01763-1
27. Lee JM, Rhee TM, Choi KH, Park J, Hwang D, Kim J, et al. Clinical outcome of lesions with discordant results among different invasive physiologic indices-resting distal coronary to aortic pressure ratio, resting full-cycle ratio, diastolic pressure ratio, instantaneous wave-free ratio, and fractional flow reserve. *Circ J.* (2019) 83:2210–21. doi: 10.1253/circj.CJ-19-0230
28. Lee JM, Lee SH, Hwang D, Rhee T-M, Choi KH, Kim J, et al. Long-term clinical outcomes of nonhyperemic pressure ratios: resting full-cycle ratio, diastolic pressure ratio, and instantaneous wave-free ratio. *J Am Heart Assoc.* (2020) 9:e016818. doi: 10.1161/JAHA.120.016818
29. Kato Y, Dohi T, Chikata Y, Fukase T, Takeuchi M, Takahashi N, et al. Predictors of discordance between fractional flow reserve and resting full-cycle ratio in patients with coronary artery disease: evidence from clinical practice. *J Cardiol.* (2020) 77:313–9. doi: 10.1016/j.jjcc.2020.10.014
30. Pellegrino T, Storto G, Filardi PP, Sorrentino AR, Silvestro A, Petretta M, et al. Relationship between brachial artery flow-mediated dilation and coronary flow reserve in patients with peripheral artery disease. *J Nucl Med.* (2005) 46:1997–2002.
31. Kim CH, Koo B-K, Dehbi H-M, Lee JM, Doh J-H, Nam C-W, et al. Sex differences in instantaneous wave-free ratio or fractional flow reserve-guided revascularization strategy. *JACC Cardiovasc Interv.* (2019) 12:2035–46. doi: 10.1016/j.jcin.2019.06.035
32. Kobayashi Y, Fearon WF, Honda Y, Tanaka S, Pargaonkar V, Fitzgerald PJ, et al. Effect of sex differences on invasive measures of coronary microvascular dysfunction in patients with angina in the absence of obstructive coronary artery disease. *JACC Cardiovasc Interv.* (2015) 8:1433–41. doi: 10.1016/j.jcin.2015.03.045
33. van de Hoef TP, Echavarria-Pinto M, Meuwissen M, Stegehuis VE, Escaned J, Piek JJ. Contribution of age-related microvascular dysfunction to abnormal coronary: hemodynamics in patients with ischemic heart disease. *JACC Cardiovasc Interv.* (2020) 13:20–9. doi: 10.1016/j.jcin.2019.08.052
34. Warisawa T, Cook CM, Howard JP, Ahmad Y, Doi S, Nakayama M, et al. Physiological pattern of disease assessed by pressure-wire pullback has an influence on fractional flow reserve/instantaneous wave-free ratio discordance. *Circ Cardiovasc Interv.* (2019) 12:e007494. doi: 10.1161/CIRCINTERVENTIONS.118.007494
35. Götberg M, Cook CM, Sen S, Nijjer S, Escaned J, Davies JE. The evolving future of instantaneous wave-free ratio and fractional flow reserve. *J Am Coll Cardiol.* (2017) 70:1379–402. doi: 10.1016/j.jacc.2017.07.770
36. Niccoli G, Indolfi C, Davies JE. Evaluation of intermediate coronary stenoses in acute coronary syndromes using pressure guidewire. *Open Heart.* (2017) 4:e000431. doi: 10.1136/openhrt-2016-000431
37. Mejía-Rentería H, Lee JM. van der Hoeven, Nina W, Gonzalo N, Jiménez-Quevedo P, Nombela-Franco L, et al. Coronary microcirculation downstream non-infarct-related arteries in the subacute phase of myocardial infarction: implications for physiology-guided revascularization. *J Am Heart Assoc.* (2019) 8:e011534. doi: 10.1161/JAHA.118.011534

38. Indolfi C, Mongiardo A, Spaccarotella C, Torella D, Caiazzo G, Polimeni A, et al. The instantaneous wave-free ratio (iFR) for evaluation of non-culprit lesions in patients with acute coronary syndrome and multivessel disease. *Int J Cardiol.* (2015) 178:46–54. doi: 10.1016/j.ijcard.2014.03.210
39. Petraco R, van de Hoef TP, Nijjer S, Sen S, van Lavieren MA, Foale RA, et al. Baseline instantaneous wave-free ratio as a pressure-only estimation of underlying coronary flow reserve: results of the JUSTIFY-CFR Study (Joined coronary pressure and flow analysis to determine diagnostic characteristics of basal and hyperemic indices of functional lesion severity-coronary flow reserve). *Circ Cardiovasc Interv.* (2014) 7:492–502. doi: 10.1161/CIRCINTERVENTIONS.113.000926
40. van de Hoef TP, van Lavieren MA, Damman P, Delewi R, Piek MA, Chamuleau SA, et al. Physiological basis and long-term clinical outcome of discordance between fractional flow reserve and coronary flow velocity reserve in coronary stenoses of intermediate severity. *Circ Cardiovasc Interv.* (2014) 7:301–11. doi: 10.1161/CIRCINTERVENTIONS.113.001049
41. Escaned J, Ryan N, Mejía-Rentería H, Cook CM, Dehbi H-M, Alegria-Barrero E, et al. Safety of the deferral of coronary revascularization on the basis of instantaneous wave-free ratio and fractional flow reserve measurements in stable coronary artery disease and acute coronary syndromes. *JACC Cardiovasc Interv.* (2018) 11:1437–49. doi: 10.1016/j.jcin.2018.05.029
42. Cook CM, Ahmad Y, Shun-Shin MJ, Nijjer S, Petraco R, Al-Lamee R, et al. Quantification of the effect of pressure wire drift on the diagnostic performance of fractional flow reserve, instantaneous wave-free ratio, and whole-cycle Pd/Pa. *Circ Cardiovasc Interv.* (2016) 9:e002988. doi: 10.1161/CIRCINTERVENTIONS.115.002988
43. Van't Veer M, Pijls NH, Hennigan B, Watkins S, Ali ZA, Bruyne B de, et al. Comparison of different diastolic resting indexes to iFR: are they all equal? *J Am Coll Cardiol.* (2017) 70:3088–96. doi: 10.1016/j.jacc.2017.10.066
44. Marcus JT, Smeenk HG, Kuijer JP, van der Geest RJ, Heethaar RM, van Rossum AC. Flow profiles in the left anterior descending and the right coronary artery assessed by MR velocity quantification: effects of through -plane and in-plane motion of the heart. *J Comput Assist Tomogr.* (1999) 23:567–76. doi: 10.1097/00004728-199907000-00017
45. Leone AM, Caterina AR de, Basile E, Gardi A, Laezza D, Mazzari MA, et al. Influence of the amount of myocardium subtended by a stenosis on fractional flow reserve. *Circ Cardiovasc Interv.* (2013) 6:29–36. doi: 10.1161/CIRCINTERVENTIONS.112.971101

Conflict of Interest: SB and MH received institutional grant support and speakers' honoraria from Abbott Vascular. HW received institutional grant support from Abbott Vascular. Abbott Vascular had no influence on the design of the study, data analysis or interpretation of findings.

The remaining authors declare that the research was conducted in the absence of any commercial or financial relationships that could be construed as a potential conflict of interest.

frontiers | Frontiers in Cardiovascular Medicine

ORIGINAL RESEARCH
published: 14 April 2022
doi: 10.3389/fcvm.2022.835270

Non-Newtonian Endothelial Shear Stress Simulation: Does It Matter?

*Vikas Thondapu[1,2,3], Daisuke Shishikura[4], Jouke Dijkstra[5], Shuang J. Zhu[2], Eve Revalor[1,6], Patrick W. Serruys[7,8], William J. van Gaal[1,9], Eric K. W. Poon[1], Andrew Ooi[2] and Peter Barlis[1]**

[1] Department of Medicine, Faculty of Medicine, Melbourne Medical School, Dentistry and Health Sciences, University of Melbourne, Parkville, VIC, Australia, [2] Department of Mechanical Engineering, Melbourne School of Engineering, University of Melbourne, Parkville, VIC, Australia, [3] Department of Radiology and Biomedical Imaging, Yale University School of Medicine, New Haven, CT, United States, [4] Department of Cardiology, Osaka Medical and Pharmaceutical University, Osaka, Japan, [5] Department of Radiology, Division of Image Processing, Leiden University Medical Center, Leiden, Netherlands, [6] Department of Biomedical Engineering, Melbourne School of Engineering, University of Melbourne, Parkville, VIC, Australia, [7] Department of Cardiology, National University of Ireland Galway (NUIG), Galway, Ireland, [8] National Heart and Lung Institute, Imperial College London, London, United Kingdom, [9] Department of Cardiology, Northern Hospital, Epping, NSW, Australia

OPEN ACCESS

Edited by:
Antonios Karanasos, Hippokration General Hospital, Greece

Reviewed by:
Monika Colombo, ETH Zürich, Switzerland
Michail Papafaklis, University Hospital of Ioannina, Greece

***Correspondence:**
Peter Barlis
peter.barlis@unimelb.edu.au

Specialty section:
This article was submitted to Cardiovascular Imaging, a section of the journal Frontiers in Cardiovascular Medicine

Received: *14 December 2021*
Accepted: *09 March 2022*
Published: *14 April 2022*

Citation:
Thondapu V, Shishikura D, Dijkstra J, Zhu SJ, Revalor E, Serruys PW, van Gaal WJ, Poon EKW, Ooi A and Barlis P (2022) Non-Newtonian Endothelial Shear Stress Simulation: Does It Matter? Front. Cardiovasc. Med. 9:835270. doi: 10.3389/fcvm.2022.835270

Patient-specific coronary endothelial shear stress (ESS) calculations using Newtonian and non-Newtonian rheological models were performed to assess whether the common assumption of Newtonian blood behavior offers similar results to a more realistic but computationally expensive non-Newtonian model. 16 coronary arteries (from 16 patients) were reconstructed from optical coherence tomographic (OCT) imaging. Pulsatile CFD simulations using Newtonian and the Quemada non-Newtonian model were performed. Endothelial shear stress (ESS) and other indices were compared. Exploratory indices including local blood viscosity (LBV) were calculated from non-Newtonian simulation data. Compared to the Newtonian results, the non-Newtonian model estimates significantly higher time-averaged ESS (1.69 (IQR 1.36)Pa versus 1.28 (1.16)Pa, $p < 0.001$) and ESS gradient (0.90 (1.20)Pa/mm versus 0.74 (1.03)Pa/mm, $p < 0.001$) throughout the cardiac cycle, under-estimating the low ESS (<1Pa) area (37.20 ± 13.57% versus 50.43 ± 14.16%, 95% CI 11.28–15.18, $p < 0.001$). Similar results were also found in the idealized artery simulations with non-Newtonian median ESS being higher than the Newtonian median ESS (healthy segments: 0.8238Pa versus 0.6618Pa, $p < 0.001$ proximal; 0.8179Pa versus 0.6610Pa, $p < 0.001$ distal; stenotic segments: 0.8196Pa versus 0.6611Pa, $p < 0.001$ proximal; 0.2546Pa versus 0.2245Pa, $p < 0.001$ distal) On average, the non-Newtonian model has a LBV of 1.45 times above the Newtonian model with an average peak LBV of 40-fold. Non-Newtonian blood model estimates higher quantitative ESS values than the Newtonian model. Incorporation of non-Newtonian blood behavior may improve the accuracy of ESS measurements. The non-Newtonian model also allows calculation of exploratory viscosity-based hemodynamic indices, such as local blood viscosity, which may offer additional information to detect underlying atherosclerosis.

Keywords: computational fluid dynamics – CFD, non-Newtonian, rheology, viscosity, optical coherence tomography, shear stress (fluid)

INTRODUCTION

Fundamentally, computational fluid dynamics (CFD) is based on the idea that, given certain assumptions, the mechanics of fluid motion can be accurately described by physical principles and mathematical equations. The computational solution of these equations allows the determination of various hemodynamic indices such as blood velocity and pressure throughout the artery, from which other parameters such as endothelial shear stress (ESS) can be further derived. With continued advances, the underlying computational methods are frequently re-evaluated to optimize the shifting balance between accuracy and complexity. One such computational model concerns the variable viscosity of blood at high and low shear rates.

Earlier studies suggest that for laminar flow in medium to large arteries, blood may be assumed a Newtonian fluid with a constant viscosity independent of shear rate (1–5). However, due partly to its dual solid and liquid phases, blood exhibits non-Newtonian behaviors (6). This includes properties such as shear-thinning, the apparent thinning of blood at high shear rates and thickening at low shear rates. While the Newtonian assumption is generally acceptable in healthy straight segments of larger arteries, it may not be as accurate as non-Newtonian rheological models in the setting of complex flow patterns (7, 8). As artery anatomy changes, high fluctuations in local shear rate are significant enough that the non-Newtonian behavior of blood may emerge (**Figure 1**). In these near-wall regions, local blood viscosity (LBV) is expected to change from location to location and from instant to instant over the cardiac cycle. However, because the Newtonian model assumes constant viscosity, changes in LBV are not detected. The non-Newtonian model encompasses the variable viscosity of blood and thus provides this information. Our underlying hypothesis is that, if non-Newtonian behavior is negligible in coronary arteries, the two models should present nearly identical results. Divergent results, however, would suggest otherwise.

MATERIALS AND METHODS

Study Design and Patient Selection

This study compares blood flow characteristics generated by CFD analysis in patient-specific coronary arteries using Newtonian and non-Newtonian blood models under pulsatile flow. Patients were retrospectively selected from a previous multicentre randomized clinical trial (NCT01776567). Inclusion criteria for the current study were the presence of an unstented, non-obstructive (diameter stenosis <50%) non-culprit lesion in the culprit vessel. Major exclusion criteria were ST-elevation myocardial infarction within the preceding 48 h, left ventricular ejection fraction <25%, and bifurcation lesions.

Three-Dimensional Reconstruction

Patient-specific 3D arterial models were reconstructed through the fusion of OCT and angiography as previously described (9). The arterial centreline was extracted from two end-diastolic angiographic images with a >25° difference in viewing angles (QAngio XA 3D, Medis Specials Bv, Netherlands). Side branches outside the region of interest were used to co-register OCT images with angiograms. OCT lumen contours were semi-automatically detected and manually corrected as necessary (QCU-CMS, Leiden University Medical Center, Netherlands). OCT contours were placed onto the angiographic centreline (MATLAB R2017b, Mathworks Inc., Natick, MA, United States) and the vessel surface was generated (Solidworks, Dassault Systèmes, Velizy, France). Vessel volume was discretised into tetrahedral elements with an average mesh size of approximately 1 to 2 million depending on the geometric complexity of individual patient-specific arteries (Pointwise v18.2R2). All discretised models included a graduated 10-prism boundary layer to further enhance the resolution of flow phenomena near the arterial wall.

Given the uniqueness and complexity of an individual patient's coronary arteries, it is difficult to isolate the specific geometric features impacting non-Newtonian blood rheology. Therefore, an idealized 2D model of intermediate stenosis was virtually created to assess the generalizability of the patient-specific results. The 2D model had a 3 mm diameter with diameter stenosis (DS) of 40%. The stenosis anatomy was assumed by the following mathematical equation:

$$D = \frac{1}{2}\left[D_{min} + (D - D_{min})\left(\sin\left(\pi x\right)\right)^2\right]$$

where, D is the artery's diameter, $D_{min} = \mathrm{DS} \times D$ is the minimum lumen diameter (MLD) and x is the longitudinal location of the stenotic segment with $x = 0$ at the MLD. The lesion length was assumed 3mm (i.e., x ranges from -1.5 to 1.5 mm). The idealized geometry was divided into 4 segments (**Figure 2**). Separating the proximal and distal stenotic geometries allows inspection of common flow phenomena – "favorable" and "adverse pressure gradient" – which are responsible for abnormal flow patterns such as flow separation and reversal.

Computational Fluid Dynamics Simulation

Computational fluid dynamics analysis was accomplished through the direct solution of the Navier-Stokes equations describing fluid motion. OpenFOAM, a finite-volume CFD solver, was run on the Magnus supercomputer, consisting of 35,712 Intel Xeon E5-2690V3 "Haswell" processors (Pawsey Supercomputing Centre, Perth, WA, Australia). A time-varying parabolic velocity profile with a mean bulk velocity calculated from the patient-specific TIMI frame count as previously described was applied at the inlet (10). The arterial wall was considered rigid with a no-slip boundary and a non-specific distal vascular resistance was applied at the outlet. A resistance boundary condition assumes linear dependence between the pressure and flow rate at each outlet. It is analogous to a constant pressure boundary condition and is suitable for unsteady simulation with only single outlet (11).

For the Newtonian simulations, blood's constant dynamic viscosity ($\mu_{\mathrm{Newtonian}}$) was assumed 0.0035Pa·s. Blood density was considered 1,060kg/m^3 and haematocrit 45%. Simulations were run for 3 cardiac cycles to ensure convergence of results, and

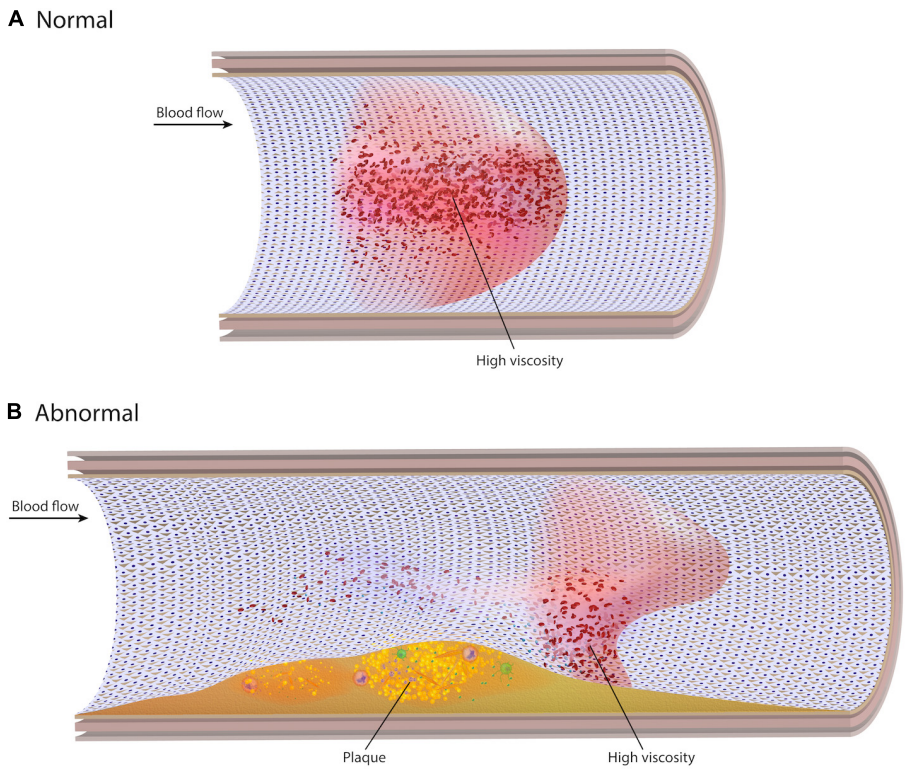

FIGURE 1 | Normal and abnormal viscosity profiles. **(A)** In a straight unobstructed artery, blood velocity takes on a parabolic profile with low shear rate (high viscosity) in the centre of the artery and low viscosity at the wall. **(B)** In the presence of stenoses, curvatures, or bifurcations, the blood velocity profile becomes distorted. Localized regions of low shear rate can develop at the wall, resulting in high viscosity near the endothelial surface.

all results presented are only from the final cycle. CFD results were post-processed to extract instantaneous and time-averaged hemodynamic indices where appropriate. ESS was calculated as described in Chen et al. (12). ESS gradient (ESSG) was calculated as the spatial gradient of ESS, representing the rate of change in ESS between adjacent spatial points in a local coordinate system (x', y', z'):

$$\mathrm{ESSG} = \nabla\mathrm{ESSG} = \begin{bmatrix} \frac{\partial \mathrm{ESS}_{x'}}{\partial x'} & \frac{\partial \mathrm{ESS}_{x'}}{\partial y'} & \frac{\partial \mathrm{ESS}_{x'}}{\partial z} \\ \frac{\partial \mathrm{ESS}_{y'}}{\partial x'} & \frac{\partial \mathrm{ESS}_{y'}}{\partial y'} & \frac{\partial \mathrm{ESS}_{y'}}{\partial z'} \\ \frac{\partial \mathrm{ESS}_{z'}}{\partial x'} & \frac{\partial \mathrm{ESS}_{z'}}{\partial y'} & \frac{\partial \mathrm{ESS}_{z'}}{\partial z'} \end{bmatrix}$$

Since ESS represents the tangential force acting on the surface, all normal components (z') of the tensor are irrelevant to the ESSG calculation. Removing all irrelevant tensor components in the z' direction, the ESSG was simplified to:

$$\mathrm{ESSG} = \begin{bmatrix} \frac{\partial \mathrm{ESS}_{x'}}{\partial x'} & \frac{\partial \mathrm{ESS}_{x'}}{\partial y'} \\ \frac{\partial \mathrm{ESS}_{y'}}{\partial x'} & \frac{\partial \mathrm{ESS}_{y'}}{\partial y'} \end{bmatrix}$$

and the ESSG magnitude is written as the diagonal components of the above matrix. Oscillatory shear index (OSI),

$$\mathrm{OSI} = 0.5 \times \left(1 - \frac{\left|\int_0^t \overrightarrow{\mathrm{ESS}}\, dt\right|}{\int_0^t \left|\overrightarrow{\mathrm{ESS}}\right| dt}\right),$$

indicates the degree of fluctuation in the direction of ESS vectors over the cardiac cycle. It is effectively an index of blood flow recirculation in a pulsating flow environment (13). Hemodynamic variables were calculated at 64 discrete timepoints per cardiac cycle (see **Supplementary Table 1** for sensitivity analysis).

Similar procedures were employed in the non-Newtonian simulations except blood was modeled by the Quemada constitutive equation to capture the local variations in blood viscosity ($\mu_{\mathrm{non-Newtonian}}$) (14). Local blood viscosity (LBV) was expressed as a ratio of non-Newtonian viscosity to the Newtonian constant viscosity model ($\mu_{\mathrm{non-Newtonian}}/\mu_{\mathrm{Newtonian}}$) for each tetrahedral element (15). In other words, LBV is a quantitative measure of the impact of non-Newtonian flow relative to that assumed by the Newtonian model. A value of 1 indicates no effect and any values >1 demonstrate the proportional influence of non-Newtonian properties locally in the bloodstream.

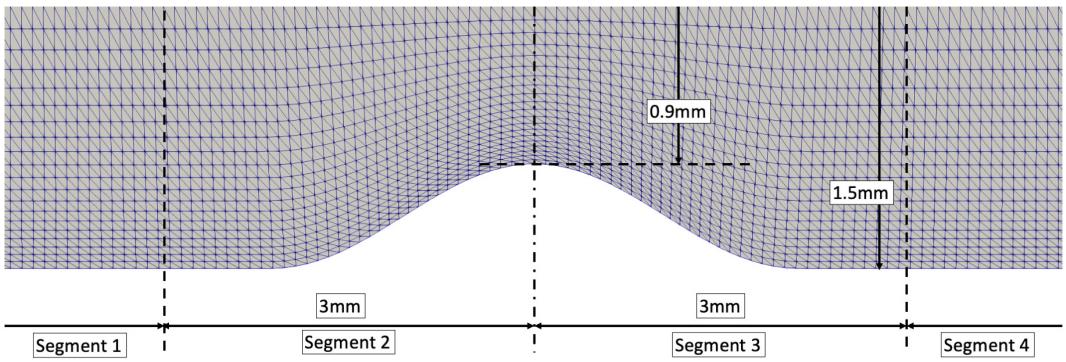

FIGURE 2 | An idealized stenotic model with an artery's diameter of 3mm and 40% DS. Segment 1: at least 1 diameter from the proximal stenotic segment; Segment 2: 1 diameter from the proximal shoulder of the stenosis to minimal lumen diameter; Segment 3: minimal lumen diameter to 1 diameter distal to the stenosis shoulder; Segment 4: remaining distal segment.

Statistical Analysis

Two simulations were carried out for each patient, one using the Newtonian model and the second using a non-Newtonian model. Since the reconstructed arterial models and computational meshes were identical for the Newtonian and non-Newtonian simulations for each patient, a rigorous point-by-point comparison of all vessel nodes was possible. Due to the paired nature of observations, the only variable within each patient was the choice of rheological model. Thus, paired comparisons of the Newtonian and non-Newtonian results were performed, as described below.

Time-averaged ESS and ESSG were calculated for each case. Instantaneous ESS was evaluated at every spatial point on the arterial wall at every step in the cardiac cycle. The maximum ESS at that spatial point was identified. To eliminate the skewing effect of extremely high and low ESS values inherently present in complex geometries, ESS was normalized using the maximum ESS value at every spatial point, yielding a value between 0 and 1. At each time step, a point-by-point comparison of normalized ESS yielded the normalized difference between the Newtonian and non-Newtonian models. The same methods were used to analyze ESSG whereas, by definition, OSI describes the general flow behavior over a cardiac cycle. Similar analyses were also carried out on the four segments of the idealized artery geometry.

Categorical variables are presented as counts and percentages, while continuous variables are presented as a mean ± standard deviation and non-parametric variables in median (interquartile range [IQR]). Because of the paired nature of the simulations within each patient, the only variable was the choice of rheological model, therefore paired *t*-test or Wilcoxon sign rank test for paired observations (as appropriate) were used. To avoid statistical dependence and to decorrelate data in the point-by-point comparison, bootstrap resampling with replacement was used to randomly select 1.5% of all mesh points and the above-mentioned statistical tests were performed to compare the results of Newtonian and non-Newtonian simulations. This process was repeated 10,000 times for comparison of ESS, ESSG, and OSI. All tests were two-tailed with an α-level of 0.05 to indicate statistical significance. Statistical analysis was performed in R statistical software (R Foundation for Statistical Computing, Vienna, Austria).

RESULTS

Wall-Based Indices: Endothelial Shear Stress, ESS Gradient, and Oscillatory Shear Index

Patient characteristics are shown in **Table 1**. Qualitative comparison of time-averaged ESS between the Newtonian and non-Newtonian simulations demonstrates broad similarity in its range and distribution for all cases (**Figure 3**). However, notable differences are found at the stenosis and curved segments (white arrows). By quantitative comparison, time-averaged ESS in the non-Newtonian simulations was significantly higher (1.69 [1.36]Pa versus 1.28 [1.16]Pa, $p < 0.001$), translating to a mean normalized percent difference of 21.72% over the entire cardiac cycle. Time-averaged ESSG in the non-Newtonian simulations was also significantly higher than the Newtonian model (1.65 ± 0.92Pa/mm versus 1.37 ± 0.78Pa/mm, 95% CI 0.20–0.37.16, $p < 0.001$). However, OSI was not significantly different between the models (0.0302 ± 0.035 versus 0.0294 ± 0.039, 95% CI 0.0059–0.0075, $p = 0.81$) (**Table 2**). The results of the analysis based on bootstrap resampling showed that the 95% confidence intervals of the mean and standard deviation/median and IQR are fully consistent with the analyses conducted on the raw data (**Supplementary Table 2**).

The absolute and normalized percent difference in instantaneous ESS and ESSG relate inversely with coronary flow rate. At the higher coronary blood flow rates associated with diastole, the difference between Newtonian and non-Newtonian simulations approaches zero, with a minimum difference in absolute ESS of 0.035 ± 0.036Pa (**Figure 4**). However, the difference increases at low and decelerating flow rates that characterize systole, with a maximum difference in absolute ESS of 1.05 ± 0.42Pa (**Figures 4B,C**).

Although the time-averaged results show that the non-Newtonian simulations estimate higher ESS and ESSG over

TABLE 1 | Patient characteristics.

	N = 16
Age (years)	64.5
Male	13 (81.3)
Diabetes	3 (18.8)
Hypertension	8 (50)
Dyslipidemia	13 (81.3)
Current smoker	2 (12.5)
Former smoker	10 (62.5)
Previous myocardial infarction	5 (31.1)
Previous coronary artery bypass graft	0
Previous percutaneous coronary intervention	4 (25)
Vessel	
Left anterior descending artery	10 (62.5)
Right coronary artery	2 (12.5)
Left circumflex artery	4 (25)
Statin	14 (87.5)
Presentation	
Stable	9 (56.3)
Unstable	2 (12.5)
Non-ST elevation myocardial infarction	5 (31.3)
Simulation variables	
Inlet flow (mL/s)	0.83 ± 0.44
Length of region of interest (mm)	13.40 ± 4.21

TABLE 2 | ESS, ESSG, and OSI between rheological models.

	Non-Newtonian	Newtonian	*p*-value
ESS (Pa), median (IQR)	1.69 (1.36)	1.28 (1.16)	<0.001
ESSG (Pa/mm), median (IQR)	0.90 (1.20)	0.74 (1.03)	<0.001
OSI, mean ± SD	0.0302 ± 0.035	0.0294 ± 0.039	0.81

ESS, endothelial shear stress; ESSG, endothelial shear stress gradient; IQR, interquartile range; OSI, oscillatory shear index; SD, standard deviation.

the cardiac cycle, during the momentary transition between end-systole and early diastole, at approximately 0.35s into the cardiac cycle, the Newtonian ESS results are higher than the non-Newtonian results by 0.89 ± 0.52Pa ($p < 0.001$), or 946.97 ± 898.72% ($p < 0.001$). However, this is transient, and the non-Newtonian results again become higher immediately thereafter (**Figures 4B,C**). The non-Newtonian model predicts the highest ESS relative to the Newtonian model during early diastole, as coronary flow is increasing rapidly. However, as the rate of rise slows in mid-diastole (at approximately 0.4s), non-Newtonian ESS is higher by 0.96 ± 0.25Pa ($p < 0.001$), or 58.13 ± 22.12% ($p < 0.001$).

The implications of these differences are most apparent by comparing vessel areas predicted to be exposed to low ESS (<1Pa), a generally accepted threshold for stimulating pro-atherogenic processes (16, 17). The Newtonian model predicts significantly greater vessel area exposure to low ESS than the non-Newtonian model (50.43 ± 14.16% versus 37.20 ± 13.57%, 95% CI 11.28–15.18%, $p < 0.001$) (**Figure 4D**).

Results from the idealized arterial geometries are consistent with the 3D patient-specific results (**Table 3**). ESS was higher in the non-Newtonian simulation in both proximal and distal healthy segments (0.8238Pa versus 0.6618Pa, $p < 0.001$ and 0.8179Pa versus 0.6610Pa, $p < 0.001$, respectively); in proximal and distal stenotic segments (0.8196Pa versus 0.6611Pa, $p < 0.001$ and 0.2546Pa versus 0.2245Pa, $p < 0.001$, respectively). Both non-Newtonian and Newtonian simulations display similar IQR ESS, except for the distal stenotic segment where non-Newtonian simulation demonstrates a significantly higher IQR

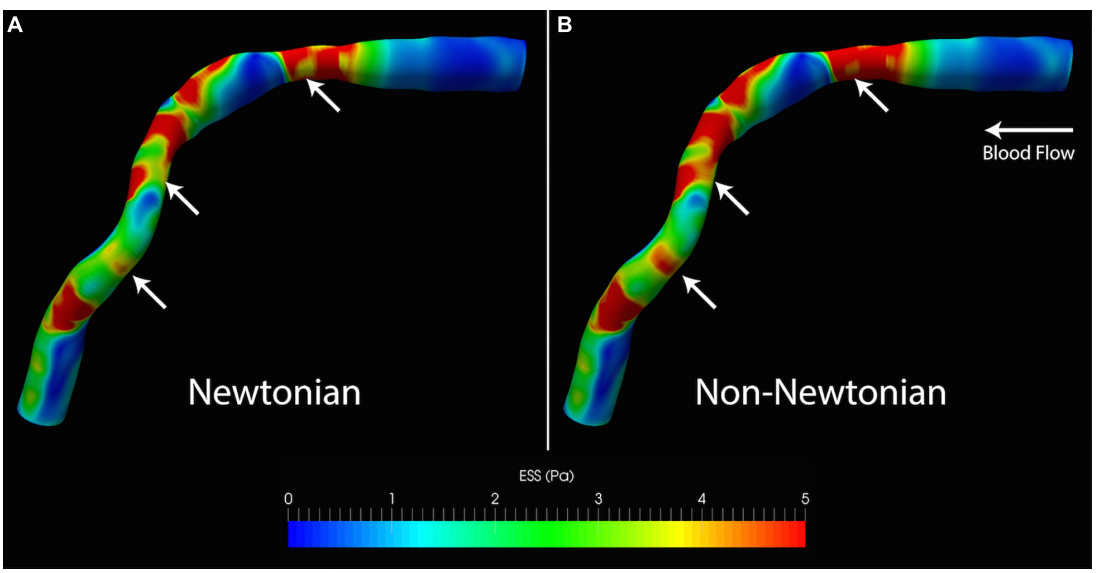

FIGURE 3 | Qualitative differences in ESS from **(A)** Newtonian and **(B)** non-Newtonian models. Although the distribution of high and low ESS is similar, the non-Newtonian model predicts higher ESS throughout the artery. This is visually most apparent from the larger areas exposed to high ESS (white arrows). ESS, endothelial shear stress.

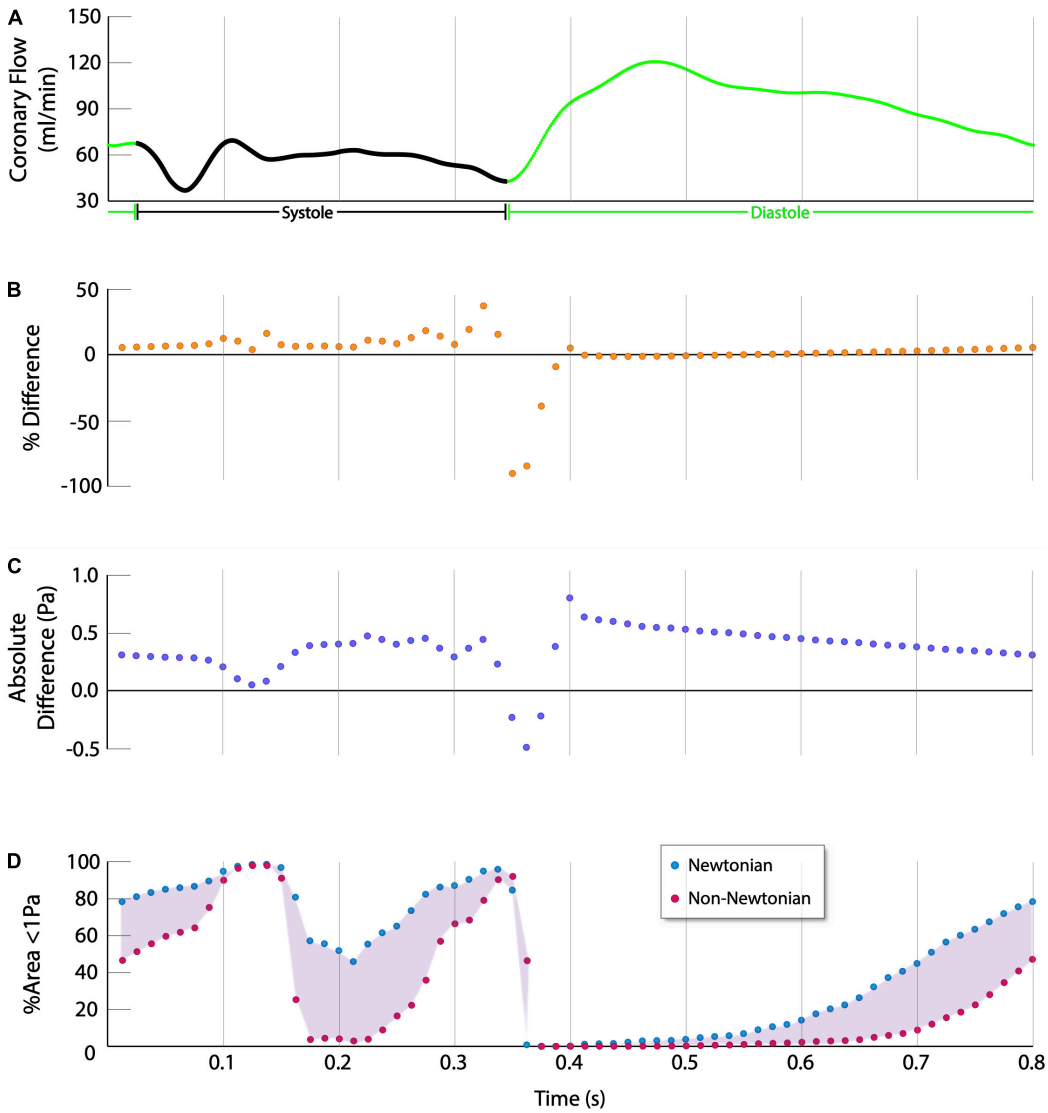

FIGURE 4 | Quantitative difference in ESS between Newtonian and non-Newtonian models (Single Representative Case). **(A)** Coronary flow rate, systole is indicated in black, diastole is indicated in green. **(B,C)** The % difference and absolute difference are calculated as (non-Newtonian ESS – Newtonian ESS), thus positive values indicate non-Newtonian results were higher whereas negative values indicate higher Newtonian results. The non-Newtonian results show consistently higher percent normalized difference and absolute difference in ESS over the cardiac cycle, except during the momentary transition between systole and diastole at approximately 0.35s. **(D)** Newtonian simulations predict more of the vessel is exposed to atherogenic levels of ESS over the cardiac cycle.

than Newtonian (0.2199Pa versus 0.08843Pa, $p < 0.001$). IQR is a measure of the data dispersion (18). In other words, IQR indicates the range of ESS within the region of interest. High IQR indicates wider spread of the ESS values and hence larger variation of ESS from the median, a condition that can be found with increasing chaotic blood flow due to vortices and flow oscillations.

Local Blood Viscosity

Like ESS, there is high spatial and temporal heterogeneity in blood viscosity over the cardiac cycle. Localized volumetric regions of high blood viscosity are observed in every case, including at the centre and walls of the artery. Across all cases, time-averaged viscosity was 1.45-fold higher than that assumed by the Newtonian model (95% CI 1.43–1.49, $p < 0.001$) (**Figure 5**). Some vessel regions are marked by an average 41.5-fold increase in maximum viscosity compared to the Newtonian model (95% CI 30.1–53.0, $p < 0.001$). In one case, peak viscosity was more than 70 times higher. The peak viscosity invariably occurs during a nadir in coronary flow – either during peak systole or the transition between end systole and early diastole.

DISCUSSION

This study demonstrates: (1) the non-Newtonian model predicts significantly higher ESS and ESSG than the Newtonian model;

TABLE 3 | ESS distribution between rheology models in an idealized artery (as depicted in **Figure 1**).

	Newtonian	Non-Newtonian	*p*-value
Segment 1, median ESS (IQR)	0.6618 (0.0000)	0.8238 (0.0015)	<0.001
Segment 2, median ESS (IQR)	0.6611 (0.2441)	0.8196 (0.2288)	<0.001
Segment 3, median ESS (IQR)	0.2245 (0.0884)	0.2546 (0.2199)	<0.001
Segment 4, median ESS (IQR)	0.6610 (0.0007)	0.8179 (0.0059)	<0.001

ESS, endothelial shear stress; IQR, interquartile range.

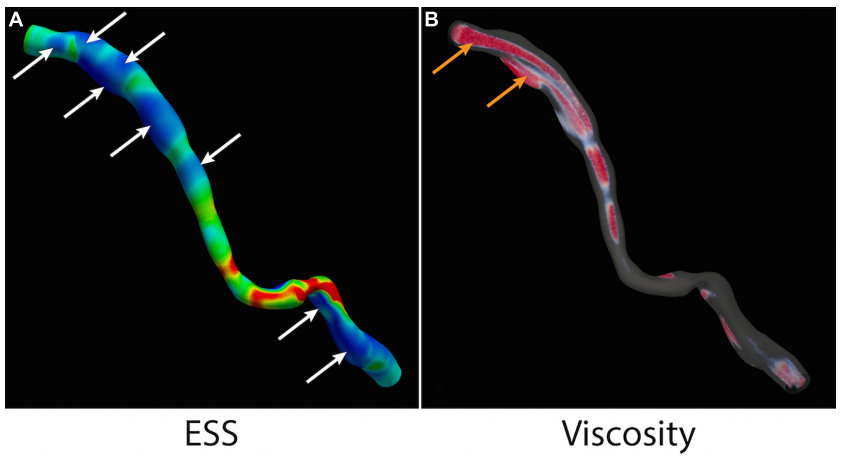

FIGURE 5 | ESS and local blood viscosity. **(A)** Multiple areas of low ESS (<1Pa) are identified (white arrows). **(B)** Non-Newtonian simulation detects regions of high LBV (>1.45) in the centre of the vessel and at the wall (orange arrows). ESS, endothelial shear stress; LBV, local blood viscosity.

(2) the Newtonian model shows significantly greater vessel areas exposed to atherogenic low ESS; (3) OSI is not significantly different between the models; and (4) the non-Newtonian model identifies regions of high LBV up to 70-fold higher than that assumed by the Newtonian model.

Local blood flow disturbances are a potent stimulus of endothelial dysfunction and biological processes underlying atherosclerosis (16, 19, 20). ESS disturbances *in vivo* have been correlated with changes in plaque composition (21, 22), morphology (23), and vessel remodeling (21, 22). Further, low ESS is independently associated with requiring future intervention or even future clinical events (24, 25). In these studies, many vessel areas were predicted to be exposed to low ESS; of lesions that caused future events, most or all were in previously low ESS areas; however, the vast majority of lesions within low ESS areas did not progress to cause events. Previous studies indicate that, while low ESS has high sensitivity to detect future events at a patient level, it has low specificity and positive predictive value (PPV) (24, 25). Furthermore, no studies have associated specific plaques exposed to low ESS as the culprit lesion of later events.

Although blood is a non-Newtonian fluid, all these studies used the Newtonian model of blood behavior. Since coronary blood flow is assumed to have shear rates above 100–200s^{-1}, such an assumption has long been valid. We investigated the effects of non-Newtonian blood rheology in a series of coronary arteries reconstructed from high-resolution imaging to test whether the Newtonian and non-Newtonian models present results within a small margin of computational error. In other words, if the shear rate was indeed high enough that blood can be assumed a Newtonian fluid, the two models should predict quantitatively similar results. However, the results of this study show that the Newtonian and non-Newtonian models consistently estimate different ESS values throughout the cardiac cycle, suggesting that there are indeed multiple factors, including the instantaneous pulsatile blood flow velocity and local geometric variations, influencing when and where the non-Newtonian behaviors of blood become apparent.

Pulsatile Flow Factor

Unlike Newtonian CFD simulations where the blood viscosity stays constant throughout the cardiac cycle, blood viscosity constantly changes from moment to moment due to the pulsatile nature of blood flow. Indeed, in a Newtonian simulation, the sudden increase in coronary blood flow rate at early diastole is usually accompanied by a very rapid increase in ESS untamed by the constant viscous forces and vice versa. However, the non-Newtonian fluid responds differently to temporal changes in flow rate and hence leads to a very dynamic pattern of the discrepancy between the Newtonian and non-Newtonian results. While non-Newtonian simulations, in general, predict a higher ESS, there is a time point between end-systole and early diastole where the non-Newtonian model momentarily predicts significantly lower ESS than the Newtonian model. Coincidentally, the difference between the two models is most remarkable during this transition phase. While it can be easily

speculated that the rapidly changing blood flow conditions play a role, the underlying haemodynamics are far more complicated. One must consider the heart rate, the historical effects of LBV, and its impact on the local flow environment.

Nevertheless, these findings are consistent with many previous fundamental studies showing that non-Newtonian simulations predict higher ESS (26–31). For instance, non-Newtonian flow decreases the area of low ESS in both straight and bent arterial segments, with the largest difference occurring in the straight rather than the bent segment (32). On the other hand, while blood viscosity affects the magnitude of ESS when the flow is disturbed, it does not affect the spatial and temporal distribution of the ESS (33, 34). Our results demonstrate that those results extend to patient-specific coronary arteries. It should be noted that while this difference was also observed for ESSG, there was no significant difference in predicted OSI values.

Reassuringly, ESS calculated by the non-Newtonian model is, on average, 0.44Pa or 21% higher than the Newtonian model in the 3D patient-specific data and 0.63Pa or 27% in the idealized 2D results. While the absolute value of the difference between Newtonian and non-Newtonian models is low, this ultimately means that the Newtonian model estimates a significantly higher percentage of the vessel area exposed to ESS <1Pa (50.43% versus 37.20%, $p < 0.001$). This could have significant repercussions in the context of earlier clinical CFD studies showing low specificity and PPV of low ESS. Despite the estimated differences in ESS and ESSG, the clinical significance of such fluctuations within a short time is unclear. However, it is hypothesized that the non-Newtonian model, as a more accurate reflection of actual blood behavior, may ultimately offer higher specificity and PPV than Newtonian simulations.

Geometric Factor

Arterial narrowing and widening are major factors in local variations of blood rheology and flow dynamics. Blood flow accelerates as the artery narrows. In haemodynamics, this segment is termed the "favorable pressure gradient" segment. In contrast, "adverse pressure gradient" refers to flow deceleration as the artery widens. The impact of "favorable" and "adverse pressure gradients" can be isolated by carrying out the Newtonian and non-Newtonian simulations in an idealized arterial geometry where the arterial flow will undergo clearly defined favorable (proximal stenotic segment) and adverse (distal stenotic segment) pressure gradients. Our idealized artery results show that the non-Newtonian model continues to display a higher median ESS value compared to the Newtonian model in all segments. However, it is the significantly lower IQR at the distal stenotic segment marked by an adverse pressure gradient in the Newtonian model that is of particular interest. While low IQR reflects lower ESS oscillation and high IQR indicates larger fluctuations in ESS values, it is unclear whether a higher IQR signifies an increase in turbulent activities or vice versa. Nonetheless, regions with adverse pressure gradients have demonstrated an increased likelihood of flow reversal (8). Clinically, flow reversal and abnormal ESS represent a location for plaque development and potentially a nidus for thrombotic events (35–37). This remarkable difference in Newtonian and non-Newtonian models in regions of adverse pressure gradients might lead to different conclusions and hence warrants further objective analyses.

The Need for a Better Reflection of True Blood Rheology

Non-Newtonian models offer other potential advantages. Although ESS, ESSG, OSI, and other wall-based metrics consider the mechanical effect of blood acting on the vessel wall, these indices inherently neglect the physiological response of whole blood. While low ESS and high OSI indicate that blood may be recirculating and stagnating in these areas, these measures do not directly capture or describe flow phenomena within the blood itself.

Compared to the constant viscosity assumed by the Newtonian model, in non-Newtonian rheological models, blood viscosity is treated as a variable dependent on instantaneous local shear rate, allowing determination of viscosity within the entire fluid domain. In this study, the non-Newtonian model identified localized regions of peak LBV, on average, 40-fold higher than that assumed by the Newtonian model. The possibility of detecting localized regions of increased blood viscosity *in vivo* is intriguing given that blood is a complex fluid with clinically relevant behaviors such as thrombosis. Further, the pathophysiologic mechanisms underlying plaque development may involve the accumulation of cholesterol, pro-inflammatory cells, and humoral mediators in characteristic vessel regions, perhaps exacerbated by increased LBV, recirculation and stagnation in these areas.

In straight unobstructed vessels, high viscosity is expected in the center of a vessel where shear rate is low, and velocity is high (**Figure 1**). Conversely, blood viscosity at the wall is low since the shear rate at the wall is high. It is hypothesized that, despite high viscosity at the vessel centre, high velocity convects blood axially downstream, preventing significant erythrocyte aggregation or contact with the endothelial surface. However, low blood velocity and recirculation can develop at the distal inner bend of curvatures, the outer walls of bifurcations, and both proximal and distal to stenoses or stent struts. In such regions of disturbed flow, blood velocity and shear rate may decrease at the wall leading to pockets of high LBV near the endothelial surface, potentially facilitating processes leading to both progressive atherosclerosis and thrombosis (38, 39).

Limitations

There are several limitations to the current study. First is a small study population retrospectively selected from a prior randomized clinical trial. However, in the context of patient-specific CFD studies quantitatively comparing rheological models, this is among the largest cohorts. As a result of retrospective patient selection, the cohort also skewed male due to the original study population characteristics (75% male in the original study). Second, we assumed a generic haematocrit of 45% based on standard reference ranges and a desire to limit confounding variables that might have been introduced by incorporating patient-specific values. However,

because haematocrit is a determinant of blood viscosity, it is possible that the observed differences between the Newtonian and non-Newtonian models may also be influenced by changes in haematocrit. Future studies should incorporate patient-specific haematocrit to better assess this possibility. Third, this study does not investigate the effect of axial and secondary flow due to the presence of helical inflow, arterial curvature, bifurcation lesions which significantly affect local flow dynamics (40). It is expected that due to the increased complexity of flow in these settings, the differences between the Newtonian and non-Newtonian models would increase further. To facilitate investigating these effects, it is important to correlate LBV with other ESS-based descriptors and helicity indices (41, 42). In terms of bifurcation lesions, future studies should prospectively image-side branches with intravascular techniques if it is feasible and safe to do so. Fourth, as a technical study, changes in plaque composition were not evaluated. Further investigation of ESS derived by Newtonian and non-Newtonian models concerning plaque composition and change over time is necessary. Ultimately, if there is a significant difference in how the models correlate with atherosclerotic plaque, future studies investigating clinical endpoints may be worthwhile.

CONCLUSION

Although blood is often assumed to be a Newtonian fluid by CFD simulations of the coronary arteries, this study demonstrates that non-Newtonian behaviors of blood are operational, yielding marked differences in calculated flow indices such as ESS and ESSG. Non-Newtonian simulations also allow the calculation of LBV and related indices, potentially presenting novel markers to detect plaques at risk for progression.

DATA AVAILABILITY STATEMENT

The CFD data supporting the conclusions of this article will be made available by the authors. Request for access to patient data (which are subjected to restriction due to the nature of personal healthcare information) can be made to the corresponding author.

ETHICS STATEMENT

The studies involving human participants were reviewed and approved by St Vincent's Ethics Committees (APPOSE HREC/12/SVH/31). The patients/participants provided their written informed consent to participate in this study.

AUTHOR CONTRIBUTIONS

VT designed the methodology, performed 3D reconstructions and CFD analysis and wrote the original manuscript, and reviewed and edited the manuscript. JD supported intravascular optical coherence tomography analysis. SZ contributed to the CFD modeling. DS, ER, and WG reviewed and edited the manuscript. PS provided expert opinion, review and edited the manuscript. EP co-designed the methodology and performed CFD analysis, co-supervised the project. AO contributed to CFD methods and co-supervised the project. PB collected all medical imaging data, conceptualized the project, supervised, and co-ordinated the project. All authors contributed to the article and approved the submitted version.

FUNDING

This research was undertaken with the assistance of resources and services from the National Computational Infrastructure (NCI), which is supported by the Australian Government.

SUPPLEMENTARY MATERIAL

The Supplementary Material for this article can be found online at: https://www.frontiersin.org/articles/10.3389/fcvm.2022.835270/full#supplementary-material

REFERENCES

1. Ballyk PD, Steinman DA, Ethier CR. Simulation of non-Newtonian blood flow in an end-to-side anastomosis. *Biorheology.* (1994) 31:565–86. doi: 10.3233/bir-1994-31505
2. Kleinstrauer C, Nazemi M, Archie JP. Hemodynamics analysis of a stenosed carotid bifurcation and its plaque-mitigating design. *J Biomech Eng.* (1991) 113:330–5. doi: 10.1115/1.2894891
3. Morbiducci U, Gallo D, Massai D, Ponzini R, Deriu MA, Antiga L, et al. On the importance of blood rheology for bulk flow in hemodynamic models of the carotid bifurcation. *J Biomech.* (2011) 44:2427–38. doi: 10.1016/j.jbiomech.2011.06.028
4. Rindt CCM, van de Vosse FN, Steenhoven AAV, Janssen JD. A numerical and experimental analysis of the flow field in a two-dimensional model of the human carotid artery bifurcation. *J Biomech.* (1987) 20:499–509. doi: 10.1016/0021-9290(87)90250-8
5. Cho Y, Kensey K. Effects of the non-Newtonian viscosity of blood on flows in a diseased arterial vessel. Part 1. Steady flows. *Biorheology.* (1991) 28:241–62. doi: 10.3233/bir-1991-283-415
6. Merrill EW, Pelletier GA. Viscosity of human blood: transition from Newtonian to non-Newtonian. *J Appl Physiol.* (1985) 1967:178–82. doi: 10.1152/jappl.1967.23.2.178
7. Bodnár T, Sequeira A, Prosi M. On the shear-thinning and viscoelastic effects of blood flow under various flow rates. *Appl Math Comput.* (2011) 217:5055–67. doi: 10.1007/s10856-010-4210-6
8. van Wyk S, Prahl Wittberg L, Bulusu KV, Fuchs L, Plesniak MW. Non-Newtonian perspectives on pulsatile blood-analog flows in a 180° curved artery model. *Phys Fluids.* (2015) 27:071901. doi: 10.1063/1.4923311
9. Papafaklis MI, Bourantas CV, Yonetsu T, Vergallo R, Kotsia A, Nakatani S, et al. Anatomically correct three-dimensional coronary artery reconstruction using frequency domain optical coherence tomographic and angiographic data: head-to-head comparison with intravascular ultrasound for endothelial shear stress assessment in humans. *EuroIntervention.* (2015) 11:407–15. doi: 10.4244/EIJY14M06_11
10. Gibson CM, Cannon CP, Daley WL, Dodge JT, Alexander B, Marble SJ, et al. TIMI Frame count : a quantitative method of assessing coronary artery flow. *Circulation.* (1996) 93:879–88. doi: 10.1161/01.cir.93.5.879

11. Grinberg L, Karniadakis GE. Outflow boundary conditions for arterial networks with multiple outlets. *Ann Biomed Eng.* (2008) 36:1496–514. doi: 10.1007/s10439-008-9527-7
12. Chen WX, Poon EKW, Hutchins N, Thondapu V, Barlis P, Ooi A. Computational fluid dynamics study of common stent models inside idealised curved coronary arteries. *Comput Methods Biomech Biomed Eng.* (2017) 20:671–81. doi: 10.1080/10255842.2017.1289374
13. Ku DN, Giddens DP, Zarins CK, Glagov S. Pulsatile flow and atherosclerosis in the human carotid bifurcation. Positive correlation between plaque location and low oscillating shear stress. *Arteriosclerosis Thrombosis Vasc Biol.* (1985) 5:293–302. doi: 10.1161/01.atv.5.3.293
14. Quemada D. Rheology of concentrated disperse systems II. A model for non-newtonian shear viscosity in steady flows. *Rheol Acta.* (1978) 17:632–42. doi: 10.1007/bf01522036
15. Poon EKW, Thondapu V, Hayat U, Barlis P, Yap CY, Kuo PH, et al. Elevated blood viscosity and micro-recirculation resulting from coronary stent malapposition. *J Biomech Eng.* (2018) 140:051006.
16. Davies PF, Remuzzi A, Gordon EJ, Dewey CFJ, Gimbrone MA. Turbulent fluid shear stress induces vascular endothelial turnover in vitro. *Proc Natl Acad Sci U S A.* (1986) 83:2114–7. doi: 10.1073/pnas.83.7.2114
17. Malek AM, Alper SL, Izumo S. Hemodynamic shear stress and its role in atherosclerosis. *JAMA.* (1999) 282:2035–42. doi: 10.1001/jama.282.21.2035
18. Manikandan S. Measures of dispersion. *J Pharmacol Pharmacother.* (2011) 2:315–6.
19. Dolan JM, Meng H, Singh S, Paluch R, Kolega J. High fluid shear stress and spatial shear stress gradients affect endothelial proliferation, survival, and alignment. *Ann Biomed Eng.* (2011) 39:1620–31. doi: 10.1007/s10439-011-0267-8
20. Gimbrone MA, Topper JN, Nagel T, Anderson KR, Garcia-Cardena G. Endothelial dysfunction, hemodynamic forces, and atherogenesis. *Ann NY Acad Sci.* (2000) 902:230–9. doi: 10.1111/j.1749-6632.2000.tb06318.x
21. Corban MT, Eshtehardi P, Suo J, McDaniel MC, Timmins LH, Rassoul-Arzrumly E, et al. Combination of plaque burden, wall shear stress, and plaque phenotype has incremental value for prediction of coronary atherosclerotic plaque progression and vulnerability. *Atherosclerosis.* (2014) 232:271–6. doi: 10.1016/j.atherosclerosis.2013.11.049
22. Samady H, Eshtehardi P, McDaniel MC, Suo J, Dhawan SS, Maynard C, et al. Coronary artery wall shear stress is associated with progression and transformation of atherosclerotic plaque and arterial remodeling in patients with coronary artery disease. *Circulation.* (2011) 124:779–88. doi: 10.1161/CIRCULATIONAHA.111.021824
23. Yamamoto E, Siasos G, Zaromytidou M, Coskun AU, Xing L, Bryniarski K, et al. Low endothelial shear stress predicts evolution to high-risk coronary plaque phenotype in the future: a serial optical coherence tomography and computational fluid dynamics study. *Circ Cardiovasc Interv.* (2017) 10:e005455. doi: 10.1161/CIRCINTERVENTIONS.117.005455
24. Stone PH, Maehara A, Coskun AU, Maynard CC, Zaromytidou M, Siasos G, et al. Role of low endothelial shear stress and plaque characteristics in the prediction of nonculprit major adverse cardiac events: the Prospect study. *JACC Cardiovasc Imaging.* (2018) 11:462–71. doi: 10.1016/j.jcmg.2017.01.031
25. Stone PH, Saito S, Takahashi S, Makita Y, Nakamura S, Kawasaki T, et al. Prediction of progression of coronary artery disease and clinical outcomes using vascular profiling of endothelial shear stress and arterial plaque characteristics: the Prediction study. *Circulation.* (2012) 126:172–81. doi: 10.1161/circulationaha.112.096438
26. Apostolidis AJ, Moyer AP, Beris AN. Non-Newtonian effects in simulations of coronary arterial blood flow. *J Non-Newtonian Fluid Mech.* (2016) 233:155–65. doi: 10.1016/j.jnnfm.2016.03.008
27. Chen J, Lu XY. Numerical investigation of the non-Newtonian pulsatile blood flow in a bifurcation model with a non-planar branch. *J Biomech.* (2006) 39:818–32. doi: 10.1016/j.jbiomech.2005.02.003
28. Choi HW, Barakat AI. Numerical study of the impact of non-Newtonian blood behavior on flow over a two-dimensional backward facing step. *Biorheology.* (2005) 42:493–509.
29. Hund S, Kameneva M, Antaki JA. Quasi-mechanistic mathematical representation for blood viscosity. *Fluids.* (2017) 2:10. doi: 10.3390/fluids2010010
30. Janela J, Moura A, Sequeira A. A 3D non-Newtonian fluid–structure interaction model for blood flow in arteries. *J Comput Appl Math.* (2010) 234:2783–91. doi: 10.1016/j.cam.2010.01.032
31. Soulis JV, Giannoglou GD, Chatzizisis YS, Seralidou KV, Parcharidis GE, Louridas GE. Non-Newtonian models for molecular viscosity and wall shear stress in a 3D reconstructed human left coronary artery. *Med Eng Phys.* (2008) 30:9–19. doi: 10.1016/j.medengphy.2007.02.001
32. Ferrarini A, Finotello A, Salsano G, Auricchio F, Palombo D, Spinella G, et al. Impact of leg bending in the patient-specific computational fluid dynamics of popliteal stenting. *Acta Mech Sin.* (2021) 37:279–91. doi: 10.1007/s10409-021-01066-2
33. Liu B, Tang D. Influence of non-Newtonian properties of blood on the wall shear stress in human atherosclerotic right coronary arteries. *Mol Cell Biomech.* (2011) 8:73–90. doi: 10.3970/mcb.2011.008.073
34. Anastasios S, Panagiotis N, Christos H. Comparison of blood rheological models in patient specific cardiovascular system simulations. *J Hydrodyn Ser B.* (2017) 29:293–304. doi: 10.1016/s1001-6058(16)60739-4
35. Tenekecioglu E, Poon EK, Collet C, Thondapu V, Torii R, Bourantas CV, et al. The nidus for possible thrombus formation: insight from the microenvironment of bioresorbable vascular scaffold. *JACC Cardiovasc Intervent.* (2016) 9:2167–8. doi: 10.1016/j.jcin.2016.08.019
36. Thondapu V, Mamon C, Poon EKW, Kurihara O, Kim HO, Russo M, et al. High spatial endothelial shear stress gradient independently predicts site of acute coronary plaque rupture and erosion. *Cardiovasc Res.* (2021) 117:1974–85. doi: 10.1093/cvr/cvaa251
37. Yamamoto E, Thondapu V, Poon E, Sugiyama T, Fracassi F, Dijkstra J, et al. Endothelial shear stress and plaque erosion: a computational fluid dynamics and optical coherence tomography study. *JACC Cardiovasc Imaging.* (2019) 12:374–5. doi: 10.1016/j.jcmg.2018.07.024
38. Dintenfass L, Julian DG, Miller GE. Viscosity of blood in normal subjects and in patients suffering from coronary occlusion and arterial thrombosis. *Am Heart J.* (1965) 71:587–600. doi: 10.1016/0002-8703(66)90308-5
39. Wells R, Merrill EW. Shear rate dependence of the viscosity of whole blood and plasma. *Science.* (1961) 133:763–4. doi: 10.1126/science.133.3455.763
40. Li Y, Gutierrez-Chico JL, Holm NR, Yang W, Hebsgaard L, Christiansen EH, et al. Impact of side branch modeling on computation of endothelial shear stress in coronary artery disease: coronary tree reconstruction by Fusion of 3D angiography and OCT. *J Am Coll Cardiol.* (2015) 66:125–35. doi: 10.1016/j.jacc.2015.05.008
41. Calo K, De Nisco G, Gallo D, Chiastra C, Hoogendoorn A, Steinman DA, et al. Exploring wall shear stress spatiotemporal heterogeneity in coronary arteries combining correlation-based analysis and complex networks with computational hemodynamics. *Proc Inst Mech Eng H.* (2020) 234:1209–22. doi: 10.1177/0954411920923253
42. De Nisco G, Kok AM, Chiastra C, Gallo D, Hoogendoorn A, Migliavacca F, et al. The atheroprotective nature of helical flow in coronary arteries. *Ann Biomed Eng.* (2019) 47:425–38. doi: 10.1007/s10439-018-02169-x

Conflict of Interest: PS reports personal fees from Sino Medical Sciences Technology, Philips/Volcano, and Xeltis.

The remaining authors declare that the research was conducted in the absence of any commercial or financial relationships that could be construed as a potential conflict of interest.

frontiers | Frontiers in Cardiovascular Medicine

ORIGINAL RESEARCH
published: 26 May 2022
doi: 10.3389/fcvm.2022.890799

Morphological and Physiological Characteristics of Ruptured Plaques in Native Arteries and Neoatherosclerotic Segments: An OCT-Based and Computational Fluid Dynamics Study

*Chongying Jin[1,2,3], Ryo Torii[4], Anantharaman Ramasamy[1,3], Vincenzo Tufaro[1,3,5], Callum D. Little[6], Klio Konstantinou[7], Yi Ying Tan[4], Nathan A. L. Yap[8], Jackie Cooper[3], Tom Crake[1], Constantinos O'Mahony[1,9], Roby Rakhit[6], Mohaned Egred[10], Javed Ahmed[10], Grigoris Karamasis[7], Lorenz Räber[11], Andreas Baumbach[1,3,12], Anthony Mathur[1,3] and Christos V. Bourantas[1,3,9]**

[1] Department of Cardiology, Barts Heart Centre, Barts Health NHS Trust, London, United Kingdom, [2] Department of Cardiology, Sir Run Run Shaw Hospital, School of Medicine, Zhejiang University, Hangzhou, China, [3] Centre for Cardiovascular Medicine and Devices, William Harvey Research Institute, Queen Mary University of London, London, United Kingdom, [4] Department of Mechanical Engineering, University College London, London, United Kingdom, [5] Department of Biomedical Sciences, Humanitas University, Milan, Italy, [6] Royal Free Hospital, University College London, London, United Kingdom, [7] Essex Cardiothoracic Centre, Anglia Ruskin School of Medicine, Essex, United Kingdom, [8] Barts and The London School of Medicine and Dentistry, London, United Kingdom, [9] Institute of Cardiovascular Science, University College London, London, United Kingdom, [10] Freeman Hospital, Newcastle University, Newcastle upon Tyne, United Kingdom, [11] Department of Cardiology, University of Bern, Bern, Switzerland, [12] Yale University School of Medicine, New Haven, CT, United States

Background: Intravascular imaging has been used to assess the morphology of lesions causing an acute coronary syndrome (ACS) in native vessels (NV) and identify differences between plaques that ruptured (PR) and caused an event and those that ruptured without clinical manifestations. However, there is no data about the morphological and physiological characteristics of neoatherosclerotic plaques that ruptured (PR-NA) which constitute a common cause of stent failure.

Methods: We retrospectively analyzed data from patients admitted with an acute myocardial infarction that had optical coherence tomography (OCT) imaging of the culprit vessel before balloon pre-dilation. OCT pullbacks showing PR were segmented at every 0.4 mm. The extent of the formed cavity, lipid and calcific tissue, thrombus, and macrophages were measured, and the fibrous cap thickness (FCT) and the incidence of micro-channels and cholesterol crystals were reported. These data were used to reconstruct a representative model of the native and neoatherosclerotic lesion geometry that was processed with computational fluid dynamics (CFD) techniques to estimate the distribution of the endothelial shear stress and plaque structural stress.

OPEN ACCESS

Edited by:
Antonios Karanasos, Hippokration General Hospital, Greece

Reviewed by:
Jiang Ming Fam, National Heart Centre Singapore, Singapore
Giulio Stefanini, Humanitas University, Italy

***Correspondence:**
Christos V. Bourantas
c.bourantas@ucl.ac.uk

Specialty section:
This article was submitted to Cardiovascular Imaging, a section of the journal Frontiers in Cardiovascular Medicine

Received: *06 March 2022*
Accepted: *04 May 2022*
Published: *26 May 2022*

Citation:
Jin C, Torii R, Ramasamy A, Tufaro V, Little CD, Konstantinou K, Tan YY, Yap NAL, Cooper J, Crake T, O'Mahony C, Rakhit R, Egred M, Ahmed J, Karamasis G, Räber L, Baumbach A, Mathur A and Bourantas CV (2022) Morphological and Physiological Characteristics of Ruptured Plaques in Native Arteries and Neoatherosclerotic Segments: An OCT-Based and Computational Fluid Dynamics Study. Front. Cardiovasc. Med. 9:890799. doi: 10.3389/fcvm.2022.890799

Result: Eighty patients were included in the present analysis: 56 had PR in NV (PR-NV group) and 24 in NA segments (PR-NA group). The PR-NV group had a larger minimum lumen area (2.93 ± 2.03 vs. 2.00 ± 1.26 mm^2, $p = 0.015$) but similar lesion length and area stenosis compared to PR-NA group. The mean FCT (186 ± 65 vs. 232 ± 80 μm, $p = 0.009$) and the lipid index was smaller (16.7 ± 13.8 vs. 25.9 ± 14.1, $p = 0.008$) while the of calcific index (8.3 ± 9.5 vs. 2.2 ± 1.6%, $p = 0.002$) and the incidence of micro-channels (41.4 vs. 12.5%, $p = 0.013$) was higher in the PR-NV group. Conversely, there was no difference in the incidence of cholesterol crystals, thrombus burden or the location of the rupture site between groups. CFD analysis revealed higher maximum endothelial shear stress (19.1 vs. 11.0 Pa) and lower maximum plaque structural stress (38.8 vs. 95.1 kPa) in the PR-NA compared to the PR-NV model.

Conclusion: We reported significant morphological and physiological differences between culprit ruptured plaques in native and stented segments. Further research is needed to better understand the causes of these differences and the mechanisms regulating neoatherosclerotic lesion destabilization.

Keywords: plaque rupture, neoatherosclerosis, optical coherence tomography, computational fluid dynamics (CFD), endothelial shear stress, plaque structural stress

INTRODUCTION

Ischemic heart disease (IHD) is the leading cause of death in the world, associated with increased morbidity and devastating financial consequences. Percutaneous coronary interventions (PCI) is an established therapy for patients with IHD and has been associated with better prognosis in acute coronary syndromes (ACS) and improved quality of life in chronic coronary syndromes (1–3). Despite the advances in stent technology that have improved stent safety profile and efficacy enabling treatment of high-risk patients and complex lesions, this treatment can fail and it appears unable to inhibit atherosclerotic disease progression in the treated segments. Numerous intravascular imaging studies have shown that neointima tissue can develop within stented segments and evolve to neoatherosclerotic high-risk vulnerable plaques which can rupture and cause adverse events (4, 5). Several reports attempted to identify predictors of neoatherosclerosis showing that conventional risk factors associated with atherosclerotic evolution, such as baseline demographics (i.e., renal failure, hypercholesterolemia, and hypertension), medications and stent type determine the long-term vessel response to therapy and are associated with the formation of intra-stent high-risk lesions (6–8). In addition, there is an association between development of neoatherosclerotic plaques and atherosclerotic disease progression in native vessels (NV) suggesting these two pathologies are regulated by similar pathophysiological mechanisms (9).

Apart from systemic factors, focal pathobiological mechanisms that are not seen in NV – such as hypersensitivity reaction to stent polymer or endothelial dysfunction induced by eluted drugs – are also involved in neoatherosclerotic lesion formation (4). The different pathogenesis of these lesions is likely to have an impact not only on their development and distribution in stented segments, but also on their destabilization and rupture (10). The objectives of the present analysis are to compare the phenotypic characteristics of lesions that ruptured and caused events in native and stented segments, reconstruct a representative geometry of a ruptured plaque in a native and stented segment and process these models with computational fluid dynamic (CFD) techniques to assess the effect of lesions physiology [endothelial shear stress (ESS) and plaque stress] on their destabilization.

MATERIALS AND METHODS

Study Population

We retrospectively enrolled patients with ST-elevation or non-ST-elevation myocardial infarction who had optical coherence tomography (OCT) of the culprit vessel prior to balloon predilatation. These patients were admitted between 2016 and 2019 in six hospitals: Barts Health NHS Trust, United Kingdom; Bern University Hospital, Switzerland; Royal Free Hospital, United Kingdom; Newcastle Upon Tyne NHS Foundation Trust, United Kingdom; Essex Cardiothoracic Centre, United Kingdom; and Sir Run Run Shaw Hospital, China.

Optical Coherence Tomography Image Acquisition

OCT imaging was performed using either C7XR, OPTIS™ (St-Jude Medical, Westford, MA, United States), or Lunawave (Terumo Corp., Tokyo, Japan) Fourier Domain system. Pullbacks were performed by using either a manual or automatic blood flushing at a constant speed ranging from 18–40 mm/s and frame rate that ranged from 100 to 180 fr/s. The collected data were stored in DICOM format and sent to Barts Heart Centre for analysis.

Optical Coherence Tomography Data Analysis

The anonymized data were reviewed by two experienced analysts (CJ and CB) and the culprit lesions were identified. Plaque rupture was defined as the presence of a fibrous cap discontinuity which connected the lumen and the inner – the necrotic core – of the plaque (11). Depending on culprit lesion location these were divided in two groups: plaque ruptures occurring in a native vessel (PR-NV) and those occurring in a neoatherosclerotic lesion (PR-NA). Cases where the plaque rupture extending across the stent edge to the native artery segment were excluded. Moreover, we excluded cases of neoatherosclerotic plaque rupture within a previously implanted bioresorbable scaffold as these devices tend to resorb with time and thus alter ESS and plaque structural stress (PSS) distribution.

The two expert analysts who had established reproducibility and were blinded to patients' characteristics performed imaging analysis using the QCM-CMS version 4.69 software (Leiden University Medical Center, Leiden, Netherlands) (10, 12). In the PR-NV group, the ruptured plaque was detected and its proximal and distal end was defined as the last and first frame that portrayed lipid tissue or had a plaque burden $\geq$40% (13). In the PR-NA group, the proximal and distal end of the ruptured plaque was defined as the most proximal and distal frame that had a mean neointima thickness $\geq$0.5 mm; in case of lesions extending beyond the stented segment, the same definition was used for the PR-NV group to define its proximal or distal end (14).

OCT pullbacks were analyzed at 0.4 mm interval (0.375 mm for Lunawave system). In the PR-NV group, the external elastic membrane (EEM) was detected, when it was visible, and used to define the proximal and distal end of the culprit lesion, while in the PR-NA group the lumen and the stent borders were identified, the mean neointima thickness was measured and the most proximal and distal frames of the lesion with thickness $\geq$0.5 mm defined its proximal and distal end. Then, the plaque composition was estimated using established criteria. A lipid pool was defined as a low signal intensity region with a circumferential arc $>45°$ with diffuse borders and increased attenuation, while calcification was characterized as a low backscattering region with clear borders (13, 15). The lateral borders of these were detected, and the lipid and calcific arc were estimated. The fibrous cap over lipid tissue was extracted using semi-automated methodology and the minimum and mean cap thickness were computed (16). Macrophages infiltration was defined as punctuated or signal-rich regions with strong signal attenuation behind. Macrophages may appear as dots (single bright spots or cluster of dots) or lines (confluent accumulations forming a thin bright line) with lateral extent $>20°$ (13). Micro-channels were characterized as continuous signal poor holes in three consecutive frames with a diameter $\leq$300 μm that were not connected to the lumen (15). Cholesterol crystals were defined as sharp, linear regions with high signal intensity (15, 17). Thrombus was classified as a mass in the lumen or attached to the lumen surface with a dimension $\geq$250 μm (**Figure 1**) (18).

A lesion was defined as fibroatheroma when it contained more than a quadrant of lipid tissue; the minimum cap thickness over this tissue type was used to classify lesions as thin (TCFA, minimum cap thickness: $\leq$65 μm) or thick cap fibroatheroma (ThCFA, minimum cap thickness: $>$65 μm) (11). The length, the maximum and mean arc of lipid tissue, calcification and lined macrophages were measured, and the lipid/calcification/macrophages index were calculated and defined as: 100 × (mean arc in degrees × length) / (lesion length × 360°) (19). In frames portraying a ruptured plaque, an additional border was drawn that connected the edges of the ruptured fibrous cap and represented the lumen surface before plaque/neointima rupture (20). This was used to define the maximum circumferential extend and depth of rupture (defined as the maximum distance between the approximated lumen and the lumen border of the cavity); in addition, the rupture extent index was defined as: 100 × (mean rupture arc × rupture length) / (lesion length × 360°) (19). The thrombus score was computed for each lesion as the sum of the quadrants with thrombus in the analyzed cross-section images divided by the total number of quadrants (21).

Each lesion was split in three segments: the upstream – defined as the segment between the proximal end of the lesion and 2.5 mm proximal to the minimum lumen area (MLA) – the MLA site – defined as the segment 2.5 mm proximally and distally to the MLA – and the downstream – defined as the segment between 2.5 mm distally to the MLA and the distal end of the lesion. For the upstream and downstream segments, we estimated the radius gradient (RG) which provides an assessment of lesion longitudinal geometry and has been found to be predictor of the location of the ruptured site; this was calculated as: (lumen radius at the proximal or distal end of the ruptured plaque – radius at the MLA site)/the length of the upstream or downstream segment respectively (**Figure 2**) (22).

Generation of Mean Anatomical Model

The mean geometrical characteristics of ruptured plaque were used to generate a representative idealized geometry of the culprit lesion before its rupture for PR-NV and PR-NA groups. For this purpose, the lumen surface before plaque/neointima rupture was used to estimate the mean proximal and distal reference lumen diameter and the mean minimum lumen diameter. In addition, the mean lesion length, the minimum and mean fibrous cap thickness (FCT), the mean lipid index and the mean location of the lipid tissue with regards to the MLA were estimated in the two groups. The stent was assumed to have a typical geometry of a drug eluting stent (Endeavor Zotarolimus Eluting Stent, Medtronic, Santa Rosa, CA, United States) with circular struts with a thickness of 90 μm and inter-strut distance of 1 mm. In the PR-NA the mean stent diameter was computed from the struts in OCT images while in the PR-NV group the EEM that was visible at the proximal and distal end of the lesions was used to estimate the mean EEM at the reference sites. At the MLA site where the EEM was not visible this was estimated assuming a remodeling index of 1.20 based on published literature assessing ruptured plaque characteristics using intravascular ultrasound imaging (21, 23). The above values were used to reconstruct pre-rupture plaque geometries in the PR-NV and PR-NA groups assuming that the vessels were straight.

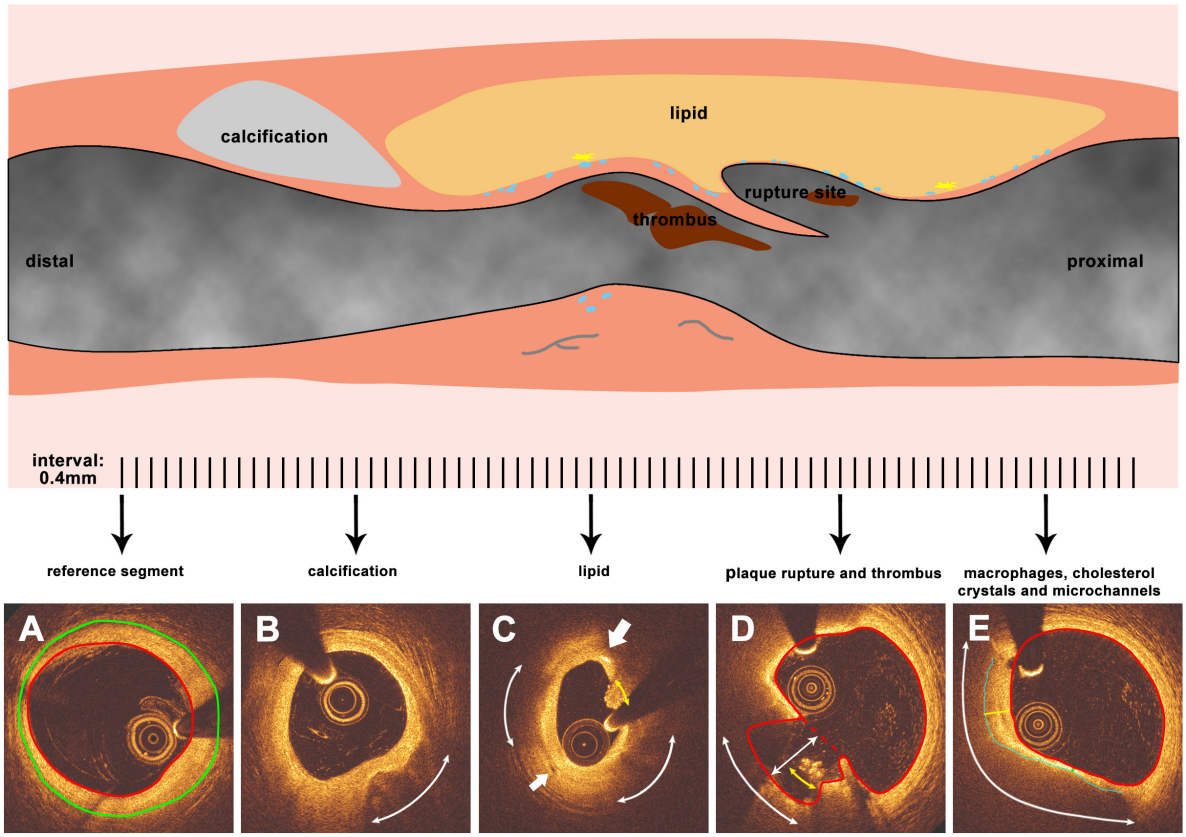

FIGURE 1 | Representative images and methodology of OCT morphology analysis. The upper part is a representative longitudinal diagram of a ruptured plaque (blue dots represent for macrophages while yellow sharp stars for cholesterol crystals, gray curved lines for microchannels), panels **(A–E)** are cross sections corresponding to the lesion segment while analyzed at 0.4 mm interval. **(A)** The reference segment of the vessel, red line indicates the lumen surface while green line indicates the EEM. **(B)** Calcification tissue in the plaque, the arc indicates the calcific arc. **(C)** Lipid tissue in the plaque, the arc indicates the lipid arc, the area enclosed by the blue line indicates the fibrous cap. Yellow and green lines which are vertical to the lumen border are maximum and minimal cap thickness respectively. **(D)** Plaque rupture and thrombus. Red line represents the lumen surface while red dash line indicates the lumen surface before plaque rupture. The white arc represent rupture circumferential extend, while yellow arc indicates thrombus circumferential distribution for generating the thrombus score. Line with arrowheads represents the depth of rupture. **(E)** Macrophages, cholesterol crystals, and microchannels. The bigger arrow points to the cholesterol crystals while the smaller arrow points to the microchannel. Arcs indicate the arc of macrophages.

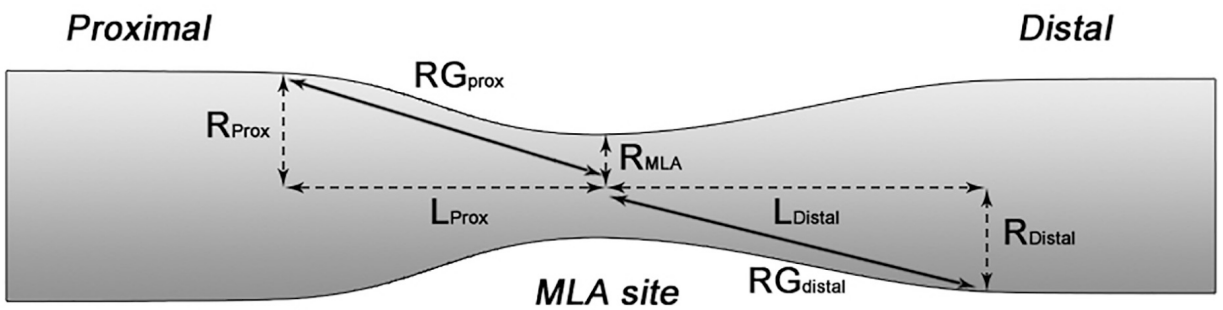

FIGURE 2 | Schematic diagram showing the calculation of RG $RG_{prox} = (R_{Prox}\text{-}R_{MLA})/L_{Prox}$ while $RG_{distal} = (R_{Distal}\text{-}R_{MLA})/L_{Distal}$.

Computational Fluid and Solid Mechanics Analysis

The two models were meshed with tetrahedral and prismatic cells for CFD analyses using ANSYS Workbench (version 2019 R3, ANSYS Inc., Cannonsburg, MI, United States). For the wall domain, the model was cut in half in reference to the symmetry plane, in order to reduce the computational cost. The resolution of computational meshes were

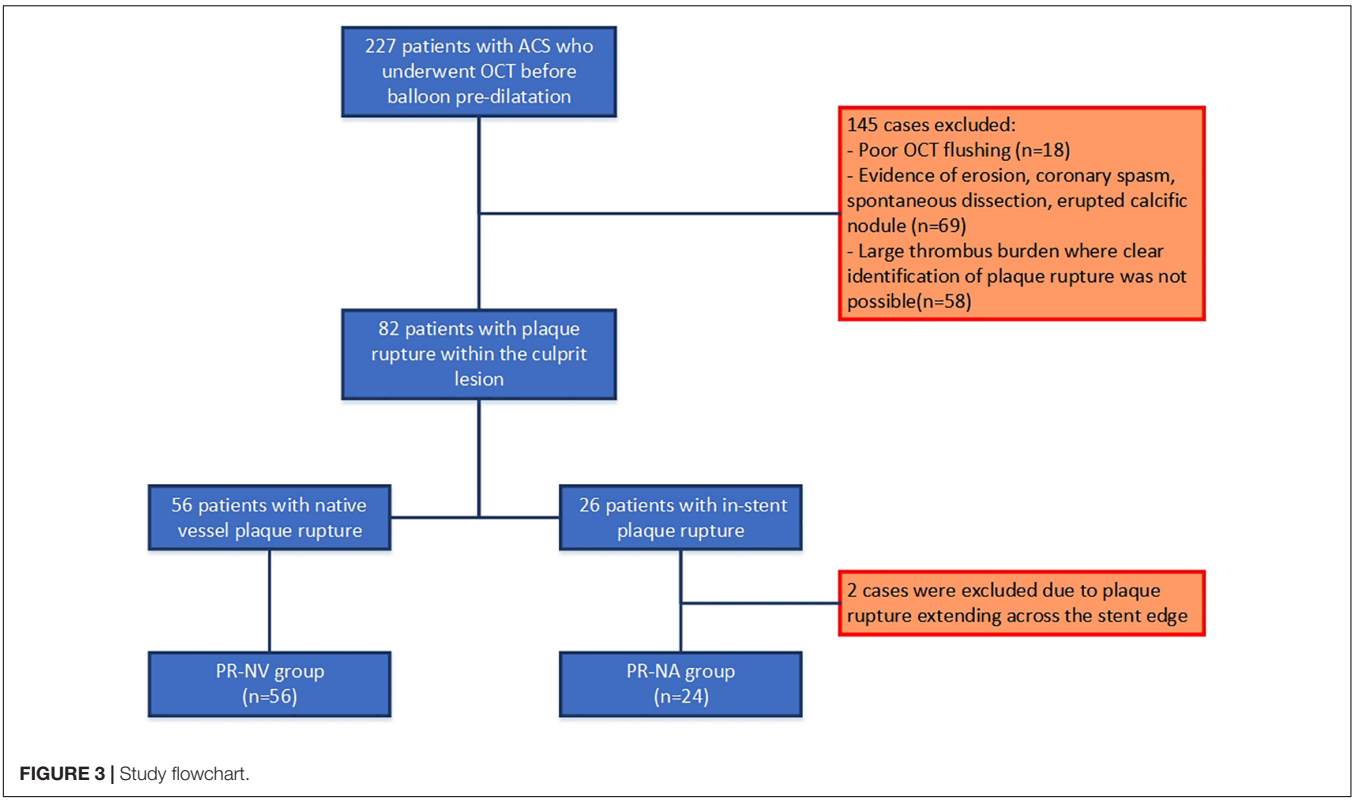

FIGURE 3 | Study flowchart.

determined through mesh convergence test, and the final model had 114,150 elements in the lumen and 5,563,033 elements in the wall.

The lumen model was used to compute the ESS by solving the 3D incompressible Navier-Stokes equations using ANSYS CFX. The blood was assumed to be homogeneous and Newtonian fluid with dynamic viscosity of 0.0035 Pa s and a density of 1,050 kg/m^3. Blood flow was considered to be incompressible and laminar, and steady state condition was assumed. A parabolic velocity profile was specified at the inlet, with 1 ml/s normal coronary inflow for both PR-NV and PR-NV cases (24). At the outlet of each model, a pressure of 100 mmHg representing normal coronary blood pressure was applied. The vessel wall of the two models was considered to be rigid and no-slip conditions were applied at the luminal surface.

The PSS in the neointima or in the plaque was computed using ANSYS Mechanical which solves force equilibrium equations. It was assumed that the pressure on the lumen-wall interface was originated from both static blood pressure and flow stream. The proximal and distal end of the PR-NV and PR-NA models were fixed in space. A 5-parameter Mooney Rivlin non-linear hyperelastic material model (25) was used for the lipid and fibrous components of neointima and the native vessel wall, while stent struts were modeled as a linear elastic material with elastic modulus 243 GPa and Poisson's ratio 0.29 assuming the material is L605 Co-Cr alloy (26). All computational analyses were conducted on a desktop workstation (Dell Precision 5120, 3.7 GHz Intel Core i9, 128 GB RAM).

Statistical Analysis

Continuous data are presented as mean ± SD if normally distributed, otherwise as median and interquartile range (IQR). Categorical data are expressed as absolute values and percentages. *T*-test was used to compare continues variables if these were normally distributed and Mann–Whitney U-test when variables were not normally distributed; comparison of categorical variables were performed using χ^2 test. Analysis was performed using MedCalc Statistical Software version 18.2.1 (MedCalc Software bvba, Ostend, Belgium). A *p*-value of <0.05 was assumed to be statistically significantly.

RESULTS

Clinical Data of Study Population

Two hundred twenty-seven patients presented with an acute myocardial infarction who underwent OCT before culprit lesion pre-dilatation were considered eligible for recruitment. From these, we excluded patients with non-interpretable OCT due to suboptimal image quality or large thrombus burden, those who suffered an event because of plaque erosion, coronary spasm, spontaneous coronary dissection, or an erupted calcific nodule and two cases because the ruptured lesion was located at the edge of a stent and extended to the native vessel (**Figure 3**).

Therefore, 80 patients were included in the final analysis: 56 had a ruptured plaque in NV and 24 in NA segment. There was no significant difference in baseline demographics between the

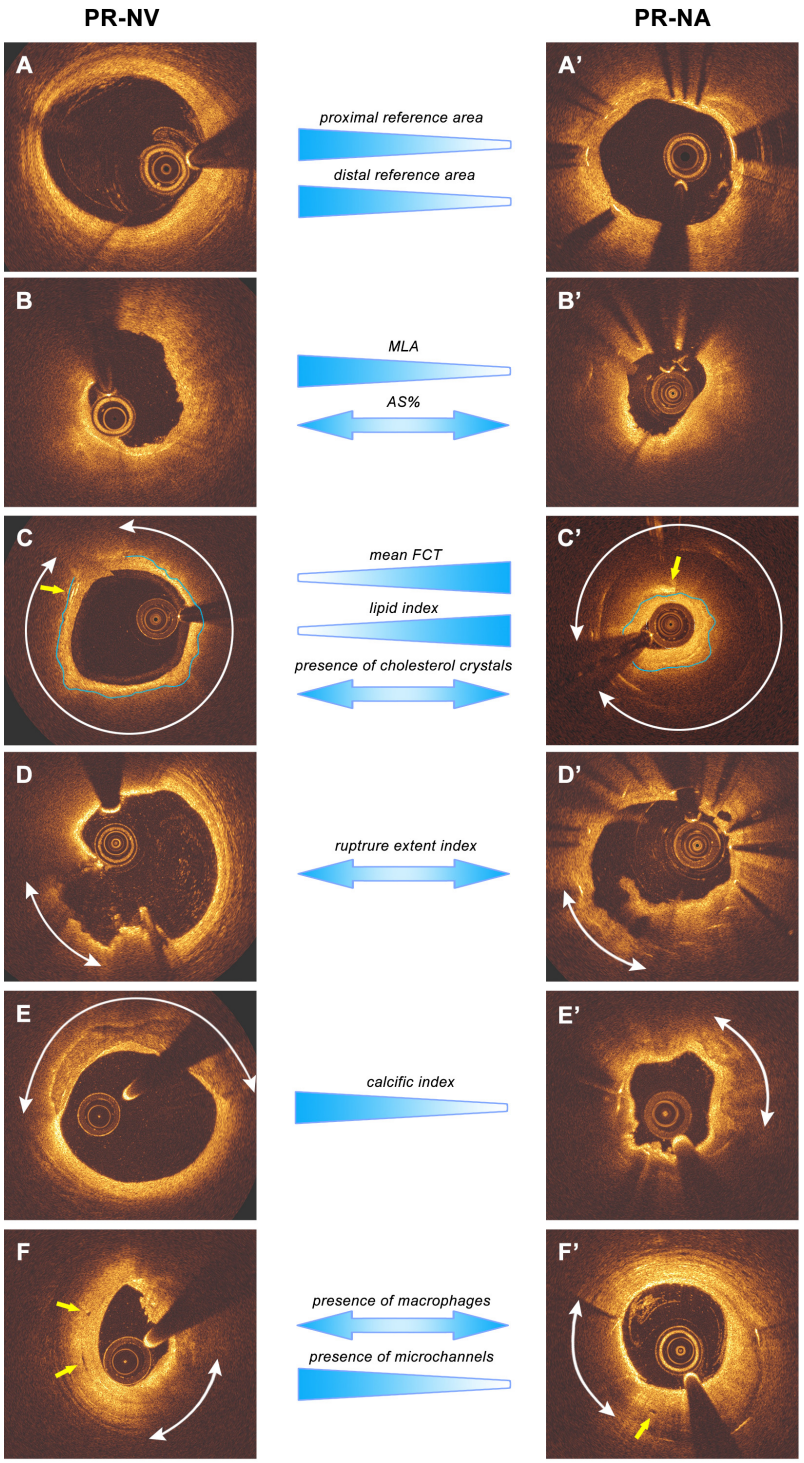

FIGURE 4 | Main results of lesion level-analysis and representative images. The images are presented as pairs from PR-NV and PR-NA groups. **(A,A′)** The reference segment, PR-NV group had larger proximal and distal reference area. **(B,B′)** The MLA site, PR-NV group reveals larger MLA than PR-NA group, while the two groups have similar AS%. **(C,C′)** Typical fibroatheroma and cholesterol crystals images, arcs indicate the lipid tissue while the yellow arrows are pointing at the cholesterol crystals. Blue lines draw the fibrous cap. PR-NV group reveals smaller mean FCT and lipid index, but similar incidence of cholesterol crystals compares to PR-NA group. **(D,D′)** Representative plaque rupture images, arcs indicate the ruptured cavity, PR-NV group reveals similar rupture extend index with PR-NA group. **(E,E′)** Typical calcification images. Arcs indicate the calcific tissue, PR-NV groups had bigger calcific index than PR-NA group. **(F,F′)** Macrophages and microchannels. Yellow arrows are pointing to the microchannels while arcs indicate the macrophages. PR-NV group has similar incidence of macrophages but more incidence of microchannels than PR-NA group.

two groups except the medication therapy at the event including anti-platelet therapy (defined as continuously taken of either aspirin or P2Y12 inhibitor or both at the event) and statin usage (**Table 1**). Thrombus aspiration was used in 23 cases (41.1%) in the PR-NV group and 11 patients (45.8%) in the PR-NA group (p = 0.693), while glycoprotein IIb/IIIa inhibitors were used during PCI in 14 (25.0%) and 12 patients (50.0%), respectively (p = 0.029).

OCT Analysis

Lesion Level-Analysis

There was no significant difference in lesion length, area stenosis, phenotype, and number of ruptured sites in the two groups. However, PR-NV lesions had a larger MLA, lager reference areas and smaller mean FCT and small lipid index compared to PR-NA lesions (**Table 2**). Moreover, the calcific index and the incidence of calcium and microchannels was higher in the PR-NV than the PR-NA group. Conversely, the incidence of macrophages, cholesterol crystals and thrombus were similar in the two groups. Likewise, there were no differences between groups in the length of plaque rupture, the mean arc of rupture, or the rupture extent index as well as the up- and downstream RG, whereas the maximum depth of rupture was greater in the PR-NV group (**Figure 4**).

TABLE 1 | Baseline demographics of the studied population.

	PR-NV group (n = 56)	PR-NA group (n = 24)	p-Value
Mean age (years)	64.5 ± 13.1	66.7 ± 12.8	0.911
Males	45 (80.4)	19 (79.2)	0.904
Clinical characteristics			
Diabetes	16 (28.6)	6 (25.0)	0.745
Hypertension	29 (51.8)	14 (58.3)	0.593
Hyperlipidemia	30 (53.6)	17 (70.8)	0.153
Current smoking	19 (33.9)	5 (20.8)	0.245
Previous MI	10 (17.9)	9 (37.5)	0.060
Clinical presentation			0.117
STEMI	29 (51.8)	17 (70.8)	
NSTEMI	27 (48.2)	7 (29.2)	
Medications at the time of the event			
Anti-platelet therapy	26 (46.4)	18 (75.0)	**0.019**
Aspirin	21 (37.5)	17 (70.8)	**0.006**
P2Y12 inhibitor	5 (8.9)	5 (20.8)	0.157
Statins	27 (48.2)	19 (79.2)	**0.010**
ACEI/ARB	24 (42.9)	15 (62.5)	0.144
β-Blockers	19 (33.9)	14 (58.3)	0.051
Culprit vessel			0.896
LAD	29 (51.8)	14 (58.3)	
LCx	12 (21.4)	3 (12.5)	
RCA	15 (26.8)	7 (29.2)	

Values are presented as n (%) or mean ± SD. MI, myocardial infarction; STEMI, ST-segment elevation myocardial infarction; NSTEMI, non-ST-segment elevation myocardial infarction; ACEI, angiotensin converting enzyme inhibitors; ARB, angiotensin receptor blocker; LAD, left anterior descending; LCx, left circumflex artery; RCA, right coronary artery. The values in bold type indicate that they are statistically significantly with p-value of <0.05.

TABLE 2 | Geometrical and morphological characteristics of the ruptured plaques in the native and stented segments.

	PR-NV group (n = 56)	PR-NA group (n = 24)	p-Value
Lesion-level analysis			
Geometrical characteristics			
Lesion length (mm)	16.3 ± 6.0	14.8 ± 11.1	0.532
MLA (mm^2)	2.93 ± 2.03	2.00 ± 1.26	**0.015**
Proximal reference area (mm^2)	9.21 ± 4.11	5.80 ± 2.99	**<0.001**
Distal reference area (mm^2)	7.78 ± 3.87	4.96 ± 2.11	**0.001**
Area stenosis (%)	66.4 ± 15.4	61.6 ± 18.1	0.227
Upstream RG	0.111 ± 0.069	0.105 ± 0.076	0.768
Downstream RG	0.112 ± 0.093	0.121 ± 0.117	0.715
Morphological characteristics			
TCFA phenotype (n, %)	41 (73.2)	14 (58.3)	0.191
ThCFA phenotype (n, %)	13 (23.2)	9 (37.5)	0.406
Minimal FCT (μm)	49 ± 22	60 ± 38	0.222
Mean FCT (μm)	186 ± 65	232 ± 80	**0.009**
Mean lipid arc (°)	150.5 ± 49.4	167.3 ± 34.0	0.141
Lipid length (mm)	6.1 ± 5.3	7.8 ± 8.6	0.280
Lipid index	62.2 ± 49.1	97.4 ± 47.8	0.005
Presence of calcific tissue (n, %)	31 (55.4)	5 (20.8)	**0.005**
Mean arc of calcific tissue (°)	62.8 ± 31.0	79.2 ± 14.7	0.309
Calcific index	29.9 ± 34.1	10.0 ± 4.0	**0.004**
Presence of macrophages (n, %)	52 (92.9)	21 (87.5)	0.440
Spotted macrophages (n, %)	50 (89.3)	20 (83.3)	0.464
Lined macrophages (n, %)	48 (85.7)	18 (75.0)	0.251
Lined macrophages index	12.1 ± 11.1	26.6 ± 33.9	0.091
Presence of cholesterol crystals (n, %)	19 (34.5)	8 (33.0)	0.917
Presence of microchannels (n, %)	23 (41.4)	3 (12.5)	**0.013**
Number of rupture sites	1.1 ± 0.4	1.2 ± 0.4	0.473
Length of plaque rupture (mm)	2.4 ± 2.2	1.9 ± 2.0	0.359
Depth of plaque rupture (mm)	0.9 ± 0.5	0.6 ± 0.3	**0.036**
Arc of rupture (°)	58.7 ± 35.1	64.7 ± 31.5	0.476
Rupture extent index	0.8 ± 1.2	0.7 ± 0.6	0.544
Presence of thrombus (n, %)	43 (76.8)	21 (87.5)	0.275
Thrombus score	21.8 ± 18.3	21.5 ± 17.3	0.948
Frame-level analysis	n = 2,307	N = 903	
Frames portraying TCFA (n, %)	391 (16.9)	121 (13.4)	**0.014**
Frames portraying ThCFA (n, %)	458(19.9)	344 (38.1)	**<0.001**
Frames portraying calcific tissue (n, %)	433 (18.8)	20 (2.2)	**<0.001**
Frames portraying macrophages (n, %)	735 (31.9)	222 (24.6)	**<0.001**
Frames portraying spotted macrophages (n, %)	440 (19.1)	112 (12.4)	**<0.001**
Frames portraying lined macrophages (n, %)	411 (17.8)	138 (15.3)	0.087
Frames portraying microchannels (n, %)	84 (3.6)	28 (3.1)	0.453
Frames portraying cholesterol crystals (n, %)	40 (1.7)	30 (3.3)	**0.006**
Frames portraying plaque rupture (n, %)	334 (14.5)	114 (12.6)	0.173
Frames portraying thrombus (n, %)	576 (25.0)	232 (25.7)	0.671

Results are presented at a lesion- and frame-level. MLA, minimum lumen area; RG, radius gradient; TCFA, thin cap fibroatheroma; ThCFA, thick cap fibroatheroma; FCT, fibrous cap thickness. The values in bold type indicate that they are statistically significantly with p-value of <0.05.

Frame-Level Analysis

Frame-level analysis showed that PR-NV lesions had more frames with a lipid-rich plaque covered by a thin fibrous cap and more frames covered by a thick cap and portrayed more often calcific tissue, spotted macrophages and less often cholesterol crystals than PR-NA lesions (**Table 2**).

Plaque Rupture Location Analysis

Most of plaque ruptures occurred at the throat followed by the upstream region in both native and neoatherosclerotic lesions (for the longitudinal distribution of plaque rupture $p = 0.098$). The distance plaque rupture to MLA was similar in the two groups (**Table 3**). In addition, there was no differences between groups in the circumferential location of plaque rupture (center vs. shoulder of the plaque, 33 vs. 31 in NV group, and 12 vs. 17 in NA group, $p = 0.363$)

TABLE 3 | Location of plaque rupture.

	PR-NV group (*n* = 56)	PR-NA group (*n* = 24)	*p*-Value
Distance to MLA site (mm)	3.6 ± 3.9	2.6 ± 3.6	0.679
Upstream (*n*, %)	26 (40.6)	5 (17.2)	
Center (*n*, %)	18 (28.1)	2 (6.9)	
Shoulder (*n*, %)	8 (12.5)	3 (10.3)	
Throat (*n*, %)	30 (46.9)	20 (69.0)	
Center (*n*, %)	12 (18.8)	10 (34.5)	
Shoulder (*n*, %)	18 (28.1)	10 (34.5)	
Downstream (*n*, %)	8 (12.5)	4 (13.8)	
Center (*n*, %)	3 (4.7)	0 (0)	
Shoulder (*n*, %)	5 (7.8)	4 (13.8)	

Computational Physiological Analysis

The reconstructed native and stented models are shown in **Figure 5**. The pressure drop across the native model was 0.95 mmHg, and 2.03 mmHg in the stented model (**Figure 5A**). The maximum ESS value was higher in the stented model (19.1 vs. 11.0 Pa) and the minimum ESS was lower in the native model (0.32 vs. 0.04 Pa). The maximum ESS value was noted in both models at the MLA; 28.5% of the culprit lesion model in the stented segment and 9.0% of the culprit lesion model in NV was exposed to high ESS (>7 Pa) (27). Furthermore, ESS was higher in the stented model over the minimum FCT which in both models were located proximally to the MLA (**Figure 5B**).

Plaque structural stress analysis showed significant differences in the two models. The maximum superficial (≤200 μm depth) PSS was noted in both models over the thinner segment of the fibrous cap proximally to the MLA and this was 95.1 kPa in the native and 38.8 kPa in the stented segment. This was also the maximum PSS value in the native culprit plaque; in the stented culprit lesion the highest plaque structural stress was noted in deeper layers in the vicinity of stent struts where its maximum value was 58.7 kPa (**Figures 5C,D**).

DISCUSSION

In this study we examined for the first time the morphological and physiological characteristics of lesions located in native and stented segments that ruptured causing a cardiovascular event. We found that (1) there are significant morphological differences between these two groups: ruptured plaques in native segments had larger reference and MLA, an increased calcific tissue component, a thinner fibrous cap, smaller lipid index, and more neo-vessels than the neoatherosclerotic plaques that ruptured and (2) that these morphological differences had an effect of lesion physiology leading to higher ESS and lower superficial PSS in the neoatherosclerotic lesions.

Plaque rupture is considered the main cause of ACS accounting for two thirds of the cardiovascular events (28). Several intravascular imaging studies, over the last years, attempted to assess the morphological characteristics of lesions that ruptured in native segments and caused events showing that these lesions have a small MLA, increased plaque burden and lipid component that is covered by a thin fibrous cap and are often exhibit macrophages accumulations and neovessels (21, 29–31). Conversely, there is lack of evidence about the morphological characteristics of ruptured neoatherosclerotic lesions. In the present analysis we found significant geometrical differences between the lesions in the PR-NV and PR-NA group. Native lesions had a larger MLA and reference lumen areas; this should be attributed that the fact that the vessel wall can remodel and accommodate the developed plaque and to fact that the neoatherosclerotic lesions were developed within stents that were implanted to treat obstructive plaques. Conversely, there were no differences between these groups in lesion length, upstream and downstream RG and the area stenosis. Ruptured neoatherosclerotic lesions similarly to the native lesions were lipid-rich, infiltrated by macrophages and often exhibited cholesterol crystals. On the other hand, the incidence of calcific tissue and micro-channels was lower and the FCT was increased while the lipid index was higher in the PR-NA group; these findings indicate that these lesions ruptured earlier after their development compared to the native that their generation begins in childhood.

Recent data indicate that the pathophysiological pathways that are involved in neoatherosclerotic lesion formation are different to those that regulate plaque evolution in native segments. These include the vessel wall injury post stent implantation, the delayed vascular healing and the endothelial barrier dysfunction caused by the antiproliferative drugs (32, 33), the unfavorable local hemodynamic milieu induced by the protruding struts post stent implantation, that create flow disturbances and recirculation zones in the vicinity of the struts (34), and the vascular inflammation caused by the polymer of the stent (4). The outcome of these processes is the formation of intraplaque hemorrhage derived from the lumen and the accumulation of foamy macrophages in the peri-strut regions that apoptose leading to necrotic core formation (35). In addition, to these mechanisms systemic factors and the patients' cardiovascular profile and vulnerability seem also to be involved and expedite neoatherosclerotic lesion formation (6–9).

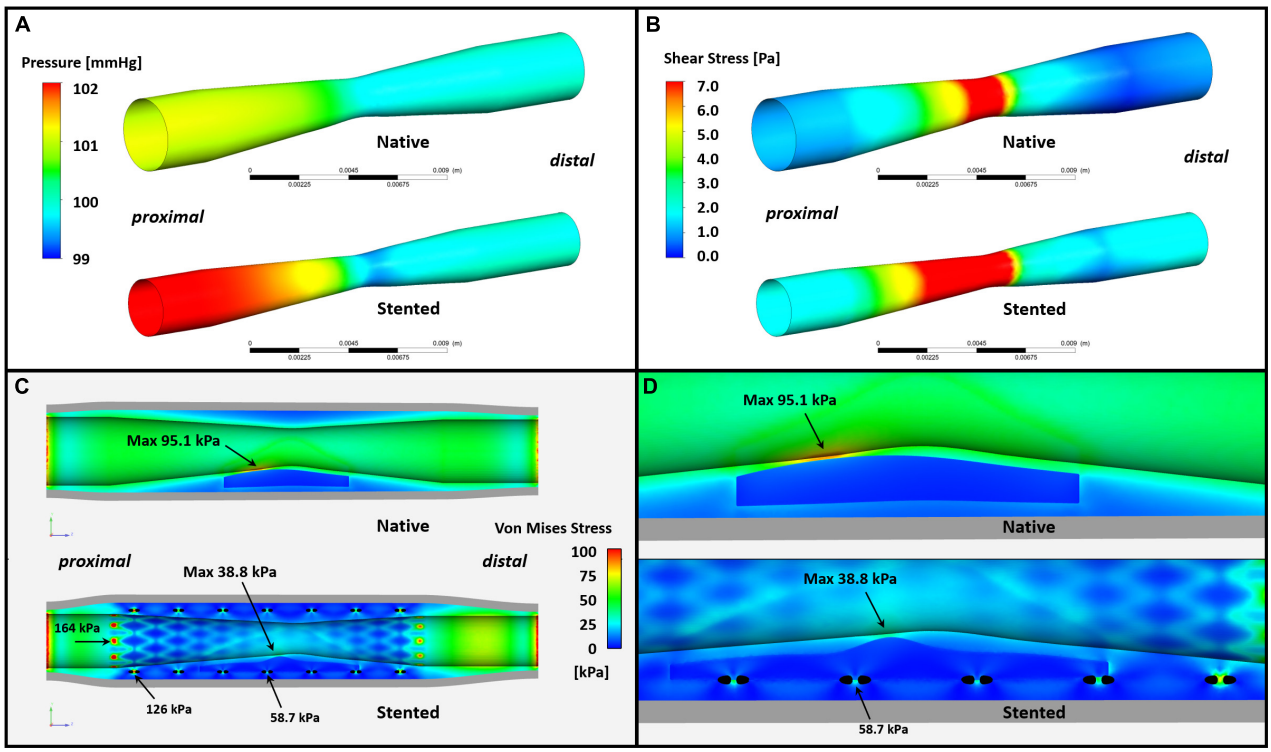

FIGURE 5 | Computational physiological analysis results. **(A)** The pressure drop across the model is 0.95 and 2.03 mmHg for native and stented vessel, respectively. **(B)** ESS distribution of the vessel. The stented model reveals higher maximum and minimum ESS value (19.1 vs. 11.0 Pa and 0.32 vs. 0.04 Pa, respectively). The maximum ESS value was located main at the MLA in both two models and 28.5% of the culprit lesion model in the stented segment and 9.0% of the culprit lesion model in NV was exposed to high ESS (>7 Pa). **(C,D)** PSS analysis results. The maximum superficial PSS in both models were over the thinner segment of the fibrous cap proximally to the MLA and was 95.1 kPa in the native and 38.8 kPa in the stented segment. A total of 95.1 kPa was also the maximum PSS value of the native model while in the stented model the highest PSS was 58.7 kPa in the vicinity of stent struts.

Although several studies have shed light onto the pathophysiological pathways that regulate vulnerable plaque development within the stents, there is limited data about the processes that contribute to their destabilization and rupture. In native lesions, local hemodynamic forces distribution seems to play a pivotal role on the final act of atherosclerosis. More specifically, high ESS promotes nitric oxide synthesis resulting in proteolytic degradation of the fibrous cap, inhibits extracellular matrix synthesis and upregulate smooth muscle cell apoptosis and vascular inflammation leading to fibrous cap thinning and fragility (36, 37). Moreover, PSS has a pivotal role on plaque destabilization as it promotes metalloproteinase synthesis, macrophages accumulation, smooth muscle cell apoptosis, and intraplaque hemorrhage (38–41) and is also considered as the main instigator of plaque rupture (42).

In contrast to the NV in stented segments there is limited evidence about the implications of the local hemodynamic forces on vulnerable plaque formation. Two recent reports have shown that low ESS is a predictor of lipid-rich neointima and neointima inflammation and are associated with the formation of neoatherosclerotic lesions, while high ESS appear to contribute to their destabilization and rupture (14, 43). However, both studies have significant limitations as they included a small number of patients, they made assumptions about vessel geometry post stent implantation, as the baseline intravascular imaging data were not available, and did not assess the PSS and its implication on neoatherosclerotic evolution.

In this analysis we examined for the first time the effect of PSS on neoatherosclerotic plaque rupture. We generated a representative idealized geometry of the culprit lesion before its rupture in native and stented segments and process this with CFD techniques to assess ESS and PSS distribution. We found high ESS values in both geometries with similar ESS distribution and the maximum ESS at the MLA; however, the ESS values were numerically higher in the stented segment. This should be attributed to the smaller MLA in this model. The higher ESS in the neoatherosclerotic lesions is likely to have clinical implications, expedite collagen degradation in the fibrous cap leading to its earlier destabilization compared to the native lesions. This hypothesis may not be supported by the FCT that is numerically higher in the stent geometry; however, it has to be acknowledged that OCT is unable to assess fibrous cap composition and the density of the collagen fibers. Conversely, the superficial PSS was higher in the native model; this should be attributed to the smaller lumen dimensions in the stent model and the fact that the neoatherosclerotic lesions were caged by the deployed stents. Stent struts also affect PSS in the deeper layers of neointima with high PSS values noted at their borders. This

may influence neoatherosclerotic lesion formation but also to its destabilization as increased PSS promotes neovessels rupture and intraplaque hemorrhage (40).

Limitations

Several limitations of the present analysis should be acknowledged. Firstly, the number of the included native and especially of the neoatherosclerotic ruptured plaques is relatively small. This should be attributed to the fact that we included only lesions that were not pre-dilated before OCT imaging and that we excluded 33.5% of the lesions because of insufficient OCT image quality that prohibited image segmentation or because it was not possible to identify the cause the event (plaque rupture vs. plaque erosion vs. calcific nodule). The strict inclusion criteria provided confidence about our findings but may have also introduced bias; nevertheless, it is reassuring that our results in the native lesions are in agreement with those reported in the literature (22). Secondly, the type of stent implanted in the PR-NA group was not always available. Thus it was not possible to assess the effect of different strut configuration polymer and drug elution on the morphological characteristics in the culprit neoatherosclerotic lesions. Thirdly, CFD analysis was performed in a representative idealized model of the stented and native lesions and not in the entire dataset. Therefore, it was not possible to examine the effect of specific morphological characteristics, seen in different lesions, on the distribution of the local hemodynamic forces. This would enable a more accurate assessment of the local hemodynamic milieu and would allow more accurate comparisons between groups. However, this analysis was not feasible as segment reconstruction could not be performed in all frames of the studied lesions, because of the increased thrombus burden and would require increased computational time and resources. Finally, we approximated tissue mechanical properties based on the published literature, and the vessel geometry before rupture as OCT imaging data were not available before the event. Considering however, that prospective large-scale studies that will include asymptomatic patients who will undergo OCT imaging in native and stented segments – so as to capture the morphological features of vulnerable plaques before their rupture – is unlikely to be feasible in future, we believe that the present analysis is important, and it provides valuable mechanistic insights about the role of ESS and PSS on neoatherosclerotic lesion destabilization.

CONCLUSION

Neoatherosclerotic lesions that ruptured, and caused events have significant morphological differences from the culprit lesions in native segments. These differences affect local hemodynamic forces distribution resulting in higher ESS and lower superficial PSS in the neoatherosclerotic plaques. These findings highlight the need to conduct large intravascular- and CFD-based studies to better understand the pathophysiological mechanisms that regulate neoatherosclerotic lesion formation and destabilization.

DATA AVAILABILITY STATEMENT

The original contributions presented in the study are included in the article/supplementary material, further inquiries can be directed to the corresponding author.

ETHICS STATEMENT

Ethical review and approval was not required for this study on human participants in accordance with local legislation and institutional requirements. Written informed consent for participation was not required for this study because the data was anonymized and the study retrospective in nature.

AUTHOR CONTRIBUTIONS

CB, AM, LR, and AB contributed to conception and design of the study. CJ, CL, KK, RR, ME, JA, and GK organized the database. CJ, CB, AR, and VT performed OCT analysis. RT and YT performed the CFD analysis. CJ and CB did the statistical analysis. CJ wrote the first draft of the manuscript. AR, VT, NY, TC, JC, and CO'M wrote sections of the manuscript. All authors contributed to manuscript revision, read, and approved the submitted version.

REFERENCES

1. Boden WE, O'Rourke RA, Teo KK, Hartigan PM, Maron DJ, Kostuk WJ, et al. Optimal medical therapy with or without PCI for stable coronary disease. *N Engl J Med.* (2007) 356:1503–16. doi: 10.1056/NEJMoa070829
2. Dalby M, Bouzamondo A, Lechat P, Montalescot G. Transfer for primary angioplasty versus immediate thrombolysis in acute myocardial infarction: a meta-analysis. *Circulation.* (2003) 108:1809–14. doi: 10.1161/01.CIR.0000091088.63921.8C
3. Fox KA, Clayton TC, Damman P, Pocock SJ, de Winter RJ, Tijssen JG, et al. Long-term outcome of a routine versus selective invasive strategy in patients with non-ST-segment elevation acute coronary syndrome a meta-analysis of individual patient data. *J Am Coll Cardiol.* (2010) 55:2435–45. doi: 10.1016/j.jacc.2010.03.007
4. Otsuka F, Byrne RA, Yahagi K, Mori H, Ladich E, Fowler DR, et al. Neoatherosclerosis: overview of histopathologic findings and implications for intravascular imaging assessment. *Eur Heart J.* (2015) 36:2147–59. doi: 10.1093/eurheartj/ehv205
5. Joner M, Koppara T, Byrne RA, Castellanos MI, Lewerich J, Novotny J, et al. Neoatherosclerosis in patients with coronary stent thrombosis: findings from optical coherence tomography imaging (A Report of the PRESTIGE Consortium). *JACC Cardiovasc Interv.* (2018) 11:1340–50. doi: 10.1016/j.jcin.2018.02.029
6. Ali ZA, Roleder T, Narula J, Mohanty BD, Baber U, Kovacic JC, et al. Increased thin-cap neoatheroma and periprocedural myocardial infarction in drug-eluting stent restenosis: multimodality intravascular imaging of drug-eluting and bare-metal stents. *Circ Cardiovasc Interv.* (2013) 6:507–17. doi: 10.1161/CIRCINTERVENTIONS.112.000248
7. Yonetsu T, Kato K, Kim SJ, Xing L, Jia H, McNulty I, et al. Predictors for neoatherosclerosis: a retrospective observational study from the optical coherence tomography registry. *Circ Cardiovasc Imaging.* (2012) 5:660–6. doi: 10.1161/CIRCIMAGING.112.976167

8. Kim C, Kim BK, Lee SY, Shin DH, Kim JS, Ko YG, et al. Incidence, clinical presentation, and predictors of early neoatherosclerosis after drug-eluting stent implantation. *Am Heart J.* (2015) 170:591–7. doi: 10.1016/j.ahj.2015.06.005
9. Taniwaki M, Windecker S, Zaugg S, Stefanini GG, Baumgartner S, Zanchin T, et al. The association between in-stent neoatherosclerosis and native coronary artery disease progression: a long-term angiographic and optical coherence tomography cohort study. *Eur Heart J.* (2015) 36:2167–76. doi: 10.1093/eurheartj/ehv227
10. Stettler R, Dijkstra J, Raber L, Torii R, Zhang YJ, Karanasos A, et al. Neointima and neoatherosclerotic characteristics in bare metal and first- and second-generation drug-eluting stents in patients admitted with cardiovascular events attributed to stent failure: an optical coherence tomography study. *EuroIntervention.* (2018) 13:e1831–40. doi: 10.4244/EIJ-D-17-00051
11. Niccoli G, Montone RA, Di Vito L, Gramegna M, Refaat H, Scalone G, et al. Plaque rupture and intact fibrous cap assessed by optical coherence tomography portend different outcomes in patients with acute coronary syndrome. *Eur Heart J.* (2015) 36:1377–84. doi: 10.1093/eurheartj/ehv029
12. Ramasamy A, Ng J, White S, Johnson TW, Foin N, Girard MJA, et al. Efficacy and reproducibility of attenuation-compensated optical coherence tomography for assessing external elastic membrane border and plaque composition in native and stented segments- an in vivo and histology-based study. *Circ J.* (2019) 84:91–100. doi: 10.1253/circj.CJ-19-0630
13. Raber L, Koskinas KC, Yamaji K, Taniwaki M, Roffi M, Holmvang L, et al. Changes in coronary plaque composition in patients with acute myocardial infarction treated with high-intensity statin therapy (IBIS-4): a serial optical coherence tomography study. *JACC Cardiovasc Imaging.* (2019) 12:1518–28. doi: 10.1016/j.jcmg.2018.08.024
14. Torii R, Stettler R, Raber L, Zhang YJ, Karanasos A, Dijkstra J, et al. Implications of the local hemodynamic forces on the formation and destabilization of neoatherosclerotic lesions. *Int J Cardiol.* (2018) 272:7–12. doi: 10.1016/j.ijcard.2018.06.065
15. Tearney GJ, Regar E, Akasaka T, Adriaenssens T, Barlis P, Bezerra HG, et al. Consensus standards for acquisition, measurement, and reporting of intravascular optical coherence tomography studies: a report from the international working group for intravascular optical coherence tomography standardization and validation. *J Am Coll Cardiol.* (2012) 59:1058–72. doi: 10.1016/j.jacc.2011.09.079
16. Radu MD, Yamaji K, Garcia-Garcia HM, Zaugg S, Taniwaki M, Koskinas KC, et al. Variability in the measurement of minimum fibrous cap thickness and reproducibility of fibroatheroma classification by optical coherence tomography using manual versus semi-automatic assessment. *EuroIntervention.* (2016) 12:e987–97. doi: 10.4244/EIJV12I8A162
17. Katayama Y, Tanaka A, Taruya A, Kashiwagi M, Nishiguchi T, Ozaki Y, et al. Feasibility and clinical significance of in vivo cholesterol crystal detection using optical coherence tomography. *Arterioscler Thromb Vasc Biol.* (2020) 40:220–9. doi: 10.1161/ATVBAHA.119.312934
18. Prati F, Capodanno D, Pawlowski T, Ramazzotti V, Albertucci M, La Manna A, et al. Local delivery versus intracoronary infusion of abciximab in patients with acute coronary syndromes. *JACC Cardiovasc Interv.* (2010) 3:928–34. doi: 10.1016/j.jcin.2010.05.017
19. Bourantas CV, Serruys PW, Nakatani S, Zhang YJ, Farooq V, Diletti R, et al. Bioresorbable vascular scaffold treatment induces the formation of neointimal cap that seals the underlying plaque without compromising the luminal dimensions: a concept based on serial optical coherence tomography data. *EuroIntervention.* (2015) 11:746–56. doi: 10.4244/EIJY14M10_06
20. van der Giessen A, Wentzel J, Groen H, de Feyter P, van de Vosse FV, van der Steen A, et al. Location of plaque ulceration in human coronary arteries is related to shear stress. In: *Proceedings of the ASME Summer Bioengineering Conference*. New York, NY: ASME (2010). p. 31–2.
21. Higuma T, Soeda T, Abe N, Yamada M, Yokoyama H, Shibutani S, et al. A combined optical coherence tomography and intravascular ultrasound study on plaque rupture, plaque erosion, and calcified nodule in patients with ST-segment elevation myocardial infarction: incidence, morphologic characteristics, and outcomes after percutaneous coronary intervention. *JACC Cardiovasc Interv.* (2015) 8:1166–76. doi: 10.1016/j.jcin.2015.02.026
22. Lee JM, Choi G, Hwang D, Park J, Kim HJ, Doh JH, et al. Impact of longitudinal lesion geometry on location of plaque rupture and clinical presentations. *JACC Cardiovasc Imaging.* (2017) 10:677–88. doi: 10.1016/j.jcmg.2016.04.012
23. Fujii K, Mintz GS, Carlier SG, Costa J Jr., Kimura M, Sano K, et al. Intravascular ultrasound profile analysis of ruptured coronary plaques. *Am J Cardiol.* (2006) 98:429–35. doi: 10.1016/j.amjcard.2006.03.020
24. Nichols WW, O'Rourke M. *McDonald's Blood Flow in Arteries: Theoretical, Experimental and Clinical Principles*, 4th ed. London: Oxford University Press (1998). p. 170–200.
25. Teng Z, Brown AJ, Calvert PA, Parker RA, Obaid DR, Huang Y, et al. Coronary plaque structural stress is associated with plaque composition and subtype and higher in acute coronary syndrome: the BEACON I (Biomechanical Evaluation of Atheromatous Coronary Arteries) study. *Circ Cardiovasc Imaging.* (2014) 7:461–70. doi: 10.1161/CIRCIMAGING.113.001526
26. Tambaca J, Canic S, Kosor M, Fish RD, Paniagua D. Mechanical behavior of fully expanded commercially available endovascular coronary stents. *Tex Heart Inst J.* (2011) 38:491–501.
27. Gijsen F, Katagiri Y, Barlis P, Bourantas C, Collet C, Coskun U, et al. Expert recommendations on the assessment of wall shear stress in human coronary arteries: existing methodologies, technical considerations, and clinical applications. *Eur Heart J.* (2019) 40:3421–33. doi: 10.1093/eurheartj/ehz551
28. Kolte D, Yonetsu T, Ye JC, Libby P, Fuster V, Jang IK. Optical coherence tomography of plaque erosion: JACC focus seminar part 2/3. *J Am Coll Cardiol.* (2021) 78:1266–74. doi: 10.1016/j.jacc.2021.07.030
29. Aguirre AD, Arbab-Zadeh A, Soeda T, Fuster V, Jang IK. Optical coherence tomography of plaque vulnerability and rupture: JACC focus seminar Part 1/3. *J Am Coll Cardiol.* (2021) 78:1257–65. doi: 10.1016/j.jacc.2021.06.050
30. Tian J, Ren X, Vergallo R, Xing L, Yu H, Jia H, et al. Distinct morphological features of ruptured culprit plaque for acute coronary events compared to those with silent rupture and thin-cap fibroatheroma: a combined optical coherence tomography and intravascular ultrasound study. *J Am Coll Cardiol.* (2014) 63:2209–16. doi: 10.1016/j.jacc.2014.01.061
31. Fujiyoshi K, Minami Y, Ishida K, Kato A, Katsura A, Muramatsu Y, et al. Incidence, factors, and clinical significance of cholesterol crystals in coronary plaque: an optical coherence tomography study. *Atherosclerosis.* (2019) 283:79–84. doi: 10.1016/j.atherosclerosis.2019.02.009
32. Habib A, Karmali V, Polavarapu R, Akahori H, Cheng Q, Pachura K, et al. Sirolimus-FKBP12.6 impairs endothelial barrier function through protein kinase C-alpha activation and disruption of the p120-vascular endothelial cadherin interaction. *Arterioscler Thromb Vasc Biol.* (2013) 33:2425–31. doi: 10.1161/ATVBAHA.113.301659
33. Harari E, Guo L, Smith SL, Paek KH, Fernandez R, Sakamoto A, et al. Direct targeting of the mTOR (Mammalian Target of Rapamycin) Kinase improves endothelial permeability in drug-eluting stents-brief report. *Arterioscler Thromb Vasc Biol.* (2018) 38:2217–24. doi: 10.1161/ATVBAHA.118.311321
34. Bourantas CV, Papafaklis MI, Kotsia A, Farooq V, Muramatsu T, Gomez-Lara J, et al. Effect of the endothelial shear stress patterns on neointimal proliferation following drug-eluting bioresorbable vascular scaffold implantation: an optical coherence tomography study. *JACC Cardiovasc Interv.* (2014) 7:315–24. doi: 10.1016/j.jcin.2013.05.034
35. Yahagi K, Kolodgie FD, Otsuka F, Finn AV, Davis HR, Joner M, et al. Pathophysiology of native coronary, vein graft, and in-stent atherosclerosis. *Nat Rev Cardiol.* (2016) 13:79–98. doi: 10.1038/nrcardio.2015.164
36. Thondapu V, Bourantas CV, Foin N, Jang IK, Serruys PW, Barlis P. Biomechanical stress in coronary atherosclerosis: emerging insights from computational modelling. *Eur Heart J.* (2017) 38:81–92. doi: 10.1093/eurheartj/ehv689
37. Slager CJ, Wentzel JJ, Gijsen FJ, Thury A, van der Wal AC, Schaar JA, et al. The role of shear stress in the destabilization of vulnerable plaques and related therapeutic implications. *Nat Clin Pract Cardiovasc Med.* (2005) 2:456–64. doi: 10.1038/ncpcardio0298
38. Lee RT, Schoen FJ, Loree HM, Lark MW, Libby P. Circumferential stress and matrix metalloproteinase 1 in human coronary atherosclerosis. Implications for plaque rupture. *Arterioscler Thromb Vasc Biol.* (1996) 16:1070–3. doi: 10.1161/01.atv.16.8.1070
39. Hallow KM, Taylor WR, Rachev A, Vito RP. Markers of inflammation collocate with increased wall stress in human coronary arterial plaque.*Biomech Model Mechanobiol.* (2009) 8:473–86. doi: 10.1007/s10237-009-0151-8

40. Teng Z, He J, Degnan AJ, Chen S, Sadat U, Bahaei NS, et al. Critical mechanical conditions around neovessels in carotid atherosclerotic plaque may promote intraplaque hemorrhage. *Atherosclerosis.* (2012) 223:321–6. doi: 10.1016/j.atherosclerosis.2012.06.015
41. Rodriguez AI, Csanyi G, Ranayhossaini DJ, Feck DM, Blose KJ, Assatourian L, et al. MEF2B-Nox1 signaling is critical for stretch-induced phenotypic modulation of vascular smooth muscle cells. *Arterioscler Thromb Vasc Biol.* (2015) 35:430–8. doi: 10.1161/ATVBAHA.114.304936
42. Richardson PD, Davies MJ, Born GV. Influence of plaque configuration and stress distribution on fissuring of coronary atherosclerotic plaques. *Lancet.* (1989) 2:941–4. doi: 10.1016/s0140-6736(89)90953-7
43. Bourantas CV, Raber L, Zaugg S, Sakellarios A, Taniwaki M, Heg D, et al. Impact of local endothelial shear stress on neointima and plaque following stent implantation in patients with ST-elevation myocardial infarction: a subgroup-analysis of the COMFORTABLE AMI-IBIS 4 trial. *Int J Cardiol.* (2015) 186:178–85. doi: 10.1016/j.ijcard.2015.03.160

Conflict of Interest: The authors declare that the research was conducted in the absence of any commercial or financial relationships that could be construed as a potential conflict of interest.

Advantages of publishing in Frontiers

OPEN ACCESS
Articles are free to read for greatest visibility and readership

FAST PUBLICATION
Around 90 days from submission to decision

HIGH QUALITY PEER-REVIEW
Rigorous, collaborative, and constructive peer-review

TRANSPARENT PEER-REVIEW
Editors and reviewers acknowledged by name on published articles

Frontiers
Avenue du Tribunal-Fédéral 34
1005 Lausanne | Switzerland

Visit us: www.frontiersin.org
Contact us: frontiersin.org/about/contact

REPRODUCIBILITY OF RESEARCH
Support open data and methods to enhance research reproducibility

DIGITAL PUBLISHING
Articles designed for optimal readership across devices

FOLLOW US
@frontiersin

IMPACT METRICS
Advanced article metrics track visibility across digital media

EXTENSIVE PROMOTION
Marketing and promotion of impactful research

LOOP RESEARCH NETWORK
Our network increases your article's readership